Modélisation multi-échelle de l'insertion du 3H et du 36Cl dans les graphites UNGG

Christoph Lechner

NNT : 2018SACLX014

Modélisation multi-échelle de l'insertion du ^{3}H et du ^{36}Cl dans les graphites UNGG

Thèse de doctorat de l'Université Paris-Saclay
préparée à l'École Polytechnique

École doctorale n°573 Interfaces : approches interdisciplinaires, fondements, applications et innovation (Interfaces)
Spécialité de doctorat: Physique

Thèse présentée et soutenue à Palaiseau, le 24 janvier 2018, par

M Christoph Lechner

Composition du Jury :

Henri-Jean DROUHIN Professeur, École Polytechnique	Président
Mireille DEFRANCESCHI Dr. HdR, ExpChem	Rapporteur
Malcolm HEGGIE Professeur, Loughborough University	Rapporteur
Nathalie MONCOFFRE Directeur de Recherche CNRS, Université de Lyon	Examinateur
Xavier BLASE Directeur de Recherche CNRS, Institut Néel	Examinateur
Andrei POSTNIKOV Professeur, Université de Lorraine	Examinateur
Stéphane CATHERIN Ingénieur, ANDRA	Examinateur
Holger VACH Directeur de Recherche CNRS, École Polytechnique	Directeur de thèse
Philippe BARANEK Dr. Ingénieur-Chercheur, EDF R&D	Encadrant

Thèse de doctorat

Acknowledgments

Three years of working on a pretty challenging topic are now coming to an end. Many aspects of this PhD thesis would have been much more difficult without the help and support of many people.

My most significant thanks goes to Philippe Baranek, my tutor at EDF R&D. He was not only a big source of scientific advice and continuous support, but also helped me with all kinds of bureaucratic tasks.

I also would like to thank my PhD director Holger Vach for his scientific advice as well as his invaluable outside view for making this topic more approachable to a broader public.

I also thank Henri-Jean Drouhin for acting as the president of the defense, Mireille Defranceschi and Malcolm Heggie for accepting to be rapporteurs of this thesis as well as Nathalie Moncoffre, Xavier Blase, Andrei Postnikov, and Stéphane Catherin for accepting to be examinateurs at the PhD thesis defense.

I also want to thank Malcolm Heggie once more who has welcomed me into his home, has showed me the point of view of the UK regarding this topic, and has given me great feedback regarding my work. All of this helped me greatly in exploring new aspects I had not thought about before.

Thank you also to Alain Chartier and Laurent Van Brutzel who kindly provided me with their nanoporous model.
I also would like to thank my colleagues at EDF R&D Lab Les Renardières, notably the PhD students at the MAI, who created a comfortable work environment which allowed me to realize this work.

A great thank you goes to my family. Even though I might have lived far away from home in the last three years, they always were there for me when I needed them. I especially thank my father and mother for the numerous times they picked me up at the airport, were my private taxi when I needed to go somewhere, and showed nothing but love and support for me. I would also like to thank my brother and sister who also supported me in case I needed them. Although my visits at home were short, they always helped me recharge my batteries because of all of you!

Last but not least, I would like to thank my girlfriend Nina. Your continuous support through all these years has made all of this possible. You made many sacrifices to be there for me. You moved away from home and came to France to be together with me even though this would mean to give up so many things which were important to you. You were there for me in good and bad times. I hope that I can give back to you some day what you have given me in this last year where we lived together. Thank you!

Contents

Abbreviations

AFM	Atomic force microscopy
AGR	Advanced gas-cooled reactor
AIREBO	Adaptive intermolecular reactive bond order potential
ANDRA	French national radioactive waste management agency
ASN	French Nuclear Safety Authority
BSSE	Basis set superposition error
BSU	Basic structural unit
BUA1	Bugey
CCSD(T)	Coupled cluster with full treatment of singles and doubles and perturbative triples
CEA	Commissariat à l'énergie atomique et aux énergies alternatives
CHA	Chinon
DFT	Density functional theory
EDF	Électricité de France
FA	Faible activité
FA-VL	Faible activité vie longue
GGA	Generalized gradient approximation
GT	Groupe de travail
GTF	Gaussian type function
HA	Haute activité
HOPG	Highly oriented pyrolytic graphite
HRTEM	High-resolution transmission electron microscopy
LCBOP	Long-range carbon bond order potential
LDA	Local density approximation
LL-LW	Low level long-lived waste
MA	Moyenne activité
MD	Molecular dynamics
MFM	Magnetic force microscopy
MSD	Mean square deviation
NPT	Isothermal-isobaric ensemble
NVE	Microcanonical ensemble
NVT	Canonical ensemble
PBE	Perdew-Burke-Ernzerhof
PKA	Primary knock-on atom
RDF	Radial distribution function
REBO	Reactive bond order potential

RN	Radionuclide
SIMS	Secondary ion mass spectrometry
SKA	Secondary knock-on atom
SLA	Saint Laurent
STM	Scanning tunneling microscopy
TEM	Transmission electron microscopy
TFA	Très faible activité
UK	United Kingdom
UNGG	Uranium-Naturel-Graphite-Gaz
VC	Vie courte
VL	Vie longue
VTC	Vie très courte
XANES	X-ray absorption near edge structure
ZBL	Ziegler-Biersack-Littmarck potential

Introduction

The first generation of French nuclear power plants of the Uranium Naturel Graphite Gaz (UNGG) type were developed after the second world war in a collaboration between the Commissariat à l'énergie atomique et aux énergies alternatives (CEA) and the enterprise Électricité De France (EDF) to produce plutonium for military purposes as well as electricity for civil use. In France, nine reactors of this type were constructed between 1954 and 1972, three by CEA and six by EDF. All reactors were shut down in the 1980's and 1990's mostly due to economical reasons.

These reactors used graphite as neutron moderator and reflector. Their dismantlement will lead to 23000 tons of graphite waste. During reactor operation graphite has been subjected to the joint effects of temperature, neutron flux and its chemical environment. Impurities which were present at the trace level in graphite have been activated. Irradiated graphite is a nuclear waste classified as low-level waste (LW) and contains some long-lived radionuclides (VL) such as ^{36}Cl and ^{14}C.

In order to find an optimal solution for the waste management of irradiated graphite, a good knowledge of the properties of this waste and the radionuclides it contains is needed. Together with the French national radioactive waste management agency (ANDRA), the producers of these wastes (EDF, CEA) have conducted several experimental studies on the behavior of graphite waste in the framework of the Groupe de Travail "GT Graphite", co-funded by EDF, CEA, and ANDRA, which involves these organisms, academic partners, and research institutes. Within the GT Graphite, the focus was laid on studying the behavior of ^{14}C, ^{36}Cl, and ^{3}H in irradiated graphite. ^{14}C and ^{3}H are among the radionuclides contributing the most to the radiological inventory of graphites (about 10^4 Bq/g).

Concerning ^{36}Cl, even though it has a very low concentration in graphite (less than 20 Bq/g), the interest is due to its long half-life of 301000 years. It can be very mobile in clay which is the surrounding environment of the disposal sites and thus could impact their safety. To date, mainly experimental work has been performed, however, certain phenomena observed at the macroscopic scale are difficult to measure and interpret due to the low concentration of radionuclides. It has therefore been decided to launch a project which models these radionuclides in graphite. This theoretical approach can then provide additional information in order to understand the phenomena observed at the macroscopic scale. This modeling approach is a shared project between the CEA and EDF. The CEA focuses on ^{14}C and the evolution of the microstructure of graphite under irradiation, whereas EDF investigates the physico-chemical properties and the diffusion of ^{3}H and ^{36}Cl in graphite and at the grain boundaries.

This thesis is carried out within the framework of said modeling project. By conducting a multi-scale approach, properties that involve different length- and time scales can be investigated. On the smallest scale, accurate *ab initio* methods

can be applied to study the stability of ^{3}H and ^{36}Cl in bulk graphite as well as on different graphite surfaces. In a next step, these results can be used to develop an approximate interaction potential which is computationally more efficient than *ab initio* methods. This step is important in order to link the two length scales of graphite models. Then, in a third step the insertion of ^{3}H and ^{36}Cl at high energies (> 1 keV) and their diffusion can be studied in large complex structures of UNGG graphite while locally reproducing the *ab initio* results. Different model structures of nuclear graphite such as crystallite surfaces, grain boundaries, and nanoporous graphite will be investigated. These models represent different environments that exist in UNGG graphite; studying them could help to possibly identify preferential trapping sites. The effects of temperature and irradiation on micro- and macroscopically observable phenomena will be studied. Finally, a link between the theoretical data and experimental results will be established in order to provide helpful complementary information to the existing knowledge on the behavior of ^{3}H and ^{36}Cl in irradiated UNGG graphite.

Chapter 1

General Context

In the following chapter the context of this study is presented. First, the history of the French reactors of the UNGG (Uranium-Naturel-Graphite-Gaz) type is discussed. This is followed by an explanation of the functioning of these reactors. Finally, the strategies for the dismantlement as well as the waste management are presented.

1.1 History of UNGG Reactors [BB06]

After the second world war France decided to independently develop a nuclear generating capability for military and civil use of nuclear energy. Due to the well-established graphite industry in France as well as the lack of heavy water or enrichment facilities, graphite was chosen as the moderator. This allowed the use of natural unenriched uranium metal as nuclear fuel, since graphite absorbs few neutrons.

In total 9 UNGG reactors were built in France, in Table 1.1 the location and duration of operation of these reactors are given. The first 3 were operated by the CEA (Commissariat à l'énergie atomique et aux énergies alternatives), Marcoule G1, G2, and G3. They were used for production of weapons-grade plutonium. Marcoule G1 was the only air cooled reactor, all other UNGG reactors used CO_2. 6 were operated by EDF (Électricité de France), Chinon A1, A2, A3, called CHA1/2/3, St. Laurent A1 and A2, called SLA1/2, and Bugey 1, called BUA1. A reactor with SLA1's design was exported to Spain and operated by the French-Spanish company Hifrensa, Vandellos 1. All of these were used for electricity generation. Only G2/G3 and SLA1/2, respectively were duplicated, all other reactors were first generation prototypes [Bas89], the different designs will be explained later on.

In 1968 the planning of a UNGG reactor in Fessenheim was stopped and the

Table 1.1: List of French UNGG reactors [Bas93].

Site	Reactor	Start of operation	Shutdown
Marcoule	G1	1956	1958
	G2	1959	1980
	G3	1960	1984
Chinon	CHA1	1963	1973
	CHA2	1965	1985
	CHA3	1966	1990
St. Laurent-des-Eaux	SLA1	1969	1990
	SLA2	1971	1992
Bugey	BUA1	1972	1994

UNGG reactor design was finally abandoned. Instead, the pressurized water reactor (PWR) design was adopted which constituted the second generation of nuclear reactors. This design was preferred due to an increased power output of over 500 MW. All UNGG reactors of EDF were shut down due to economical reasons, the others due to technical reasons [Bas96].

1.2 Functioning of UNGG Reactors [Bas93, BB06]

In Figure 1.1, the design of the power plant SLA2 is shown. In short, nuclear power plants convert heat generated by nuclear fission to electricity via steam generation which drives a turbine connected to a generator.

The three principal constituents of a nuclear reactor are the nuclear fuel, the moderator, and the coolant which are explained in detail further down. For the design of SLA1/SLA2/BUA1, the nuclear reactor is surrounded by a concrete vessel which protects the outside from radiation and fission products but also protects the inside from external impacts. Another layer of security are the two separated heat exchange circuits. For UNGG reactors, the reactor core is cooled by CO_2 in the primary circuit which is contained within the core. Via heat exchangers the heat is transferred to a second circuit where water is converted to steam which then drives the turbine and is condensed again to water in a condenser. The turbine is connected to a electricity-producing generator.

Since the UNGG reactors were first generation reactors, some design details changed and were optimized as the experience in construction and operation of the reactors increased. The evolution of the reactor design will be presented later on.

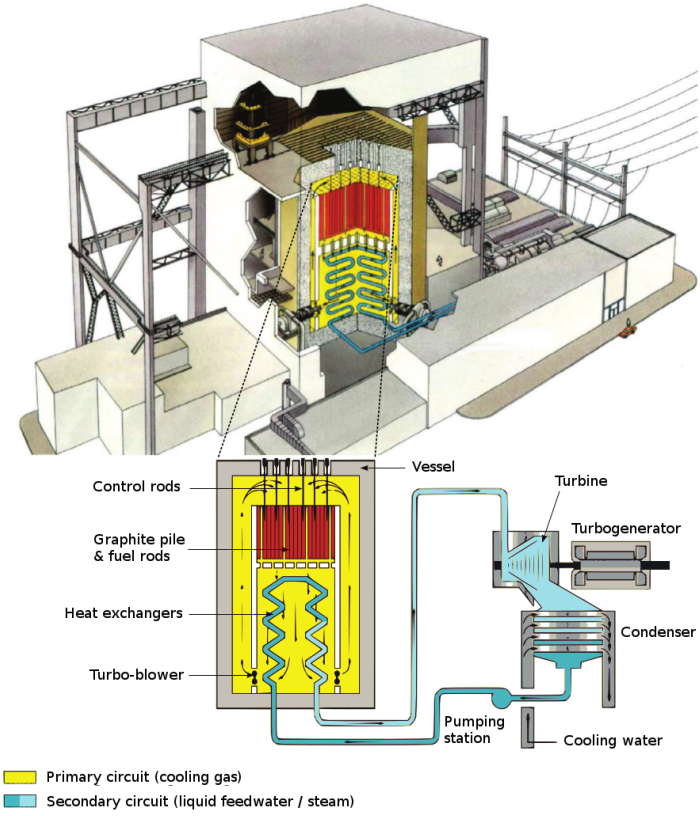

Figure 1.1: Design of a UNGG reactor of the type SLA2 [Pet09].

1.2.1 Nuclear Fuel [Ner79, BB06]

The underlying principle of energy generation in nuclear reactors is the induced fission of ^{235}U by neutron bombardment. This isotope's natural abundance is 0.72%. It is the only fissile U isotope which means that it is able to sustain a chain reaction. The nuclear cross section of ^{235}U (probability of fission) is 584.994 barns for slow thermal neutrons which have an energy of 0.025 eV and about 1 barn for fast neutrons which have an energy on the order of 1 MeV. When ^{235}U is hit by a neutron and fission occurs, the reaction is as following:

$$^{235}\mathrm{U} + {}^{1}\mathrm{n} \longrightarrow {}^{236}\mathrm{U} \longrightarrow \mathrm{X} + \mathrm{Y} + \mathrm{z}\,{}^{1}\mathrm{n} + \mathrm{E}. \tag{1.1}$$

For only about 18% of neutron captures of ^{235}U, ^{236}U is the product. The large majority of neutron captures (82 %) results in fission which releases a large amount of energy on the order of 200 MeV. This high energy release is a major advantage of nuclear reactors; one gram of ^{235}U can yield the same amount of energy as several tons of coal.

In addition, fission products X and Y are generated such as ^{85}Kr, ^{90}Sr, ^{99}Tc, ^{129}I, or ^{137}Cs. These products are not stable either and decay via different types of decay which also releases energy.

Finally, depending on the fission products, z neutron are created; as long as one neutron again induces fission of ^{235}U the chain reaction is sustained (a moderator is needed for this, see section 1.2.2). On average 2.48 neutrons are released by fission of ^{235}U. Their kinetic energies are in the range of 0-10 MeV, the average energy is about 2 MeV.

Figure 1.2 shows the assembly of a fuel element with graphite sleeve of SLA1/2 (and Vandellos) [IAE06]. All UNGG reactors used natural uranium metal as nuclear fuel in the form of an alloy to improve mechanical properties [Bas89]. The metallic form was needed since the uranium was not enriched. The nuclear fuel was placed in a cladding made of an MgZr alloy (0.6 % Zr). The cladding's purpose was to prevent release of fission products and avoid direct contact of the uranium metal and the gas phase [Bas89, Bas93]. Together, they were put inside a graphite sleeve. A graphite support fixed in the center by stainless steel wires assured their stability inside the block. The gas passed through the void between the sleeve and the cladding; the cladding had fins to improve the heat exchange.

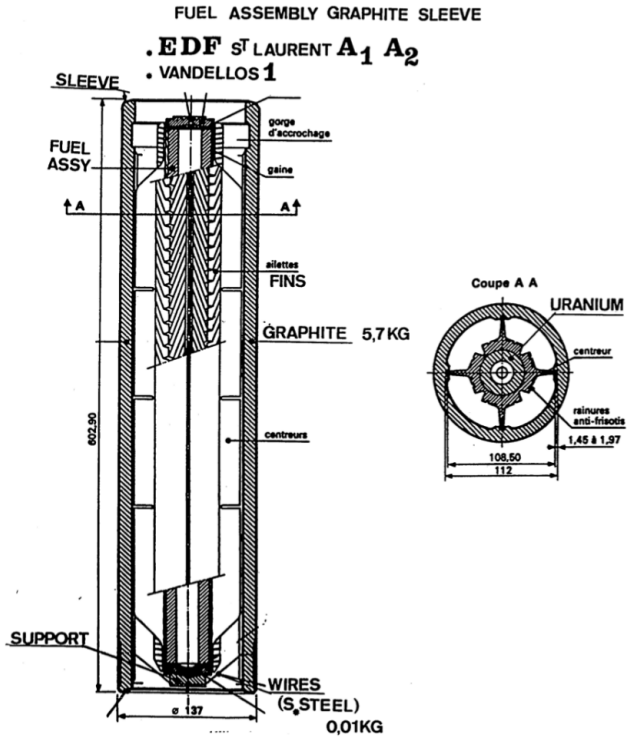

Figure 1.2: Fuel assembly of the type SLA1/2 (and Vandellos) [IAE06].

Since natural uranium contains less fissile ^{235}U compared to enriched uranium, much more nuclear fuel was used compared to more recent reactors to achieve an acceptable power output (430 t U for SLA2 vs. 114 t U for British AGR reactor Hinkley Point B) [BB06]. The choice of cladding material also imposed restrictions on the operating temperature (its melting temperature is 660 °C [Bas89]) which limited the net efficiency to about 29%.

About 2-3 channels containing fuel elements were replaced per day while the reactor was operating. This was performed with a sophisticated handling system which was placed above the reactor core.

1.2.2 Graphite Moderator [BB06]

Since ^{235}U has a much higher fission cross section for slow neutrons, a moderator is needed which reduces the speed of neutrons to ensure the continuity of the fission chain reaction. In order for the neutrons to slow down, they must collide with the moderator material. Thus a high neutron scattering cross section is preferable. However, materials can also absorb neutrons by neutron capture which is indicated by a high neutron absorption cross section. This is an undesired effect in nuclear reactors since they remove neutrons from the chain reaction. The scattering and absorption cross sections of ^{12}C are shown in Figure 1.3 [END]. Scattering is more likely by several orders of magnitude over the whole range of neutron energies in the reactor which makes graphite a suitable moderator. Other moderators in use are light water (H_2O) and heavy water (D_2O) which both have a higher scattering and absorption cross section. As stated in section 1.1, graphite was mostly used due to availability but also due to the use of unenriched uranium which makes a low neutron absorption necessary. Nowadays however, the majority of reactors uses H_2O as moderator [MS08] since uranium is enriched.

The lower scattering cross section compared to hydrogen lead to a rather large size of the moderator blocks. This together with the higher number of fuel rods was the reason for the very large reactor core. The power density was only about 1 $\mathrm{MW\,m^{-3}}$ which on one hand increased reactor safety but on the other hand reduced the economic efficiency of the power plant [BB06].

Pictures of a graphite pile and a graphite block are shown in Figure 1.4. Each graphite block had a cylindrical hole where the fuel was placed. The moderator was formed of hexagonal graphite blocks forming a cylindrical pile. For example in SLA2, the diameter of the pile was 15.7 m and its height was 10.2 m, its total mass amounted to 2680 t [BB06].

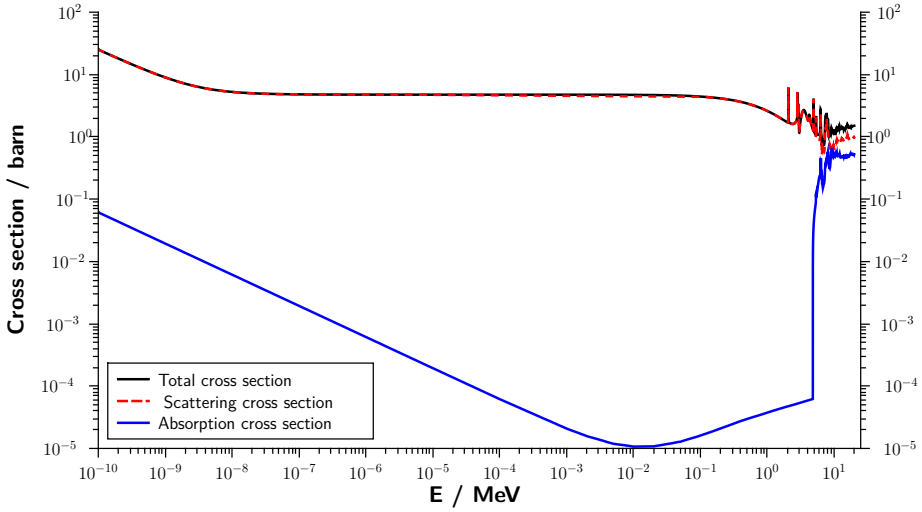

Figure 1.3: Total neutron cross section (black full line), scattering cross section (red dashed line), and absorption cross section (blue line) of ^{12}C with respect to the neutron energy [END].

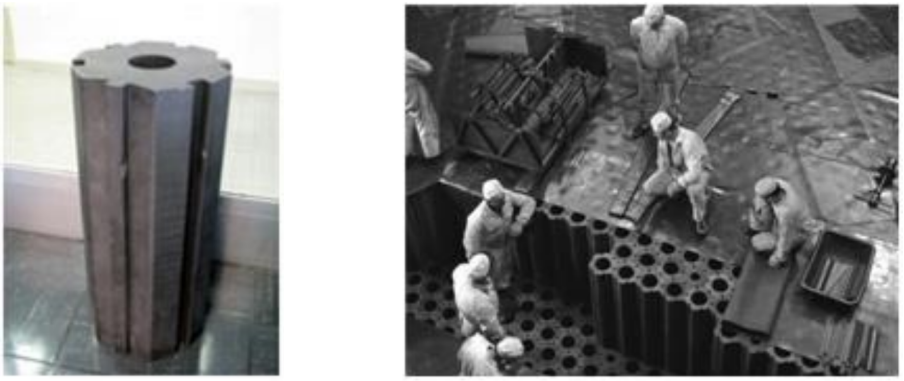

(a) (b)

Figure 1.4: a) Brick element of the graphite pile and b) construction of the graphite pile of Chinon A3 - Photothèque EDF [Pet09, PCP+15].

1.2.3 Coolant [BB06]

In UNGG reactors, CO_2 was chosen as cooling gas. The same choice was made for British MAGNOX and AGR reactors. It was used due to to its low cost, availability and well known properties in industry applications. For a gas, its heat

transfer properties are also rather good and neutron capture is very low. It also is compatible with the other components of the reactor. However, at temperatures > 650°C CO_2 can oxidize both, metals and graphite. When CO_2 is exposed to irradiation, radiolytic oxidation of other materials also plays an important role. These two processes are important with respect to the limits of the reactor operation conditions.

The majority of the cooling gas was CO_2, however several other species were also present in low concentrations. The composition of the gas is given in Table 1.2.

Table 1.2: Concentrations of different compounds in the cooling gas in vol.%.[Bla84] Note that the concentration of CH_4 is relatively high compared to other species due to its deliberate injection to reduce radiolytic oxidation (see section 2.3.5).

Compound	CO_2	CO	CH_4	O_2	H_2O	H_2
Concentration / vol%	97.43	2.50	5×10^{-4}	10^{-4}	10^{-4}	$5\text{-}100\times10^{-6}$

Since a gas has a significantly lower heat capacity than a liquid, the reactor operated at a high pressure (29 bar for SLA2) and a CO_2 flow rate of 8.6 t/s in order to transport the heat fast enough from the core to the heat exchangers [BB06]. This was achieved with four high performance turbo-blowers. In the case of SLA1/SLA2/BUA1, the reactor core was surrounded by a pre-stressed concrete vessel which was lined with 25 mm thick steel on the inside to prevent gas leakage from the reactor core due to the high pressure. In the coldest zones of the reactor (before passing the core) the gas had a temperature of about 200°, after passing the core its temperature increased to about 400°.

The heat was then transferred from the primary to the secondary cooling circuit via four CO_2-steam heat exchangers. The steam flow rate was about 0.6 t/s.

The gas was continuously analyzed for the presence of fission gases to detect failures of the cladding [BB06].

1.2.4 Evolution and Optimization of the Reactor Design

Since UNGG reactors were first generation reactors, most of them were prototypes with different designs (except G2/3 and SLA1/2). They were used to increase the experience and learn about the advantages and disadvantages of the different technologies. In Table 1.3, the different key characteristics of the reactors are given.

G1/2/3 used a vertical pile, all other reactors switched to a horizontal positioning [Bas93]. In order to increase the power output several changes were made.

Table 1.3: Key characteristics of the UNGG reactors. Net power output P in MW, Pile orientation (Orient.), total mass (m_{tot}) of graphite pile in tons, graphite temperature T in °C, type of coolant, its pressure p in bar, the direction of gas flow (gas fl.), heat exchanger (Heat ex.) location (integrated into the core or not), and nuclear fuel design [Bas89, Bas93, IAE06, Ven12].

Reactor	P	Graphite pile			Coolant				Fuel
		Orient.	m_{tot}	T	Type	p	Gas fl.	Heat ex.	
G1	2	horizontal	1200	30-230	Air	1	longitudinal	Not integr.	Slug
G2	38	horizontal	1300	140-400	CO_2	15	longitudinal	Not integr.	Slug
G3	38	horizontal	1300	140-400	CO_2	15	longitudinal	Not integr.	Slug
CHA1	70	vertical	1120	150-360	CO_2	25	ascending	Not integr.	Tube
CHA2	210	vertical	1650	190-390	CO_2	26.5	ascending	Not integr.	Tube
CHA3	480	vertical	2350	240-410	CO_2	26.5	ascending	Not integr.	Tube
SLA1	480	vertical	2572	230-430	CO_2	26.5	descending	Integr.	Tube
SLA2	515	vertical	2440	240-440	CO_2	28.5	descending	Integr.	Tube
BUA1	540	vertical	2039	220-450	CO_2	40	descending	Integr.	Ring

The number of fuel rods was increased which made an increase of the graphite pile size necessary. The operation temperature was increased to improve the heat exchange rate, the highest temperature of the graphite pile was 450°C. Due to this the gas pressure was also increased to a maximum of about 40 bar for BUA1 [Bas93]. For the horizontal piles the gas flowed in two directions, upwards for the earlier reactors G2/3 and CHA1-3 and downwards for the other three reactors.

The design of the fuel also changed in order to improve the power output and safety of the reactors [Bas89]. The type of alloy differed among the reactors, for G2/G3, SLA1, and BUA1 Sicral F1 was used which contains 700 ppm Al, 300 ppm Cr, and 100 ppm Si. For CHA1, an U-Mo 0.5 (0.5 % Mo) alloy and for CHA2/CHA3 and SLA 1 an U-Mo 1.1 (1.1 % Mo) alloy was used. The form of the fuel changed from a slug form (G2/G3) to tubes (CHA1-3, SLA1/2) and finally a ring (BUA1). The use of tubes increased the specific power, the ring form allowed cooling from two sides. Starting from SLA2 a graphite core was placed in the center of the nuclear fuel to increase the resistance to compression.

These improvements also lead to unwanted consequences. The high CO_2 pressure in BUA1 caused high amounts of radiolytic oxidation [PPB93]. This effect was minimized by adding CH_4 to the cooling gas, however a too high CH_4 concentration caused carbon deposits.

1.3 Dismantlement and Waste Management of UNGG Reactors [PCP+15]

The dismantlement of the UNGG reactors will lead to 23000 t of irradiated graphite waste. About 81 % of the waste stems from the graphite pile, the rest from the graphite sleeves. The worldwide total amount of graphite waste is about 250000 t; until today no country has found a long term solution for its waste management. In France, the majority of the irradiated graphite is classified as low level long-lived waste (LL-LW) which means that it has a low activity and contains radionuclides with a long half-life. In French, it is called FA-VL waste. However, the majority of the waste (in the form of the graphite pile) is still located inside the reactors as the dismantlement is not yet fully completed. The sleeves, which are operational waste are stored in silos. Currently two different options for permanent disposal are investigated. The different aspects of the dismantlement and waste management will be explained in detail in the following.

1.3.1 Low Level Long-lived Waste

Radioactive waste in France is classified with respect to two properties; the radioactivity and the half-life. In Figure 1.5 an overview of the different classes is given.

The radioactivity is measured in Becquerel (Bq) per gram or kilogram. In the case of graphite, the source of the radioactivity are radionuclides which were activated during the operation of the reactor. Other types of waste can also be radioactive due to contamination. The four different classification levels are high activity (HA = haute activité), intermediate activity (MA = moyenne activité), low activity (FA = faible activité) and very low activity (TFA = très faible activité).

The half-life is measured in suitable time units (days or years) and describes the time scale after which the radioactivity of the waste has halfed. In general there are three different classes, very short half-life (VTC = vie très courte), short half-life (VC = vie courte), and long half-life (VL= vie longue). However, only the last two are relevant to the waste management.

Besides irradiated graphite, the second major contributor to LL-LW waste is radiferous waste (containing radium) from mineral extraction processes of the chemical industry. Other sources are bitumen which contains radioactive mud, sealed radioactive sources from fire alarms or lightning rods, or various old objects containing radium (pharmaceuticals or radioluminescent materials), thorium (aircraft landing gear or helicopter gear-boxes), or uranium (formerly used as a pigment in ceramics).

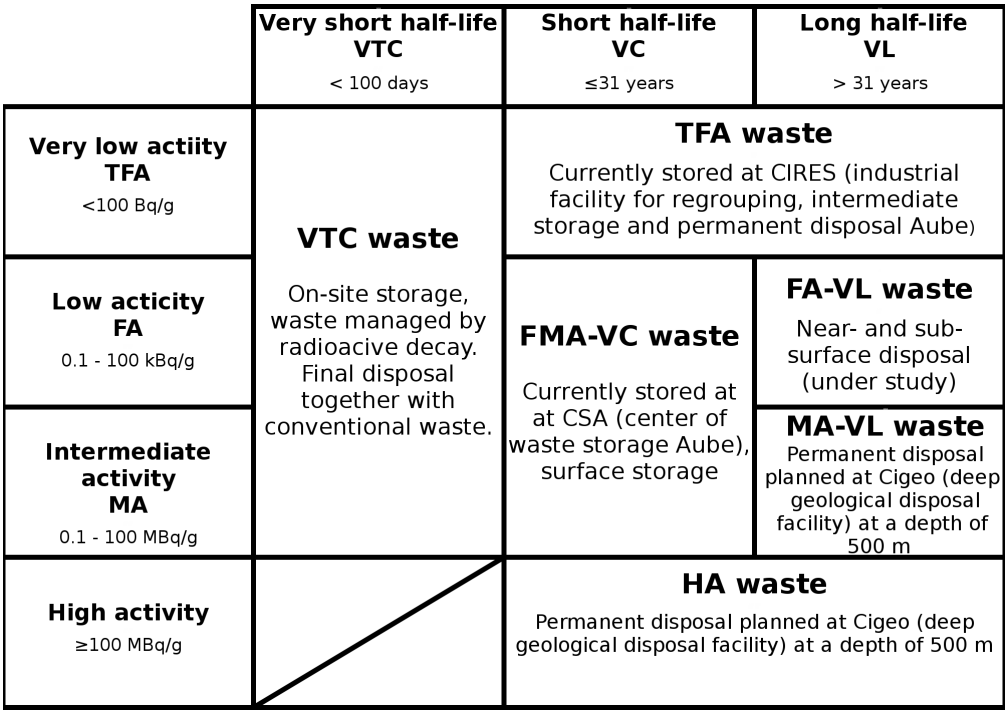

Figure 1.5: The different categories and waste management options of French radioactive waste [PCP+15]

.

1.3.2 Strategy until 2016

Dismantlement of Reactors

The shutdown and dismantlement of nuclear power plants consists of three levels [Ave05]. The complete dismantlement process spans over several decades. The three different levels are:

- Level I - Shutdown under surveillance: The power plant is fully closed down and nuclear fuel is unloaded and interimly stored in deactivation pools for 2-5 years. The circuits are drained and radioactive fluids are evacuated from the reactor. The barriers separating the core from the outside are kept in place. 99.9 % of the activity is removed.

- Level II - Partial decommissioning: Decontamination of buildings and equipment followed by the destruction of all buildings except for the reactor building. Material with medium or low activity is removed, the containment of the reactor building is dismantled to a minimum.

- Level III - Complete decommissioning: Dismantlement of heat exchangers and the reactor block followed by the destruction of the reactor building. All reactor elements with a significant radioactive level are evacuated.

All six UNGG reactors of EDF are in the final phase or close to the final phase of the second level [Pet09]. The reactor BUA1 was chosen as a pilot project for level III decommissioning. Within this project, this reactor would be the first to be fully dismantled and used to increase the experience and learn from the dismantlement process for the dismantlement of the other five reactors [Val17].

The dismantlement of the heavily irradiated upper part of the reactor vessel was planned under water and the lower part under air [Sil13]. The same dismantlement process was conceived for SLA1/2. For CHA1-2, a full dismantlement under air was needed since water could not be held back in the case of an accidental draining due to the reactor design. For CHA3, a final plan was not yet developed since dismantlement under water faced several problems due to its reactor design.

Waste Management Options for LL-LW Waste [PCP+15]

In the framework of the project FAVL all phases regarding the permanent disposal of LL-LW-classified waste are studied; from the search of a disposal site to the commissioning on the industrial scale. The project explicitly focuses on assuring the long-term safety of such disposal sites.

In 1993 even before the shutdown of the last UNGG reactor the French national radioactive waste management agency (ANDRA), which is responsible for the management of all French nuclear waste, was instructed to find a disposal solution for radiferous waste. Disposal strategies were developed which could show the feasibility of sub-surface disposal until in 2001 it was decided to extend the scope of this project to graphite waste. The total amount of waste (about 90000 m^3 graphite [AND15] and 45000 m^3 radiferous waste [AND15] in concrete packages) called for a solution on the industrial scale.

On June 26th, 2006 a law was passed demanding a focusing on permanent disposal solutions for radiferous and graphite waste in order to commission a suitable disposable site in 2013. Due to time constraints and difficulties in finding a suitable site, the commissioning was delayed to 2030.

Two options of permanent disposal are considered [AND15] which differ by their construction. After evaluating the geological features of the designated site

in Soulaine, the waste will be stored at a depth of 20-30 m for both options. The lower guard of clay is 20-30 m thick.

The first option would be a near-surface disposal (stockage avec terassement depuis la surface) where the topmost layers would be removed to access the disposal layer. After disposal of the waste, the previously extracted material would be used to cover the disposal layer (see Figure 1.6). The different types of waste would be separately disposed at adjacent disposal sites.

The second option would be a near-surface disposal (stockage en galerie souterraines) where excavated caves in the middle of the clay formation would serve as storage cells. They would be accessible through two tunnels to transport the waste. The waste packages would be disposed in longitudinal galleries (about 400 m length) which would be sealed when the site is fully exploited (see Figure 1.7).

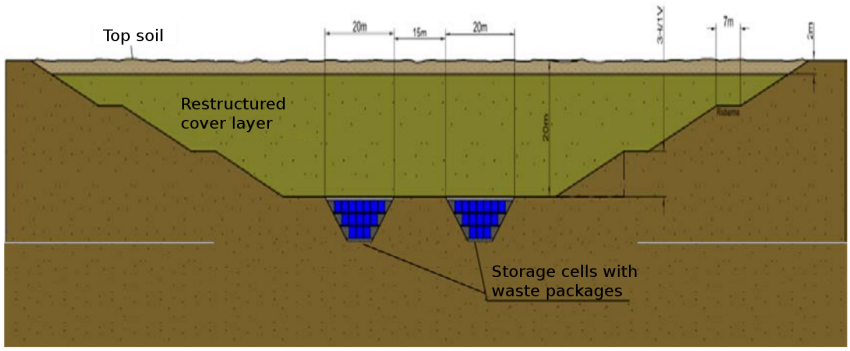

Figure 1.6: Schematic representations of the near-surface disposal with restructured cover layer [AND15].

Due to the earlier mentioned delays, in 2010 the French Nuclear Safety Authority ASN demanded ANDRA to re-evaluate other waste management options. In 2012, they presented some treatment scenarios before permanent disposal [AND12]. The first scenario would be sorting of graphite waste by its activity. Pile graphite would be disposed at the near-surface disposal site whereas more active sleeves would be disposed in a deep geological disposal facility [PCP$^+$15]. In the second scenario, radionuclides would be partially extracted by a heat or chemical treatment of the waste before disposal in order to reduce the activity whenever possible. The waste could then be disposed in near-surface disposal sites and the extracted radionuclides would be handled accordingly depending on their properties [PCP$^+$15]. The third option would be a complete destruction (gazification) of the graphite waste after decontamination. The waste treatment residues would be disposed in a deep geological disposal facility [AND12].

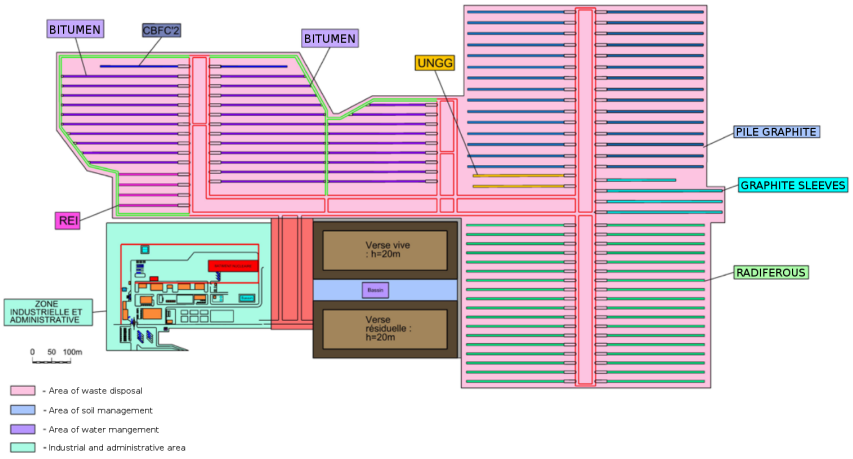

Figure 1.7: Schematic top view of the near-surface disposal with storage in subterranean galleries [AND15].

Radiological Inventory of Irradiated Graphite [PCP+15]

The management of graphite waste needs to be adapted not only to the global activity and half-life, but also to the different radionuclides that contribute to these two properties. This is important since the different radionuclides can have a completely different behavior with respect to the interaction with water, the air or the environment at a suitable site for permanent disposal.

Figure 1.8 shows the contributions of different radionuclides to the total activity with respect to time. The three radionuclides which are relevant to this work are ^{3}H, ^{14}C, and ^{36}Cl. For the other species, more information can be found in Ref. [IAE98].

^{3}H only contributes significantly to the total activity in the initial phase after shutdown. After 100 years it has passed over 7 half-life periods and is a negligible source. The high interest in its properties is due to the risk of its release during decommissioning of the reactor and preparation of the waste for permanent disposal.

^{14}C is the most important source of graphite's activity in the initial phase and due to its long half-life of about 5700 years its properties also need to be considered over a long period of time. Thus, it ultimately determines the size of an eventual storage site.

The initial contribution of ^{36}Cl is rather negligible, however its long half-life of 301000 years makes it the major contribution of radioactivity on the time scale of 100000s of years. In addition, its strong mobility in clay formations is an important concern.

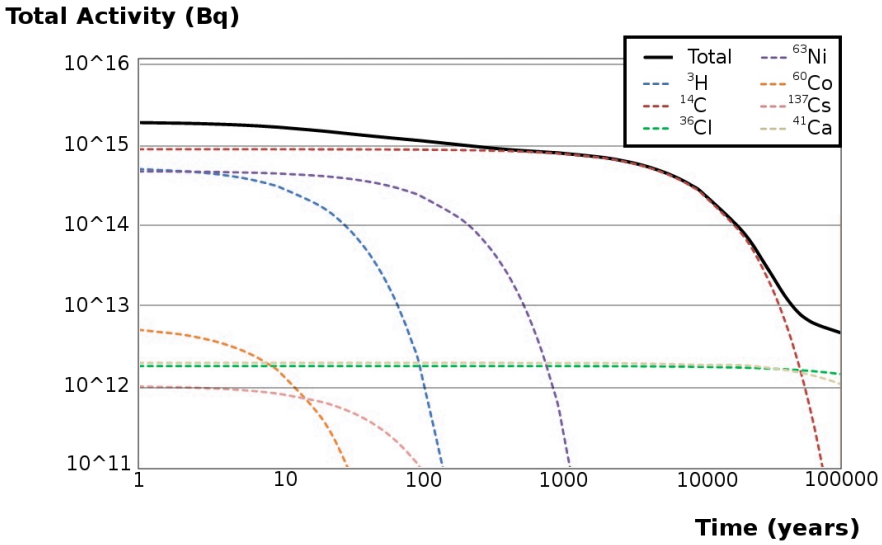

Figure 1.8: Decrease of the total activity of the graphite waste and the activity of specific radionuclides over time (starting from 2030). Note that this graph only contains waste of EDF and CEA sites [PCP+15].

1.3.3 Revised Strategy [ASN]

In 2016, EDF decided to revise the dismantlement process of the reactor core in order to conform to the new planning for the availability of a disposal for graphite waste. Instead of a partial dismantling under water, all reactors are planned to be dismantled exposed to air. This strategy change was proposed to the French nuclear security agency ASN on March 29th, 2016. As a consequence the complete decommissioning of several reactors would be postponed by several decades. In the following, ASN requested complementary informations before making a final decision regarding the new strategy. As of now the decision is still pending.

In the case of an approval, this would also have consequences for the issues concerning LL-LW waste. The postponing of the decommissioning would naturally also lead to a postponing of the permanent disposal of the waste. In particular, ^{3}H would already have decayed for multiple half-life periods. Thus, the risk of exposure to released ^{3}H during preparation for permanent disposal could be reduced.

Chapter 2

Properties of ^{3}H and ^{36}Cl in Nuclear Graphite - Literature Review

In this chapter, the current state of knowledge is reviewed. In the following, the differences of nuclear graphite with respect to a perfect monocrystal as well as its industrial synthesis are explained. During reactor operation, graphite is subjected to elevated temperatures and high energy radiation; both have an impact on the properties of graphite which is presented and discussed in this chapter. Furthermore, the origins and properties of ^{3}H and ^{36}Cl in nuclear graphite are described. Finally, the state of knowledge is summarized.

2.1 Properties of Nuclear Graphite

Graphite is the thermodynamically most stable allotrope of carbon under standard conditions [Lid91]. It is composed by a regular stacking of bidimensional hexagonal layers (graphene planes). The most stable stacking of carbon layers corresponds to the ABAB stacking shown in Figure 2.1. The corresponding crystal structure has the space group symmetry of $P6_3/mmc$; the unit cell geometry is fully defined by the **a** and **c** lattice parameters and the fractional coordinates of two non equivalent carbons $(0., 0., 1/4)$ and $(1/3, 2/3, 1/4)$, respectively. Within the graphitic planes, the carbons are covalently bound due to the sp^2 hybridization. At 300 K, **a** is 2.461 Å and the C-C bond length 1.421 Å [Don74]. In the **c**-direction there is only weak interlayer binding. This is supposed to arise from dispersion or van der Waals (vdW) interactions. Thus, **c** is much larger than **a**, at 300 K, it is 6.706 Å and the interlayer distance is 3.353 Å.

The semi-metallic character and highly anisotropic structure of graphite lead

to very interesting properties. It is an electrical and thermal conductor similar to a metal; however it is rather chemically inert. In addition, it has a melting point of 3800 K and lubricity that resembles more closely the one of a non-metallic compound. Highly oriented pyrolytic graphite (HOPG) is a material which resembles monocrystalline graphite the most, however it is polycrystalline and thus contains grain boundaries.

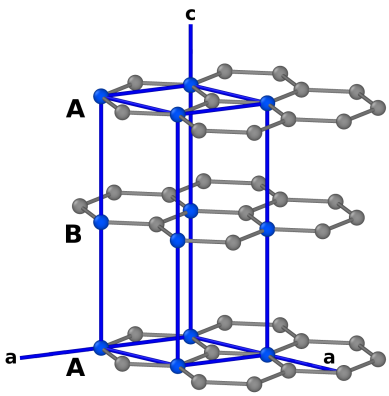

Figure 2.1: The structure of ABAB-stacked graphite with the hexagonal unit cell and the crystal axes **a** and **c**.

2.1.1 Multi-scale Structure

Nuclear graphite differs quite substantially from the previously discussed structure of a perfect monocrystal. It is a complex multi-scale material, a general scheme of this multi-scale structure is shown in Figure 2.2.

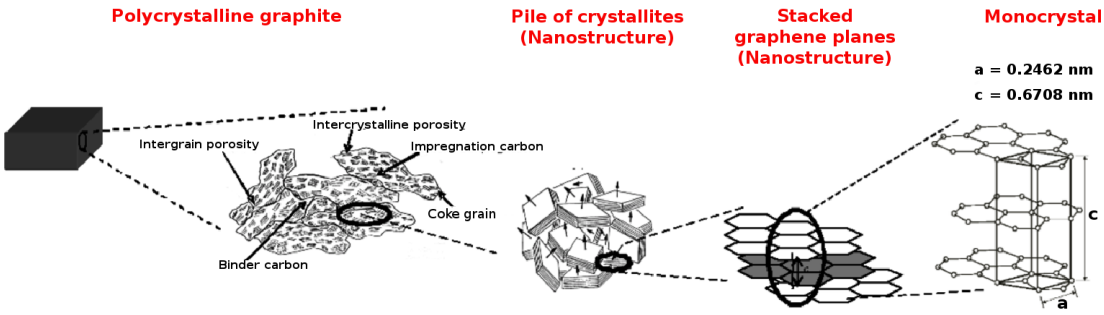

Figure 2.2: Schematic representation of the multi-scale structure of nuclear graphite.

On the largest scale, it consists of grains of graphitized coke, called filler particles, and a binder which is added to fill voids between coke grains. These two

parts are called filler and binder phase, respectively. Two types of coke grains are shown in Figure 2.3: needle coke with long coke grains (like needles) which are mostly aligened parallel with respect to each other and spherical coke where each grain has a structure resembling the layers of an onion. For UNGG graphite, mostly needle coke was used [PCP+15].

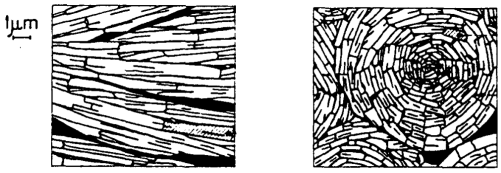

Figure 2.3: Two different types of coke, needle coke (left) and spherical onion-like coke (right) [Cor81].

Due to the two different phases, the material is also heterogeneous . In Figure 2.4 a polarised light micrograph of British "pile grade A" graphite which is similar to UNGG graphite is shown together with a schematic description of the two phases. This heterogeneity has an important influence on the material properties as well as on the location of trapped extrinsic defects. Deviations from the macroscopic average are found for both depending on the structural features of the studied sample. As can be seen in this picture, pores and cracks are characteristic macroscopic defects for nuclear graphite.

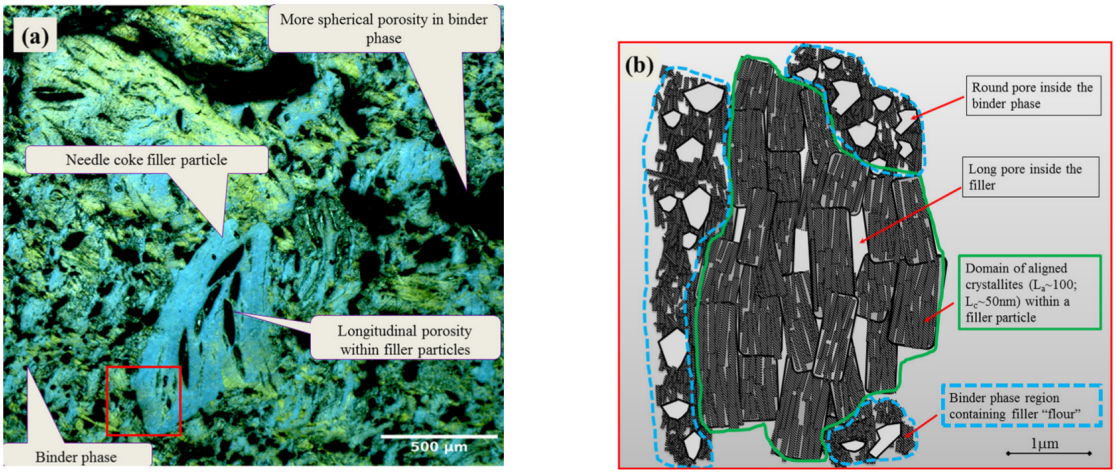

Figure 2.4: Polarised light micrograph of the heterogeneous structure of British "pile grade A" graphite [MFB+15].

They are formed during the fabrication process when volatile compounds are released by heating. In addition, the binder phase can not completely fill out

the free space between filler particles. The open pores build a three-dimensional network which is accessible to water or gaseous compounds. Closed pores also exist which are isolated from this network. The ratio between these two types depends on the used material for the production; for "Pile Grade A" graphite, which is similar in its properties to UNGG graphite, the open porosity accounts for about 20 % and the closed porosity for about 2-5% of the total volume of the material [PCP+15].

In Figure 2.5 an X-ray tomography of the porosity is shown for a graphite sample of a British reactor.

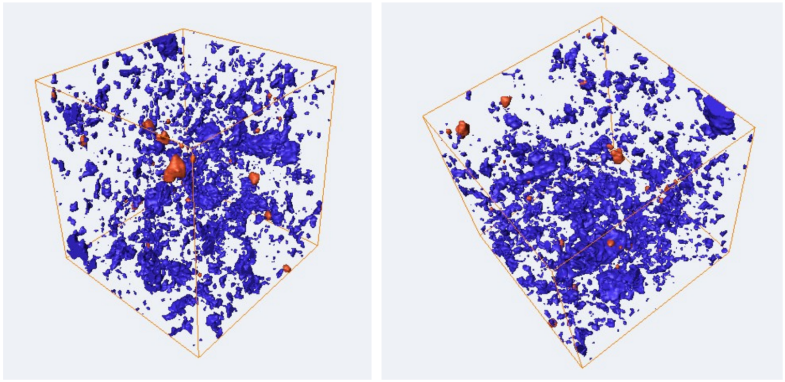

Figure 2.5: 3D volume reconstructions of BEPO graphite obtained by X-ray tomography [McD11].

The porosity also leads to a decreased density of nuclear graphite compared to a perfect monocrystal ($\rho = 2.27$ g/cm^3). Depending on the fabrication (see section 2.2), impregnation steps were performed to reduce the porosity and increase the density; the density of UNGG graphite ranges from about 1.6 to 1.7 g/cm^3 (see Table 2.1) [Cor81, BBP02]. However, this treatment is not homogeneous, thus local densities can differ strongly from the macroscopic average density. The heterogeneous distribution of pores can be seen in Figure 2.4.

On the smaller scale, both the binder and filler phase consist of grains of coke. The grains are polycrystalline structures; they are built of clusters of more or less aligned crystallites. These crystallites are built by stacking of graphene planes similar as described before for the monocrystal and are called basic structural units (BSU).

However, even on the scale of BSUs, nuclear graphite shows significant differences with respect to a perfect crystal. For example, complete ABAB stacking is seldom observed, stacking failures are known to exist. Additionally, it contains a large number of intrinsic and extrinsic defects, which will be discussed in detail later on. Its micro- and macroscopic structure strongly depends on the coke and

Table 2.1: Density ρ in g/cm^3 of the graphite used in the different UNGG reactors. The type of coke used for the filler and the number of impregnation steps (see section 2.2) are also given [Cor81, BBP02].

Reactor	Type of coke	Nb. of impregnations	ρ
G1	Spécial A	0	1.60
G2/G3 - Pile	Spécial A	1	1.71
G2/G3 - Reflector	Lockport L	1	1.68
CHA1	Lockport L	1	1.69
CHA2	Lockport L	1	1.67
CHA3	Lockport L	1	1.70
	Lockport M	1	1.70
SLA1	Lockport M	1	1.68
SLA2 - Pile	Lima	1	1.68
SLA2 - Sleeves	Lima	2	1.72
BUA1	Lima	1	1.68

filler as well as on the conditions used during the manufacturing process. In the case of UNGG graphite, its properties are anisotropic due to forming of blocks by extrusion (see section 2.2).

On this length scale, microscopical defects are known to exist in addition to the macroscopically observable imperfections of the crystalline structure.

One dimensional defects, called line defects or dislocations, can be subdivided into four groups as first proposed by Fujitu and Izui [IF61]: basal, prismatic edge, prismatic screw, and non-basal edge dislocations. Two vectors are sufficient to describe these dislocations: the vector $\mathbf{l}$ lying in the line of dislocation propagation, and the Burgers vector $\mathbf{b}$ which is a measure of the distortion of the perfect crystal lattice by the dislocation. The four line defects differ in whether these two vectors lie in or out of the basal plane, called basal and prismatic direction, respectively. For the basal dislocation, both vectors are in basal direction, prismatic screw has both in prismatic direction. For prismatic edge, $\mathbf{b}$ is in prismatic and $\mathbf{l}$ in basal direction, whereas for non-basal edge it is the opposite. More detailed discussions can be found in Refs [Ous98, TEEBH03, SMSH$^+$07].

Two dimensional defects in a graphite crystallite can be divided into two groups.

The first group includes misorientations of two basal planes next to each other such as stacking faults or planes which are translated and rotated with respect to each other. Since the interaction in between two basal planes is very weak, these defects are rather common and the energy cost of creating such defects is lower compared to other defects. Ref. [TEEBH03] could show that the energy increase

caused by shearing of two planes is on the order of meV.

The second group contains surfaces and grain boundaries of the crystal. Both are deviations of the perfect infinite crystal and are naturally occurring in any polycrystalline material.

Three surfaces of graphite, that are more or less stable, are known. By cutting the perfect crystal along a basal plane, the (001) surface is created. This surface has no dangling bonds and is thus the most stable one. The other two, called armchair or (110) and zig-zag or (100) surface, are obtained by cutting along planes orthogonal to the basal plane (see Figure 2.6). They are less stable due to the created dangling bonds. Reconstructions of these surfaces which increase their stability were determined by experiments [RCG13]. An example is also shown in Figure 2.6. Theoretical calculations determined edge reconstructions for graphene [KMH08, WSS+08, KObuQF11], a link with surface reconstructions in graphite was not yet established.

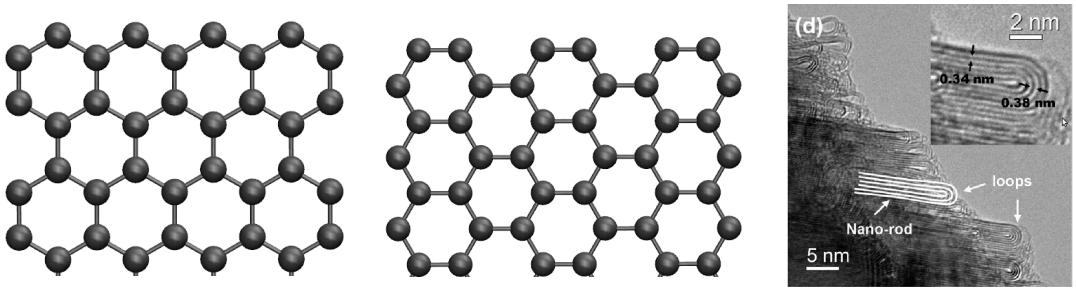

(a) (b) (c)

Figure 2.6: Side view of a) the (100) surface and b) the (110) surface of graphite along the [001] direction. c) HRTEM image of reconstructed surfaces of graphitized nanofibers [GDLK11].

Grain boundaries are two-dimensional defects, which are located at the boundary of two graphite crystallites, which have different orientations. An example which is also used in this work is shown in Figure 2.7. They are generally classified by the relative angle of the crystallites with respect to the grain boundary line [SGT+02]. Little is known on the local structure of graphite at grain boundaries, STM studies combined with modeling could show that in some cases, a succession of five and seven-membered rings is built [icvF09, SGT+02]. Nevertheless, it is clear that this restructuring depends on the angle between the two crystallites.

Experimentally, the intrinsic defects of graphite can be detected by direct techniques, such as scanning tunneling microscopy (STM) [HK99, ČF09, HKSJ96, BKK11a], transmission electron microscopy (TEM) [BKK11a], magnetic force microscopy (MFM) [icvF09], or atomic force microscopy (AFM) [HKSJ96], and by indirect techniques such as X-ray-absorption near-edge structure (XANES)

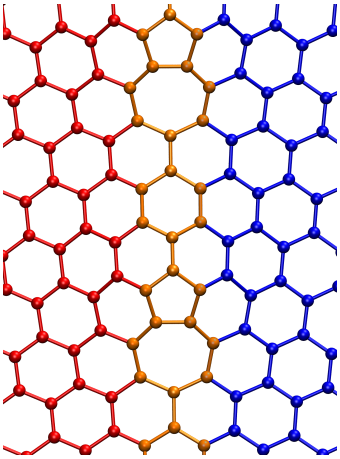

Figure 2.7: Example of a grain boundary. The red and blue parts constitute the two grains with different orientations, the orange part is the grain boundary.

[HYX+12] or Raman spectroscopy [RT04, ARV+10, AR12]. Here, only the features of the Raman spectrum of nuclear graphite will be shortly reviewed. Raman spectroscopy is of special interest in this project due to the fact that a lot of Raman data of the CEA is available in the framework of GT Graphite. Having in mind the symmetry of a perfect graphite crystal ($P6_3/mmc$ or D_{6h}, respectively), there are six optical vibrational modes with the following irreducible representations at the Γ point:

$$\Gamma = A_{2u} + 2B_{2g} + E_{1u} + 2E_{2g}$$

Only the two E_{2g} modes at 42 cm^{-1} and 1582 cm^{-1}, respectively are Raman-active [NWS72, NS79] in the first order region. Any kind of polycrystalline graphite, including nuclear graphite, has three additional peaks, called defect bands. In Figure 2.8 the Raman spectra of HOPG and polycrystalline nuclear graphite are shown. The G band belongs to the E_{2g} mode at 1582 cm^{-1}, the defect bands are called D_1, D_2, and D_3. D_1 appears at around 1360 cm^{-1} and is attributed to a breathing mode with A_{1g} symmetry which does not exist for the perfect infinite crystal. According to Ref. [TK70] the ratio of the intensities of D_1 and G is inversely proportional to the mean size of the crystallites which is obtained by X-ray diffraction. The D_2 band at around 1620 cm^{-1} is supposed to stem from a lattice vibration due to a distribution of interlayer spacings on the surface of the graphite crystallite. The D_3 band at approximately 1500 cm^{-1} is very broad and thought to be due to a decreased order within the crystallites. This decreased order is generated by interstitial carbon atoms in the interlayer space as well as sp^3 hybridized carbons. All three defect bands increase upon irradiation. However, for graphite which was subjected to strong irradiation and therefore has a highly

amorphous structure, the D3 band is overwhelmingly large and masks all other bands [ARV+10].

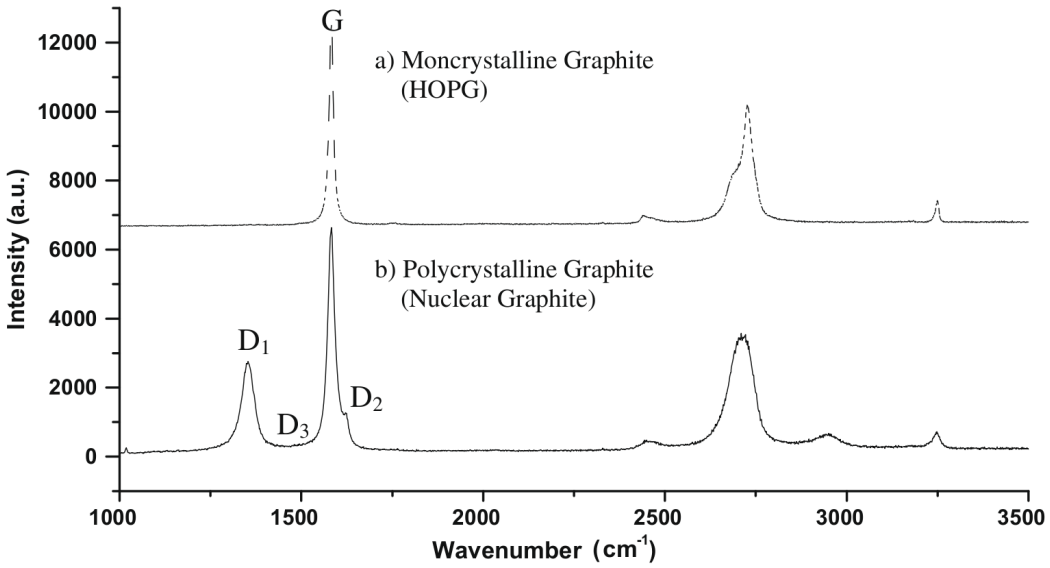

Figure 2.8: Raman spectra of a) HOPG and b) nuclear graphite [ARV+10].

In addition to the large number of intrinsic defects, extrinsic defects exist in graphite which are explained in the following section.

2.1.2 Impurities

Even though nuclear graphite is a high quality product with high purity (see section 2.2), small amounts of extrinsic defects are still present. Knowledge of the concentration and type of these impurities is important for two reasons: First, they could increase the absorption neutron cross-section which would alter the moderator properties of the graphite. Second, the impurities themselves can be activated by neutron capture which increases the radiological inventory and thus has consequences for the waste management. In Table 2.2 the concentrations of several important impurities are given for different samples of virgin UNGG graphite which were used in the nuclear power plants.

As can be seen, concentrations of many impurities show variations among different nuclear power plants as well as in the different parts of the nuclear power

Table 2.2: Concentrations of impurities found in virgin UNGG graphite [BB00].

	Reactor								
	Pile						Sleeves		
Element	CHA1	CHA2	CHA3	SLA1	SLA2	BUA1	CHA2	CHA3	SLA1-2/BU1
H (ppm)	-	20	-	-	20	20	20	20	-
Li (ppm)	0.15	0.03	-	0.08	0.07	0.10	0.00	0.00	0.10
B (ppm)	0.137	0.118	0.110	0.091	0.110	0.110	0.130	0.120	0.176
Na (ppm)	14.0	2.0	-	-	-	11.0	0.90	0.8	-
Mg (ppm)	-	0.0	-	-	-	-	2.1	-	-
Cl (ppm)	6	10	-	-	-	-	12	-	-
K (ppm)	-	-	-	-	-	11.0	1.4	0.9	-
Ca (ppm)	23.00	0.63	-	-	-	5.00	5.20	4.00	-
Ti (ppm)	0.00	0.75	-	-	-	-	0.20	-	-
V (ppm)	30.0	26.6	30.0	-	-	-	17.6	7.6	-
Fe (ppm)	0.0	4.1	-	-	-	7.0	3.7	5.0	-
Co (ppm)	0.040	-	0.540	-	0.050	-	0.029	-	0.080
Sm (ppb)	25.20	5.20	-	-	1.50	3.00	1.80	0.73	-
Eu (ppb)	-	0.30	-	-	0.50	0.62	0.12	0.80	-
Dy (ppb)	0.65	1.00	-	-	0.75	0.45	0.85	0.22	-

plants (sleeves and pile). Metals such as Na, Ca, V, and Fe as well as H are the most abundant impurities throughout the different graphites. It should be noted that also Cl is found in several samples.

2.1.3 Mechanical, Thermal, and Electrical Properties

In Table 2.3 several mechanical, thermal, and electrical properties are given for nuclear graphite "Pile Grade A" which was used in British Magnox reactors [IAE06]. This graphite was produced using mostly the same process as applied for UNGG graphite. For both, the blocks were formed by extrusion (see section 2.2 for details). During this process graphite crystallites which are randomly oriented are forced into parallel alignment. This step preserves the anisotropy that is observed for graphite monocrystals to some extent, although the differences are much smaller.

Concerning the mechanical properties, graphite shows increasing strength with temperature and reaches a maximum around 2500°C [Bak70]. Its strength is higher parallel to the direction of extrusion due to the orientation of the crystallites and the stronger covalent forces that arise along these directions. This is true for most mechanical properties listed in Table 2.3.

Thermal properties show the same trend. Thermal conductivity describes the heat transport which for graphite is mainly due to lattice vibrations of atoms. Heat conduction is easier where atoms are covalently bound, which explains the higher conductivity parallel to the direction of extrusion. Thermal expansion is also a consequence of lattice vibrations of atoms. It is higher perpendicular to the

direction of extrusion, since mainly weak van der Waals forces are acting in this direction.

The electrical resistivity shows the same behavior as the thermal conductivity. Parallel to the direction of extrusion, an electrical current can flow easier due to the overlapping electron densities in the graphene plane. However, the resistivity only differs by a factor of about 2 in the two directions which is significantly smaller than for graphite monocrystals. This is a consequence of intrinsic defects. They can decrease the conductivity by acting as scattering centers of electrons, but also increase conductivity across two graphene planes by bond formation.

Table 2.3: Selected mechanical and thermal properties of "Grade A" nuclear graphite. $\parallel$ and $\perp$ denominate properties measured parallel and perpendicular to the extrusion direction [IAE06].

Property	Unit	$\parallel$	$\perp$
Young's modulus (20°C)	$10^9\,\mathrm{N\,m^{-2}}$	11.7	5.4
Tensile strength	$10^6\,\mathrm{N\,m^{-2}}$	17	11
Bend strength	$10^6\,\mathrm{N\,m^{-2}}$	19	12
Compression strength	$10^6\,\mathrm{N\,m^{-2}}$	27	27
Thermal expansion coefficient (20-120°C)	$10^{-6}\ \mathrm{K^{-1}}$	0.9	2.8
Thermal conductivity (20°C)	$\mathrm{W\,m^{-1}\,K^{-1}}$	200	109
Electrical resistivity	$10^{-6}\,\Omega\,\mathrm{cm^{-1}}$	620	1100

2.2 Industrial Production of Nuclear Graphite [Bak70]

Nuclear graphite usually consists of two ingredients; a filler material on the basis of petroleum coke or pitch coke and a tar pitch binder. A scheme of the industrial production process is shown in Figure 2.10. In a first step the coke is calcined in order to remove volatile hydrocarbons. Then the material is crushed and separated by particle size into four fractions (the size of the sieves are 0.4, 0.8, and 1.6 mm). The smallest particles, the fines, are milled and mixed with the larger particles (coke blend). At 165°C, the coke blend is mixed with the pitch binder. The forming of blocks can either be performed by extrusion or molding. These blocks are called the "green" article. This step is responsible for the anisotropy of properties of nuclear graphite. When formed by extrusion, the filler coke particles are aligned with the long dimension parallel to the direction of extrusion (see Figure 2.9). When formed by molding, the alignment direction is orthogonal to the molding force. UNGG graphite blocks were formed by extrusion.

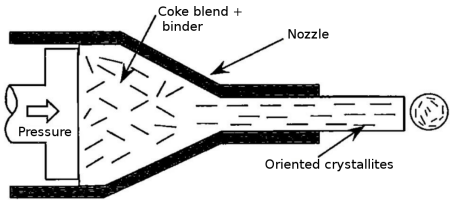

Figure 2.9: Alignment of crystallites when blocks are formed by extrusion [Del00].

The material is then heated to about 800°C in a period of 3 to 6 weeks, in order to prevent the formation of cracks by the escaping gases. In this phase the binder polymerizes and links are created at the filler-binder interface. A mass loss of about 10% and volume shrinkage of about 3% is observed. Due to the release of volatile compounds a large amount of open and closed pores are formed. In the case of UNGG graphite production (and many other nuclear graphites), an impregnation step with pitch is performed in order to increase the density and reduce the porosity. The impregnation is conducted in an autoclave. First, a vacuum is created to remove gases from the porosities. Then, pitch is added at a pressure of about 10 bar to maximize the penetration and filling of pores. This impregnation step was applied for most moderator/reflector graphites; only the pile graphite of G1 and the reflector graphite of G2 and G3 were not impregnated. The graphite sleeves were impregnated twice. In the graphitization step the material is heated to 2500-3000°C for about 21-27 days. In a final purification step compounds such as NaF, MgF_2, or Cl_2 are added at temperatures of 2800-3000°C in order to remove impurities from the graphite.

During this process, the microstructure of the starting material changes significantly. As shown by Rouzaud and Oberlin for anthracene- and saccharose-based carbons [RO89], four different stages can be defined. A schematic description can be found in Figure 2.11. At low temperatures (before the baking step), the material consists of basic structural units (BSU) which are small crystallites with a diameter and thickness of less than 1 nm. During the first heating to 800-900°C, the main

process is the release of heteroatoms into the gas phase. In the second step up to 1500°C, BSUs start to stack and form columns; the diameter of the BSUs remains rather stable whereas the thickness increases significantly and interlayer defects are released. From 1500 to 2000°C, the crystallites start to grow. In-plane defects are annealed and BSUs join to form larger distorted layers. In the final step above 2000°C, these distortions are annealed and layers become perfect. This can be seen from the decrease of the interlayer distance.

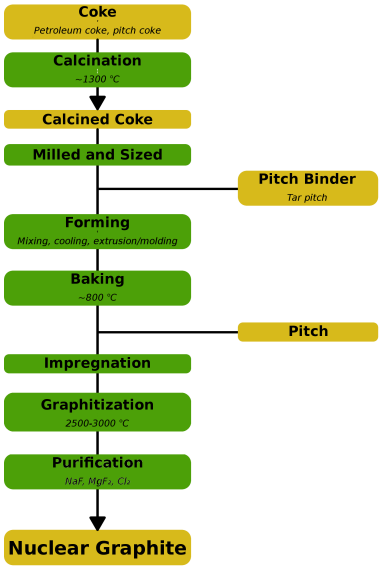

Figure 2.10: Flowchart representation of the synthesis of nuclear graphite. Boxes in yellow describe materials, boxes in green describe the different steps of the procedure.

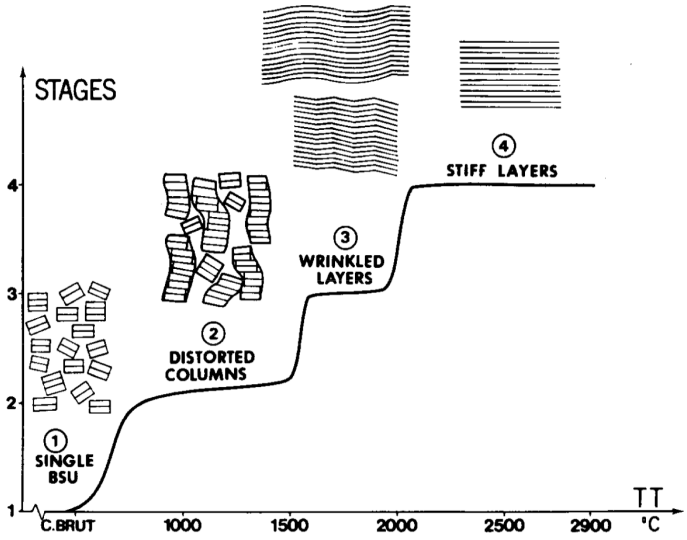

Figure 2.11: Schematic representation of microstructural changes of the precursors of nuclear graphite with respect to temperature [RO89].

2.3 Influence of Irradiation and Temperature on the Properties of Nuclear Graphite

During its exploitation in the nuclear reactors, nuclear graphite is subjected to irradiation as well as elevated temperatures. This leads to an increase of diffusion inside the material which can have consequences for micro- and macroscopic properties. The nuclear fission of ^{235}U leads to the release of several high energy neutrons per U atom ranging from 0-10 MeV (on average 2 MeV) which then can interact with the surrounding graphite.

There are two different ways in which the neutrons can interact with the atoms of graphite; elastic and inelastic collisions. Elastic collisions are defined as an encounter of two bodies where kinetic energy is transferred from one body to the other while the total kinetic energy is conserved. This is a ballistic effect and the origin of the primary irradiation damage.

Inelastic collisions are encounters of two bodies where the total energy is conserved, thus a transformation of kinetic energy to potential energy takes place. For example, this is observed when a partially charged particle collides with an atom and interacts with its electrons leading to electronic excitations or ionizations. Another possibility are vibrational excitations. Since neutrons are uncharged, they interact with the atom core which reduces their kinetic energy and further ballistic effects.

The primary damage induced by the radiation particles depends on their kinetic energy. If it is higher than the energy needed to displace an atom of the matrix (E_d), the collision partner will move out of its lattice position. This creates a vacancy and an interstitial, which is called a Frenkel pair.

If the kinetic energy supersedes $2\,E_d$, the collision partner becomes a projectile called primary knock-on atom (PKA) which itself displaces other matrix atoms out of their lattice position. Depending on the kinetic energy, those can become projectiles as well, leading to a cascade of atomic displacements. This is schematically shown in Figure 2.12.

The constant exposure to irradiation leads to changes in the properties of the nuclear graphite; over time damage caused on the microscopical level also leads to observable changes of macroscopic properties. Additionally, the elevated temperatures (150-450°C depending on the reactor) and interaction of γ-radiation with the gas phase can lead to corrosion of the material and a degradation of the mechanical stability. These different processes will be explained in the following.

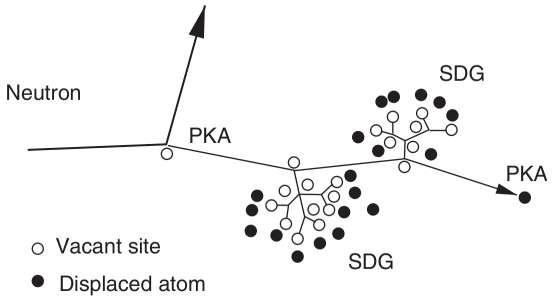

Figure 2.12: Schematic representation of a cascade of atomic displacements [TH07].

2.3.1 Microstructural Irradiation Damage

The primary damage leads to an oversaturation of point defects; as a consequence the diffusion of bulk atoms is accelerated due to the irradiation. Phase transitions which are too slow to be observed at standard conditions can take place. Other observed phenomena are for example agglomerations of point defects.

Different types of point defects are known to exist in irradiated graphite. One of them is the Stone-Thrower-Wales defect where a bond which is shared by two atoms is rotated by 90° (see Figure 2.13). When the kinetic energy of a particle is high enough (> 30 eV), a Frenkel-pair is created (see Ref. [TH07] and references therein). This interstitial-vacancy pair as well as other single interstitials have been investigated theoretically [TEEBH03, LRR05, TOTS10]. In general, interstitials are found to be more mobile than vacancies [ZZY$^+$10]. This leads to a higher concentration of monovacancies compared to single interstitials [TH07]. However, diffusion of vacancies is possible as well either by thermal excitation or irradiation. Theoretical predictions for the migration barrier of a single vacancy lie in the range of 1.3-1.6 eV [KP88, KLFN06, ZZY$^+$10] and are in agreement with the activation energy of 1.8 eV obtained from Raman measurements [AKNK93]. The height of this barrier allows for an accumulation of vacancies to occur which can create divacancies or even extended vacancy lines (see Ref. [TH07] and references therein). As pointed out in Ref. [ZZY$^+$10] and also shown by molecular dynamics simulations [LWY$^+$05], coalescence of two monovacancies to form a divacancy has a barrier of 2.2 eV. UNGG reactors operated with high temperature differences (150-450 °C), however as shown in Ref. [YXQ$^+$09] monovacancies are systematically annealed from 200 °C onwards. Thus, both point defects might coexist under reactor conditions. A more detailed discussion of point defects can be found in Ref. [TH07].

The microstructural damage is indirectly observable by Raman spectroscopy (see section 2.1.1). The D3 defect band increases with an increasing neutron flu-

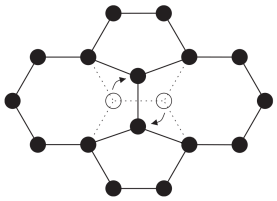

Figure 2.13: Visualization of the Stone-Thrower-Wales defect [TH07].

ence; at a fluence of 7.0×10^{20} n cm^{-2} (fast neutrons > 1 MeV) which is equivalent to 0.1-1 dpa [a] an amorphization of the material was observed [NNST90]. Thus, depending on the fluence and energy of neutrons the microstructural changes can be much more extended than point defect creation.

The irradiation damage of the graphite matrix also affects macroscopic properties. The influence on the bulk dimensions, mechanical, and thermal properties is presented in the following.

2.3.2 Dimensional Change

For an irradiated single crystal of graphite, an expansion along the direction perpendicular with respect to the basal plane and a contraction along the basal plane is observed. This is shown in Figure 2.14. This trend affects the lattice constants in the same way but is less pronounced, which was detected experimentally [Got97, AMY$^+$05, TH07]. These changes are due to the creation of extended defects. Currently two different hypotheses on the nature of these defects exist.

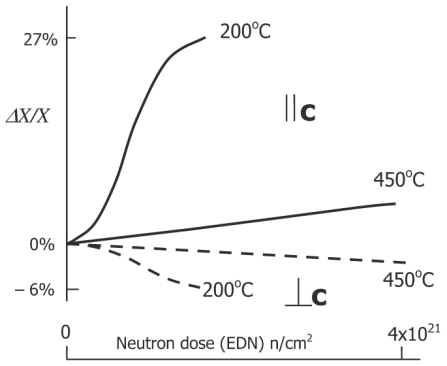

Figure 2.14: Schematic description of the fractional dimensional changes of a graphite monocrystal with respect to neutron dose parallel to **c** (solid lines) and perpendicular to **c** (dashes lines) [HSMDH11].

The first hypothesis is shown in Figure 2.15. According to Ref. [MH12], dislocation loops are created in graphite. These are two dimensional defects, where

[a] dpa: Displacements per atom. The number of times that an atom is displaced for a given fluence.

the dislocation line is closed within the crystal (see Ref. [TH07]). In graphite they are thought to develop either by an interstitial or vacancy accumulation through diffusion of point defects. Interstitials regroup to form a basal plane of finite size and increase the interlayer distance by pushing the adjacent basal planes away. Dangling bonds created by a vacancy accumulation along a line can be saturated by a restructuring of the plane around the vacancy site. Bonds are created between opposing carbons with dangling bonds. This leads to an overall contraction in the **a**-direction. A vacancy accumulation forming an extended hole in a basal plane leads to a collapse of the upper and lower planes.

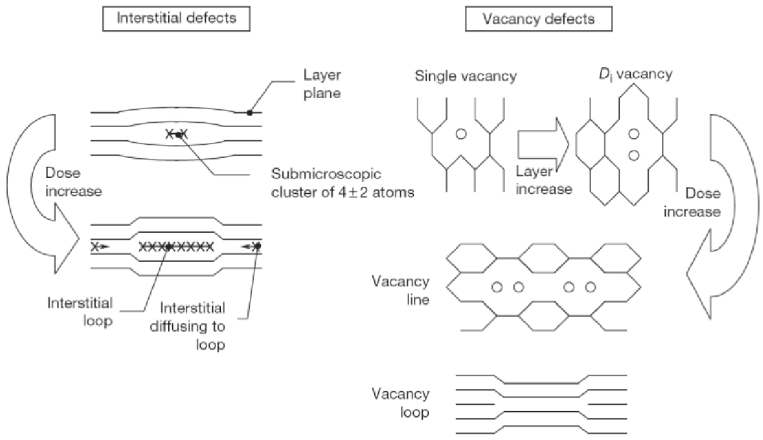

Figure 2.15: Schematic representation of an interstitial accumulation (left) and a vacancy accumulation (right) leading to the creation of dislocation loops [MH12].

The second hypothesis is shown in Figure 2.16. It explains the increase along the **c**-axis by a buckling of basal planes [HSMDH11]. If adjacent basal planes are locally connected by two interstitials and the planes have different lengths between the two connection points, the longer plane will buckle. This leads to an expansion in the **c**-direction. The buckling is thought to happen below 250 °C. At higher temperatures a defect called ruck and tuck by the authors of Ref. [HSMDH11] is supposed to be created. Schematically a basal plane is folded twice creating a s-like shape.

The size of the crystallites is found to decrease for irradiated graphite compared to virgin material [AIS96, ARV$^+$10].

The dimensional change of nuclear graphite due to irradiation is more complex. In Figure 2.17 a schematic description is shown. For low neutron doses shrinkage is found (A-B curve). This is explained by a shrinkage in the a-direction as found for single crystals, however the expansion in the **c**-direction is balanced by the closure of pores and cracks. Thus a net shrinkage is observed. With a further increase

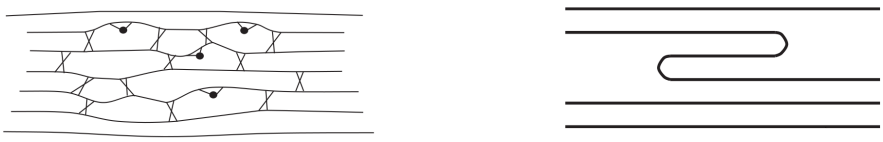

(a) (b)

Figure 2.16: Schematic representation of a) the buckle and b) the ruck and tuck defects [HSMDH11].

of the dose the dimensional change runs through a minimum, called turnaround (B-C curve). In this phase, expansion in the **c**-direction is counterbalanced by pores being generated due to radiolytic oxidation (see section 2.3.5) which delays the turnaround. From this phase onward a steady expansion is observed. Here, the c-axis expansion creates large internal stresses which lead to the formation of cracks and pores [Nei00].

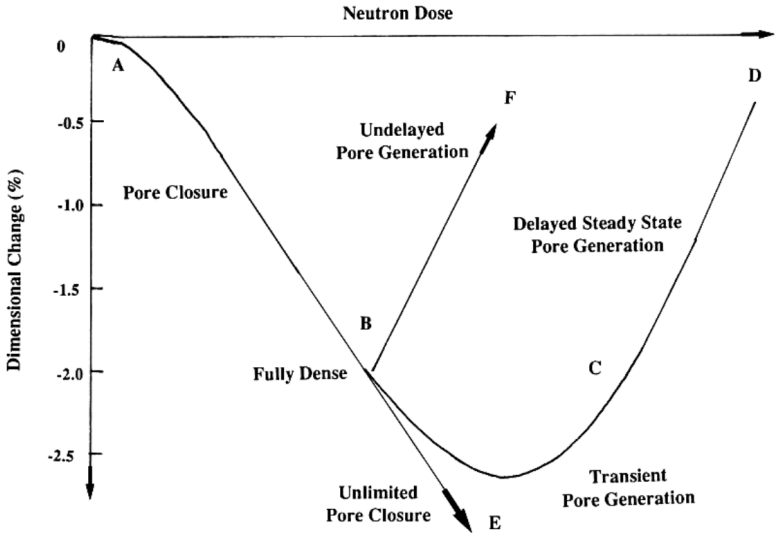

Figure 2.17: Schematic description of the dimensional change by irradiation in AGR nuclear graphite [Nei00].

2.3.3 Wigner Energy [BB06]

Defects which are created due to irradiation lead to an increase of the internal energy of the graphite system. This increase in energy is called the Wigner energy. This process is observed when graphite is irradiated at a temperature less than 115°C and a neutron fluence higher than 1.6 $\cdot 10^{20}$ n cm^{-2}ΦFG[b] (about 0.11 dpa). If these conditions are satisfied, the Wigner energy increases rather quickly. In Figure 2.18 a representative spectrum of the Wigner energy is shown. The stored Wigner energy can be released when the temperature is raised so that created defects are annealed. This creates the peak of the enthalpy differential $\frac{dH}{d\Theta}$ at about 200°C in the spectrum. Irradiated graphite is energetically stable if $\frac{dH}{d\Theta}$ is lower than the heat capacity C_p of unirradiated graphite for all temperatures. For the example shown in Figure 2.18 this is not the case; starting from temperature Θ_D the temperature increases adiabatically and heat is released spontaneously. This can lead to local temperature spikes of 1200°C which could be a risk to the safety of a nuclear power plant and was the underlying reason for the fire at the Windscale Pile 1 reactor in UK in 1957 [Arn92]. For higher irradiation temperatures, the peak of $\frac{dH}{d\Theta}$ gets smaller and smaller and completely disappears at T > 300°C since the defects are sufficiently mobile to recombine.

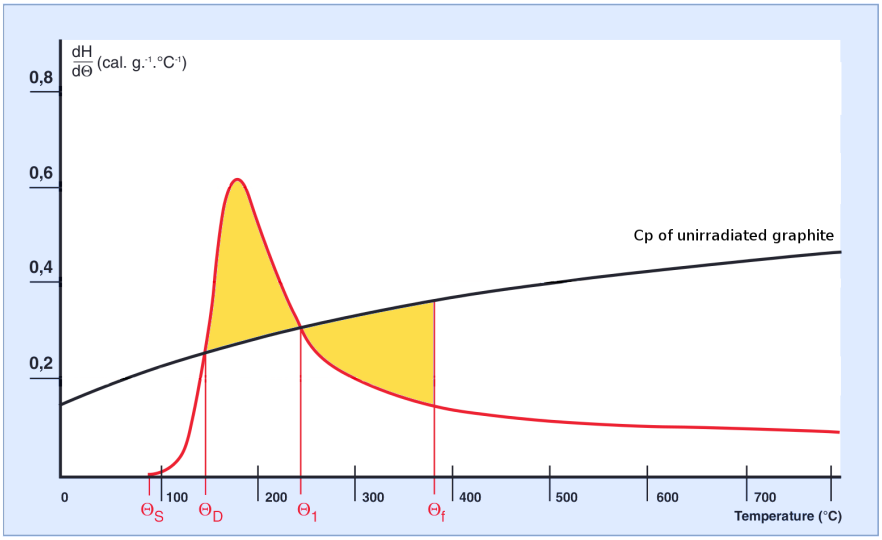

Figure 2.18: Spectrum of the Wigner energy of graphite irradiated at 60°C at a neutron fluence of 1.74 $\cdot 10^{20}$ n cm^{-2}ΦFG [BB06].

[b] ΦFG: Equivalent fission fluence for graphite. 10^{21} n cm^{-2} ΦFG equals a fluence of 0.96×10^{21} n cm^{-2} (neutrons > 0.1 MeV)

2.3.4 Mechanical and Thermal Properties [BB06]

Mechanical properties of nuclear graphite change due to the created irradiation damage. The Young's modulus increases when graphite is subjected to irradiation. This is shown in Figure 2.19 for quasi-isotropic graphite. This increase can be explained by the formation of defects which interconnect graphene planes and block shear movement. It is already seen for a rather low neutron fluence and is higher for lower irradiation temperatures. At higher temperatures, defects are more mobile and are either annealed or form new graphene planes which facilitates shear movement.

Thermal conductivity gets smaller when graphite is irradiated which is shown in Figure 2.20. It is found to decrease monotonously until it saturates at a fluence of about 4 $\times 10^{21}$ n.cm^{-2} (E $>$ 0.1 MeV) for irradiation temperatures of 500-1000°C. The higher the irradiation temperature in this range is, the lower is the decrease of the thermal conductivity. This decrease is due to the creation of defects which lead to phonon scattering. For temperatures lower than 700°C, the phonon scatterers were identified as interstitial groups and vacancies [TGK69, TH07]. At higher temperatures the scattering mechanism is different, the phonon scatterers are thought to be uncollapsed vacancy loops [Kel81, TH07].

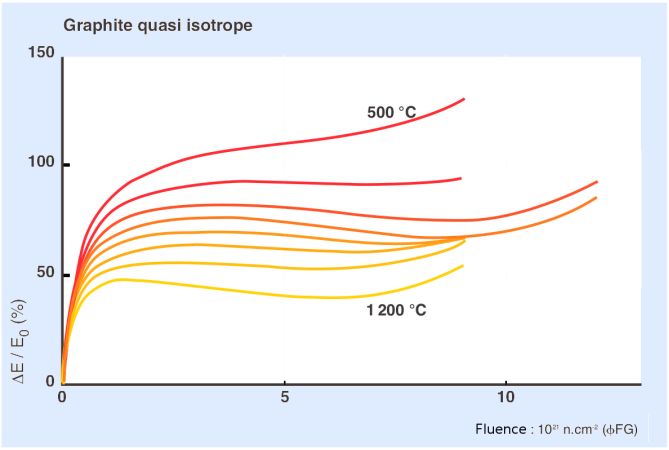

Figure 2.19: Relative change of the Young's modulus of nuclear graphite with respect to neutron fluence at different irradiation temperatures. The graphite sample is quasi-isotropic polycrystalline graphite from coal-tar pitch [BB06].

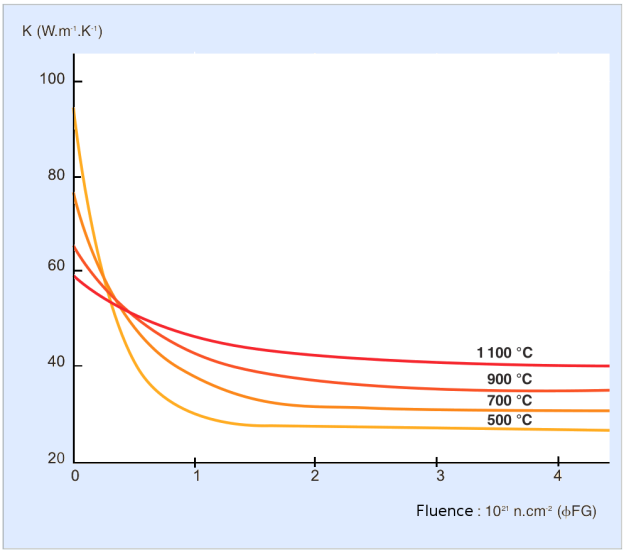

Figure 2.20: Change of the thermal conductivity of nuclear graphite with respect to neutron fluence at different irradiation temperatures. The graphite sample is quasi-isotropic polycrystalline graphite from coal-tar pitch. The thermal conductivity was measured at the irradiation temperature in the direction of extrusion [BB06].

2.3.5 Corrosion

In addition to the changes of properties which are directly connected to the irradiation of the graphite matrix, the conditions in the reactor also cause corrosion by thermal and radiolytic oxidation. These processes are solid-gas reactions that occur on surfaces inside the porous system. The degradation of the material is not only an important factor with respect to the reactor safety, but also creates defective zones which may play a role in the trapping of radionuclides or reactions with the gas phase.

Thermal Oxidation

Even though graphite is a rather inert material, it can in principle react with compounds that are present in the gas phase. These reactions depend not only on the temperature and partial pressure of the compounds, but also on macro- and microscopic properties of the graphite such as crystal structure, pore structure, particle size, or the presence of impurities. At low temperatures oxidation occurs uniformly in a graphite block, however at elevated temperatures mainly the surface is attacked. This is connected with a macroscopically observable degradation of mechanical and thermal properties [Bak70, IAE00], which, in extreme cases, could have an impact on the safety of the reactor.

The gaseous compounds which can act as an oxidizing agent are mainly O_2, CO_2, and H_2O. If no catalyst is present, classical reactions between solid state

carbon and these compounds are the most likely to occur. However, products created from these reactions could again react in the gas phase which increases the complexity of the overall reaction processes.

In order for those solid-gas reaction to occur the gaseous compounds needs to chemisorb on the surface. When carbon is transferred to the gas phase, this process is intrinsically linked with a breaking of C-C bonds. The remaining dangling bonds are highly reactive and can then further facilitate the chemisorption of the gaseous compounds. Additionally, the atoms can undergo local rearrangements to form new C-C bonds or, if no reaction partner is present, the dangling bonds remain.

In the following, the possible reactions with CO_2, O_2, and H_2O are given together with the respective standard enthalphy of formation ΔH at 25°C [IAE00].

$$\mathrm{C} + \mathrm{CO_2} \rightleftharpoons 2\,\mathrm{CO} \qquad \Delta H = +172.5\,\mathrm{kJ\,mol^{-1}} \tag{2.1}$$

$$\tfrac{1}{2}\mathrm{O_2} + \mathrm{C} \rightleftharpoons \mathrm{CO} \qquad \Delta H = -110.5\,\mathrm{kJ\,mol^{-1}} \tag{2.2}$$

$$\mathrm{O_2} + \mathrm{C} \rightleftharpoons \mathrm{CO_2} \qquad \Delta H = -393.5\,\mathrm{kJ\,mol^{-1}} \tag{2.3}$$

$$\mathrm{C} + \mathrm{H_2O} \rightleftharpoons \mathrm{CO} + H_2 \qquad \Delta H = +131.3\,\mathrm{kJ\,mol^{-1}} \tag{2.4}$$

$$\mathrm{C} + 2\,\mathrm{H_2O} \rightleftharpoons \mathrm{CO_2} + 2\,H_2 \qquad \Delta H = -82.4\,\mathrm{kJ\,mol^{-1}} \tag{2.5}$$

$$\mathrm{C} + 2\,\mathrm{H_2} \rightleftharpoons \mathrm{CH_4} \qquad \Delta H = -74.8\,\mathrm{kJ\,mol^{-1}} \tag{2.6}$$

$$\mathrm{CO} + \mathrm{H_2O} \rightleftharpoons \mathrm{CO_2} + \mathrm{H_2} \qquad \Delta H = -213.7\,\mathrm{kJ\,mol^{-1}} \tag{2.7}$$

Equation 2.1 is the most relevant for UNGG reactors due to the omnipresence of CO_2 in the gas phase. All of these oxidation reactions share the same features of temperature dependence. Three different zones are known to exist [LX04] for graphite oxidation with O_2.

The chemical regime (up to 600°C) which is controlled by the reaction of O_2 with graphite. This is a slow homogeneous process and little mass is lost.

The second zone (up to 900-1000°C) is called the diffusion regime. Oxidation increases due to the opening of meso- and macropores in graphite which are accessible to the gas. This is a heterogeneous process limited by the diffusion through pores.

The third zone (from 900-1000°C onwards) is called the regime of gas phase transfer. Here, the speed of oxidation is high and is limited by the transport of the oxidizing compound to the material.

Radiolytic Oxidation [IAE00]

Radiolytic oxidation of nuclear graphite differs substantially from thermal oxidation. The underlying principle of this mechanism is the radiolysis of CO_2 which in this case is a dissociation caused by γ-radiation [IAE00]. While CO_2 seems to be stable with respect to ionizing radiation up to very high doses, it is in fact a dynamic process of dissociation and recombination [IAE00]. The reaction is [FNP80, BC80, IAE00]

$$CO_2 \rightleftharpoons CO + O. \tag{2.8}$$

The back reaction to reform CO_2 occurs very quickly. If creation of the reactive species occurs close to the graphite matrix, the active species might react with graphite. In this case, carbon is removed from the bulk material.
This process is described very generally by the following reaction

$$O + C \rightarrow CO, \tag{2.9}$$

and the overall reaction reads

$$CO_2 + C \rightarrow 2\ CO. \tag{2.10}$$

Radiolysis of CO_2 is increasing with the neutron flux [Gau86]. A higher porosity and smaller pores both increase the oxidation rate of the surface [Gau86, MSW95]. This is due to the approximate lifetime of the active species of about 10^{-7} s. For small pores the active species is close to the surface and can react before recombining [MSW95]. For new cooling gas, the CO concentration is less than 1%; an increase up to 3% was detected for operating reactors [EDF67]. No firm conclusion exists on the nature of the active species. However, there is evidence which shows that different kinds of ionic species could contribute, such as $[CO_2]_n^+$ [WBW77, Woo82, NSW83, IAE00] or $CO_3{}^-$ [MSW95, IAE00].

Two additional processes can happen other than recombination of CO_2 or reaction with a surface [IAE00]. First, the reactive species can collide and react with another molecule of CO_2. Second, it can collide and react with CO or other molecules present in the gas phase. Both these processes deactivate the reactive species and inhibit radiolytic oxidation of graphite [IAE00]. CH_4 was added to the gas phase as an inhibitor in French UNGG reactors (BUA1) [PPB93] as well as in British gas-cooled reactors [MSW95].

The presence of CO and CH_4 in the gas phase has another consequence: deposition of carbon species is observed on both, metal surfaces and graphite surfaces. On metal surfaces, amorphous carbon, filaments, and structures close to graphite were observed [Bak80]. Radiolysis of CO can form C_3O_2 which can polymerize and forms deposits on graphite surfaces in colder zones of the pile [FNP80, DM82]. Larger

hydrocarbons can be formed by reaction of CH_4 and CO_2 under γ-irradiation. Further oxidation reactions create oxygen-containing compounds which tend to form deposits on graphite surfaces in hotter zones of the pile [FNP80, PPB93].

These deposits influence the properties of graphite in several different ways. By forming a protective layer on top of graphite, they can limit corrosion to some extent [FNP80, DM82, PPB93]. However, these layers have much lower heat conductivity than graphite. Thus, they lower the efficiency of heat exchange between the solid phase and gas phase [PPB93]. Elevated concentrations of Ni, Fe, and Cl were measured [Yva73]. Thus they could be potential traps for Cl; the presence of metals is due to their catalytic activity in the creation of these deposits. Furthermore, thermal and radiolytic corrosion of these deposits as well as reactions with Cl were detected adding to the complexity of the possible processes occurring in graphite.

2.4 ^{3}H in Nuclear Graphite

Contrary to the two lighter isotopes hydrogen (^{1}H) and deuterium (^{2}H), tritium (^{3}H) is unstable and decays to $^3_2$He via β^- decay. The relative abundances of ^{1}H and ^{2}H are 99.985% and 0.015%; ^{3}H's abundance is at the trace level. ^{3}H is rather short lived, its half-life is about 12.3 years. However, it can be formed in several ways during the operation of the reactor which will be discussed in the following.

2.4.1 Origins of ^{3}H in Nuclear Graphite

^{3}H is produced via two different processes in the reactor. First, it can be a product of a ternary fission (three products are produced instead of two) of either ^{235}U or ^{239}Pu [MCP16]. Second, it can be created by neutron activation of impurities present in different parts of the reactor: the cooling gas, concrete, control rods, or the graphite moderator [MCP16].

The concentration of water steam in the cooling gas is very low (5-100 ppm). Thus, tritium production by neutron activation of cooling gas compounds is negligible.

In practice, the production by neutron activation occurs via four major processes:

$$^6\mathrm{Li} + {}^1\mathrm{n} \longrightarrow {}^3\mathrm{H} + {}^4\mathrm{He} \tag{2.11}$$

$$^{10}\mathrm{B} + {}^1\mathrm{n} \longrightarrow {}^3\mathrm{H} + 2\ {}^4\mathrm{He} \tag{2.12}$$

$$^{11}\mathrm{B} + {}^1\mathrm{n} \longrightarrow {}^3\mathrm{H} + {}^9\mathrm{Be} \tag{2.13}$$

$$^3\mathrm{He} + {}^1\mathrm{n} \longrightarrow {}^3\mathrm{H} + {}^1\mathrm{H} \tag{2.14}$$

Both, lithium and boron are natural impurities in nuclear graphite (see Table 2.2), but they also stem from external sources. ^{6}Li is found in concrete; here it has the highest concentration relative to the other parts of the reactor [MCP16]. Boron is mainly used as a neutron absorber in the control rods which contain boron carbide (B_4C) [MCP16]. ^{3}He is itself the product of the decay of ^{3}H. Thus, reaction 2.11 occurs in concrete as well as in graphite, whereas reactions 2.12-2.13 occur in the control rods and nuclear graphite.

The concentration of Li and B in UNGG graphite is very similar (about 0.1 ppm), however their respective cross sections differ substantially. For thermal neutrons (E = 0.025 eV), the cross section for ^{6}Li (reaction 2.11) is 5 orders of magnitude higher than that for ^{10}B. In this energy range, neutron capture of ^{10}B to give ^{6}Li by α-decay is more efficient [END]. For fast neutrons up to about 3 MeV, the difference of cross sections decreases, but ^{3}H production via equation 2.11 is still preferred [END]. A reaction via equation 2.13 occurs only for high energy neutrons ($> 10\,\text{MeV}$) [END]. The neutron flux of thermal neutrons is about 63 times higher than for fast neutrons (6.31×10^{14} n cm^{-2} vs. 1×10^{14}n cm^{-2} maximum neutron flux of SLA2) [LG14]. Thus, ^{6}Li is the main source of ^{3}H in the moderator [MCP16].

2.4.2 Diffusion and Trapping of ^{3}H

Atsumi and coworkers [ATM88, AIS92, AIS96, AI00, Ats02, Ats03, AT03, ATS11, ATM$^+$13] have studied the diffusion and adsorption of hydrogen in graphite over a time span of more than two decades and successively refined and expanded their theory. Figure 2.21 shows a summary of all occurring processes.

Molecular hydrogen can freely diffuse through the open pores of graphite and reach the filler grains. The diffusion along the grains is assumed to consist of a sequence of dissociation and recombination reactions of hydrogen on the surfaces. Hydrogen adsorption in graphite follows Sievert's law [c] for hydrogen pressures up to 10 kPa [AI00] indicating that hydrogen is adsorbed in its atomic form. Diffusion measurements and thermal desorption spectroscopy could show that hydrogen is trapped in two different traps with different adsorption enthalpies. Kanashenko *et al.* [KGC$^+$96] estimated the adsorption enthalpies theoretically. Following his nomenclature, trap 1 with an adsorption enthalpy of about -4.4 eV per H_2 was attributed to zigzag edges of dislocation loops in the crystallite. Trap 2 was attributed to the (100) or zigzag edge surface of the crystallite with an adsorption enthalpy of about -2.3 eV per H_2. Atsumi obtained -4.4 eV (trap 1) and -2.6

[c] Law describing the solubility of diatomic gases in metals when the gas molecules dissociate in the metal. $c_{at} = \sqrt{K p_{mol}}$, where c_{at} is the concentration of the dissolved atoms, K is the equilibrium constant, and p_{mol} is the partial pressure of the gas at the interface.

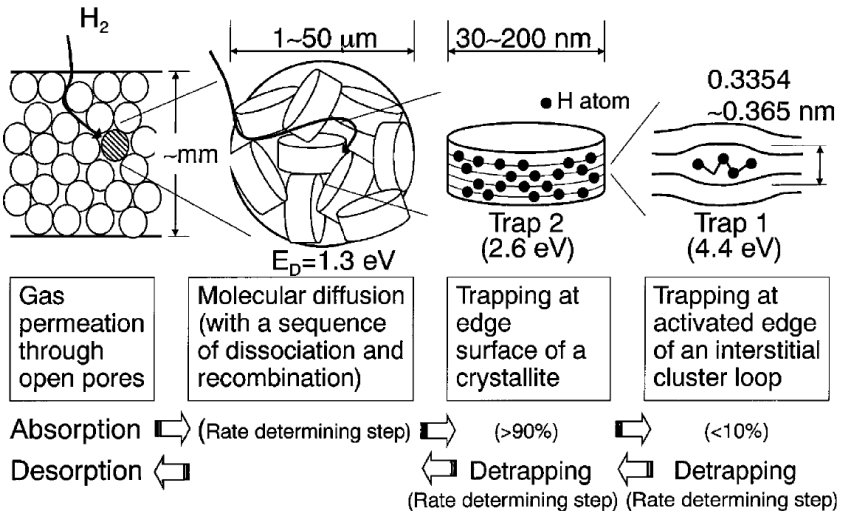

Figure 2.21: The different processes occurring when hydrogen is absorbed (or desorbed) in graphite [Ats03].

eV per H_2 (trap 2) experimentally [ATS11]. The difference is explained by the reconstruction of the (100) surface. Dislocation loops within the crystallite cannot reconstruct and thus saturation of the dangling bonds with hydrogen stabilizes the system to a higher extent compared to the surface. This part of the hypothesis relies until today on very crude calculations from the 1960's [CP64]. Thus, these assumptions should be reviewed with modern *ab initio* methods to check the validity of this hypothesis.

In the thesis of Le Guillou [LG14], which was conducted in the framework of the GT Graphite, the migration of deuterium in graphite was explored. Similar conclusions as Atsumi's were drawn for samples of HOPG and UNGG graphite. The main migration mechanism of D in graphite is thermal release [GTP+14] which occurs through the network of open porosities [GTP+15]. It is more easily released in porous, less graphitized parts of the material compared to highly graphitized zones [GTP+14]. In addition, release also occurs in two stages which is in line with the observations of Atsumi [GTP+14]. The part of tritium released during reactor operation was located close to the free surface; it should be lower than 30% of the total amount of produced tritium [GTP+15]. The remaining part is likely to be located in the coke filler grains [GTP+15]. A complete release of tritium is observed at 1200-1300°C [GMT+16]. Finally, deuterium shows the same behavior as tritium [GTP+14].

Since graphite is also often considered as a potential material for hydrogen storage, a vast number of theoretical studies have already been published. For graphene, spin polarization of the edges [WSS+08, KN10, DP10, KObuQF11,

BKK11b, NST$^+$12] as well as the influence of edge reconstruction on hydrogen adsorption [WSS$^+$08, KN10, KMH08] have been studied. However, a link to phenomena found in graphite has not yet been established. Considering graphite's literature, physisorption of atomic and molecular hydrogen on the (001) surface was studied on a theoretical level in Refs. [JS99, SJ02, PTY$^+$05, BMTP07, PF09, FDC10, RKNB10, CSA12, DGHkAt15]. However, these interactions are far too weak ($\approx$ 0.05 eV) compared to the experimentally measured adsorption energies, therefore they are not relevant to the experimentally observed phenomena. Both H and H_2 can also chemisorb on this surface [JS99, SJ02, ZGS$^+$02, AFA$^+$05, BKL08, PF09, ŠRH$^+$09, BJW$^+$09, IZTB$^+$10, LF11]. The chemisorption of these two species on the (100) or zigzag surface and (110) or armchair surface of graphite was shown by Yang *et al.* [YY02]; Diño *et al.* [DNK$^+$04, DMN$^+$04] and Sha *et al.* [SJ04] studied the potential energy surface for H_2 dissociation on these surfaces. In the graphite literature, it is not completely clear which surface binds hydrogen more strongly. Yang *et al.* [YY02] and Sha *et al.* [SJ04] found a stronger adsorption on the (100) surface, whereas Diño *et al.* [DNK$^+$04, DMN$^+$04] found a stronger adsorption on the (110) surface. Thus, this problem should be revisited with more accurate models to solve this ambiguity.

2.5 ^{36}Cl in Nuclear Graphite

The behavior of chlorine in nuclear graphite is more complex compared to hydrogen due to its electronic structure. It is an element of the 7th main group and has a high electron affinity. Thus, it likely reacts with any kind of species which has a lower electronegativity. Since most elements of the periodic table have a significantly lower electronegativity, covalent bonds will be polarized; *i.e.* they will be partly ionic, partly covalent. Due to its rather large electron cloud, chlorine is polarizable and non-covalent interactions should not be neglected. In addition, due to its electron affinity also charge transfer may play an important role. The bond strength of Cl_2 is significantly lower than that of H_2 (2.5 vs. 4.5 eV), therefore dissociation reactions are more likely. Three naturally occurring isotopes of chlorine exist. ^{35}Cl and ^{37}Cl are stable, their abundance is 76 % and 24 %, respectively. The third is ^{36}Cl, its natural abundance is only at the trace level. However, its long half-life of 301000 years is the reason of its importance for the waste management. It decays mostly via β^- decay to give ^{36}Ar (98.1%), β^+ decay to ^{36}S is also observed (1.9%).

2.5.1 Origins of ^{36}Cl in Nuclear Graphite

^{36}Cl may be formed in the reactors via three main processes:

$$^{35}Cl + {}^{1}n \longrightarrow {}^{36}Cl + \gamma \tag{2.15}$$

$$^{39}K + {}^{1}n \longrightarrow {}^{36}Cl + {}^{4}He \tag{2.16}$$

$$^{34}S + {}^{1}n \longrightarrow {}^{35}S \longrightarrow {}^{35}Cl + e^{-} \tag{2.17}$$

The process described in equation 2.17 finally produces ^{36}Cl via equation 2.15. In UNGG graphite, the most important reaction is the neutron capture of ^{35}Cl [BPW99]. Since ^{35}Cl is the principal source of ^{36}Cl, this shows that a relevant amount of Cl was already present in the unirradiated material. Several hypotheses exist on its origin [Pet11]:

- Cl was already present in the materials used for the synthesis of nuclear graphite
- Cl_2 was used in some cases for purification of nuclear graphite (see section 2.2)
- During some maintenance operations graphite was exposed to air for the purpose of cooling; Cl may have been present in the air
- Cl could have been an impurity of the CO_2 used as cooling gas

The first hypothesis seems the most likely, since some data exists which shows that Cl is present in virgin graphite. However, the other ones can not be completely ruled out due to lack of data.

2.5.2 Diffusion and Trapping of ^{36}Cl

Two theses by Vaudey [Vau10] and Blondel [Blo13] together constitute a large portion of the known properties of chlorine in nuclear graphite. It was found that chlorine is heterogeneously distributed across the nuclear graphite by studying graphite samples from the SLA2 UNGG reactor. The measured content varied by two orders of magnitude [VGT^{+}11]. Figure 2.22 shows secondary ion mass spectrometry (SIMS) measurements which created a 3D cartography for ^{35}Cl in graphite. They revealed that there are clusters of ^{35}Cl on the scale of micrometers [VGT^{+}11]. A strong accumulation of chlorine on the surface of the sample was also found. X-ray photoelectron spectroscopy (XPS) measurements yielded a speciation of the Cl shown in a scheme in Figure 2.22. On the surface, it was shown to be inorganic chlorine probably in the form of chlorites (ClO_2^-) and chlorates (ClO_3^-)

[VTMB10]. Organic chlorine (C-Cl) is also found; it forms bonds with the graphite matrix, either to aromatic rings or to aliphatic chains [VTMB10, VGT+11]. The ratio of these two species obtained with XPS is about 70/30 for organic vs. inorganic chlorine [VTMB10]. Later on this was revised by XANES measurements which have a larger penetration depth. With this method, they obtained a total amount of inorganic chlorine of only 5-10 % [VGT+11]. These measurements also showed that the inorganic chlorine is located close to the surface and organic chlorine is found in bulk graphite [Vau10]. It should be noted that no evidence of Cl_2, intercalated Cl (between graphene layers), or metal chlorides (for example Fe, Ni, or Zn) was found [VGT+11].

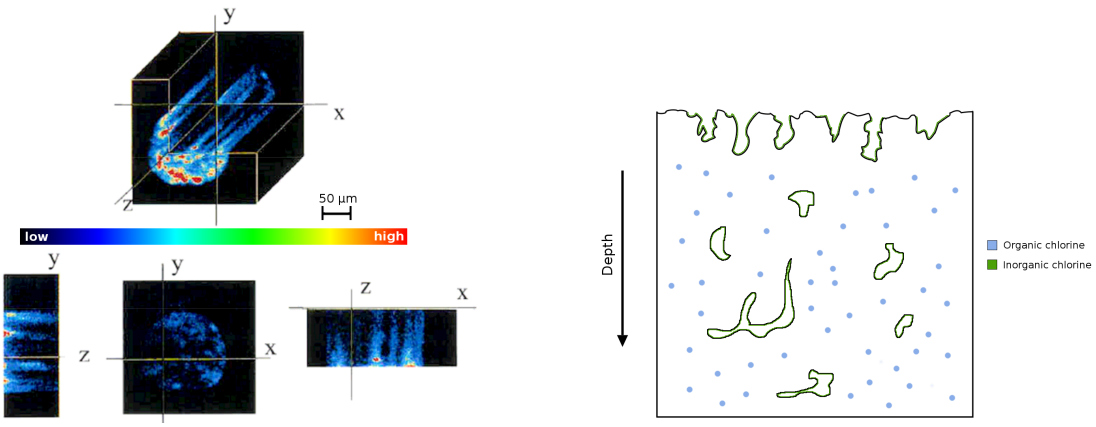

(a) (b)

Figure 2.22: a) 3D cartography of ^{35}Cl [Pet11] and b) scheme of Cl speciation and location [Vau10, Blo13] in virgin UNGG graphite.

Much alike for hydrogen in graphite, chlorine gets released in two steps as was observed by thermodesorption spectrosopy. SIMS measurements showed that there is no evidence of diffusion or transport following the insertion of Cl into graphite [VTM+09]. For the first step the release is quasi athermic; the activation energies for the release are as low as 0.1 eV [VTM+09]. The second step is 10 times slower than the first one and starts after heating for more than 8 hours; from then on the release is quasi stable [BMT+14]. At 1450°C all chlorine is released. This is accompanied by a restructuring of the graphite matrix which can be observed by a shrinking of the D3 band in the Raman spectrum. It was hypothesized that the first step up to a heating of 1200°C corresponds to the release of chlorine which is located at crystallite edges [BMT+14]. Above 1200°C the chlorine which is located inside the crystallites becomes mobile and is then subject to release. In graphite which was subject to much stronger irradiation, the release of chlorine changes significantly. The release is observed between 500-

1300°C, however the graphite matrix never completely restructures and remains partially disordered. This is directly connected to the large irradiation damage of the crystalline structure during the chlorine implantation [Blo13]. Chlorine is released in the form of HCl [VTM$^+$09], Cl_2 was not detected [VTM$^+$09].

Several theoretical papers were published on the interaction of graphene with different chlorine species [WKL09, YZW$^+$12, SC12, ZZY$^+$13, LZX14, SSD$^+$15]. The most stable state is molecular Cl_2 adsorbed on top of graphene interacting via weak van der Waals forces [YZW$^+$12, SC12, LZX14]. Atomic chlorine forms a charge-transfer complex with graphene with an interaction energy of -0.7 to -1.1 eV depending on the method used (LDA and GGAs obtain a stronger interaction than hybrid functionals) [WKL09, YZW$^+$12, SC12, ZZY$^+$13, LZX14]. For high Cl concentrations, additional metastable states are found: A non-bonding monolayer of Cl atoms which is a precursor for Cl_2 formation, and cluster formation on graphene of covalently bonding Cl which is also found for hydrogen or fluorine [YZW$^+$12]. The possible adsorption sites of Cl are very similar in energy (Δ E $\approx$ 0.02 eV) [SSD$^+$15], in addition, the migration barrier is rather small (92 meV at most). Thus the diffusion should be almost unhindered.

Xu et al. [XZL06] studied the interaction of dihalogenides, including Cl_2, with models of the (001), (100), and (110) surfaces. For the (100) surface the adsorption energy is 2.09 eV and for the (110) 2.68 and 5.03 eV, depending on the adsorption site. Thus, the (110) surface binds chlorine more strongly than the (100) surface which is mainly due to the steric repulsion of the adjacent chlorines according to their explanation. It should be noted that these results are very likely due to errors in their calculations as shown in the Appendix E.

2.6 Summary and Objectives of this Thesis

Nuclear graphite is a heterogeneous multi-scale material with polycrystalline binder and filler phases. Both, open and closed pores exist throughout the system, making the material accessible to gaseous compounds and water. In the case of UNGG graphite, the mechanical, thermal, and electrical properties are anisotropic due to the fabrication process which preserves the anisotropy of graphite monocrystals.

The irradiation damage of the graphite matrix created during operation of the nuclear reactor leads to several micro- and macroscopic changes of the properties. Displacement cascades initiated by neutrons produce point defects. Through diffusion these point defects can accumulate and build larger structures such as interstitial or vacancy loops. This microstructural damage is macroscopically observable by a contraction in the **a**-direction (due to vacancy lines) and expansion in the **c**-direction (due to interstitial loops). The increase in energy due to these point defects (Wigner energy) needs to be treated by their systematic annealing at

elevated temperatures for a safe operation of the reactor. Mechanical and thermal properties also change. Point defects increase the Young's modulus as well as the thermal conductivity in the **c**-direction, but also decrease thermal conductivity in the **a**-direction by acting as phonon scatterers. Other than irradiation damage, thermal oxidation as well as radiolytic oxidation of graphite by compounds of the cooling gas play a role in the deterioration of properties.

While the macroscopic properties of graphite are mostly well-understood, very often the link between microscopic deviations from the ideal state and the effect on macroscopic observables is not. This thesis aims at providing insight and extending the knowledge of this link. In a multi-scale approach, the results obtained with an accurate method on a small scale are applied to large systems by using an approximative method which is able to describe these properties at a lower cost. For some interaction types (C-C and C-H), such approximative interaction potentials already exist, for C-Cl interaction it needs to be developed from scratch. This multi-scale approach can be used to study the stability of different surfaces and the relation of this property to surface reconstructions or grain boundaries of graphite crystallites.

^{3}H is mostly formed by neutron capture of ^{7}Li which is found in the concrete of reactors as well as in graphite. For ^{36}Cl, the major source is neutron capture of ^{35}Cl which is also found in virgin nuclear graphite.

The structural changes of nuclear graphite when subject to irradiation and the behavior of ^{3}H and ^{36}Cl are closely related. For both radionuclides, evidence exists that they are trapped at two different sites: one is supposed to be the edges of crystallites, the other is located in the bulk and might be the edges of dislocation loops. For both traps, the number of available sites increases by irradiation which can be deduced from the decrease of the average crystallite size as well as the expansion in the **c**-direction.

For ^{3}H, the hypothesis regarding the traps is mostly supported by experimental evidence. However, the assumptions concerning the exact location of the traps and influence of surface reconstructions rely on very crude theoretical calculations from the 1960s. These assumptions need to be revisited with modern methods to better understand the interplay of the type of surface and ^{3}H-trapping.

For ^{36}Cl much less is known, but the similarities of obtained results to experiments with H suggest an analogous mechanism. Almost all published theoretical studies considered graphene, thus the influence of a 3D system on the interaction properties needs to be explored. This aspect is very important since the size of Cl could play an important role even though its chemical properties might seem similar to H at a quick glance (both need one electron for a full outer shell). Thus, a special focus needs to be laid on the insertion into bulk graphite as well as the influence of its size on the stability of surface-trapped Cl. In addition, all different

covalent and non-covalent interaction types need to be carefully studied since these results are used for the potential development.

Except for thermal migration, no significant diffusion is observed following the implantation of ^{3}H and ^{36}Cl into the material. This also shows a strong interaction of the radionuclides and their environment. This is in line with the observations of a reordering of the structure coupled to the thermal release of the radionuclides.

The hypothesis regarding the mechanism of thermal release is more complete for H. Release from the two sites is observed, afterwards diffusion is controlled by a successive adsorption and dissociation of H_2 along the crystallite surfaces. Finally it is released through open porosities in the form of H_2.

For Cl, evidence for a similar process was found with respect to the initial release from the trapping sites. This is followed by a process with a very low activation energy (0.1 eV). This is on the order of the theoretically calculated activation barrier of Cl diffusion on graphene. However, Cl is released in the form of HCl. It is unclear if hydrogen plays a role in the initial release of Cl from the trapping sites which would negate the existence of atomic Cl or if HCl is formed in later steps.

Finally, the heterogeneous distribution of Cl in bulk graphite is not well understood. While evidence exists that the preferential locations do not correlate with aggregation sites of metals, other specific properties of the environment responsible for the clustering of Cl are not known.

Using approximative potentials and molecular dynamics simulations allows to study many of these aspects. Implantations can be studied theoretically by simulating surface irradiation using radionuclides as radiation particles. This allows to explore several different aspects which are completely unknown until today: the irradiation damage created by inserted radionuclides, the interaction of the radionuclides with the damaged environment, and the diffusion properties following the insertion. Since molecular dynamics give access to temperature, all these properties can be explored with respect to temperature as well as with respect to initial energies of the inserted species. With these results, a relation between microstructural damage and macroscopic property changes can be established.

However, even though the use of potentials allows a much larger system size, it is impossible to fully cover the complexity of nuclear graphite. Thus, several different model system must be used which represent the different environments found in the real material. With this approach the influence of the environment such as surfaces (and reconstructions), grain boundaries, or porosity on the diffusion properties can be studied and insight on the atomic level is still possible. The study of diffusion properties with respect to different environments could then possibly allow to identify preferred sites for the radionuclides. For Cl, this could offer new insights on the observed heterogeneous distribution.

Together these results could extend the knowledge of processes occurring in nuclear graphite on length- and time scales differing in the range of several orders of magnitude. Finally, they could provide helpful complementary informations to increase the knowledge regarding the long-term behavior of radionuclides in irradiated graphite.

Chapter 3

Theoretical Background

The multi-scale aspect of this work is due to the demands to predict different properties which are of interest for a given system such as local adsorption properties or diffusion simulations in complex large-scale systems. Chemical bonding with defects or adsorption are rather local processes. However, the quantum nature of these interactions makes an accurate treatment necessary. Different methods exist, but all of them share a high computational cost which significantly limits the length scale of the studied system as well as the time scale for dynamic properties. Other methods which are less computationally demanding allow one to increase the system size and time scales by several orders of magnitude, but usually lack the accuracy to describe the complex interactions of a specific system. The method of choice here is to connect the two different methods by studying the interactions on a small scale and then apply these findings to larger scales by approximating them with a simpler interaction potential. In the following, the different methods used in this work will be introduced: density functional theory which is applied on the smallest scale, molecular dynamics simulations, and finally semi-empirical potentials which describe the interactions during the molecular dynamics simulations on large scales.

3.1 Density Functional Theory [PY89]

In order to describe a quantum system the Schrödinger equation needs to be solved. The time-independent form reads

$$\hat{H}\Psi = E\Psi. \tag{3.1}$$

$\hat{H}$ is the Hamiltonian, which contains the physics of the system, Ψ is the wave function of the state and E is the corresponding energy of that state. However, there is no analytical solution for systems with more than two particles, thus the

Schrödinger equation needs to be approximated. A fundamental approximation is the Born-Oppenheimer approximation. Since the electrons are at least 1836 times lighter than the nuclei, it is assumed that the nuclei's positions are fixed while the electrons are moving. The resulting Hamiltonian in atomic units is

$$\hat{H} = \underbrace{-\sum_i \frac{1}{2}\nabla_i^2}_{1} \underbrace{-\sum_{i,A} \frac{Z_A}{r_{iA}}}_{2} + \underbrace{\sum_{i>j} \frac{1}{r_{ij}}}_{3} + \underbrace{\sum_{A>B} \frac{Z_A Z_B}{R_{AB}}}_{4}. \tag{3.2}$$

Z_A is the charge of nucleus A, r_{iA} the distance between electron i and nucleus A, r_{ij} the distance between electron i and j and R_{AB} the distance between nuclei A and B. The different terms are explained in the following:

1. The operator of the kinetic energy of the electrons.
2. The operator of Coulomb interaction between the electrons and nuclei.
3. The operator of Coulomb interaction between the electrons.
4. The operator of Coulomb interaction between the nuclei.

It should be noted that temperature is absent in this Hamiltonian, thus this method calculates properties at 0 K. However, temperature dependence is in principle accessible by applying statistical physics.

For solid state calculations which usually have periodic boundary conditions, the method of choice is density functional theory (DFT). This method is based on determining the 3-dimensional electron density $\rho(\mathbf{r})$. All electron density based methods state that there is a functional dependence of the ground state energy on the electron density of a system

$$E[\rho] = T[\rho] + V_{ne}[\rho] + V_{ee}[\rho]. \tag{3.3}$$

The total functional $E[\rho]$ is split into a functional of the kinetic energy ($T[\rho]$), of the Coulomb interaction of nuclei and electrons ($V_{ne}[\rho]$), and of the Coulomb interaction of the electrons ($V_{ee}[\rho]$). The sum of $T[\rho]$ and $V_{ee}[\rho]$ is called $F[\rho]$. In 1964, Hohenberg and Kohn published their two Hohenberg-Kohn theorems, which were fundamental for the success of this method. In Kohn-Sham density functional theory, a non-interacting reference system is defined which excludes the electron-electron interaction. $F[\rho]$ can be rewritten to

$$F[\rho] = T_s[\rho] + J[\rho] + E_{xc}[\rho], \tag{3.4}$$

where $T_s[\rho]$ is the kinetic energy of the electrons of the reference system, $J[\rho]$ is the classical electron-electron repulsion, and $E_{xc}[\rho]$ is the part which includes all

the complicated non-classical physics of the electron-electron interaction and the difference of the kinetic energy of the interacting and non-interacting system.

$E_{xc}[\rho]$ is called the exchange-correlation functional which unfortunately is not known exactly. Thus, it has to be approximated, which leads to the myriad of different density functionals that are in use today.

3.2 Molecular Dynamics [FS96, Jen06]

The methods introduced in the previous section usually yield results at 0 K which are time-independent. Both, temperature- and time-dependent physical quantities are accessible with molecular dynamics. Equilibrium and transport properties of a classical many-body system which obeys the laws of classical mechanics can be determined with this simulation method. Since the nuclei are heavy enough compared to electrons, this approximation is reasonable in most cases. For a given set of initial coordinates $\mathbf{r}_0$, velocities $\mathbf{v}_0$, and the potential energy V which describes the interactions of a system, a new set of coordinates and velocities can be obtained by numerical integration of Newtons's second equation of motion $\mathbf{F} = m\mathbf{a}$. The differential form of this equation is

$$-\frac{dV}{d\mathbf{r}} = m\frac{d^2\mathbf{r}}{dt^2}. \tag{3.5}$$

The vector $\mathbf{r}$ contains the Cartesian coordinates ($3N_{atoms}$ elements), t denotes the time. The negative gradient of the potential energy is equivalent to the force acting on the particles. Starting from coordinates $\mathbf{r}_i$ at time t, the coordinates $\mathbf{r}_{i+1}$ for a time step Δt later (which should be small) can be obtained from a Taylor expansion

$$\begin{aligned} \mathbf{r}_{i+1} &= \mathbf{r}_i + \frac{\partial \mathbf{r}}{\partial t}(\Delta t) + \frac{1}{2}\frac{\partial^2 \mathbf{r}}{\partial t}(\Delta t)^2 + \frac{1}{6}\frac{\partial^3 \mathbf{r}}{\partial t}(\Delta t)^3 + \dots \\ \mathbf{r}_{i+1} &= \mathbf{r}_i + \mathbf{v}_i(\Delta t) + \frac{1}{2}\mathbf{a}_i(\Delta t)^2 + \frac{1}{6}\mathbf{b}_i(\Delta t)^3 + \dots \end{aligned} \tag{3.6}$$

In this equation, $\mathbf{v}_i$ denotes the velocities, $\mathbf{a}_i$ the acceleration, and $\mathbf{b}_i$ the hyperacceleration at time t. The same expansion can be made to obtain positions at a time step $-\Delta t$ earlier in time

$$\mathbf{r}_{i+1} = \mathbf{r}_i - \mathbf{v}_i\Delta t + \frac{1}{2}\mathbf{a}_i\Delta t^2 - \frac{1}{6}\mathbf{b}_i\Delta t^3 + \dots \tag{3.7}$$

By adding equations 3.6 and 3.7, the Verlet algorithm is obtained which was the first time-integration algorithm applied for MD simulations. It predicts the coordinates at time step Δt by only using coordinates at time t and the previous time step $-\Delta t$ as well as the current acceleration.

$$\mathbf{r}_{i+1} = (2\mathbf{r}_i - \mathbf{r}_{i-1}) + \mathbf{a}_i(\Delta t)^2 + \dots \tag{3.8}$$

Since the term including $\mathbf{b}_i$ is canceled out the error is of order $\mathcal{O}(\Delta t^4)$. The acceleration at time t can be derived from equation 3.5 for a given potential V. A disadvantage of this algorithm is the lack of the velocity since many useful properties can be derived from it. It can be obtained from the trajectory using a central difference approximation to the first derivative:

$$\mathbf{v}_i = \frac{r_{i+1} - r_{i-1}}{2\Delta t} + \mathcal{O}(\Delta t^2) \tag{3.9}$$

The error of the velocity is of order $\mathcal{O}(\Delta t^2)$. Additionally, the coordinates for the next time step need to be known, thus the velocity is not available for the current time step. Modifications to this algorithm have been proposed which account for this problem, such as the Leap Frog algorithm or the velocity Verlet algorithm. Since the velocity Verlet algorithm was used in this work exclusively, only this method will be presented in the following. It is equivalent to the Verlet algorithm, but explicitly includes the velocity at time t to generate the new coordinates

$$\mathbf{r}_{i+1} = \mathbf{r}_i + \mathbf{v}_i\Delta t + \frac{\mathbf{a}_i}{2}\Delta t^2. \tag{3.10}$$

After obtaining the new coordinates, the velocity can be approximated by using

$$\mathbf{v}_{i+1} = \mathbf{v}_i + \frac{\mathbf{a}_{i+1} + \mathbf{a}_i}{2}\Delta t. \tag{3.11}$$

Thus, to obtain the new velocity, the acceleration has to first be determined for the new coordinates. Practically this means that first coordinates are updated using the current positions, velocities, and accelerations of the particles. In the next step the updated accelerations are determined from the potential V at the new positions. Finally, velocities can be updated using the new accelerations.

A standard MD simulation runs with a constant number of particles, a constant volume, and, due to the conservation of energy, a constant total energy. This is called a microcanonical or NVE ensemble. This means that the temperature and pressure fluctuate, quite contrary to experiment where one or both of the quantities are kept constant. For example, the temperature T can be extracted from the average kinetic energy E_{kin} of the system

$$E_{kin} = \frac{1}{2}(3N_{atoms} - N_{constraint})k_B T \tag{3.12}$$

where $N_{constraint}$ is the number of constraints and k_B the Boltzmann constant. $N_{constraint}$ is usually three due to the conservation of linear momentum.

In many cases it is more suitable to simulate under conditions with constant temperature (canonical or NVT ensemble) or constant temperature and pressure (Isothermal-isobaric or NPT ensemble). Several different strategies exist to perform such simulations, the ones used in this work are the Nosé-Hoover thermostats/barostats. For these methods, a heat bath (and/or pressure bath) is created which is integral to the system studied and has its own fictive variables which evolve alongside the other variables of the system. Thus, during a simulation the velocities (and/or volume of the system) are dynamically changed to achieve a chosen target temperature/pressure.

3.3 Interaction Potentials

As discussed in the previous section, in order to perform molecular dynamics simulations the forces acting on all particles of a system must be known to apply the Newtonian mechanics.

The forces can be derived from the potential V describing the interactions in the system. This potential can, for example, be determined from quantum methods such as DFT. However, this is in general not applicable for systems larger than several hundreds of electrons, since DFT scales at least with the cube of the number of electrons.

Another possibility are force field methods. They were introduced to avoid the necessity of solving the Schrödinger equation for every nuclei configuration explicitly to obtain information about the potential energy surface of a system. In this approach the energy of a system is split up into valence (or bonded) and non-bonded contributions, *i.e.* $E_{total} = E_{valence} + E_{nonbonded}$. All these contributions are modeled to be only depending on the nuclei configuration and atom type. Furthermore, they are approximated as two-, three-, or four-body interactions at the most, neglecting the surroundings of the considered atoms. Thus, this method is completely parametrized; parameters can be obtained by fitting to experimental data or to electron structure calculations.

The valence contributions are usually split into bond stretch, angle bending, torsion, and more complex interactions. Established general purpose force fields such as AMBER [CCB+95], CHARMM [BBO+83] or UFF [RCC+92] are used in numerous scientific works, however they all share the disadvantage that creation and breaking of a bond is not possible. Atoms which are connected by covalent bonds need to be defined as such at the start of a simulation and will remain connected whether this is physically correct or not.

One type of interaction potentials which tries to resolve this inconvenience is the

family of bond order (BO) potentials. First introduced by Tersoff [Ter88] for group IV systems in 1988, there exist now many more which are able to describe surface reactions, defect creations, or phase transitions with changing connectivities.

Two potentials of the BO potential family which are frequently used when simulating graphite are the reactive bond order potential (REBO) and the long-range carbon bond order potential (LCBOP) which will be introduced in the following. Another reactive potential is ReaxFF which is more versatile and defined for many different atom types, however, it is rather complex and more computationally demanding.

The Reactive Bond Order Potential (REBO) [BSH+02, STH00]

This potential was originally introduced by Brenner [BSH+02] to describe the properties of hydrocarbons. Several different versions of this potential were published and are in use. The one presented here is the AIREBO potential of Stuart *et al.* [STH00] which uses the REBO potential for the covalent interactions and added non-covalent dispersion interactions for condensed matter applications. The central element of this potential is the bond order b_{ij}. The covalent interaction potential V_{ij}^{tot} of two atoms is defined as

$$V_{ij}^{REBO}(r_{ij}) = V_{ij}^{rep}(r_{ij}) + b_{ij}V_{ij}^{att}(r_{ij}), \tag{3.13}$$

where V_{ij}^{rep} and V_{ij}^{att} are the repulsive and attractive part of the potential and r_{ij} is the distance between the two particles.

The repulsive term V_{ij}^{R} is

$$V_{ij}^{rep} = w_{ij}(r_{ij}) \left(\frac{Q_{ij}}{r_{ij}} + 1\right) A_{ij} e^{-\alpha_{ij} r_{ij}}, \tag{3.14}$$

and the attractive term V_{ij}^{A} is

$$V_{ij}^{att} = w_{ij}(r_{ij}) B_{ij} e^{-\beta_{ij} r_{ij}}. \tag{3.15}$$

The parameters $A_{ij}, \alpha_{ij}, B_{ij}, \beta_{ij}$, and Q_{ij} are atom type-dependent. w_{ij} switches off the covalent REBO interactions smoothly

$$w_{ij}(t_c) = \Theta(-t_c) + \Theta(t_c)\Theta(1 - t_c)\tfrac{1}{2}[1 + \cos(\pi t_c)], \tag{3.16}$$

here $\Theta(t_c)$ is the Heaviside function and t_c is a scaling function

$$t_c(r_{ij}) = \frac{r_{ij} - r_{ij}^{min}}{r_{ij}^{max} - r_{ij}^{min}}. \tag{3.17}$$

The bond order b_{ij} can be a number between 0 and 1. Thus, depending on this parameter, two particles can form a bond or repel each other at a given distance r. It includes the many-body effects and is defined as

$$b_{ij} = \frac{1}{2}[p_{ij}^{\sigma\pi} + p_{ji}^{\sigma\pi}] + \pi_{ij}^{rc} + \pi_{ij}^{dh}. \tag{3.18}$$

$p_{ij}^{\sigma\pi}$ contains angle-dependent and coordination number-dependent terms whereas π_{ij}^{rc} is a three-dimensional cubic spline accounting for radical and conjugation effects. π_{ij}^{dh} penalizes rotations around multiple C-C bonds. $p_{ij}^{\sigma\pi}$ is defined as follows

$$p_{ij}^{\sigma\pi} = \left[1 + \sum_{k\neq i,j} G(\cos(\theta_{ijk}))e^{\lambda_{ijk}} + P_{ij}(N_C, N_H)\right]^{-1/2}. \tag{3.19}$$

$G(\cos(\theta_{ijk})$ depends on bond angles in order to describe the repulsion between two covalent bonds which approach each other; $e^{\lambda_{ijk}}$ is a term which improves the potential energy surface for hydrogen exchange reactions:

$$\lambda_{jik} = 4\delta_{iH}[(\delta_{kH}\rho_{HH} + \delta_{kC}\rho_{CH} - r_{ik}) - (\delta_{jH}\rho_{HH} + \delta_{jC}\rho_{CH} - r_{ij}), \tag{3.20}$$

where δ_{ij} is the Kronecker delta and ρ_{ij} are fitted parameters. Finally, $P_{ij}(N_C, N_H)$ is a two-dimensional cubic spline which is needed to reproduce the different bond energies depending on the coordination number. The carbon-only coordination number N^C is defined as

$$N_{ij}^C = \left(\sum_{k\neq i} \delta_{kC} w_{ik}(r_{ik})\right) - \delta_{jC} w_{ik}(r_{ij}) \tag{3.21}$$

The hydrogen-only coordination number is defined analogously, with C replaced by H in the Kronecker delta expression.

The three-dimensional cubic spline π_{ij}^{rc} depends on the total coordination numbers N_i and N_j, which are the sum of the carbon- and hydrogen-only coordination numbers, as well as on N_{conj}:

$$N_{conj} = 1 + \left[\sum_{k\neq i,j}^{carbon} w_{ik}F(x_{ik})\right]^2 + \left[\sum_{l\neq i,j}^{carbon} w_{jl}F(x_{jl})\right]^2 \tag{3.22}$$

N_{conj} accounts for conjugation effects where

$$F(x_{ik}) = \begin{cases} 1 & x_{ik} < 3 \\ [1 + \cos(2\pi(x_{ik} - 2))]/2 & 2 \leq x_{ik} < 3 \\ 0 & x_{ik} \geq 3 \end{cases}$$

and

$$x_{ik} = N_k - w_{ik}(r_{ik}). \tag{3.23}$$

A more extensive explanation for the short-range part can be found in the original paper by Brenner [BSH+02].

Due to the initial applications to hydrocarbons and diamond where covalent interactions dominate, the original version of this potential lacked long-range non-covalent interactions which are necessary to describe the larger part of condensed matter. Stuart *et al.* extended the REBO potential and created the adaptive intermolecular REBO (AIREBO) potential [STH00]. The total interaction of two particles is defined as

$$V_{ij}^{tot}(r_{ij}) = V_{ij}^{REBO}(r_{ij}) + V_{ij}^{VDW}(r_{ij}) + V_{ijkl}^{tors}(\omega_{ijkl}). \tag{3.24}$$

Thus, the REBO part was left as proposed by Brenner and two terms were added: The non-covalent interaction potential V_{ij}^{VDW} and torsional interactions $V_{ijkl}^{tors}(\omega_{ijkl})$ to better describe rotations about single C-C bonds. The latter will not be explained here since a different potential was used to describe C-C interactions and can be found in the original paper [STH00]. In the first version of AIREBO, the non-covalent interactions were described by a Lennard-Jones potential. While this model potential is computationally efficient and sufficient in treating equilibrium properties, it is known to be too repulsive for short distances. Since an important part of this work is the simulation of irradiation processes where short distances between particles are naturally occurring during collisions, another more recent version of this potential (AIREBO-M) was chosen. Here, the interactions are treated by Morse potentials which perform much better at higher pressures and short distances. It is defined as

$$V_{ij}^{Morse}(r_{ij}) = -\epsilon_{ij}\left[1 - \left(1 - e^{-\alpha_{ij}(r - r_{ij}^{eq})}\right)^2\right]. \tag{3.25}$$

Here, the parameters are the standard parameters of a Morse potential, which describe the depth (ϵ_{ij}) of the potential, the equilibrium location (r_{ij}^{eq}) and the second derivative at r_{ij}^{eq} (α_{ij}).

In order to allow a smooth switching between non-covalent and covalent interactions, $V_{ij}^{Morse}(r_{ij})$ is multiplied with switching functions

$$V_{ij}^{VDW}(r_{ij}) = S(t_r(r_{rij}))S(t_b(b_{ij}^*))C_{ij}V_{ij}^{Morse}(r_{ij}) + [1 - S(t_r(r_{rij}))]C_{ij}V_{ij}^{Morse}(r_{ij}). \tag{3.26}$$

$S(t_r)$ is a universal switching function similar to equation 3.16 for the covalent part and reads

$$S(t_r) = \Theta(-t_r) + \Theta(t_r)\Theta(1 - t_r)[1 - t^2(3 - 2t)], \tag{3.27}$$

where the argument t_r has the same definition as equation 3.17 with different parameters. The switching function $S(t_b)$ takes the same form; its argument depends on the bond order and is defined as

$$t_b(b_{ij}) = \frac{b_{ij} - b_{ij}^{min}}{b_{ij}^{max} - b_{ij}^{min}}. \tag{3.28}$$

For high bond orders ($> b_{ij}^{max}$), this switching function turns off non-covalent repulsion for short distances in order to allow the creation of covalent bonds. For low bond orders ($< b_{ij}^{min}$), the non-covalent repulsion remains to inhibit the formation of bonds. Since b_{ij} would be zero for distances where non-covalent interactions play a role, it is determined at r_{ij}^{min} yielding a hypothetical bond order. Finally, C_{ij} is a connectivity switch which aims to exclude interactions between (1,3) and (1,4) neighbors by setting C_{ij} to zero.

A more detailed description of the potential can be found in the original paper by Stuart *et al.* [STH00] and O'Connor *et al.* [OAR15]

The Long-range Carbon Bond Order Potential (LCBOP) [LF03]

The LCBOP potential uses similar ideas as the REBO potential and was originally created to describe allotropes of carbon (graphite and diamond) and is as such only defined for carbon atoms.

Since long-range interactions are crucial to describe the interplanar interaction in graphite, they were included in the potential from the start. The total binding energy E_b is written as

$$E_b = \frac{1}{2}\sum_{i,j}^{N} f_{c,ij} V_{ij}^{SR} + S_{ij} V_{ij}^{LR}, \tag{3.29}$$

where $f_{c,ij}V_{ij}^{SR}$ is the short-range covalent interaction and $S_{ij}V_{ij}^{LR}$ is the long-range non-covalent interaction. $f_{c,ij}$ and S_{ij} are smooth cutoff functions and are related by $S_{ij} = 1 - f_{c,ij}$. $f_{c,ij}$ is defined as follows

$$f_{c,ij}(x) = \Theta(-x) + \Theta(x)\Theta(1 - x)\exp\left(\frac{\gamma x^3}{x^3 - 1}\right). \tag{3.30}$$

Here, $\Theta(x)$ is the Heaviside function; x is a scaling function

$$x(r_{ij}) = \frac{r_{ij} - r_1}{r_2 - r_1}, \tag{3.31}$$

and γ is a fitted parameter.As for the REBO potential, the short-range part of the potential is a sum of a repulsive and attractive part. The attractive part is again multiplied with a bond order term. It reads as follows

$$V_{ij}^{SR} = V_R(r_{ij}) - B_{ij}V_A(r_{ij}). \tag{3.32}$$

Here, r_{ij} is the distance between neighbors i and j; $V_R(r_{ij})$ and $V_A(r_{ij})$ are the repulsive and attractive pair potentials and read as

$$V_R(r_{ij}) = A\exp(-\alpha r_{ij}), \tag{3.33}$$

and

$$V_R(r_{ij}) = B_1\exp(-\beta_1 r_{ij}) + B_2\exp(-\beta_2 r_{ij}). \tag{3.34}$$

B_{ij} is the bond order term, which takes the many-body effects into account. It is defined as

$$B_{ij} = \frac{1}{2}[b_{ij} + b_{ji} + F(N_{ij}, N_{ji}, N_{ij}^{conj})]. \tag{3.35}$$

b_{ij} depends on bond angles and $F(N_{ij}, N_{ji}, N_{ij}^{conj})$ is a function that depends on coordination numbers used to describe the different C-C bond types. b_{ij} is defined as

$$b_{ij} = \left(1 + \sum_{k\neq i,j} f_c(r_{ik})G(\cos\theta_{ijk})H(\delta r_{ijk})\right)^{-\delta}. \tag{3.36}$$

$G(\cos(\theta_{ijk})$ depends on bond angles to describe the repulsion between two covalent bonds that approach each other, $\delta r_{ijk} = r_{ij} - r_{ik}$, and $H(\delta r_{ijk})$ is a function which was fitted to surface properties, elastic properties, and the energy barrier of the transformation of diamond to graphite.

A more extensive explanation of the short-range part can be found in the original paper by Los and Fasolino [LF03].

The long-range potential is a sum of two functions

$$V_{ij}^{LR} = \Theta(r_0 - r_{ij})V_1^M(r_{ij}) + \Theta(r_{ij} - r_0)V_2^M(r_{ij}) \tag{3.37}$$

with $V_i^M (i = 1, 2)$ being simple Morse functions

$$V_i^M = \epsilon_i[\exp(-2\lambda_i(r_{ij} - r_0)) - 2\exp(-\lambda_i(r_{ij} - r_0))] + \nu_i, \tag{3.38}$$

and ν_i is a shift to generate a smooth behavior between the two functions.

The Ziegler-Biersack-Littmarck Potential (ZBL)

As explained previously, standard potentials are often constructed to describe systems close to equilibrium. Thus, usually the repulsive part of the potential is only well described for distances slightly lower than the equilibrium bond length. In contrast to that, the Ziegler-Biersack-Littmarck potential [ZBL85] is a potential that models the screened nuclear repulsion for very short distances. This is needed for high-energy collision simulations which are performed in this work. It is strictly repulsive, therefore it needs to be coupled with another potential which can describe bonding interactions. The potential is defined as follows

$$V_{ZBL} = \frac{Z_i Z_j e^2}{r_{ij}} \phi(r_{ij}/a), \tag{3.39}$$

where Z_i and Z_j are the atomic charges of the particles i and j, r_{ij} is the distance, e is the electronic charge, and $\phi(r_{ij}/a)$ is the screening function. The product of the classical Coulomb interaction with this screening function leads to a lower repulsion of the nuclei. This is the expected behavior when two point charges are surrounded by a charge distribution of countercharges.

Chapter 4

Physico-chemical Properties of ^{3}H and ^{36}Cl in Graphite: Insights from the Atomic Scale - *Ab Initio* Calculations

In this chapter, the physico-chemical properties of the radionuclides ^{3}H and ^{36}Cl in graphite are presented. This step is an important part of the present multi-scale study since this kind of information can only be obtained at this level of theory due to the quantum nature of the interactions. First, a thorough search for a Hamiltonian which can describe the structural, electronic, dynamic, and mechanical properties of graphite is presented. Following that, the methodology for the calculations of H and Cl in graphite is explained. Then, the interactions of ^{3}H and ^{36}Cl with different structures, such as differently oriented surfaces and their reconstructions, as well as point defects caused by irradiation are explained. Finally, the results are discussed and a conclusion is drawn from the findings.

4.1 Methodology

In this section, the methodology for the investigation of the physico-chemical properties of hydrogen and chlorine in graphite is presented. The DFT calculations were performed with the periodic code CRYSTAL09 [DOC^{+}05, DSR^{+}09]; calculations with QUANTUM ESPRESSO [GBB^{+}09] were also performed in order to find a suitable Hamiltonian for describing graphite. Within CRYSTAL, both the Hartree-Fock and Kohn-Sham equation as well as hybrid schemes, such as B3LYP [Bec93, LYP88, dPRMIM02] or PBE0 [AB99], where the exchange operator is a linear combination of the HF and DFT ones, can be solved self-consistently. Pseu-

dopotential and all-electron Gaussian-type basis sets can be used. The QUANTUM ESPRESSO code, on the other hand, uses the density functional techniques as well as the hybrid schemes [Bec93, LYP88, dPRMIM02, AB99] with different plane wave pseudopotentials [GBB$^+$09].

4.1.1 The Choice of Hamiltonian for Graphite

This section is a summarized form of the original paper [LPB$^+$16], a more extensive analysis of the performance of the different exchange-correlation functionals, basis sets, and dispersion corrections can be found in Ref. [LPB$^+$16].

In order to find a functional which can describe the properties of graphite to a satisfying extent, several exchange-correlation functionals based on the local density approximation and generalized gradient approximation were used. They will be indicated as follows: LDA for Dirac-Slater [Dir30] exchange plus Perdew-Zunger [PZ81] correlation potential; PBE for Perdew-Burke-Ernzerhof [PBE96] exchange-corre-lation functional, and PBEsol [PRC$^+$08] corresponds to the revised PBE improving the description of the equilibrium properties of solids. Two hybrid HF/KS functionals were also considered, namely B3LYP [Bec93, LYP88, dPRMIM02] and PBE0 [AB99].

For the Gaussian basis sets, carbon was described by an all-electron basis set [DCO$^+$90, CPDS93]. The basis set is a contraction of – 6s-211sp-1d* – GTFs (a contraction of 6, 2, 1, 1 and 1 Gaussian type functions for the 1s, 2sp, 3sp, 4sp, and d shells, respectively). The outer exponents of C were optimized using an energy criterion and are reported in Table 4.1. The basis set optimization was carried out using the LoptCG [ZW06] script, which performs numerical gradient optimizations based on the conjugate gradient method [HS52].

Table 4.1: Exponents and coefficients of the contracted Gaussian basis set adopted in the present study for C. Only the most diffuse 211sp-1d^* GTFs are given (see Ref. [DCO$^+$90, CPDS93] for a complete set of data).

Shell	Exponent	Coefficient	
		$s(d)$	p
sp	11.705961	-0.160393	0.296329
	2.877171	-0.645825	1.383579
	0.792605	1.	1.
	0.234684	1.	1.
d	0.927994	1.	

Within QUANTUM ESPRESSO, projector augmented waves (PAW)[a] with a scalar relativistic pseudopotential were used as basis set. In this pseudopotential, $2s$ and $2p$ electrons of carbon were treated as valence electrons.

In order to take the contribution of dispersion interactions to the interlayer interaction of HOPG into account more reliably, two types of Grimme's correction were investigated: the semi-empirical London dispersion type correction [Gri04, Gri06] (the D2 correction implemented in CRYSTAL and QUANTUM ESPRESSO), and the most recent dispersion correction D3 [GAEK10], which was implemented in CRYSTAL09 as part of this presented work.

For the D2 correction, the original dispersion coefficient C_6^{ij} and atomic van der Waals radius R_{vdW} as proposed by Grimme [Gri04, Gri06] were used, since the net atomic charge of C in graphite and diamond is close to the one of neutral carbon according to a Mulliken population analysis. These values are 1.75 $\mathrm{J\,nm^6\,mol^{-1}}$ and 1.452 Å, respectively. The damping function steepness d was fixed at 20 Å. The cutoff distance to truncate the direct lattice summation was 30 Å. Only the scaling factor s_6[b] was optimized in order to obtain a **c** parameter with an error of less than 0.5 % with respect to experiment. For each level of approximation, the used values for the s_6 parameter are given in Table 4.2. In the following, the obtained corrected results will be referred to with the suffix "-D2".

Regarding the D3 correction, only zero damping was used. With s_6 fixed at 1.0, the s_8 [b] parameter was optimized to obtain a **c** parameter with an error of less than 0.5 % with respect to experiment. This approach offers the same flexibility as the reparameterization of the D2 correction, while preserving the correct asymptotic behavior of the dispersion interactions. The cutoff values for dispersion interaction and coordination number were 50 Å and 20 Å, respectively. The three-body terms were not included since they are not recommended as default [GAEK10] and are not impacted by a modification of the s_8 parameter. For each level of approximation used within CRYSTAL, the used values for the s_8 parameter are given in Table 4.2. In the following, the obtained corrected results will be referred to with the suffix "-D3".

For the evaluation of the Coulomb and exchange series within CRYSTAL, the truncation thresholds for the bielectronic integrals, as defined in the CRYSTAL manual [DSR+09], were set to 10^{-8}, 10^{-8}, 10^{-8}, 10^{-8} and 10^{-16} a.u., respectively. Smearing of the Fermi surface was not used. Due to CRYSTAL09's limit with respect to the number of irreducible k-points, different Monkhorst-Pack meshes [MP76] were used in order to balance the increase in k-points with the various reductions of symmetry, as needed for the determination of the elastic constants

[a] The pseudopotentials C.pbe-n-kjpaw_psl.0.1.UPF, C.pbesol-n-kjpaw_psl.0.1.UPF, and C.pz-n-kjpaw_psl.0.1.UPF from `http://www.quantum-espresso.org` were used.

[b] Global density functional-dependent scaling parameters for the nth order interaction (n=6,8)

Table 4.2: s_6 (D2) and s_8 (D3) scaling factors used for each Hamiltonian and basis set.

Basis	HF	LDA	PBE	PBEsol	B3LYP	PBE0
GTF-D2	0.585	-0.470	0.250	-0.087	0.350	0.167
GTF-D3	1.340[a]	-2.740[a]	0.410	-0.460	0.740	0.255
PAW-D2		-0.025	0.5775	0.2325		

[a]To be consistent with the parameterization of the D3-correction at the PBE, PBEsol, B3LYP and PBE0 levels, $s_{r,8}{}^{c}$ radii [Gri15] has been set to 1. for HF and LDA.

and frequencies. For the evaluation of the interlayer interaction energy, the mesh was reduced due to a degeneracy at high symmetry points, sampling these points leads to severe convergence issues. The meshes are listed in Table 4.3.

Table 4.3: Monkhorst-Pack k-point meshes used for CRYSTAL calculations.

Calculation	Mesh
Optimization	$18 \times 18 \times 18$
Frequencies	$16 \times 16 \times 16$
Elastic constants	$14 \times 14 \times 14$
Cohesive energy	$18 \times 18 \times 18$
Interlayer energy	$16 \times 16 \times 16$

For QUANTUM ESPRESSO, plane wave cutoffs of 900 and 250 a.u. were used for HOPG and diamond, respectively. Methfessel-Paxton first order spreading of 0.01 a.u. was applied. For QUANTUM ESPRESSO, all calculations were performed with $18 \times 18 \times 18$ and $16 \times 16 \times 16$ Monkhorst-Pack k-point meshes [MP76] for HOPG and diamond, respectively.
For both codes, the convergence criteria on total energies (and for the elastic constants and frequencies determination) were 10^{-9} (10^{-12}) a.u. Atomic displacements and force thresholds were 1.8×10^{-3} and 4.5×10^{-4} a.u., respectively. With these computational conditions, the obtained data can be considered as fully converged.

With QUANTUM ESPRESSO, the "Elastic" script [GPS+13] was used for the determination of the elastic constants. The graphics were created with MOLDRAW [UBV88, UV88, UVC93] and POV-Ray [pov15].

Computational details for the calculations of properties are given in the Appendix B.

Structure Optimization

Figure 4.1 shows the relative errors obtained for the C-C bond length d_{C-C} and the interplanar distance d_g without dispersion correction with respect to experiment [BM55].

The computed d_{C-C} are in good agreement with the experimental data, whatever the basis set and Hamiltonian; the average relative error is ≈ -0.3 % with a mean total deviation of ≈ 0.5 %. HF and LDA underestimate **a** and d_{C-C} by 1 %, but not for the same reasons: LDA systematically underestimates the lattice parameters of crystals whatever their nature. At the HF level, the electronic charge is more concentrated around the atoms or around the bond due to the lack of correlation; in other words, the system is more ionic or covalent (see for instance Ref. [BLOD01, LBD$^+$07]). Among the GGA functionals, PBE overestimates **a** and d_{C-C} while PBEsol corrects this tendency to reach a good agreement with the experimental data. As for other materials [RKV08, CPR$^+$09], the obtained error with the PBEsol functional is less than ≈ 0.1 %. Among the hybrid functionals, PBE0 provides results with the same accuracy as HF and LDA; however, for ionic materials [LBD$^+$07, SBS$^+$13] this functional is better adapted. The best description of d_{C-C} is obtained with the B3LYP functional: the deviation with respect to experimental data is ≈ 0.2 %.

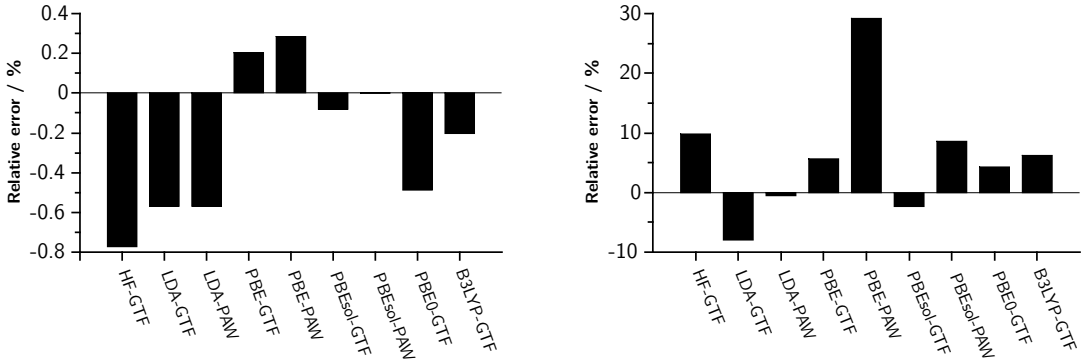

(a) (b)

Figure 4.1: Relative errors of a) the distance d_{C-C} and b) the interlayer spacing d_g (right) of HOPG with respect to experimental data at 4 K [BM55] for different Hamiltonians and basis sets without dispersion correction.

Since d_g is driven by the weak interlayer binding, the obtained theoretical data characterize the difficulties of taking the dispersion interactions into account. For instance, without dispersion correction this parameter is underestimated or overestimated by 0.3 Å to 1 Å at the LDA–GTF and PBE–PAW levels, respectively (the other Hamiltonians giving intermediate results). This behavior is linked to the

dispersive character of the interlayer interaction which is not correctly accounted for at the various levels of approximation (as it was shown for other materials [KP94, PJB95, BLOD01]).

The obtained data for d_g are always lower for GTF with respect to the ones obtained with PAW due to the BSSE. Except for LDA, d_g is largely overestimated ($\approx +10\,\%$). The LDA data show an underestimation of d_g by about -10 %; this is not surprising as it is well known that LDA overbinds systems held together by dispersive forces [KP94, PJB95]. This overestimation is compensated by adding Grimme's dispersion corrections. It represents an attractive contribution to the interlayer interactions. However, the used parameterization has to be adapted to the material of interest [BHLA10, CZWVU08, UZWTC09].

Cohesive and Interlayer Interaction Energies

For cohesive energies E_{coh} , the contribution of covalent interactions is much more important. The order of magnitude of E_{coh} is eV/atom (exp. 7.36 eV [Lid91]), whereas for the interlayer interaction energy E_{IL} it is meV/atom (exp. 35-52 meV [BCC$^+$98, ZUH04]). As expected, HF underestimates E_{coh} by about 30 % (5.39 eV), on the other hand LDA largely overbinds the two systems by about 20 % (8.90 eV). The other functionals provide data between HF and LDA and closer to experiment: the best agreement is found for B3LYP–GTF–D3 (7.32 eV).

For E_{IL}, the choice of the dispersion correction is very important. D2 and D3 tend to not only correct, but even overcorrect this energy. While for E_{coh}, no significant advantage is gained by using D3, the interlayer energies show the limits of D2 and the improvement offered by D3: They are in general underestimated by D2 due to the s_6 parameter being largely decreased with respect to Grimme's original parameters; additionally, the asymptotic behavior of the dispersion interaction is not correct for all Hamiltonians (since $s_6 \neq 1$). By using D3 both of these problems are solved. Keeping $s_6 = 1$ assures the correct asymptotic behavior, tuning the s_8 parameter alters the force, but the total dispersion correction remains negative. Overall, PBE–GTF–D3 (43 meV), PBE0-GTF-D3 (33 meV), and B3LYP–GTF–D3 (42 meV) have the best agreement with the experimental data.

Band Structure

Figure 4.2 shows the band structure obtained with PBE–GTF and PBE–PAW as well as the density of states (DOS) obtained with PBE–GTF. They are typical for semi-metallic materials: no or a small gaps at specific k-points (here at the K and H points) and no density-of-states at the Fermi level. The projected DOS show that: near the Fermi level, the states are mainly $\pi(p_z)$-states in the valence band

(between 0 and -5 eV) and $\pi^*(p_z)$-states in the conduction band (between 0 and 7.5 eV); as expected, the $\sigma(sp_xp_y)$-states are lower in energy (between -2.5 and -17 eV) and the $\sigma^*(sp_xp_y)$-states higher up in the conduction band (over 7.5 eV). The obtained band structures show that GTF and PAW basis sets give different

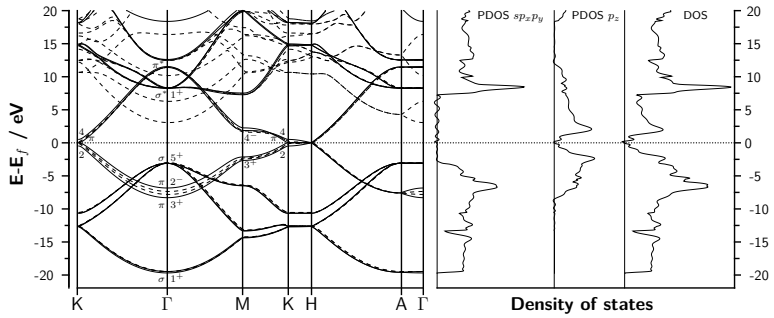

Figure 4.2: Band structures and DOS of HOPG obtained at the PBE level. On the left, the calculated band structures with GTF (full lines) and PAW (dashed lines) are shown; on the right, the projected density of states on the $2s2p_x2p_y$ AOs (PDOS sp_xp_y) and on the p_z AOs (PDOS p_z) as well as the total density of states (DOS) are shown.

descriptions of certain valence and conduction bands. This is illustrated in Figure 4.3, which shows the relative errors with respect to the bandwidths and interband separations.

To evaluate the overall performance of the functionals, the root mean square deviation (RMSD) and mean average error (MAE) were determined with respect to experimental data. Overall, functionals using a GTF basis describe the band structure better. The best agreement is obtained for LDA–D2/D3 (MAE = 0.36, RMSD = 0.55) , PBE–D2/D3 (MAE = 0.39, RMSD = 0.54) and PBEsol–D2/D3 (MAE = 0.40, RMSD = 0.56) functionals with a GTF basis. All other functionals yield MAEs and RMSDs > 1.0.

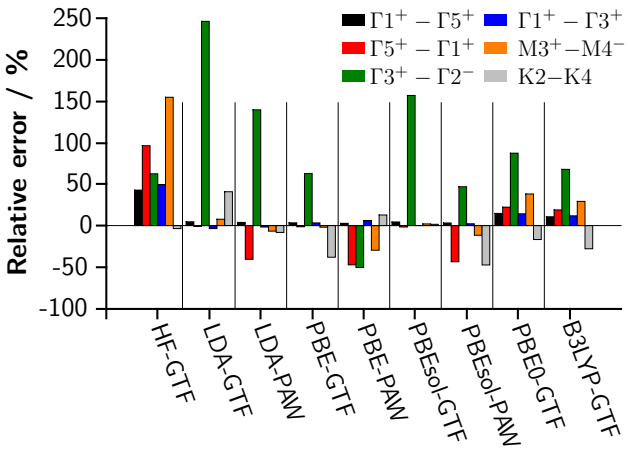

Figure 4.3: Relative errors of the band widths with respect to the experimental data [HLR82, THR81] for different Hamiltonians and basis sets without dispersion correction.

Frequencies

Figure 4.4 shows the IR and Raman spectra obtained with PBE–D3–GTF. The two E_{2g} modes are Raman-active (exp. 42 cm^{-1} and 1582 cm^{-1}, respectively) [NWS72, NS79], the A_{2u} and E_{1u} modes are IR-active (exp. 868 cm^{-1} and 1588 cm^{-1}, respectively) [NLS77]. The two B_{2g} modes are inactive. However, one was determined by neutron scattering at 127 cm^{-1} [NWS72], whereas the other one is expected to be close to the A_{2u} mode at 868 cm^{-1} [NS79]. The obtained relative errors are presented in Figure 4.5. The results are coherent with the established influences of the Hamiltonian on vibrational properties [SR96].

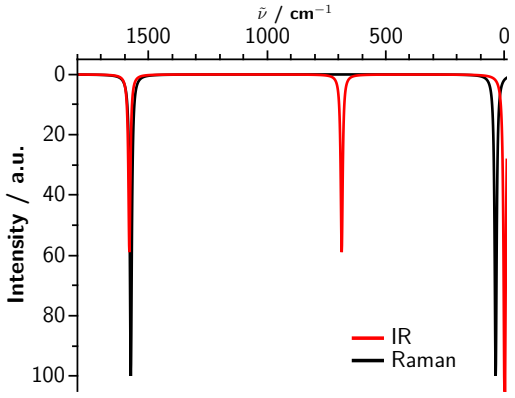

Figure 4.4: Raman and IR spectra of HOPG obtained at the PBE-GTF-D3 level. Intensities are only schematic and obtained from MOLDRAW [UBV88, UV88, UVC93].

Using the mean average error (MAE) and RMSD with respect to experimental results shows the following: The PAW basis sets (MAE < 15, RMSD < 20 for all functionals) perform better than the GTF basis sets (MAE > 40, RMSD > 70 for all functionals); LDA, PBE, and PBEsol yield similar results. Among the GTF basis sets PBE and B3LYP can reproduce the experimental results the best.

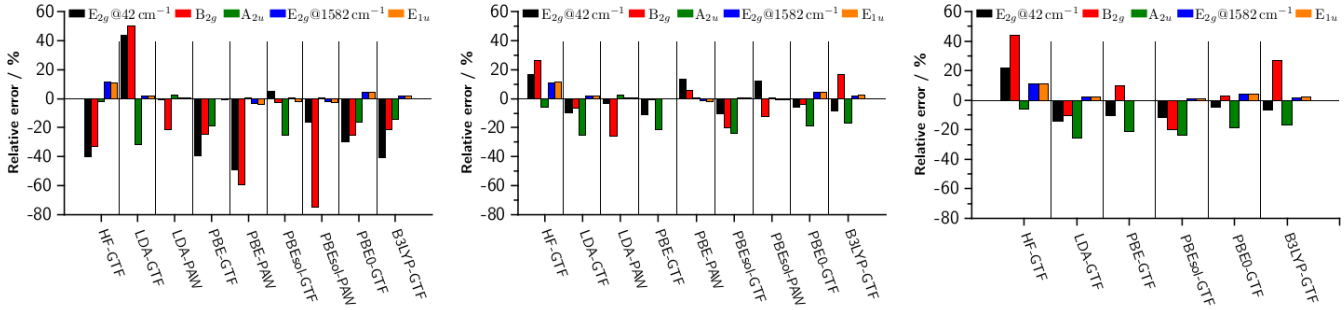

(a) (b) (c)

Figure 4.5: Relative errors of the frequencies with respect to the experimental data [NWS72, NLS77, NS79] for different Hamiltonians and basis sets: a) without, b) with D2, and c) with D3 dispersion correction.

Elastic Constants

In the Voigt notation, the elastic properties of HOPG are characterized by six elastic constants: C_{11}, C_{12}, C_{13}, C_{33}, C_{44}, and C_{66}, however $C_{66} = (C_{11} - C_{12})/2$. The obtained errors for these data with respect to experimental results are shown in Figure 4.6.

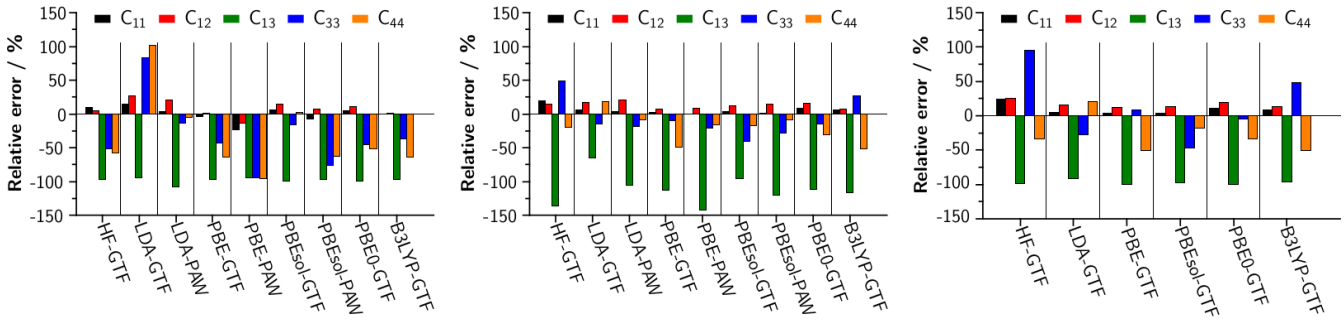

(a) (b) (c)

Figure 4.6: Relative errors of the elastic constants with respect to the experimental data at 4 K [BM55] for different Hamiltonians and basis sets: a) without, b) with D2, and c) with D3 dispersion correction.

Considering the MAE and RMSD with respect to experimental data, the best results are obtained with PBE-D2 and PBEsol-D2 with a PAW basis (MAE < 13, RMSD < 15). Among the functionals using a GTF basis, PBE–GTF–D3 performs the best (MAE $= 15$, RMSD $= 21$). Given that the shear elastic constant C_{13} is negative for PAW basis sets, PBE–GTF–D3 represents the best compromise to obtain a reasonable description of the elastic properties of graphite.

Summary

The various obtained results illustrate some well-known characteristics of the various functionals: LDA overbinds and the other Hamiltonians underbind the graphitic planes. For GTF, the BSSE allows to artificially correct for the lack of dispersion interaction. Therefore, the interlayer interactions are stronger than for PAW; thus, with respect to PAW and without dispersion corrections, the **c** parameter is underestimated, the interlayer frequencies are overestimated and elastic constants, such as C_{33}, are overestimated. It is difficult to state if GTF or PAW are more suitable to describe these compounds: in certain cases the BSSE allows to improve the description of given properties, in other cases it worsens the results. However, if dispersion corrections are included, the results are of comparable quality.

With respect to the dispersion correction, D3 globally performs better than D2 (as it was also mentioned for other types of materials [IZW15, STP$^+$15]), and should therefore be the method of choice for the HOPG system.

Based on the overall results, PBE–GTF–D3 is the best compromise to describe the properties of HOPG.

4.1.2 ^{3}H in Graphite

To study the interaction of hydrogen and graphite, the PBE (for Perdew–Burke–Ernzerhof exchange-correlation) functional [PBE96] combined with the D3 dispersion correction [GAEK10] as given in section 4.1.1 was used to describe the properties of graphite.

For the Gaussian basis sets, carbon and hydrogen were described by an all-electron basis set. The C basis set [DCO$^+$90, CPDS93] is the same as given in section 4.1.1. The H basis set [LOM$^+$00] is a contraction of – 511s-1p^* – GTFs and is given in Table 4.4. The outer exponents 11s-1p^* of the H basis were optimized for CH_4 by using an energy criterion. The basis set optimization was carried out using the LoptCG [ZW06] script, which performs numerical gradient optimizations based on the conjugate gradient method [HS52].

A two-dimensional (2-D) slab model is used to study the surface properties: the surface consists of a slab formed by a sufficient number of atomic layers parallel to a given plane. It is limited by two surface planes and has 2-D periodic boundary conditions; thus in this framework the system is two-dimensional and isolated. To treat the defective crystals and adsorbed surfaces a supercell approach has been adopted. The sizes of the used supercells were $5 \times 5 \times 2$ for bulk HOPG, a 5×5 supercell of a 4-layer slab for the (001) surface, a 3×2 supercell of a 24-layer slab for the (100) surface, and a 2×2 supercell of a 14-layer slab for the (110) surface. The number of carbon atoms for these different models ranges from 192 to 224

Table 4.4: Exponents and coefficients of the contracted Gaussian basis set adopted in the present study for H. Only outer s and p GTFs are given (see Ref. [DCO$^+$90, CPDS93] for a complete set of data).

Shell	Exponent	Coefficient
s	0.230254	1.0
	0.083915	1.0
p	1.030824	1.0

atoms. For the in-plane reconstructed surfaces, a 4×2 supercell of a 24-layer slab for the (100) surface and a 2×2 supercell of a 14-layer slab for the (110) surface was used; for arch-shaped reconstructions a 3×1 supercell of a 66-layer slab for the (100) surface and a 2×1 supercell of a 36-layer slab for the (110) surface. The various cells are sufficiently large (224-288 carbon atoms) to allow full relaxation of the reconstructed surfaces. Hydrogen was always adsorbed only on one side of the slab. Adsorption of multiple hydrogen atoms is done successively, thus the optimized structure for $(n-1)$ hydrogen atoms is the starting point for adsorption of n hydrogen atoms. Only the most stable position for the additional hydrogen is reported.

The methods for the calculation of surface energies E_{surf} and formation energies E_{form} of the studied surfaces and vacancies are described in the Appendix B. The adsorption energy E_{ad} is defined as the energy difference between the energy of the graphite-adsorbate structure and the sum of energies of the graphite structure and a hydrogen in its reference state:

$$E_{ad} = \frac{E_0 - E_G^{opt} - nE_H}{n} \tag{4.1}$$

where E_0 is the total energy of the optimized system, E_G^{opt} the energy of the optimized surface without adsorbates, E_H the energy of the isolated hydrogen and n the number of adsorbed H–atoms. All E_{ad} are reported with respect to atomic hydrogen. In some cases, E_{ad} is also considered with respect to H_2 for the purpose of discussion and linking to experimental results, here the used binding energy for H_2 is -4.5 eV.
The adsorption energies were BSSE corrected by using a modified version of the counterpoise method of Boys and Bernardi [BB70]. This is described in detail in the Appendix B. To quantify the influence of surface restructuring, the deformation energy E_{def} is defined as the energy difference of the optimized pristine surface and the optimized surface deformed due to the adsorption.

For the evaluation of the Coulomb and exchange series within CRYSTAL, the truncation thresholds for the bielectronic integrals, as defined in the CRYSTAL

manual [DSR+09], were set to 10^{-8}, 10^{-8}, 10^{-8}, 10^{-8} and 10^{-16} a.u. The calculations were performed with $10 \times 10 \times 10$ (10×10) Monkhorst-Pack k-point meshes [MP76] for the pure bulk (surfaces) and defective systems, respectively. The bilayer models use a mesh of 10 k-points along the periodic direction. Spin polarized calculations were carried out whenever necessary. The convergence criteria for total energies, atomic displacements and forces were 10^{-7}, 1.8×10^{-3} and 4.5×10^{-4} a.u., respectively. For the SCF cycles, Anderson's method [And65] as proposed by Hamann [Ham79] was applied. In order to facilitate the convergence, a Fermi broadening corresponding to a $k_B T = 0.001$ a.u. (with k_B the Boltzmann constant) was used. Figures of optimized structures were created with VMD [HDS96].

4.1.3 ^{36}Cl in Graphite

Most computational parameters for Cl-graphite calculations are the same as described in the previous section 4.1.2. Thus, only the unique methodological aspects will be explained in the following. To find a suitable functional the C-Cl bond energy of C_6H_5Cl was determined. This molecule was used since it can be considered as a small size model of a graphite surface (due to the aromatic bonds) and experimental data with high accuracy are available. The PBE0 functional performed better compared to PBE (4.22 vs. 4.35 eV, exp. 4.14 eV [Luo02]), thus it was used to describe the covalent interactions. For the potential curve of Cl on the (001) surface, the PBE functional was used for several reasons. As shown in section 4.1.1, PBE overall describes the properties of graphite better than PBE0. As presented in section 4.3, the findings obtained with PBE for non-covalent bonding also agree better with available experimental and theoretical data. Finally, a layer of ghost atoms needs to be added to the surface to well reproduce the surface properties. For hybrid functionals, this lead to numerical instabilities and divergence of the electronic wave function.

The basis set for Cl is a contraction of – 8s6s-2111*sp*-1d* –; the inner exponents (8s6s) are taken from Ref. [ACP+93]. The outer exponents were optimized at the HF level for CCl_4 by using an energy criterion and are given in Table 4.5. The basis set optimization was carried out using the LoptCG [ZW06] script.

For the calculation of the potential energy curve of Cl adsorption on the (001) surface, a modified approach was used to obtain a better accuracy. The surface was reduced to one layer of graphene after finding that the adsorption energy is already converged for one layer. The supercell was increased to 6×6; at this size the Cl atom can be viewed as isolated, a further increase in size did not change the results noticeably. In order to improve the description of the wave-function on the surface, one layer of ghost atoms was added above and below the graphene layer as proposed in Ref. [Dol06]. The ghost atoms were placed at carbon lattice positions of ABAB stacked graphite and consist of one s function with an exponent of 0.150.

Table 4.5: Exponents and coefficients of the contracted Gaussian basis set adopted in the present study for Cl. Only the most diffuse 2111sp-1d^* GTFs are given (see Ref. [DCO^+90, CPDS93] for a complete set of data).

Shell	Exponent	Coefficient	
		$s(d)$	p
sp	4.654960	-0.263857	-0.064039
	1.937992	-0.550549	0.172036
	0.964781	1.	1.
	0.405514	1.	1.
	0.145237	1.	1.
d	0.816872	1.	

No ghost function was placed on the Cl adsorption site.

For the insertion of Cl and Cl_2 into bulk graphite, the supercell size was increased to $10 \times 10 \times 1$ to allow for a deformation of the graphene planes.

4.2 Properties of ^{3}H in Graphite

As explained in section 2.4.2 two different traps are found for hydrogen. The first is supposed to be the zigzag edges of dislocation loops in graphite crystallites, and the second the zigzag edges of graphite crystallites. In the following this hypothesis is tested by studying different systems which can model these traps. This section is based on Ref. [LBV18].

4.2.1 Surfaces

The surface energies of the (001), (100), and (110) surface were determined and are given in Table 4.6. The (001) surface has the smallest surface energy since no C-C bonds are broken in order to create it. Compared to the (001) surface, the (100) and (110) surface energies are higher by a factor of 30 - 40, the (100) surface has the highest one. The obtained relative stability of the (100) and (110) surface is due to atomic relaxation processes on the surface, which are much more pronounced at the (110) surface. Both relaxed surfaces are shown in Figure 4.7 together with the periodic boxes. When the (110) surface is allowed to relax it forms stronger bonds between pairs of edge carbons. This decreases the C1-C2 (C3-C4) bond length from 1.42 Å to about 1.23 Å (see Figure 4.7 for the description of atoms), which is an indication that the bond is almost a triple bond (the bond length in ethyne is 1.20 Å). The ground state of the (110) surface shows no spin localization on the edge carbons and is non-magnetic.

Table 4.6: Surface energies (E_{surf} in J/m^2) of the three studied surfaces.

System	E_{surf}
(001)	0.19
(100)	6.15
(110)	5.29

When the (100) surface is optimized, it hardly changes with respect to the geometry obtained by cutting through graphite along the plane. The edge carbons move slightly inward by 0.03 Å, the angle between the edge carbon and its two carbon neighbors, ∡C4-C1-C5, increases to 126 degrees. However, a strong spin localization on the edge carbons is observed. This is in line with the findings of several authors [DP10, OGK11, KObuQF11]. Each edge carbon has a magnetic moment of roughly 1.3 μ_B (the excessive magnetic moment is due to spin contamination).

Atomic hydrogen is rather reactive with respect to graphite. It is known to chemisorb on the pristine (001) surface by forming a weak covalent bond with a

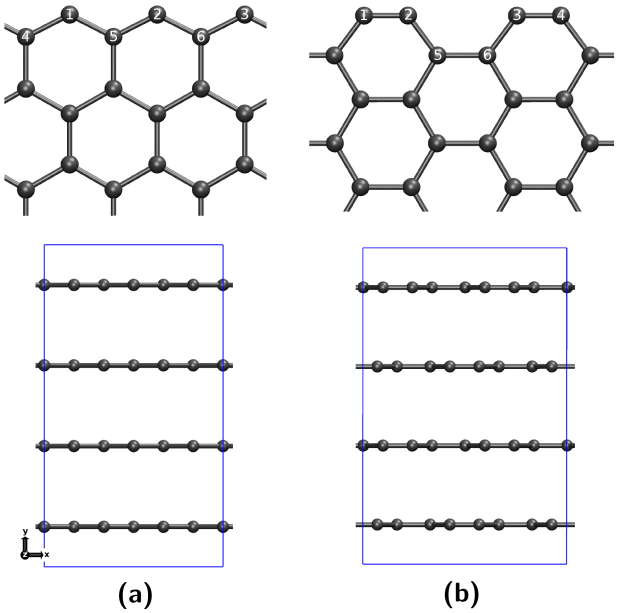

Figure 4.7: Optimized structures and top view of the a) (100) and b) (110) surfaces.

carbon atom of the surface. The two possible adsorption sites are shown in Figure 4.8. The adsorption is linked to a lifting of this carbon atom out of the graphene plane by about 0.49 Å(puckering) due to the increase of its sp^3 character (see Figure 4.8). E_{ad} for both positions are very similar: -0.68 eV and -0.73 eV for position 1 and 2, respectively. This weak adsorption energy is also reflected in a rather long C-H bond of 1.13 Å (for CH_4 it is 1.09 Å). The results are in good agreement with literature values for graphene, which range from -0.87 to -0.67 eV [CLMT09, SJ02, HŠX$^+$06, KJ08, FMA03, DSL04, RDN$^+$07, CCPC07, LFM$^+$04]. For comparison the insertion of hydrogen in bulk graphite was studied. As for the surface, hydrogen forms a weak covalent bond with the graphite matrix. The insertion energies are almost equal to the adsorption energies for the (001) surface: -0.63 eV and -0.76 eV for position 1 and 2, respectively. Position 2 is slightly preferred since the hydrogen is centered exactly above the center of a six-membered ring.

Contrary to the (001) surface, both the (100) and (110) surfaces have dangling bonds, which become saturated when hydrogen is adsorbed. The adsorption of H_2 on the (100) and (110) surface of HOPG was studied by Diño *et al.* [DNK$^+$04, DMN$^+$04]. However, since they explored the potential energy surface of this process they did not optimize the surface (all C-C bond lengths are 1.42 Å). This leads to a broad range of their E_{ad}: from -5.0 to -4.0 eV per H_2 for (110) and from -4.7 to -3.2 eV per H_2 for (100). All the other available literature values are reported as E_{ad} per H atom. The H_2 bond energy is about -4.5 eV (at the

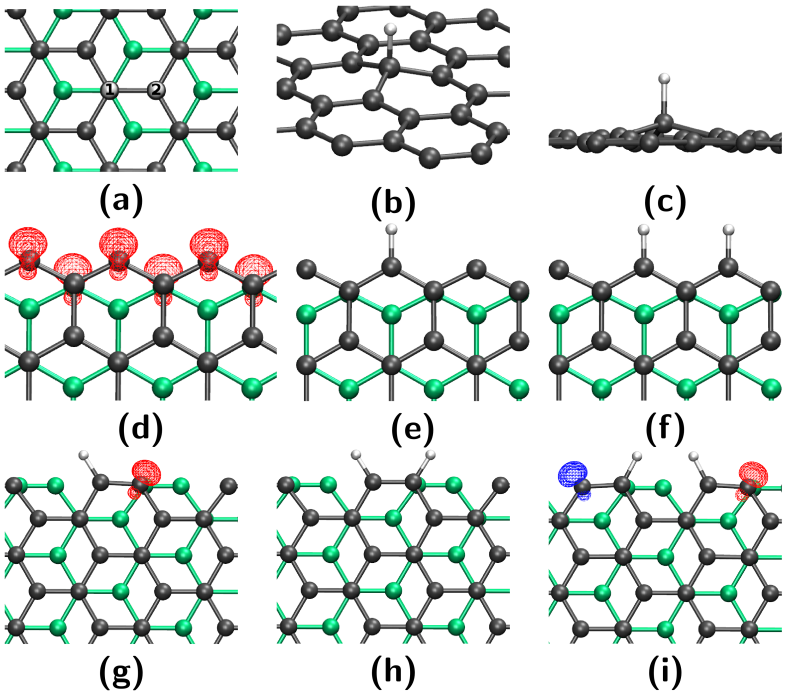

Figure 4.8: Optimized structures obtained for different cases of hydrogen adsorption on the (001), (100) and (110) surfaces. a) Top view of the two adsorption sites for hydrogen on the (001) surface. b) Top and c) side views of the chemisorption of hydrogen on the (001) surface. d) Spin density plot for the (100) surface. Each edge carbon has a localized spin. (100) surface with e) one and f) two chemisorbed hydrogen atoms. Spin density plots are omitted for better visibility, but all unsaturated edge carbons have a localized spin. g) Spin density plot for the (110) surface with one chemisorbed hydrogen. h) and i) show the (110) surface with two chemisorbed hydrogen atoms for the h) 110-2H-a and i) 110-2H-b configurations, respectively. Isovalues for spin density plots are 0.05 (red) and -0.05 (blue) e/bohr^3.

PBE level); this yields E_{ad} from -4.8 to -4.3 and from -4.6 to -3.9 eV per H for the (110) and (100) surface, respectively. The calculated E_{ad} for adsorption of two H on the (110) and (100) surface of Yang *et al.* [YY02] are -3.7 and -3.9 eV per H, respectively. Sha *et al.* [SJ04] obtained an E_{ad} of -5.0 eV for H on the (100) surface. Thus, in the literature it is not completely clear which surface binds hydrogen more strongly.

In Table 4.7, the E_{ad} for all investigated adsorption processes are summarized. In the following the focus is laid on adsorption on surfaces (100) and (110). In sections 4.2.2 and 4.2.3, adsorption on reconstructed surfaces and vacancies is explained.

Adsorption on the (100) surface is a much more stabilizing process (E_{ad} differs by a factor of 7) compared to the adsorption on the (001) surface. The adsorption of H on the (100) surface hardly perturbs the surface structure: E_{def} of the lattice is only 0.05 eV (see Table 4.7).

The ground state of the (100) surface is the high-spin state. Due to spin contamination the magnetic moment per unsaturated carbon is about 1.3. For each adsorbed hydrogen the total magnetic moment decreases by one. The magnetic moment of the neighboring edge carbons shows no significant change.

When a second hydrogen adsorbs on the same graphene plane of this surface, E_{ad} doubles. This shows that there is almost no interaction between neighboring hydrogen atoms (they are 2.5 Å apart) and that the adsorption of H on the (100) surface is a highly local process.

For three adsorbed hydrogen atoms which corresponds to a fully covered plane in this model, the angle ∡C4-C1-C5 decreases to 122 degrees and approaches the ideal value of 120 degrees for a sp^2 carbon as in benzene.

E_{def} for 1 to 3 adsorbed hydrogen atoms never exceeds 0.13 eV, which is almost negligible. This shows that the graphite matrix does not change significantly upon hydrogen adsorption since the edge carbons are almost perfectly oriented to bind an approaching hydrogen.

Furthermore, when two hydrogen atoms bind to two edge carbons which belong to two different planes, there is hardly any difference between the two adsorption energies (the energy difference ΔE is 0.01 eV). This shows as well that the hydrogen atoms barely interact with each other. The structure of Diño *et al.* [DNK$^+$04] which yields an E_{ad} of -4.6 eV resembles this structure. Their result agrees rather well with the E_{ad} of -5.0 eV obtained here (full relaxation of Diño's structures might have yielded even better agreement). Excellent agreement with the result of -5.0 eV reported by Sha *et al.* [SJ04] is found.

Hydrogen adsorption on the (110) surface is also a more stabilizing process (E_{ad} differs by a factor of 5) compared to the adsorption on the (001) surface. When atomic hydrogen adsorbs on the (110) surface and forms a bond with C1 the local deformation of the graphite lattice is more pronounced. The ground state has a magnetic moment of 1.0 μ_B; the unpaired electron is strongly localized on the neighboring carbon atom C2 as shown in the spin density plot in Figure 4.8. This adsorption leads to a weakening of the C1-C2 bond, which can be seen by the C1-C2 bond length increase to about 1.34 Å, and the C1-C2-C5 angle decrease by almost 10 degrees. The weakening of the C1-C2 bond as well as the local deformation of the surface are major factors for this E_{ad} being higher than on the (100) surface, as shown in Table 4.7. E_{def} is 10 times higher for the (110) surface (0.54 eV), which accounts for 40 % of the difference in adsorption energies. The other part is due to the spin localization.

Table 4.7: Hydrogen adsorption (E_{ad} in eV/H atom) and deformation (E_{def} in eV) energies on the different graphite surfaces with respect to the number of adsorbed H. $(100)_{rec}/(110)_{rec}$ denote the in-plane reconstructions, $(100)_{arch}/(110)_{arch}$ and $(100)^{bilayer}_{arch}/(110)^{bilayer}_{arch}$ denote the slab and bilayer models of the arch-shaped reconstruction, respectively. Vac(α, β) and Divac denote the (001) surface with mono- and 5-8-5-divacancies, respectively. The different explored configurations are: a) on the same graphene plane, b) on two different graphene planes, c) two H per edge carbon, d) 110-2H-a, e) 110-2H-b, f) 100_{rec}-2H-a/110_{rec}-2H-a, g) 100_{rec}-2H-b/110_{rec}-2H-b, h) *ortho*, i) *meta* and j) *para* (see Figure 4.8); k) correspond to the vacancies on the (001) surfaces (in parentheses, the adsorption energies of H with the same defects in bulk graphite are given for comparison).

System	Nb. of H	Conf.	E_{ad}	E_{def}
(100)	1	-	-4.99	0.05
	2	a	-4.99	0.10
		b	-5.00	0.11
		c	-3.89	0.60
	3	-	-4.98	0.13
	4	c	-3.63	1.12
(110)	1	-	-3.73	0.54
	2	d	-4.37	0.72
		e	-3.64	1.02
		b	-3.73	1.08
		c	-2.68	1.59
	3	-	-4.08	1.13
	4	a	-4.29	1.25
		c	-3.40	2.54
$(100)_{rec}$	1	-	-2.80	0.93
	2	f	-3.80	1.35
		g	-2.81	1.78
$(110)_{rec}$	1	-	-2.63	0.79
	2	f	-3.68	1.27
		g	-2.62	1.55
$(100)_{arch}$	1	-	-2.19	0.77
	2	h	-2.86	1.52
		i	-2.35	1.61
$(110)_{arch}$	1	-	-2.39	0.61
	2	h	-2.56	1.20
		i	-2.42	1.40
		j	-2.64	1.24
$(100)^{bilayer}_{arch}$	1	-	-1.24	1.01
	2	h	-2.02	2.34
		i	-1.37	2.46
		j	-1.88	2.08
$(110)^{bilayer}_{arch}$	1	-	-1.28	1.00
	2	h	-2.22	2.54
		i	-1.37	2.26
		j	-1.94	1.98
Vac(α)	1	k	-4.17 (-4.13)	0.25 (0.26)
	2	k	-3.34 (-3.39)	1.16 (0.39)
Vac(β)	1	k	-4.15 (-4.15)	0.28 (0.22)
	2	k	-3.31 (-3.35)	1.19 (0.35)
Divac	1	k	-2.27 (-2.21)	0.77 (0.69)
	2	k	-3.28 (-3.30)	2.31 (2.24)
	3	k	-3.25	3.68
	4	k	-3.55	3.98

There are two ways to add a second hydrogen adjacent to the first one on the same graphene plane: either on the same six-membered ring (C2) or on the neighboring six-membered ring (C3). These two configurations are called 110-2H-a and 110-2H-b, respectively. They are shown in Figure 4.8. For these structures major differences are found. The configuration 110-2H-a is largely favored; E_{ad} per H atom differs by 0.8 eV with respect to 110-2H-b. This is due to the fact that the saturation of both adjacent edge carbons recreates a system of conjugated bonds. The C1-C2 bond length is 1.37 Å, the angle ∡C2-C1-C5 (and its symmetric counterpart) for the edge carbons are 120.6 degrees. This is not the case for 110-2H-b, in fact its formation creates another local deformation of a six-membered ring. E_{def} is 0.25 eV higher with respect to 110-2H-a. The ground state of 110-2H-b is antiferromagnetic, but the magnetic state with 2.0 μ_B lies only 0.06 eV higher in energy. Diño *et al.*[DMN$^+$04] found the same trend for the difference of the adsorption energies (0.5 eV/H) of the two configurations, but their adsorption energies are underestimated by 0.4 eV for 110-2H-a and 0.7 eV for 110-2H-b. However, since their graphite surface is not fully relaxed the contribution of lattice deformation energy is excluded, which decreases adsorption energies.

For the adsorption of a third hydrogen, the only possibility is to bind to a carbon with an unsaturated edge carbon neighbor, thus the same trends as for one adsorbed H are observed. For a fourth adsorbed hydrogen the trend of 110-2H-a is reproduced.

The same trend as for configuration 110-2H-b is found when the two hydrogen atoms adsorb on two carbons which belong to different graphene planes. The slightly lower E_{ad} (ΔE = 0.09 eV) is due to less steric repulsion between the hydrogen atoms for this structure.

To summarize, for the (110) surface the adsorption processes are no longer independent. Formation of 110-2H-a like structures is favored over other structures; this configuration is more stable by at least 0.6 eV per H atom compared to all the other.

For both surfaces, (100) and (110), it is possible that two hydrogen atoms adsorb on one edge carbon. This leads to a sp^3 hybridization of the edge carbon. Optimized structures are shown in the Appendix C. Adsorption on the (100) surface is more stable, E_{ad} per H atom differs by 1.2 eV per H atom. This trend agrees qualitatively with the results of Yang *et al.* [YY02], but their E_{ad} are overestimated by 1.1 and 0.7 eV per H atom for the (100) and (110) surface, respectively (this might be due to their use of molecules as surface models). The angle H-C1-H takes 106.5 degrees for the (100) and 105.2 degrees for the (110) surface, thus showing the increased sp^3 character of the edge carbon. Both hydrogen atoms are above the interlayer space (see Appendix C). Since these structures are far less stable (ΔE is 1.07 and 1.69 eV per H atom for the (100) and (110) surfaces, respectively)

only E_{ad} for adsorption on one and two carbons are reported in Table 4.7.

When adsorption of hydrogen on the three surfaces is compared, the trend of stability is (100) > (110) > (001), thus the (100) surface forms the most stable bonds. Considering the surface energies of these three surfaces, it can be noticed that these two properties are directly related: A higher surface energy leads to a more stable structure for hydrogen adsorption.

In the next section the focus is laid on the change of adsorption properties of hydrogen when the surfaces (100) and (110) are allowed to reconstruct.

4.2.2 Reconstructed Surfaces

Surface reconstructions of the (100) and (110) surfaces can be divided into two groups. The first group consists of reconstructions where edge carbons of one graphene plane can regroup to create patterns which differ from the zigzag or armchair edges. For graphene nanoribbons, several reconstructed surfaces as well as their interaction with hydrogen were studied on a theoretical level [KMH08, WSS$^+$08, KObuQF11]. For this study the two reconstructions were chosen which yield weaker adsorption energies than for the unreconstructed armchair edge since this makes them possible candidates for the second trap according to Kanashenko's and Atsumi's hypothesis. These in-plane reconstructions are shown in Figure 4.9. The first reconstruction stems from the (100) surface by rotating a C-C bond by 90° similar to the Stone-Thrower-Wales defect (C5-C6 in Figure 4.9). It results in a sequence of heptagons and pentagons. The second one stems from the (110) surface and yields a sequence of two heptagons and one hexagon by rotating a C-C bond which connects two armchair hexagons by 90° (C5-C6 in Figure 4.9).

The second group consists of reconstructions where dangling bonds of the (100) and (110) surface are saturated by forming bonds between edge carbons of two adjacent graphene planes, called arch-shaped edges. This effect was observed by conducting TEM and HRTEM measurements (see Ref.[RCG13] and references therein).

As shown in Figure 4.9 only two limiting cases are considered for the arch-shaped edges with respect to the curvature of the arch: The first case is the surface reconstruction of a graphene bilayer which is only periodic in one dimension and allows full relaxation orthogonal to the graphene plane (called bilayer model). This reconstruction results in a low curvature. The second case is the surface reconstruction of slab models with two graphene planes per supercell which is periodic in 2 dimensions and limits the relaxation to give a surface with a high curvature (called slab model). The difference in periodicity of these two models as well as a schematic description of the reconstruction process are shown in Figure 4.10. A model similar to the slab model used here was already used to study the chemistry of sulfur in graphite [ALO$^+$13].

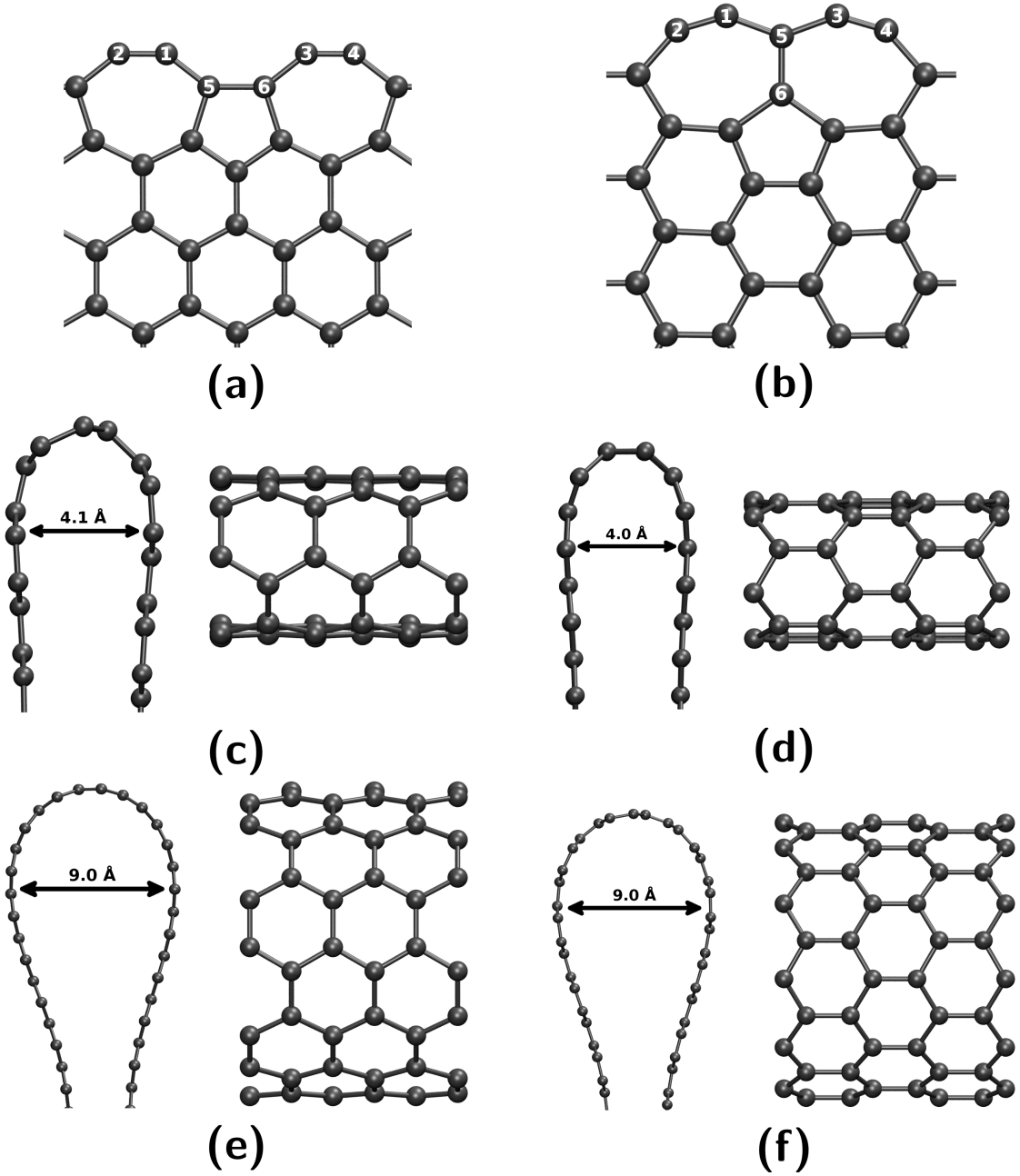

Figure 4.9: Reconstructed surfaces of in-plane and arch-shaped reconstructions. In-plane reconstruction of the a) (100) and b) (110) surface, arch-shaped reconstructions for c) (100) and d) (110) slab models, and for e) (100) and f) (110) bilayer models. For c)-f) the left and right pictures are their side and top views (perpendicular to the z-axis), respectively. Slab models are periodic in x- and y-directions, bilayer models only in the x-direction.

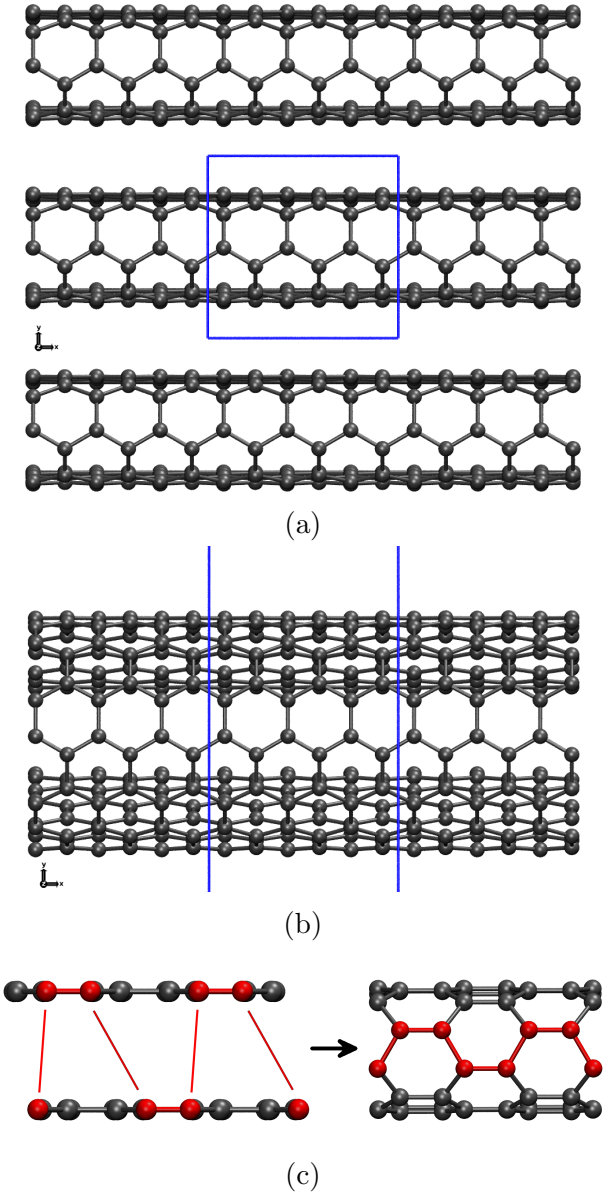

Figure 4.10: Top view of the a) 2-D slab model and b) 1-D bilayer model of the reconstructed (100) surface. The system within the blue lines shows the supercell used for the calculations; the replication in the a) x- and y-directions and b) x-direction show the periodicity of the slab and bilayer models. c) Schematic description of the (110) surface reconstruction. Red atoms constitute the surface atom layer, red lines show the new interlayer bonds.

The formation energies of the different reconstructed surfaces are given in Table 4.8. The in-plane reconstruction is only exothermic for the (100) surface which is in line with Ref. [KMH08]. For all arch-shaped edges this process leads to more stable structures since no dangling bonds remain. It can be seen that reconstruction of the (100) surface is systematically more stabilizing whatever the reconstruction type. This is coherent with the higher surface energy.

Table 4.8: Formation energies (E_{form} in eV) of the reconstructed surfaces and bilayers per edge carbon and of the mono- (Vac(α), Vac(β)) and 5-8-5-divacancies (Divac) on the (001) surface. $(100)_{rec}/(110)_{rec}$ denote the in-plane surface reconstructions; $(100)_{arch}/(110)_{arch}$ and $(100)^{bilayer}_{arch}/(110)^{bilayer}_{arch}$ denote the slab and bilayer models of the arch-shaped reconstructions, respectively.

System	E_{form}
$(100)_{rec}$	-0.55
$(110)_{rec}$	0.15
$(100)_{arch}$	-1.61
$(110)_{arch}$	-1.04
$(100)^{bilayer}_{arch}$	-2.04
$(110)^{bilayer}_{arch}$	-1.37
Vac(α)	7.39
Vac(β)	7.35
Divac	6.94

For both in-plane reconstructions studied, the edge carbons which are available for hydrogen adsorption belong to heptagons. The local structure is similar to the (110) surface, C1-C2 bond lengths for both systems decrease to 1.24 Å (see Figure 4.9 for the description of atoms). The optimized structures for adsorption of one and two H atoms on the two studied reconstructed surfaces are shown in Figure 4.11. The adsorption of one H on the reconstructed (100) surface is more stabilizing by 0.2 eV. This agrees with the findings of Ref. [KMH08]. For both systems a localized spin is observed on C2 (the C-H bond is formed with C1), the ground state has a magnetic moment of 1.0 μ_B. The H adsorption locally deforms the surface (E_{def} is 0.93 eV and 0.79 eV for the (100) and (110) surface, respectively).

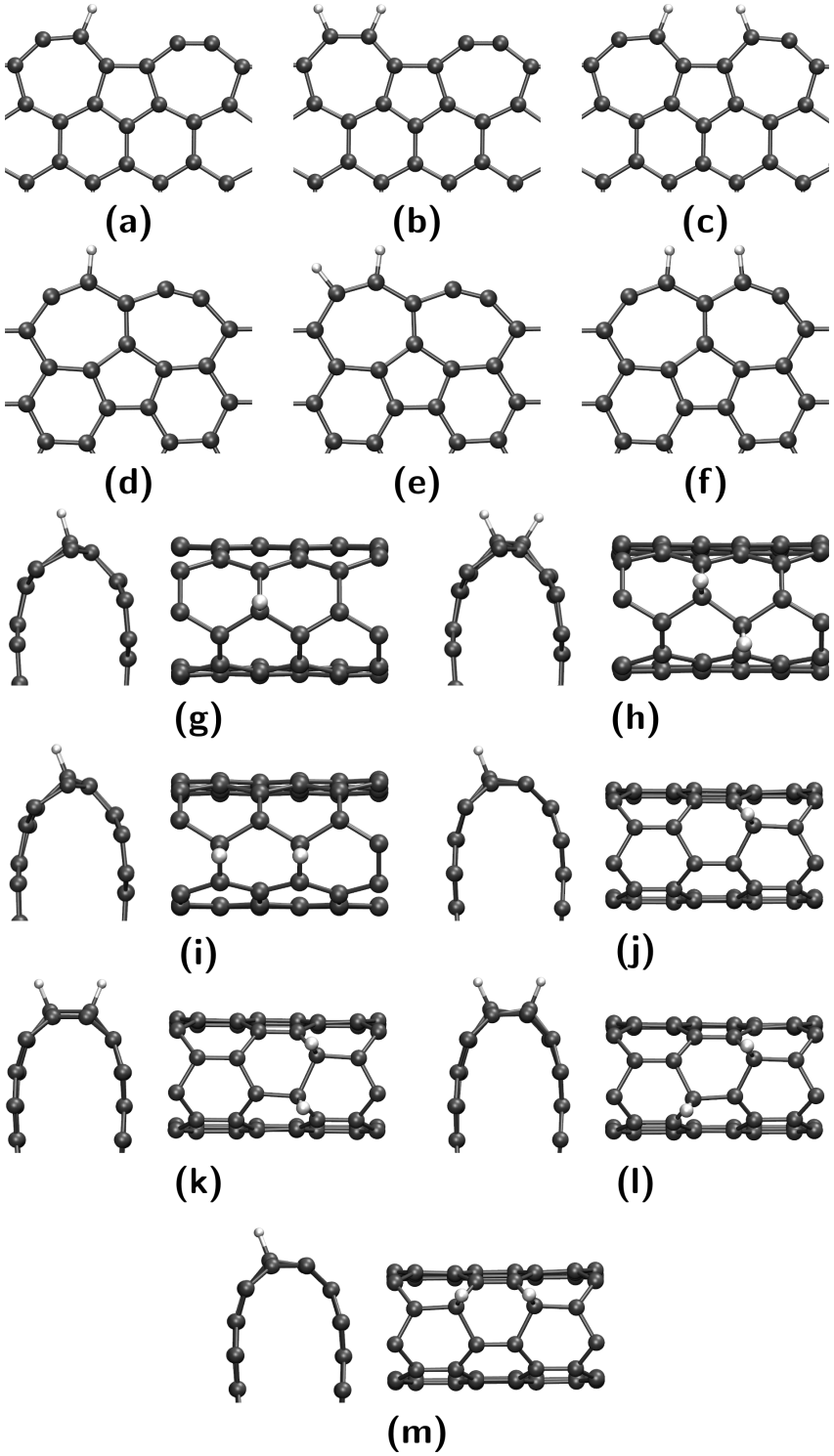

Figure 4.11: Optimized structures of different cases of hydrogen adsorption on the reconstructed (100) and (110) surfaces: The in-plane reconstructed (100) surface with a) one H and two H for b) configuration $(100)_{rec}$-2H-a and () configuration $(100)_{rec}$-2H-b. The in-plane reconstructed (110) surface with d) one H and two H for e) configuration $(110)_{rec}$-2H-a and f) configuration $(110)_{rec}$-2H-b. The arch-shaped reconstructed (100) surface with g) one H and two H in h) *ortho* and i) *meta* positions; the reconstructed (110) surface with j) one H, two H in k) *ortho*, l) *meta* and m) *para* positions. The left and right pictures for g)-m) are their side and top views, respectively.

The second H can again be adsorbed in two different ways as for the (110) surface as shown in Figure 4.11. These structures are called 100_{rec}-2H-a/110_{rec}-2H-a and 100_{rec}-2H-b/110_{rec}-2H-b. 100_{rec}-2H-a/110_{rec}-2H-a are the more stable configurations since the deformation is much less pronounced (E_{def} is 0.3-0.4 eV smaller) and the ground state is non-magnetic with no localized spins. Configurations 100_{rec}-2H-b and 110_{rec}-2H-b are less stable, E_{ad} per H atom differs by 1.0 eV and 1.1 eV, respectively. For these structures a second localized spin is found at C4 (the second C-H bond is formed with C3), however the ground state is also non-magnetic. E_{def} is about two times higher than for adsorption of one H. Thus for H adsorption, the same tendencies as for the (110) surface are found.

For the arch-shaped reconstruction the curvature leads to an increased sp^3 character of the surface carbons even though no dangling bonds remain. A measure of this curvature can be the dihedral angle between an edge carbon and its three next neighbors. The angles are 39° and 40° for the (100) and (110) slab models, and 17° and 18° for the (100) and (110) bilayer models, respectively (the angles for the (001) surface of graphite and diamond are 0° and 60°, respectively). Another measure is the maximum separation between the two layers. It is 4.1 and 4.0 Å for the (100) and (110) slab models, respectively and 9.0 Å for both bilayer models. Both of these measures show that the curvature is much higher for the slab models. A higher curvature increases the the C-H bond strength; thus adsorption of atomic H is more stable by a factor of 2 for the bilayer models and 4 for the slab models compared to the (001) surface. This trend agrees qualitatively with the findings of Ruffieux *et al.* [RGB$^+$02], who compared hydrogen adsorption on graphite to a carbon nanotube and C_{60}, as well as Tozzini *et al.* [TP11], who studied hydrogen adsorption on curved graphene. Both found an increasing C-H bond strength with increasing curvature. This leads to a shortening of the C-H bond to about 1.10 Å compared to 1.13 Å on the (001) surface. As is also observed for the pristine (001) surface the formation of the C-H bond lifts the C atom by about 0.25 and 0.18 Å for the reconstructed (100) and (110) surfaces, respectively. E_{ad} for both surfaces is almost the same, which is due to their similar curvature.

The H atoms have the tendency to form dimers [BJW$^+$09] and clusters [HRX$^+$06] on the graphene planes. For the adsorption of a second H atom on the (001) surface, it was shown that the preferred adsorption sites are in vicinity of the first hydrogen [ŠRH$^+$09]. For the *ortho* and *para* configurations, adsorption of two hydrogen atoms is a more stabilizing process (by a factor of two) than the adsorption of two isolated hydrogen atoms. This leads to the preferred formation of dimers [BJW$^+$09] and clustering [HRX$^+$06]. The order of stability is *ortho* > *para* > *meta* for these three configurations [ŠRH$^+$09]. However, the *ortho* and *para* configuration differ only by 0.03 eV.

For the reconstructed (110) slab model, the order is switched to *para* > *ortho*

> *meta*, but E_{ad} of all three configurations lies in a close range of 0.2 eV (as opposed to 1.1 eV for the (001) surface[ŠRH+09]). For the reconstructed (100) slab the same order is found for the two configurations studied, *i.e. ortho* > *meta* (the *para* configuration was omitted since the C atoms in *para* position are at least 0.4 Å below the surface).

For the bilayer models, the trend of Ref. [ŠRH+09] is reproduced. Compared to the slab models, H adsorption is a less stabilizing process due to the smaller initial curvature as well as the higher flexibility of the bilayers which leads to a higher deformation. The maximum separation between the two layers decreases by 1.3 Å for one hydrogen and by 1.9-2.7 Å for two chemisorbed hydrogen atoms. This leads to E_{def}, which are 50-100 % higher compared to the slab models (see Table 4.7). Figure 4.11 shows the optimized structure for adsorption of hydrogen on the slab model surfaces (the ones for the bilayer model surfaces are shown in the Appendix D).

It should be noted that E_{ad} more than doubles (which means E_{ad} per H atom decreases) for all reconstructed surface models when a second H adsorbs in either the *ortho*, *meta*, or *para* position. Thus, a preferred formation of dimers is also found as for the pristine (001) surface.

In the next section the focus is laid on the influence of point defects, which for instance are created by irradiation, on the adsorption properties of hydrogen.

4.2.3 Point Defects

Creation of monovacancies and divacancies on the (001) surface by removal of a carbon atom is a highly endothermic process. These defects were already studied in detail by several authors [TEEBH03, LFM+04, ZZY+10]. The three treated vacancies are shown in Figure 4.12. The E_{form} for the creation of a monovacancy (7.4 eV, see Table 4.8) agrees well with literature values of 7.5 ± 0.5 eV (see Ref. [TH07] and references therein). A monovacancy leads to a surface reconstruction with one dangling bond remaining. The formed C1-C2 bond is rather weak with a bond length of 2.05 Å. Due to the dangling bond the local spin density on the unsaturated carbon is ≈0.97 μ_B (the total magnetic moment is about 1.5 μ_B due to spin contamination). For graphite, two different monovacancies are possible. For the α-vacancy, the vacancy is atop of a carbon atom of the graphene plane underneath the surface plane, whereas for the β-vacancy it is atop the center of a six-membered ring of the underlying plane.

For divacancies, several reconstruction processes are known [KIYL11]. For the 5-8-5 divacancy, the surface reconstructs in a manner that no dangling bond remains and the ground state is non-magnetic. This reconstruction is also found for extended vacancy lines [TLH+14], which shows that the model system is a reasonable approximation for bigger systems.

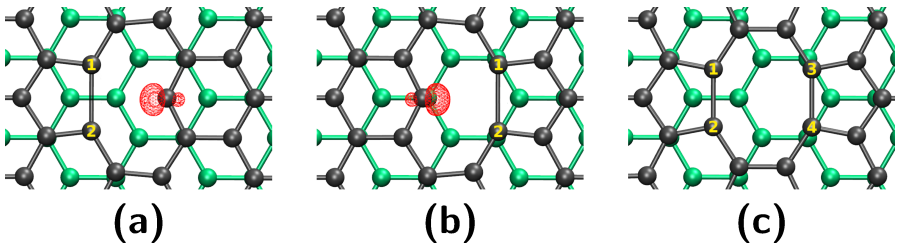

Figure 4.12: Top view of the optimized structures for the a) α- and b) β-vacancies, and c) the 5-8-5 divacancy on the (001) surface. Isovalues for spin density plots are 0.05 e/bohr^3.

In Table 4.7 the adsorption energies for the saturation of monovacancies with atomic hydrogen are shown.

The saturation of the dangling bond leads to a non-magnetic ground state. As can be seen in Figure 4.13 hydrogen does not remain in the graphene plane when it is chemisorbed on the vacancy on the (001) surface. Two conformations with very similar adsorption energies were found. The first and more stable one is similar to the findings of Allouche *et al.* [AF06], where the hydrogen and its bonded carbon are above the graphene plane. For the second conformation both are directed toward the plane lying below the surface. ΔE between the two conformations is only 0.02 eV. The obtained adsorption energies (-4.15 and -4.17 eV for the α and β-vacancy, respectively) are in good agreement with the published results for adsorption at a vacancy in graphene (-4.36 eV [LFM$^+$04] and -4.14 eV [AF06]).

A second hydrogen can be adsorbed on the carbon where the first hydrogen is adsorbed to. E_{ad} for this process is 1.7 eV less than twice E_{ad} for the first hydrogen due to the sp^3 hybridization and larger deformation of the lattice. Again, two different conformations are found for both vacancies which are similar in stability (ΔE = 0.04 eV). For the first one both hydrogen atoms as well as the carbon are above the graphene plane. For the second one the carbon is lying in the graphene plane, one hydrogen is above and one below the surface. No stable conformation is found where both hydrogen atoms are beneath the surface. When the bond energy of H_2 is taken into account the adsorption energies are about -2.1 eV, thus a dissociation and adsorption of H_2 at a monovacancy is a highly exothermic process (even though there is likely a barrier to overcome). Lehtinen *et al.* [LFM$^+$04] and Allouche *et al.* [AF06] showed that a second more stable structure exists. Here, one H atom binds to the unsaturated C and the second one forms a bond with either C1 or C2 (see Figure 4.12 for the description of atoms).

For the divacancy, there are no dangling bonds; thus the adsorption of hydrogen is much less stable (by 45 %) compared to α or β-vacancies (see Table 4.7). However, the strain in the formed 5-8-5 ring still leads to a stronger H adsorption

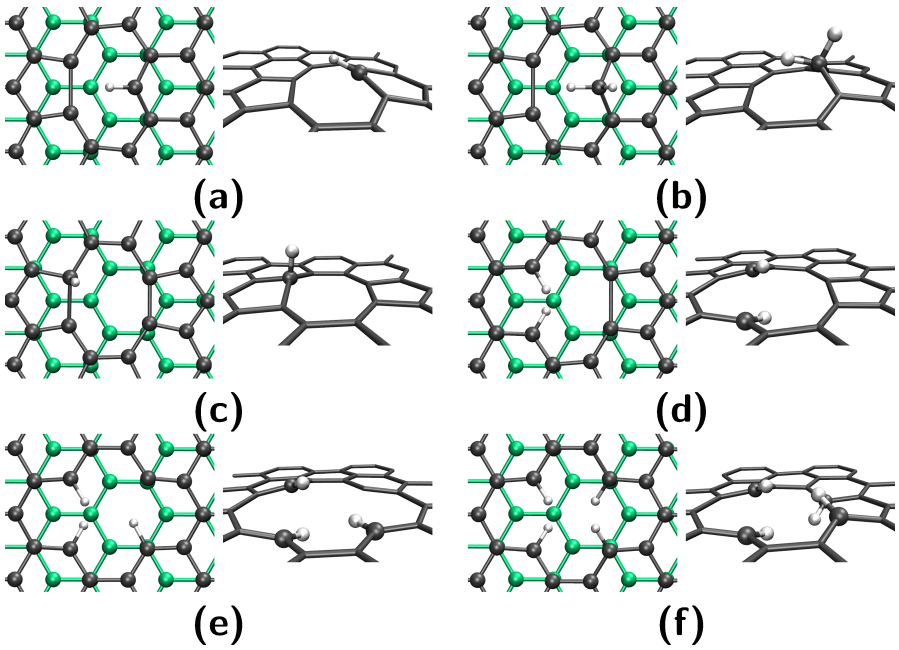

Figure 4.13: Top (left) and perspective (right) views of the optimized structures of hydrogen chemisorption on the mono and divacancies. Vacancy(α) with a) one and b) two hydrogen atoms. Divacancy with c) one, d) two, e) three, and f) four hydrogen atoms, respectively.

than for a pristine (001) surface. The preferred adsorption position is above the carbon (C1) with which the covalent bond is formed (see Figure 4.13). The elongated bonds make it easier for the carbon to move out of the graphene plane by about 0.15 Å. However, the relative rigidity of the graphene plane leads to a structure, which resembles the adsorption on the pristine (001) surface. This results in a C-H bond length of 1.11 Å, thus 0.03 Å longer than the usual C-H bond length ($\approx$ 1.08 Å), but 0.02 Å shorter than for adsorption on the (001) surface.

A second hydrogen can either adsorb on C2 or on the opposite end of the divacancy (C3/C4). Here, only the first case is considered since it is thermodynamically more stable (E_{ad} for the second case is about twice the E_{ad} for one chemisorbed hydrogen). For this configuration one hydrogen is above and one below the surface since this minimizes steric repulsion between the hydrogen atoms. The C1-C2 bond is broken by this process. Even though this bond breaking costs energy (E_{def} increases by 1.4 eV), E_{ad} is much more (1.0 eV per H atom) than twice the E_{ad} for the first hydrogen. The reason for this large stabilization is the increased strength of the C-H bond, which shortens the C-H bonds to 1.08 Å. For this configuration, E_{ad} with respect to H_2 is also -2.1 eV, thus dissociation at a divacancy also is exothermic (although this dissociation also likely has a barrier).

To fully saturate the divacancy, two hydrogen atoms can adsorb on the opposite side of the divacancy. The adsorption of a third H does not resemble the first process. E_{ad} per H atom is 1.0 eV more stabilizing compared to the first H even though E_{def} of the lattice is 0.6 eV higher (when comparing the difference between E_{def} for 3 and 2 H to that for one H). For the relaxed geometry the H lies in the graphene plane. Contrary to the first adsorption, the C3-C4 bond is very elongated in the initial state due to the strain induced by the two adsorbed H. The bond length is 2.08 Å but no spin localization is observed, which implies a very weak bond that can easily be broken by H adsorption. A localized spin can be observed on C4, when H forms a bond with C3. Finally, for a full saturation of this defect the most stable conformation has two H lying above the surface and two beneath the surface: E_{ad} per H atom is the most stable for four hydrogen atoms. The increase of only 0.3 eV for E_{def} shows that C4 in the initial state is already well-positioned for the adsorption.

Hydrogen binds to vacancies and divacancies in graphite bulk as strongly as on the (001) surface. The trapped hydrogen atoms are located in the interlayer space. However, since the formation energies are slightly lower ($\approx$ 0.05 eV) than E_{ad} on the surface, this shows that steric repulsion is negligible when hydrogen is trapped at a vacancy in the bulk. This correlates well with the change of the lattice parameter c, which only increases by 0.02 to 0.06 Å. It should be noted that the only stable conformation for two hydrogen atoms at a monovacancy in bulk graphite is the one with one hydrogen above and one below the graphene plane. This explains the lower E_{def} since the lattice is hardly perturbed.

4.2.4 Discussion

Trap 1 in nuclear graphite is supposed to be the zigzag edges of dislocation loops. Following Kanashenko's hypothesis, the (100) surface model is assumed to be equivalent to these edges. The adsorption energy is about -5.5 eV/H_2 compared to Kanashenko's -4.4 eV/H_2, which is a quite large difference. However, Kanashenko obtained his result by assuming a C-H bond energy of -4.45 eV (taken from the bond energy of benzene) and a H-H bond energy of -4.5 eV. While the H-H bond energy is correct, the C-H bond energy for benzene was shown to be -4.86 eV [DBD$^+$95]. This would result in an estimate of -5.2 eV, which is much closer to the result of this study. The most recent experimental adsorption energy is reported as -4.6 eV [ATS11]. Thus, both Kanashenko's estimate and the presented results for the zigzag edges underestimate this experimental result (by 0.6 eV and 0.9 eV, respectively). For prismatic edge dislocations, Suarez-Martinez *et al.* [SMSH$^+$07] showed that the zigzag edge carbons actually form two interlayer single bonds and become fully saturated. However, the armchair edge forms no interlayer bonds and is very similar to the (110) model surface. This suggests that only the

armchair edges are available for hydrogen adsorption without breaking of C-C bonds. E_{ad} for configurations 110-2H-a and 110-2H-b of the (110) surface model are -4.2 eV/H_2 and -2.8 eV/H_2, respectively. The more stable configuration 110-2H-a overestimates the experimental results only by 0.4 eV. Thus the measured value lies between the theoretical results of the two model systems. The differences could be due to the difficulty to compare experimental data measured at elevated temperatures (> 750 °C) with theoretical *ab initio* results of well defined structures at 0 K. The obtained results clearly show that Kanashenko's conclusion for trap 1 in nuclear graphite needs a revision. First, his estimation needs to be corrected and second, both zigzag and armchair edges should be considered as traps.

Atsumi reports an adsorption enthalpy of -2.6 eV/H_2 for H_2 adsorption on graphite [ATS11] in agreement with the extrapolated adsorption enthalpy of -2.5 eV/H_2 obtained by Redmond and Walker [RW60]. For the studied in-plane reconstructions, the adsorption energies with respect to H_2 are -3.1 eV/H_2 for configuration $(100)_{rec}$-2H-a and -2.9 eV/H_2 for $(110)_{rec}$-2H-a. For the arch-shaped reconstructions, the lowest adsorption energies with respect to H_2 are -1.2 and -0.8 eV for the (100) and (110) slab, respectively. For both types of reconstructions, these results agree with Kanashenko's hypothesis that the (100) edges of crystallites are preferred. However, the differences are rather small which implies that both reconstructed surfaces can be traps. Compared to experiment the in-plane reconstructions underestimate and arch-shaped reconstructions overestimate the adsorption energy. However, the in-plane reconstructions are in better agreement with experiment which suggests that this type is predominantly found in nuclear graphite. Finally, taking into account that the in-plane reconstruction of the (110) surface is endothermic, this suggests that the second trap is indeed the in-plane reconstructed (100) surface of crystallites. The better agreement of experiment with calculated H adsorption energies on in-plane reconstructions serves as indirect evidence that crystallite edges are open in nuclear graphite.

Point defects caused by irradiation also serve as a strong trap for hydrogen. Compared to the surfaces the formed bonds are stronger than on all surfaces except the (100) surface. Extended defects, such as the 5-8-5 divacancy, are a weaker trap compared to monovacancies. This is true for the surface as well as for bulk graphite.

Thus the overall order of reactivity for adsorption on defects is (100) > Vac > (110) > $(100)_{rec}$ > $(110)_{rec}$ > $(110)_{arch}$ > Divac > $(100)_{arch}$.

4.3 Properties of ^{36}Cl in Graphite

4.3.1 Surfaces

The adsorption of Cl was studied on the three surfaces (001), (100), and (110). E_{ad} are given in Table 4.9. It should be noted that the general trends of the relative stabilities are the same for the applied functional PBE0 as those obtained with PBE presented in section 4.2.1. For systems with non-covalent interactions, results obtained with PBE and PBE0 are presented since they differ quite strongly

In Figure 4.14, representative images of the optimized structures after Cl adsorption are shown. Cl does not form a covalent bond on the (001) surface, however E_{ad} is still -0.99/-0.53 eV (PBE/PBE0). This is a rather strong non-covalent interaction, analysis of the Mulliken charges reveals that about 0.49/0.58 electrons are transferred to Cl. Thus, the Cl adsorbs on the (001) surface by forming a charge transfer complex. This was also shown by several authors for a Cl adsorption on graphene [WKL09, YZW$^+$12, SC12, ZZY$^+$13, LZX14]. This phenomenon is not found for adsorption of Cl_2 on this surface. The Cl-Cl bond is orthogonal with respect to the surface for its most stable structure. Here, E_{ad} is only -0.33 eV and the Mulliken charge associated with the Cl_2 is only -0.10 for the Cl closer to the surface and -0.08 for the other. In Figure 4.15, the BSSE corrected interaction energy curve for the Cl adsorption on graphene is shown which was used to fit the charge transfer interactions of the developed potential (see section 5.1.4). The interaction decays very slowly with increasing distance, at a separation of 10 Å the interaction has only decreased by about 50 %.

Table 4.9: Chlorine adsorption energies (E_{ad} in eV/Cl atom) on the different graphite surfaces with respect to the number of adsorbed Cl atoms. The different explored configurations are: a) on the same graphene plane, b) on two different graphene planes, c) 110-2Cl-a, d) 110-2Cl-b.

System	Nb. of Cl	Conf.	E_{ad}
(001)	1	-	-0.99^a/-0.53^b
	2^c	-	-0.33^a/-0.11^b
(100)	1	-	-4.12^b
	2	a	-3.89^b
	3	a	-2.57^b
(110)	1	-	-3.10^b
	2	c	-3.48^b
		d	-2.50^b

^{a}PBE; ^{b}PBE0; ^{c} Cl_2

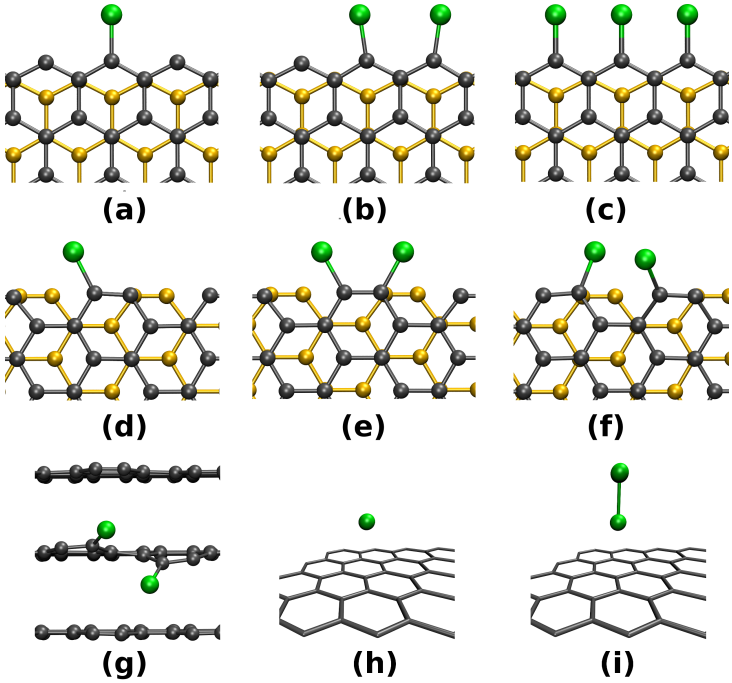

Figure 4.14: Optimized structures obtained for different cases of Cl adsorption on the (001), (100), and (110) surfaces. a) (100) surface with (a) one, b) two, and c) three chemisorbed Cl atoms. Spin density plots are omitted for better visibility, but all unsaturated edge carbons have a localized spin. d) (110) surface with one chemisorbed Cl. e), f), and g) show the (110) surface with two chemisorbed Cl atoms for the e) 110-2Cl-a, f) side view and g) top view of 110-2Cl-b configurations, respectively. Adsorption of h) Cl and i) Cl_2 on the (001) surface.

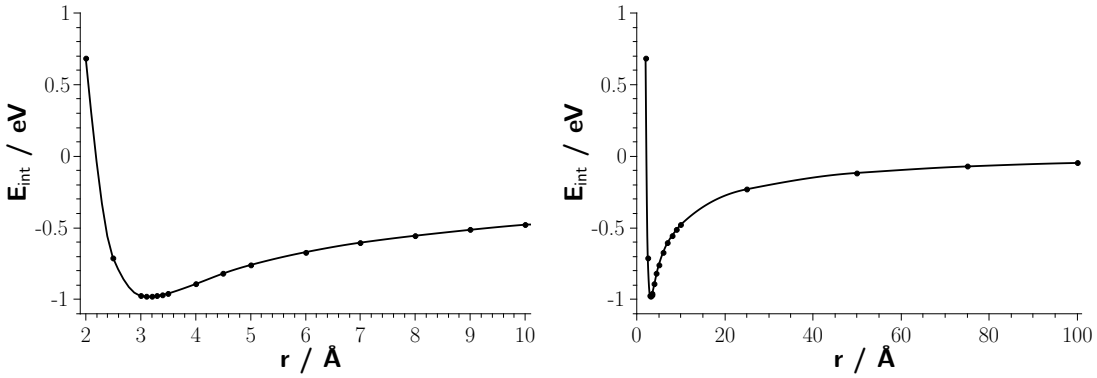

(a) (b)

Figure 4.15: Interaction energy of Cl on the (001) surface. a) is a zoom around the equilibrium, b) shows the long-range behavior of the interaction.

For the other two surfaces, (100) and (110), Cl forms covalent bonds. This is due to the unsaturated carbons that are formed upon creation of these surfaces. Cl forms a stronger bond with the (100) surface. When Cl adsorbs on the (110) surface, the C-C triple bond is broken and approaches the aromatic C-C bond length. In addition, a localized spin is found on the surface carbon next to the carbon that forms the C-Cl bond. This adsorption also deforms the surface, which can be seen from Figure 4.15, whereas it stays almost unchanged for adsorption on the (100) surface. These three processes are the reason why adsorption on the (110) surface is weaker by 1.0 eV.

Size effects of Cl can already be seen when a second Cl adsorbs on a surface carbon next to the first one; E_{ad}/Cl is weaker by 0.2 eV. For a fully covered graphene plane, this trend is even more pronounced; a weakening of E_{ad}/Cl by 1.5 eV is found. Two different configurations were studied for a second Cl adsorption on the (110) surface (see Figure 4.15). If a bond is formed with a carbon atom which belongs to the same six-membered ring as the carbon atom with a C-Cl bond, called 110-2Cl-a, E_{ad}/Cl decreases by 0.4 eV. This is due to the saturation of the six-membered ring. The spin localization is annihilated and the local deformation reversed. All these processes improve the stability of the system. On the contrary, adsorption on another six-membered ring next to the first, called 110-2Cl-b, would lead to two Cl atoms which are only separated by about 1.6 Å if both rested in-plane. This is circumvented by an opposing out-of-plane deformation of both Cl atoms, however this large deformation in addition to a second localized spin leads to a much less stabilized system; E_{ad}/Cl differs by 1.0 eV with respect to 110-2Cl-a.

At this point, it should be noted that these results show exactly the opposite behavior as found by Xu *et al.* However, a rerun of his calculations revealed some kind of systematic error in his published results, since the relative stabilities for the molecular systems approximating the (100) and (110) surface obtained here show the same trend as the larger periodic model surfaces. The results for the molecular systems can be found in the Appendix E.

In summary, Cl shows a complex behavior when interacting with the different graphite surfaces. Ionic interaction via charge transfer is found for the (001) surface, whereas covalent bonds are formed on the (100) and (110) surface.

4.3.2 Point Defects

Atomic chlorine forms covalent bonds with α- and β-vacancies as well as the 5-8-5-divacancy. The adsorption energies are given in Table 4.10 and the optimized structures are shown in Figure 4.16.

When Cl adsorbs to a monovacancy, the formed bond creates a strong out-of-plane deformation of the surface; the Cl is 2.3 Å above the graphene plane. Due to this, the adsorption process is significantly less stabilizing compared to adsorption on the (100) surface (ΔE = 1.7 eV). The localized spin of the unsaturated C is annihilated when the C-Cl bond is formed.

The interaction of Cl_2 with a monovacancy leads to a barrierless dissociation of Cl_2. This results in a metastable state where the first Cl is located above the vacancy position; thus it is effectively interacting covalently with three carbons. A Mulliken charge analysis shows that it is positively charged (+0.9). The second Cl is separated by 2.6 Å and has a Mulliken charge of -0.6. Thus, the interaction is ionico-covalent. This state is less stable than a Cl adsorbed on a monovancancy and a Cl adsorbed on the (001) surface by about 1.5 eV. Is should be noted that the position of the adsorbed Cl screens the vacancy which avoids the formation of a second covalent C-Cl bond.

For a divacancy, Cl adsorbs atop of a carbon atom. The form covalent bond is rather weak (-1.1 eV) due to the sp^3 hybridization of the carbon the Cl forms a bond with. No C-C bond is broken during this process.

A second Cl can adsorb on different positions. The configuration shown in Figure 4.16 is the most stable one. It is about twice the E_{ad} for one Cl; thus, steric repulsion is negligible if the two Cl adsorb on opposite sides of a divacancy. Adsorption on the same side of the divacancy was also tested, this configuration is much less stable (ΔE = 1.0 eV).

Table 4.10: Chlorine adsorption energies (E_{ad} in eV/Cl atom) on the (001) surface vacancies. Vac(α, β) and Divac denote the (001) surface with mono- and 5-8-5-divacancies, respectively.

System	Nb. of Cl	E_{ad}
Vac(α)	1	-2.49
	2	-0.98
Vac(β)	1	-2.49
	2	-1.07
Divac	1	-1.10
	2	-1.17

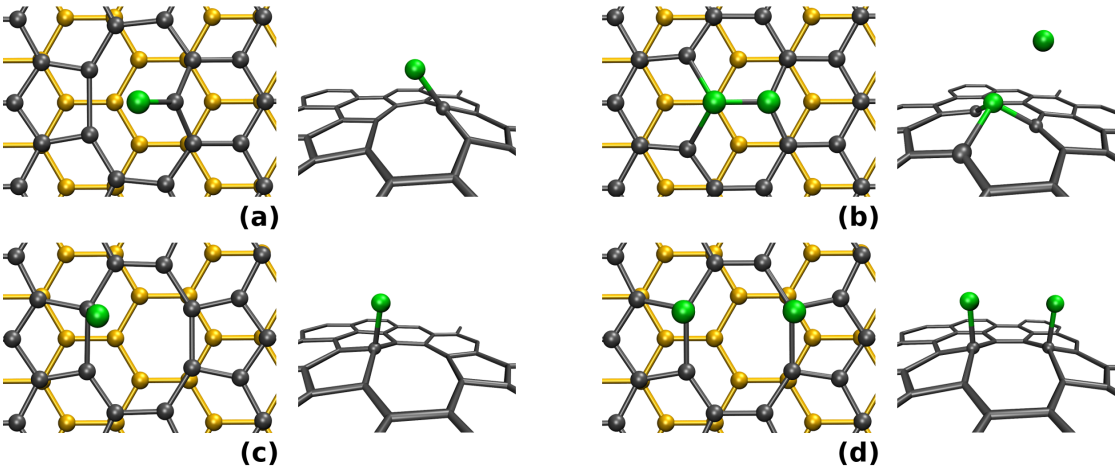

Figure 4.16: Optimized structures for adsorption of a) one and b) two Cl atoms on the (001) surface monovacancy and c) one and d) two Cl atoms on a (001) surface divacancy.

4.3.3 Bulk Graphite

Due to its size, it is clear that Cl will have a large influence on its environment, when it is inserted into bulk graphite. A larger supercell size (10 × 10) is needed in order to allow the carbon planes to bend around the Cl (see Figure 4.17). For the 5×5 super cells, the interlayer distance between graphene planes with an inserted Cl increases to 5.4 Å, but no deformation is found due to the periodic constraints. The Cl does not bond covalently to a graphene plane, but rests exactly in the middle of two planes. As for the (001) surface, charge transfer occurs from graphite to the Cl; the Mulliken charge is 0.12 and 0.16 for PBE and PBE0, respectively. However, contrary to the (001) surface, the total insertion energy is positive, thus Cl is not stable in graphite. For Cl_2, a similar behavior is found; the insertion energy is 3.84 and 4.10 eV/Cl, the total Mulliken charge of Cl_2 is 0.10 and 0.03 electrons/Cl for PBE and PBE0, respectively. Compared to Cl, this shows that two isolated Cl in bulk graphite are the preferred state. Electrons transferred to Cl_2 occupy antibonding σ^* states, this weakens the Cl-Cl bond. For PBE, spontaneous dissociation is found, the Cl-Cl distance increases to 2.98 Å. For PBE0, there is almost no charge transferred; the bond length of Cl_2 remains constant.

Mono- and divacancies in bulk graphite show an important difference with respect to the (001) surface. Again, significant size effects of Cl are found. For both monovacancies the trapping of Cl is much less stabilizing than on the (001) surface; the difference is almost 2 eV. This is due to the same reason as for the Cl insertion in bulk graphite; the adjacent graphene plane is deformed due to the

size of the Cl atom. For the divacancy, the completely opposite behavior is found. The trapping and C-Cl bond formation can not counterbalance the deformation and the trapped state is less stable than the dissociated state.

These results show that extended bulk defects could be selective toward Cl trapping. Edge carbons which resemble a monovacancy and have a dangling bond are able to trap chlorine, whereas carbons that underwent a reconstruction and have three C-C bonds can not.

Table 4.11: Insertion energies (E_{ins} in eV/Cl atom) for Cl and Cl_2 in bulk graphite and chlorine trapping at bulk vacancies. Vac(α, β) and Divac denote bulk graphite with mono- and 5-8-5-divacancies, respectively.

System	Nb. of Cl	E_{ins}
Bulk	1	$3.19^a/3.51^b$
	2^c	$3.84^a/4.10^b$
Vac(α)	1	-0.64
	2	0.11
Vac(β)	1	-0.59
	2	0.16
Divac	1	0.69
	2	0.39

^{a} PBE; ^{b} PBE0; ^{c} Cl_2

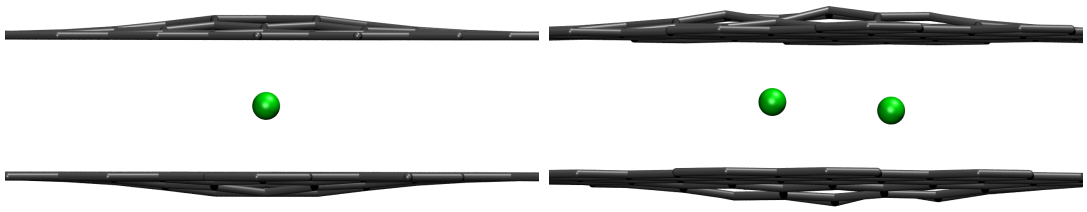

(a) (b)

Figure 4.17: Optimized structures of a) Cl and b) Cl_2 in bulk graphite obtained with PBE. The distance between the two Cl atoms is 2.98 Å which shows full dissociation.

4.3.4 Discussion

The interactions of chlorine with graphite are found to be rather complex. On the three principal surfaces it behaves completely opposite depending on its form (atomic or molecular) and the features of the surface.

On the (001) surface, atomic Cl forms a charge transfer complex with the surface; a Mulliken charge analysis revealed that it is partially negatively charged. However, in the form of Cl_2 the interactions are much weaker (by a factor of three). Only a small amount of charge transfer is observed, the other part of the attractive interaction stems from van der Waals interactions. Cl_2 adsorbed on this surface is the most stable state.

Both the (100) and (110) surface have dangling bonds; thus, atomic Cl forms strong covalent bonds when adsorbing on both of them. Both of these reactions are barrierless as for hydrogen. Size effects are already observable for two adjacently adsorbed Cl atoms on the (100) surface. If one dangling bond is surrounded by Cl-saturated carbons, a significant barrier can be expected. This is indicated by the larger Cl-Cl distance for two adsorbed Cl compared to the distance of two adjacent unsaturated carbons. This shows that the steric repulsion of Cl-Cl is too large at 2.54 Å. Additionally, the difference of E_{ad}/Cl for one and three Cl atoms is quite big (ΔE = 1.5 eV). Thus a full saturation of the (100) surface with Cl might not be possible.

On the (110) surface, adsorption of one atomic Cl is less stable than on the (100) surface which is due to the deformation of the surface and spin localization. Adsorption of a second Cl is largely preferred in the form of configuration (110)-2Cl-a, the difference of E_{ad}/Cl is 1.0 eV. The large out-of-plane deformation for (110)-2Cl-b also indicated that a full saturation of this surface with Cl is very unlikely.

A monovacancy on the (001) surface also forms a covalent bond with Cl. However, it is weaker compared to the (100) and (110) surface due to the steric repulsion of Cl which causes a large out-of-plane deformation. The overall trend of stability is (100) > (110) > Vac. Cl_2 spontaneously dissociates and forms a ionico-covalent metastable state. The most stable state is a Cl-saturated vacancy and an adsorbed Cl on the (001) surface. Trapping at a divacancy is significantly weaker; Cl adsorption does not cause a breaking of C-C bonds. Due to steric repulsion, adsorption on opposite sites of a divacancy is preferred for two Cl atoms.

Compared to H, trapping of Cl is less stabilizing on the (100) and (110) surfaces as well as at vacancies. When Cl is released by heating, no Cl_2 was found in the released gas [VGT+11]. The only species containing Cl was HCl. The bond strengths of HCl and H_2 are rather similar (4.44 eV and 4.48 eV, respectively). However, the bond energy of Cl_2 is significantly lower (2.51 eV).

From a thermodynamic point of view, two scenarios are possible: first, a gas phase reaction of H_2 + Cl_2 $\longrightarrow$ 2 HCl with ΔE= -1.89 eV. This is energetically very favorable, however it depends on the gas concentration of H_2 and Cl_2. Since the concentration of Cl is very low in nuclear graphite and a no traces of Cl_2 are found, this is unlikely the sole source of HCl. The second scenario involves surface reactions. Since the bond energies of H_2 and HCl are almost the same, any exchange reaction of the kind $\sim$C–Cl + H_2 $\rightarrow$ $\sim$C–H + HCl is thermodynamically favored when H trapping is stronger than Cl trapping. This is at least the case for the (100) and (110) surfaces as well as for vacancies. A third scenario which is controlled by kinetics is the concerted detrapping of H and Cl from a surface to give HCl. In reality, the surfaces are saturated by many different species. H atoms could be adsorbed next to Cl atoms. If the barrier for detrapping of HCl is smaller than for detrapping of Cl_2 or H_2, the existence of HCl in the gas phase could be due to the faster detrapping reaction of HCl compared to other detrapping processes.

Cl is not stable in bulk graphite due to its size. The steric repulsion can not be counterbalanced by the small amount of charge transfer which is observed. However, the charge transfer is consistent with the findings that Cl is an acceptor graphite intercalation compound (see Refs. [Hen52, JJS57]). The same is found for Cl_2; comparing the insertion energies shows that two isolated Cl atoms are more stable than a Cl_2 in bulk graphite; for PBE spontaneous dissociation is observed. Thus, under reactor conditions it is likely dissociated. This agrees with the experimental lack of Cl_2 in bulk graphite [VTM$^+$09].

The non-covalent interactions were investigated with two functionals PBE and PBE0 due to the lack of comparable data. They yield rather different results on the (001) surface; interactions for Cl and Cl_2 obtained with PBE are 2-3 stronger compared to PBE0. In addition, PBE predicts a dissociated Cl_2 in bulk graphite whereas there is a barrier for PBE0. Experimental evidence indicates that Cl_2 does not exist in nuclear graphite [VTM$^+$09]. MP2 calculations for Cl_2 adsorption on coronene as a model of the (001) surface agree well with E_{ad} of Cl on the (001) surface obtained with PBE (see section 5.1.3). Both of these findings support the behavior described by PBE which indicates that this functional is better suited to describe the non-covalent interactions of Cl with graphite. Thus, the parameters for the potential will be fitted to the PBE results.

4.4 Summary and Conclusion

The findings of these *ab initio* calculations are useful in two ways: first, they help to understand the interaction of the radionuclides with its local environment and second, the found properties can be used for the development of model potentials.

For H, adsorption on the surfaces (001), (100), and (110) yields the relative reactivities (100) >(110) > (001). Thus, the (100) surface forms the most stable structures with hydrogen. The hypothesis of trap 1 in nuclear graphite (zigzag edges of dislocation loops) is confirmed; a good agreement between the E_{ad} on the (100) and Kanashenko's estimation is found after correcting an error in Kanashenko's assumption of the C-H bond energy. However, compared to the experiment, the obtained adsorption energies are overestimated for the (100) surface and underestimated for the (110) surface. This is likely due to the difficulty to compare experimental data of complex ill-defined microstructures measured at elevated temperatures (> 750 °C) with theoretical *ab initio* results of well-defined structures at 0 K. Nevertheless, the unreconstructed zigzag edges cannot be the only traps in graphite crystallites contrary to Kanashenko's and Atsumi's claims; the (110) edges are also possible traps. Thus the current hypothesis for the first trap needs to be refined.

Two types of reconstructions of (100) and (110) surfaces have been studied: first, in-plane reconstructions which yield heptagon edge carbons and second, arch-shaped reconstructions which result in no dangling bonds for both systems. For both types, a decreased stability of H adsorption is found compared to unreconstructed surfaces. For arch-shaped reconstructions, hydrogen adsorption is considerably stronger than on a pristine (001) surface due to the curvature of the surface. Hydrogen adsorbs stronger on the reconstructed (100) surfaces which agrees with Kanashenko's hypothesis of the second trap in nuclear graphite. H adsorption energies on in-plane reconstructed surfaces are in better agreement with experiment. Since the in-plane reconstruction of the (110) surface is endothermic, this suggests that the second trap is, indeed, the in-plane reconstructed (100) surface of crystallites.

Point defects caused by irradiation, such as mono- and divacancies, are also able to bind hydrogen strongly; a divacancy binds hydrogen less strongly than a monovacancy. Thus, extended defects are weaker traps than monovacancies.

For Cl, similar trends are found when covalent bonds are formed. Adsorption on the (100) surface is more stable compared to the (110) surface. A stark contrast to hydrogen is found for the (001) surface. Isolated atomic Cl forms a rather strong charge transfer complex with the surface and is partially negatively charged. For Cl_2, this behavior is not found; adsorption on the (001) surface is much weaker for this species.

As for hydrogen, trapping of Cl at a monovacancy is much stronger than at a

divacancy. However, compared to the surfaces (100) and (110) it is significantly weaker. Cl_2 spontaneously dissociates at a monovacancy which is not found for H_2.

The behavior in bulk graphite is another important difference of Cl and H. Neither Cl nor Cl_2 are stable in bulk graphite due to their size. Isolated Cl atoms are more stable than Cl_2, dissociation of Cl_2 has a very low barrier. This means that under reactor conditions Cl_2 very likely does not exist which is consistent with experimental findings.

When the results for H and Cl are compared, H adsorption is stronger than Cl adsorption for all investigated traps. When graphite samples are heated, no Cl_2 but only HCl is detected. From the *ab initio* calculations, several scenarios are deducible: a gas phase reaction of H_2 and Cl_2 to give HCl, a surface exchange reaction $\sim$C–Cl + H_2 $\rightarrow$ $\sim$C–H + HCl, or a preferred concerted detrapping of HCl from the surface. These scenarios should be studied further in detail to determine the barriers of these reactions.

In summary, the behavior of hydrogen is more simple than that of Cl. In its atomic form H forms covalent bonds with all surfaces as well as in the bulk. Contrary to that, interactions of Cl are sensitive to its chemical environment and can be either covalent, charge transfer complex formation or simply van der Waals interactions.

Thus, all of these interaction types are critically dependent on the electron structure of the system. This shows the great challenge to the potential development, where electrons are not explicitly considered and these informations need to be extracted from structural features of the environment.

Chapter 5

Preparation for Complex Large-scale Simulations - Potential Development

In this section the fitting procedure and performance of the potential is described in detail. This step is necessary in order to make the accuracy obtainable by DFT accessible to large-scale simulations which are more computationally efficient. The potential aims to describe all possible interactions that can occur in graphite: Covalent interactions that arise for trapping processes as well as non-covalent interactions which are important for diffusion processes. In the first part, the fitting procedure is explained; for the C-C interactions, only the changes to the original LCBOP potential are given. For C-Cl and Cl-Cl interactions, the fitting is described in detail. The notation of Ref. [LF03] is used for all parts concerning LCBOP and that of Ref. [STH00] for all concerning the AIREBO-type potential. In the second part, the potential is validated by studying the interactions and diffusional properties on graphite surfaces and in the bulk material. Finally, the results are summarized and conclusions are drawn.

5.1 Fitting Procedure

5.1.1 C-C Interactions

LCBOP Modifications for a C-Cl Potential

The potential was fitted for the simultaneous use of LCBOP for the C-C interactions and an AIREBO-type bond order potential for the C-Cl and Cl-Cl interactions. For LCBOP, two modifications to the short range interaction are introduced, since the original version does not consider other neighbors than the carbon atoms.

Both parts of the bond order B_{ij}, the angle-dependent part b_{ij} and $F(N_{ij}, N_{ji}, N_{ij}^{conj})$, which accounts for conjugations effects, are affected when chlorine atoms ($k = Cl$) are taken into account as neighbors of a carbon bonding pair ($i = j = C$). The original definition of b_{ij} (see eq. 3.36) was extended to

$$b_{ij} = \left(1 + \sum_{k \neq i,j} f_c(r_{ik}) G(\cos\theta_{ijk}) H(\delta r_{ijk}) \delta_{kC} + S'_{CCl}(t_c) G(\cos\theta_{ijk}) H_{Cl}(\delta \tilde{r}_{ijk}) \delta_{kC} \right)^{-\delta}. \tag{5.1}$$

It was found that the original G function can also be used for neighbors $k =$ Cl. However, a function H_{Cl} needs to be defined. It was fitted to reproduce the single, double, and triple C-C bond lengths for the molecules C_2Cl_6, C_2Cl_4, and C_2Cl_2.

The cutoff function $S'_{CCl}(t_c)$ is chosen according to the definition of Brenner's REBO potential (see equation 3.16) to assure consistency with the potential that covers the C-Cl and Cl-Cl interactions.

The function H_{Cl} takes a different argument $\delta\tilde{r}_{ijk} = r_{ij} - r_{ik} + r_{off}$. r_{off} is needed since the average C-C and C-Cl bond lengths are quite different, but the functional form of H_{Cl} assumes that $\delta r_{ijk} = 0$ at the equilibrium. The final form of H_{Cl} is

$$H_{Cl}(x) = \begin{cases} L^{Cl} \left(1 + \kappa^{Cl}(x+d) \left(\frac{1}{1+[\kappa^{Cl}(x+d)]^{10}} \right)^{1/10} \right), & x < -d \\ a_0 + a_1 x + a_2 x^2 + a_3 x^3 + a_4 x^4 + a_5 x^5, & -d \leq x \leq d \\ R_0^{Cl} + R_1^{Cl}(x-d), & x > d \end{cases} \tag{5.2}$$

The fitted parameters are given in Table 5.1. The coordination number N_i is extended and also defined for $i =$ Cl and $k =$ Cl. It is defined as follows:

$$N_i = \sum_k f_c(r_{ik}) \delta_{kC} + S'_{CCl}(t_c) \delta_{kCl} \tag{5.3}$$

The definitions of N_{ij}, N_{ij}^{conj}, N_{ij}^{el}, and M_{ij} remain unchanged. In Ref. [LF03], $\tilde{M}_{ij}$ is defined as the number of neighbors $k \neq j$ of the atom i, which have a coordination number ≥ 4. To account for neighbors $k =$ Cl the extended function is

$$\tilde{M}_{ij} = \sum_{k \neq i,j} f_c(r_{ik}) F(x_{ik}) \delta_{kC} + S'_{CCl}(t_c)^4 \delta_{kCl}. \tag{5.4}$$

Since Cl only forms σ-bonds with C where both contribute one electron, the cutoff function $S'_{CCl}(t_c)$ was found to be well-suited. The exponent of $S'_{CCl}(t_c)$ was

set to four since Cl exchange reaction barriers as described in section 5.1.2 were better reproduced.

Table 5.1: Parameters for the H_{Cl} function.

r_{off}	0.5	a_0	2.29000
d	0.2	a_1	1.42625
L^{Cl}	1.8	a_2	-4.25000
κ^{Cl}	1.8	a_3	11.56260
R_0^{Cl}	2.5	a_4	17.50000
R_1^{Cl}	1.0	a_5	-86.71875

LCBOP Modifications for a C-H Potential

To describe interactions between carbon species and hydrogen, the LCBOP potential was coupled with the existing AIREBO/M potential. The same approach as presented in the previous section was adopted. All parts of the LCBOP potential modifications developed for the C-Cl potential can be applied to a potential describing the C-H interaction. Only the parameter r_{off} was changed to -0.25 to reproduce the bond length of a single, double, and triple C-C bond for the molecules C_2H_6, C_2H_4, and C_2H_2.

ZBL Potential for Irradiation Simulations

Since the LCBOP potential was fitted to equilibrium data (binding energies, elastic constants, etc.) its performance strongly depends on the simulation conditions. This is especially true for irradiation simulations. The covalent interaction is described by a sum of the exponentials. Thus, at a C-C distance of 0 the interaction is finite and not physically correct. In addition, a comparison with a DFT potential of the C_2 dimer (see Figure 5.1) shows that it is too repulsive for distances between 0.05-0.5 Å. Thus, the standard LCBOP potential is not suited to perform high-energy irradiation simulations where two atoms can get very close when they collide.

The standard procedure for such simulations is to couple the potential describing covalent interactions to the ZBL potential (see section 3.3 for a description). For C-C interactions, this procedure was already implemented in LAMMPS [Pli95] for the Tersoff potential and also adopted for the EDIP potential [CRR+15]. Following the approach of LAMMPS, the total interaction is defined as

$$V_{ij} = (1 - f_F(r_{ij}))V_{ij}^{ZBL} + f_F(r_{ij})V_{ij}^{LCBOP}. \tag{5.5}$$

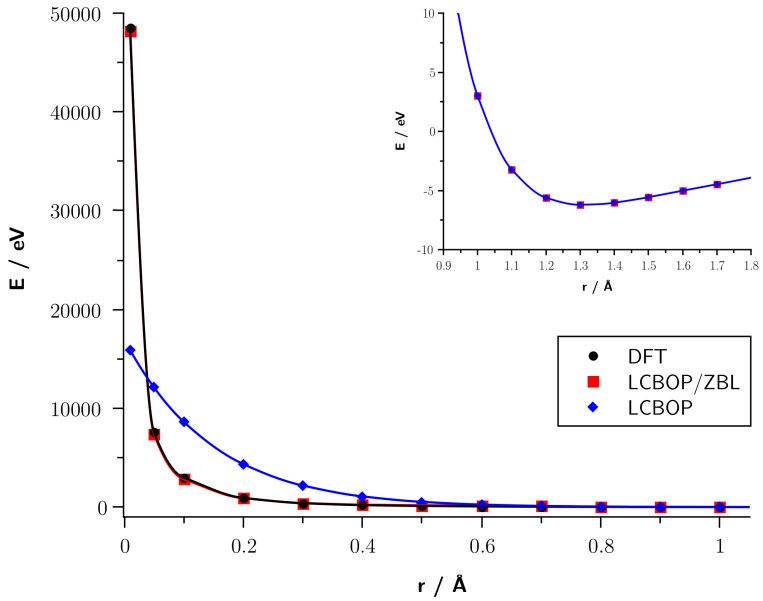

Figure 5.1: Comparison of the LCBOP potential (blue) for C_2 to the DFT potential (black) obtained with PBE0/Def2-TZVP and the coupled LCBOP/ZBL potential. The figure in the right upper corner shows the region around the equilibrium distance.

f_F is a Fermi-like cutoff function assuring a smooth scaling between the two potentials that reads

$$f_F(r_{ij}) = \frac{1}{1 + e^{-A_F(r_{ij} - r_C)}}. \tag{5.6}$$

The parameter A_F defines the sharpness of the transition and r_C is the cutoff of the ZBL potential. A_F was set to 65.26077 and r_C to 0.95926. For the fit of these two parameters the standard parameters of the ZBL potential as implemented in LAMMPS [Pli95] were used. They were fitted in a way that the DFT potential is reproduced in the repulsive region, but also maintaining the good description of equilibrium properties of LCBOP. This required a rather sharp transition between the two potentials. However, as can be seen in Figure 5.1, the coupled potential describes both, the repulsive and the equilibrium region very well. This also shows that the standard parameterization of the ZBL potential is well-suited for C-C interactions.

5.1.2 Covalent C-Cl and Cl-Cl Interactions

The bond order potential for the C-Cl and Cl-Cl interactions was developed from scratch, following loosely the fitting procedures described in Ref. [BSH+02] and Ref. [STH00].

The atom-type dependent parameters for the covalent interactions are A_{ij}, α_{ij}, B_{ij}, β_{ij}, and Q_{ij}. Data were calculated with NWChem [VBG+10]. The CCSD(T) method [IB82, RTPHG89, WGB93] was applied for smaller systems; larger systems with many Cl atoms were calculated with the DFT functional M06-2X [ZT08b, ZT08a] which well reproduced the CCSD(T) bond energies (see Table 5.3 for a list of molecules and methods applied). The basis sets for C and Cl were aug-cc-pVnZ and aug-cc-pV(n+d)Z [DJ89, KDJH92, WDJ93], n=T,Q and were extrapolated to the complete basis set (CBS) limit with the two parameter function [HHJ+98] following the approach of Ref. [DP01]. For the CCSD(T) calculations, the frozen core approximation was applied and geometries were optimized with basis sets n=T. For DFT calculations the basis set Def2-TZVP [WA05] was used.

For the C-Cl pair interactions, it was found that bond lengths and dissociation energies show strong variations for different chemical environments. For the fitting, the bond length of CCl_4, the average of the C-Cl dissociation energies of CCl_4, CCl_3, CCl_2, and CCl, the energy at $r = 0.5$ Å for C-Cl and the force constant of the C-Cl bond vibration of the molecule $(CH_3)_3$C-Cl were chosen. All Cl-Cl parameters were obtained from CCSD(T) calculations. The parameters for pair interactions were fitted to the same four properties as mentioned before. The parameters are presented in Table 5.2.

Table 5.2: Parameters for the C-Cl and Cl-Cl bond order potentials.

Parameter	C-Cl	Cl-Cl
Q_{ij} / eV	0.261321	0.217854
A_{ij} / eV	2090.393898	3379.567443
B_{ij} / eV	27.843502	557.752686
α_{ij} / Å^{-1}	4.385167	3.373152
β_{ij} / Å^{-1}	0.944076	2.190954
r_{ij}^{min} / Å	2.05	2.30
r_{ij}^{max} / Å	2.65	2.70

The bond order b_{ij} includes many-body effects and is defined as

$$b_{ij} = \frac{1}{2}[p_{ij}^{\sigma\pi} + p_{ji}^{\sigma\pi}] + \pi_{ij}^{rc}. \tag{5.7}$$

Note that in the original definition of Ref. [STH00] (see eq. 3.18) there is

another term π_{ij}^{dh}, which penalizes rotations around multiple C-C bonds. It is neglected, since C-C interactions are described by the LCBOP potential.

$p_{ij}^{\sigma\pi}$ contains angle-dependent and coordination number-dependent terms

$$p_{ij}^{\sigma\pi} = \left[1 + \sum_{k \neq i,j} G(\cos(\theta_{ijk}))e^{\lambda_{ijk}} + P_{ij}(N_i^C, N_i^{Cl})\right]^{-1/2}, \tag{5.8}$$

whereas π_{ij}^{rc} is a three dimensional cubic spline accounting for radical and conjugation effects. The fitting procedure of the different terms will be explained in the following in a chronological order.

The Bicubic Spline $\mathbf{P_{CCl}}$

Since the C-C interactions are covered by LCBOP, the P_{ij} term only covers C-Cl pairs. Thus, only the parameters of P_{CCl} are given in Table 5.3 for integer values of N_i^C and N_i^{Cl}. They were fitted to reproduce the thermodynamic bond energies, thus it takes into account the relaxation of the molecule after bond dissociation. The appropriate values for G_C were determined for the equilibrium angles of Cl-C-Cl and Cl-C-C bonds.

Table 5.3: Parameters for the bicubic spline P_{ij}. All P_{ij} values and derivatives that are not given in the table are set to 0 for integer values of N_i^C and N_i^{Cl}. The given C-Cl bond energies (BE) in eV were used to derive the parameters. Available experimental data BE_{exp} are given for comparison (error bars are only available for the bond energy of C_2Cl_2).

N_i^C	N_i^{Cl}	P_{CCl}	Fitted Molecule	BE	BE_{exp}[Luo07]
0	1	0.349950	CCl_2 [a]	3.41	-
0	2	0.653938	CCl_3 [a]	2.98	-
0	3	0.750768	CCl_4 [a]	3.01	3.07
1	0	0.782629	C_2Cl_2 [a]	4.90	4.59 ± 0.52
1	1	0.508697	C_2Cl_4 [a]	4.00	3.98
1	2	0.345196	C_2Cl_6 [b]	3.05	3.15
2	0	0.703240	$(Cl_3C)ClC{=}CCl(CCl_3)$ [b]	3.28	-
2	1	0.220803	*c*-C_6Cl_{12} [b]	2.29	-
3	0	-0.044134	*i*-C_4Cl_{10} [b]	2.63	-

The superscripts for the molecules indicate the applied method: [a] CCSD(T) and [b] DFT.

The Angle Function G

The angle-dependent function G_i is applied in the same way as proposed by Brenner and is different according to the type of atom i = C,Cl. For a bond $i-j$, the angle function determines the interaction of bond $i-j$ with all other bonds formed with neighbors k of atom i. It depends on the angle between bonds $i-j$ and $i-k$. For the case i = C, we use the function as proposed by Brenner with AIREBO parameters [STH00] is used. For i = Cl, the function was fitted to the Cl_3 molecule. The state with C_{2v} symmetry was optimized at fixed angles of 180, 150, 120, 90, and 60 degrees. The respective parameters at each angle were then determined from the bond energies. It should be noted that the molecule has two equivalent bonds for angles from 90 to 180 degrees, but three equivalent bonds for 60 degrees. A 5th order spline was fitted for the intervals [180,150), [150,120), and [120,0], to obtain a function that is continuous up to the second derivative. The parameters needed for the spline coefficients are given in Table 5.4 and a plot of G_{Cl} is shown in Figure 5.2. Note that the value G(1.0) was chosen to allow for a function which has neither a cusp nor a negative gradient at $\cos\theta = 1.0$. Since the minimum of Cl_3 with C_{2v} symmetry is at 146°, the function is not monotonically increasing in the interval [-1,1] contrary to the G_H function of Brenner.

Table 5.4: Parameters for the function G_{Cl}

$\cos\theta$	G_{Cl}	$G_{Cl}/d\cos(\theta)$	$d^2G_{Cl}/d\cos(\theta)^2$
-1.0	4.208656	0.0	116.124437
-0.866025	2.425248	-7.269911	78.404147
-0.5	3.342242	8.572603	17.223726
0.0	8.429036	-	-
0.5	36.41574	-	-
1.0	80	-	-

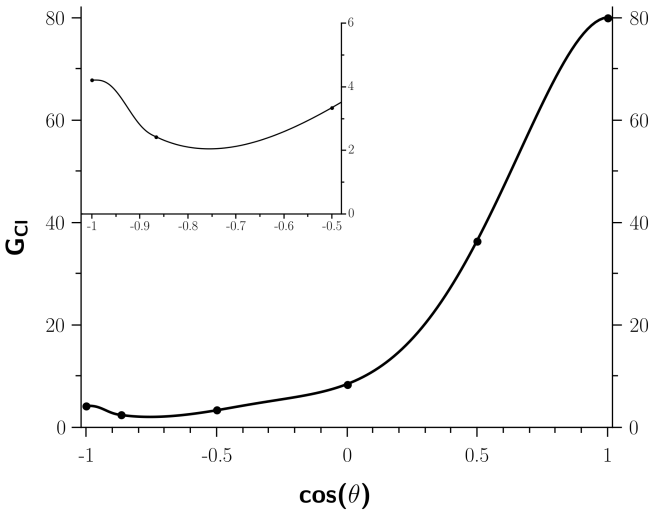

Figure 5.2: The angle-dependent function G_{Cl}. The small figure in the upper left corner shows a zoom in the interval [-1,-0.5].

$e^{\lambda_{jik}}$ and π_{ij}^{rc}

In the following the fitting process for the two functions $e^{\lambda_{jik}}$ and π_{ij}^{rc} will be explained together since both needed to be fitted to the same data in an iterative fashion. All relevant parameters are shown in Tables 5.5 and 5.6. The fitting data were the energy barriers E_b of the following four exchange reactions:

$$(CCl_3)_3CCl + Cl \rightarrow (CCl_3)_3C + Cl_2 \qquad E_b = 0.8\,eV \tag{5.9}$$

$$(CCl_3)_3CCl + CCl_3 \rightarrow (CCl_3)_3C + CCl_4 \qquad E_b = 0.9\,eV \tag{5.10}$$

$$(CCl_3)_3CCl + CCl_2 \rightarrow (CCl_3)_3C + CCl_3 \qquad E_b = 0.7\,eV \tag{5.11}$$

$$(CCl_3)_3CCl + C_2Cl \rightarrow (CCl_3)_3C + C_2Cl_2 \qquad E_b = 0.2\,eV \tag{5.12}$$

The energy barriers were determined by a transition state calculation with NWChem using the M06-2X functional. Within NWChem, the search is performed by following the mode of the hessian matrix with the lowest (or negative) eigenvalue. The frequencies of the found transition state were calculated to verify that it only had one imaginary frequency. For the first step of fitting, the parameters ρ_{CCl} and ρ_{ClCl} were determined for reaction 5.9. Then, π_{CCl}^{rc} for $N_C = 1 - 3$ and $N_{Cl} = 1$ were fitted for reactions 5.10-5.12. Since $\pi_{CCl}^{rc}(3,1,1)$ also occurs in

reaction 5.9, these steps were repeated until all energy barriers could be reproduced to a satisfying extent.

Another important exchange reaction which models the reaction of Cl on graphite crystallite edges is:

$$C_6Cl_5 + Cl_2 \rightarrow C_6Cl_6 + Cl \tag{5.13}$$

This reaction is barrier-free. $\pi^{rc}_{CCl}(2,1,5-9)$ and $\pi^{rc}_{ClCl}(1,0,2-9)$ were fitted to reproduce this behavior.

$\pi^{rc}_{ClCl}(1,1,1)$ was fitted to guarantee a smooth behavior of G_{Cl} for an angle of 60° same as for Brenner's potential. In order to improve the barriers for the exchange reaction 5.9, $\pi^{rc}_{ClCl}(1,0,1)$ was added. Since this has a direct impact on the overall potential of Cl_3, a constant λ_{ClClCl} was fitted to reproduce the correct angular behavior.

Table 5.5: Parameters for $e^{\lambda_{jik}}$.

ρ_{CCl}	0.10
ρ_{ClCl}	0.38
$\lambda_{\mathrm{ClClCl}}$	0.50

Finally, several specific parameters were added which account for reactions that occur in graphite or inhibit processes which are inexistent according to DFT data.

Table 5.6: Parameters for three-dimensional cubic spline π^{rc}_{ij}. All π^{rc}_{ij} values and derivatives that are not given in the table are set to 0 for integer values of N_{ij}, N_{ji}, and N^{conj}_{ij}.

	N_{ij}	N_{ji}	N^{conj}_{ij}	π^{rc}_{ij}	Fitting species
π^{rc}_{CCl}					
	1	1	≥1	-0.070	Eq. 5.10-5.12
	2	0	≥5	0.100	C_6Cl_6
	2	1	1-4	-0.065	Eq. 5.10-5.12
	2	1	≥5	-0.060	Eq. 5.13
	3	0	≥5	-0.400	Cl on (001)
	3	1	1-4	-0.060	Eq. 5.10-5.12
	3	1	≥5	-0.400	Cl_2 on (001)
π^{rc}_{ClCl}					
	1	0	1	-0.034	Eq. 5.10-5.12
	1	0	≥2	-0.100	Eq. 5.13
	1	1	1	0.309	Cl_3

5.1.3 Dispersion Interactions

The parameters of the Morse potential used to describe the dispersion interactions are shown in Table 5.7. First, the Cl-Cl parameters were fitted to the interaction potential of a Cl_2 dimer where the two Cl-Cl bonds are aligned in parallel (and thus depends only on two different Cl-Cl distances). Since DFT is not a reliable method to calculate dispersion interactions, all dispersion interaction potentials were determined at the BSSE-corrected MP2/aug-cc-pVTZ level following O'Connor *et al.*'s approach for the fitting of AIREBO/M [OAR15].

The model system to fit the C-Cl parameters was chosen to be Cl_2 adsorbed on coronene with the Cl_2 bond parallely aligned to the surface. This choice was made since the major interest of this potential is to reliably reproduce the interaction of Cl_2 on the (001) surface of graphite. Coronene was shown to be a finite model of moderate size which can approximate the (001) surface for systems where weak van der Waals interactions are dominant [DGHkAt15]. In order to fit the potential, the parameters of H-Cl interactions were assumed by using the standard mixing rules applied to the AIREBO/M H-H parameters and previously fitted Cl-Cl parameters. Thus, the geometric mean was used for ϵ and the arithmetic mean for α and r_{eq} which were derived from σ following Ref. [OAR15]. The full set of fitted parameters is given in Table 5.7.

Table 5.7: Dispersion interaction parameters for the C-Cl and Cl-Cl bond order potentials.

Parameter	C-Cl	Cl-Cl
ϵ / eV	0.01116041	0.01135557
α / Å^{-1}	1.53824982	1.75750150
r_{eq} / Å	3.75953677	3.90675046
$r_{ij}^{',min}$ / Å	2.05	2.65
$r_{ij}^{',max}$ / Å	2.30	2.70
r_{VDW}^{min} / Å	3.349	3.485
r_{VDW}^{max} / Å	3.760	3.908
b_{ij}^{min}	0.73	0.75
b_{ij}^{max}	0.85	0.85

5.1.4 Charge Transfer Interactions

The interaction potential for the charge transfer interaction of Cl on the (001) surfaces was calculated as described in section 4.1.3. Instead of assigning charges to C and Cl, a generalized force shifted potential as proposed by Steinbach and Brooks [SB94] was chosen to allow for a more efficient computation:

$$V_{CCl}^{CT} = q_{CT}\left(\frac{1}{r_{ij}} + \frac{r_{ij}^{\beta}}{\beta r_{max}^{\beta+1}} - \frac{\beta+1}{\beta r_{max}}\right) \tag{5.14}$$

The fitted parameters were determined as $q_{CT} = -0.17305$ and $\beta = 4.51576$, r_{max} was chosen as the cutoff of dispersion interactions to keep the consistency with other non-covalent interactions. In order to assure that this interaction only arises between C atoms belonging to a (001) surface and atomic Cl, a charge transfer switch was implemented into the potential which decides whether the charge transfer interaction is added on top of the dispersion interaction or not. This switch was defined using only parameters that are already available to minimize the changes of the potential. Since any carbon belonging to an infinite (001) surface has three carbon neighbors, the interaction is activated when, for a C-Cl pair, $N_C = 3, N_{Cl} = 0, N_{conj} = 10$. Parameters were added to $\pi_{CCl}^{rc}(3, 0, \geq 5)$ to inhibit covalent bonding on this surface.

5.1.5 Cl and Cl_2 in Bulk Graphite

Both species, Cl and Cl_2 were found to be unstable in bulk graphite (see section 4.3.3). To reproduce this behavior within the potential, first the case C/Cl_2 in bulk graphite needs to be defined. To determine whether or not a Cl species is in bulk graphite, a similar switch as for the (001) surface was defined. For a C-Cl pair, the bulk case is applied when $N_C = 2, N_{Cl} \leq 1, N_{conj} > 1$ for a C-Cl distance $\leq r_{CCl}^{max}$. Thus, both Cl and Cl_2 are covered by this definition. As shown in section 4.3.3, Cl_2 dissociates in bulk graphite during the geometry optimization. Thus, for the conditions that are studied in this work, Cl_2 can be considered as fully dissociated. While defining the presence of chlorine species in bulk graphite is rather easy for a C-Cl pair (the needed neighbor counts are readily available), it is more difficult for a Cl-Cl pair. The definition is the following: For a pair of Cl atoms i and j, the coordination number N_{conj} is calculated for all carbon atoms k and l within the radius σ_{CCl} ($\equiv r_{eq}/2^{1/6}$). N_{conj} is slightly modified with respect to Brenner's definition:

$$N_{conj} = 1 + \left[\sum_{k\neq i,j}^{carbon} F(x_{ik})\right]^2 + \left[\sum_{l\neq i,j}^{carbon} F(x_{jl})\right]^2 \tag{5.15}$$

thus the weighting function w_{ik}/w_{jl} is 1.0 for all C-Cl pairs within the cutoff radius.

$F(x_{ik})$ is defined as

$$F(x_{ik}) = \begin{cases} 1 & x_{ik} < 3 \\ [1 + \cos(\pi x_{ik})]/2 & 3 \leq x_{ik} < 4 \\ 0 & x_{ik} \geq 4. \end{cases}$$

x_{ik} is the standard definition of the number of neighbors as shown in equation 3.23. The presence of Cl_2 in bulk graphite is then defined for $N_{conj} \geq 50$. This number was found to well separate the bulk case from other cases such as the (001) surface.

When applying the DFT results within the framework of a bond order potential, the C-Cl and Cl-Cl interactions are as follows:

Cl and Cl_2 inserted into graphite is unstable. This means that the C-Cl interaction is still in the repulsive region at the equilibrium C-Cl distance. No covalent bonds are formed between C atoms of graphene sheets and Cl. Thus, the repulsive force felt by the Cl continuously increases when approaching a graphene layer. The bond order for covalent C-Cl interactions is therefore set to 0 for Cl/Cl_2 in bulk graphite. In addition, non-covalent interactions are fully taken into account regardless of the C-Cl distance. This inhibits a local minimum when the C-Cl distance decreases below r_{ij}^{max} where non-covalent interactions normally would be turned off (see equation 3.26). Together, this assures a continuously increasing interaction potential for decreasing C-Cl distances.

Cl_2 dissociates in bulk graphite. Thus, covalent Cl-Cl interactions are repulsive. To describe this within the potential, the same settings are applied as for the C-Cl interactions. When Cl_2 is found in graphite, the Cl-Cl bond order is 0 and non-covalent interactions are fully taken into account regardless of the Cl-Cl distance. This assures a continuously increasing interaction potential for decreasing Cl-Cl distances.

5.2 Validation of the Potentials

The bond order potential for C-Cl and Cl-Cl interactions was created by fitting to molecular data. In order to assure that it also works as intended for interactions of solid state graphite and chlorine, the potential needs to be validated. In the following several key features of covalent and non-covalent interactions are tested and compared to *ab initio* data.

5.2.1 C-Cl Potential

Covalent Interactions

Covalent interactions of Cl with graphite are mostly important when Cl is trapped at defects. As explained in section 4.3.1, these traps can for example be the surfaces (100) and (110), or vacancies. In Table 5.8, the adsorption energies and insertion energies for Cl are given. For the sake of completeness, the adsorption energy for Cl on the (001) surface and insertion energy of Cl in bulk graphite are also included.

For the two studied surfaces, the correct trend is obtained. Adsorption on the (100) surface is preferred over the (110) surface. For one adsorbed Cl, the adsorption energies are slightly underestimated (the error is less than 10 %). For adsorption of a second Cl, the correct behavior is recovered; for the (100) surface the steric repulsion between adjacent Cl atoms destabilizes the system and E_{ad}/Cl increases. For the (110) surface the correct order of configurations 110-2Cl-a and 110-2Cl-b (see section 4.3.1 for description) is obtained. However, for 110-2Cl-b the out-of-plane deformation is not well described (probably due to the lack of torsional interaction in LCBOP) which leads to an underestimation of E_{ad}/Cl for the potential.

Trapping at surface vacancies can also be described by the potential. For monovacancies, E_{ad}/Cl is underestimated. This is again due to the lack of torsion terms in LCBOP, thus the energy increase caused by the deformation of the lattice is underestimated. Trapping at a divacancy is less favorable in good agreement with the DFT calculations.

The repulsive interaction of Cl in bulk graphite is well described, a more detailed discussion can be found in section 5.2.1. Cl trapped at monovancies is stable at the DFT level, whereas an optimization with the potential yields an unstable final state for the α-vacancy (however, the β-vacancy is well-described) . It should be noted, that this is more likely due to the implementation of the concerted optimization of the cell and atoms in LAMMPS which is not fully equivalent to implementations for *ab initio* calculations. Moreover, during a NPT simulation at 300 K and 1.013 bar the average potential energy for a Cl trapped at a vacancy is

lower than for a vacancy alone. Thus, for the MD runs trapping is observed. For a divacancy, the trapping is unstable as for DFT.

Table 5.8: Comparison of the chlorine adsorption energy (E_{ad} in eV/Cl atom) on the different graphite surfaces with respect to the number of adsorbed Cl atoms for the potential and the DFT results of section 4.3.1.

System	Nb. of Cl	Conf.	Potential	Reference
(001)	1		-0.87	-0.87
(100)	1	-	-4.14	-4.12
	2	-	-3.97	-3.89
(110)	1	-	-3.18	-3.10
	2	a	-3.69	-3.48
		b	-3.20	-2.50
Vac-(001)	1	-	-4.19	-2.49
Divac-(001)	1	-	-0.86	-1.10
Bulk	1	-	2.48	$2.76^a/3.18^b$
Vac(α)-Bulk	1	-	0.36	-0.64
Vac(β)-Bulk	1	-	-0.59	-0.59
Divac-Bulk	1	-	1.19	0.69

^{a} PBE; ^{b} PBE0

Dispersion Interactions

A comparison between the MP2 interaction potential and the fitted potential of the coronene/Cl_2 system is shown in Figure 5.3. The overall shape of the MP2 curve is well reproduced. The exponential form of the Morse potential is able to describe the repulsive part accurately. The region around the equilibrium is slightly shifted to smaller distances, the adsorption energy and equilibrium distance are -0.281 eV and 3.45 Å compared to -0.284 eV and 3.39 Å for MP2. Finally, the asymptotic behavior is also correct.

As discussed in section 4.3.1, Cl_2 does not dissociate on the (001) surface contrary to its behavior in bulk graphite. To ensure that this behavior is correctly described by the fitted potential, the diffusion of Cl_2 on the (001) surface was simulated in the NVT ensemble at 300 K. On a surface of 120 Å × 120 Å 114 Cl_2 molecules were randomly distributed. In Figure 5.4, the radial distribution functions (RDF) for C-Cl and Cl-Cl pairs are shown. The RDF for C-Cl is zero for distances lower than about 3.0 Å, thus no covalent bonds are formed with the surface which is the correct behavior. The first peak corresponds to the average C-Cl distance between the Cl_2 molecule and the (001) surface of graphite (the

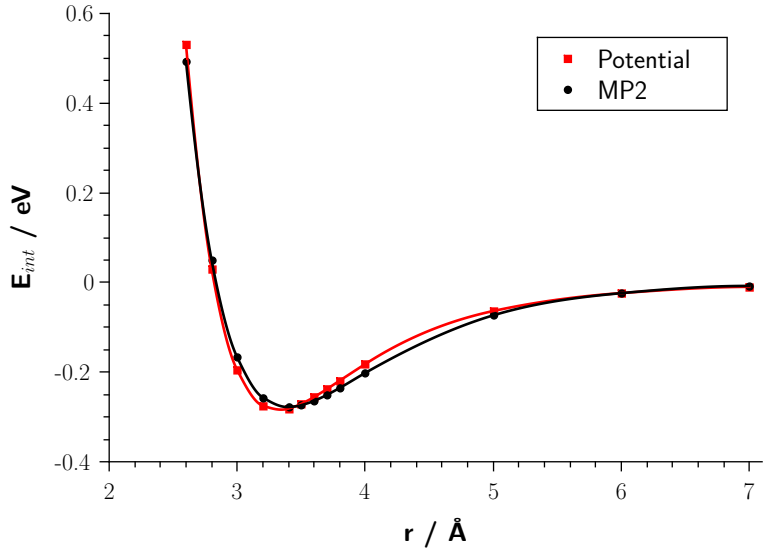

Figure 5.3: Interaction energy (E_{int}) curve of the coronene-Cl_2 system obtained with MP2 (black curve) and the fitted potential (red curve).

first graphene layer), the second peak to the average C-Cl distance between the Cl_2 molecule and the graphene layer below the (001) surface (the second graphene layer). Considering the RDF for Cl-Cl, it can be seen that the first peak has its maximum at about 2.0 Å which is the equilibrium distance of Cl_2. Since the concentration of Cl_2 was sufficiently diluted, no distinct features can be found for larger distances.

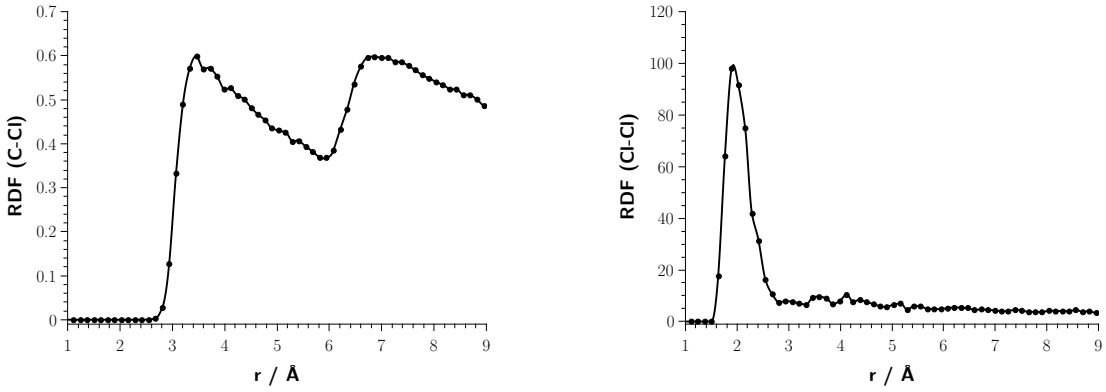

(a) (b)

Figure 5.4: RDF for a) C-Cl pairs and b) Cl-Cl pairs for a diffusion simulation of Cl_2 along the (001) surface.

Charge Transfer Interactions

A comparison of the calculated and the fitted potential can be found in Figure 5.5. The equilibrium properties are quite well reproduced (see Table 5.8); the charge transfer interaction is only underestimated by 2 meV, whereas the equilibrium distance is underestimated by 0.19 Å. However, the generalized force shifted potential is not able to describe the long-range interaction at larger distances due to its cutoff which is a compromise between accuracy and computational performance. A higher cutoff would certainly improve the long-range behavior, but comes at a higher computational cost. The computational time scales approximately with N^2 where N is the number of particles due to the double sums over atoms i and j.

To validate the chosen cutoff for the potential, the diffusion along the (001) surface was simulated for the temperature range of interest for this study. The RDFs are shown in Figure 5.6. The overall shape of all curves is the same; the decreasing intensity with increasing temperature is due to the formation of Cl_2. As explained in section 4.3.1, Cl_2 adsorbed on the (001) surface is more stable. However, since it interacts only weakly with the surface it is also easily desorbed. Thus, for an increasing temperature the number of Cl_2 molecules in the gas phase increases and the number of adsorbed Cl atoms decreases as it should be expected from the *ab initio* results.

This shows that the potential is able to describe the equilibrium properties in the temperature range that is relevant to the study. However, it should be noted that at higher temperatures, desorption processes might occur also for the Cl species that would not be found with a potential that describes the correct long-range behavior; *i.e.* the present model potential overestimates the importance of desorption processes with increasing temperature.

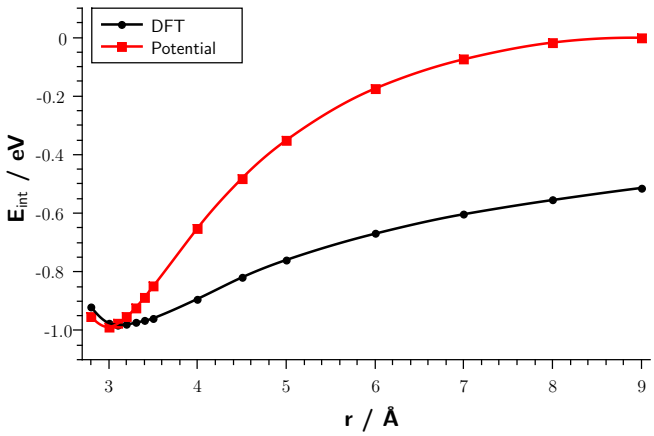

Figure 5.5: Interaction energy (E_{int}) curve of the graphite-Cl system obtained with DFT (black curve) and the fitted potential (red curve).

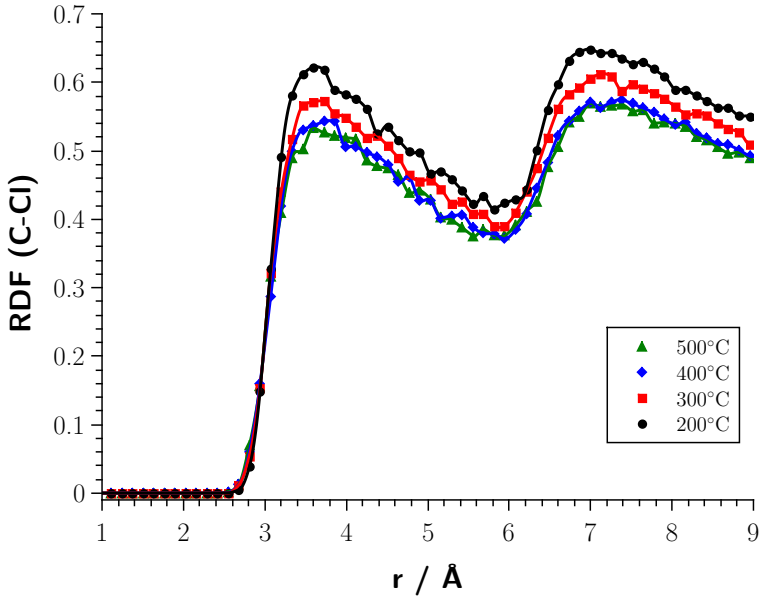

Figure 5.6: RDF for C-Cl pairs for a diffusion simulation of atomic Cl on a (001) surface for the studied temperature range.

Bulk Dissociation

As shown in section 4.3.3, Cl_2 dissociates in bulk graphite during the geometry optimization which is performed at 0 K. Thus, Cl_2 can be considered to be fully dissociated under reactor conditions where the temperature is at least 150°C as well as for permanent disposal conditions. To validate the developed potential for this dissociation process, the diffusion of Cl_2 in bulk graphite in was studied. After an initial equilibration phase of 5 ps in the NPT ensemble at 300 K and 1.013 bar, the RDFs were determined in the NVT ensemble at 300 K and are shown in Figure 5.7. At the start of the simulation Cl_2 molecules were created, but as can be seen, the RDF for Cl-Cl pairs is zero below a distance of about 2.6 Å (2.7 Å is the cutoff for covalent Cl-Cl interactions). Thus, all Cl_2 dissociates in the equilibration phase as it is expected from the DFT results. The first peak is at 3.2 Å, well beyond the cutoff of covalent interactions. From the RDF function for C-Cl pairs in Figure 5.7, it can be concluded that also no covalent bonds are formed with carbons of the graphite matrix, since this function also is zero for distances below the covalent cutoff.

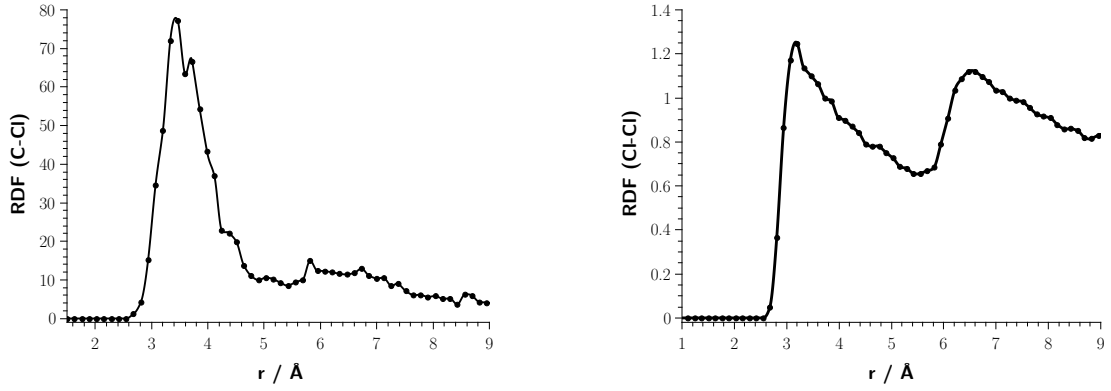

(a) (b)

Figure 5.7: RDF for a) C-Cl pairs and b) Cl-Cl pairs for a diffusion simulation of Cl_2 in bulk graphite.

5.2.2 C-H Potential

In Table 5.9, the adsorption energies of hydrogen on the different surfaces are given and compared to the DFT results. As can be seen, it works very well for surfaces with dangling bonds. It also reproduces the correct order of stabilities for the (100) and (110) surface.

Table 5.9: Comparison of the hydrogen adsorption energy E_{ad} in eV on the different graphite surfaces for the potential and the DFT results of section 4.2 as reference.

System	Potential	DFT
(001)	-1.5	-0.8
(100)	-4.5	-5.0
(110)	-3.8	-3.7
Vac(α)	-3.9	-4.2

However, adsorption on the (001) surface is not correctly reproduced. It is overestimated by a factor of 2. This alone would be acceptable for a semi-empirical potential. The barrier for chemisorption is shown in Figure 5.8 and compared to the barrier calculated with the PBE functional. The PBE barriers of about 0.3 eV agrees with the literature values of 0.2-0.3 eV [ŠRH$^+$09, IZTB$^+$10]. The height of the barrier with respect to the van der Waals minimum is only about 0.1 eV higher and shifted to a shorter C-H distance by about 0.2 Å compared to the DFT barrier. These features also agree reasonably well with the DFT results. Figure 5.8 also shows the force acting along the C-H bond for the two potential curves

which give more insight. The DFT potential for this reaction is much smoother. When the H atom approaches the surface, a repulsive force arises as soon as the C-H distance decreases below the van der Waals minimum at about 3.0 Å up to the transition state at about 1.8 Å. However, for the potential this force is almost zero up to the cutoff of the covalent interaction at 1.8 Å. Below this distance the repulsive force is six times higher than for the DFT potential. Due this rapid change in the force, the barrier is rarely overcome. In fact, this rapid arisal of a repulsive force rather leads to a deformation of the (001) surface toward the bulk since the acting forces in this direction are only weak van der Waals forces.

This analysis also offers a solution. In order to smoothen the forces, the cutoff for covalent C-H bonds needs to be increased (and parameters refitted accordingly). Bachellerie *et al.* [BSA+09] used this approach (among other modifications) to study the Eley-Rideal formation of H_2 on graphene. However, this modification restricts the applicability of this potential since it was adapted to work on graphene. Thus, the amelioration of the chemisorption on the (001) surface can impact the performance on other sites which were well-described by the original potential. In order to resolve this issue, separate cutoffs for the surfaces with and without dangling bonds should be used.

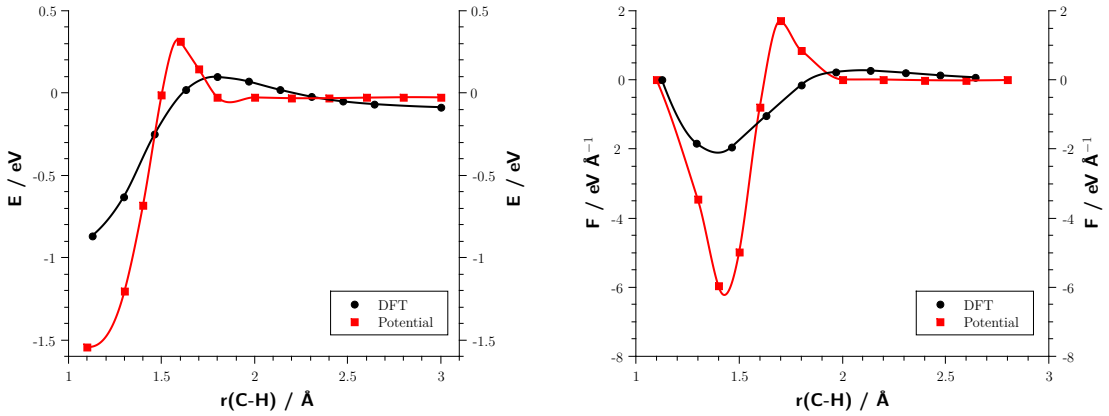

(a) (b)

Figure 5.8: a) Potential energy curve and b) force curve with respect to the C-H bond length for chemisorption of H on the (001) surface calculated with the PBE functional and the AIREBO/M potential.

The diffusion in bulk graphite leads to the same issues. This is not surprising since there is no difference in covalent C-H interactions between the (001) surface and a basal plane of graphite within the framework of the AIREBO potential. In diffusion simulations, H strictly propagates between graphene layers and never forms a covalent bond when starting from this state. When starting from a covalent

C-H bond, it either remains bonded to the same C for the whole simulation or dissociates and does not form a new covalent bond. Thus, the expected behavior obtained by tight binding simulations [HR10], which shows that H hops between two adjacent planes, is never observed.

5.3 Summary and Conclusion

A bond order potential for C-Cl and Cl-Cl interactions in graphite, which covers all possible interactions types, has been developed from scratch. Modifications to the LCBOP potential have been made to account for Cl neighbors; C-Cl and Cl-Cl interactions are described by an AIREBO-type potential. The potential is able to describe processes that have been obtained at the *ab initio* level, such as trapping on crystallite edges (surfaces (100) and (110)) and charge transfer interactions on the (001) surface. Complex interactions, which can usually only be obtained at the *ab initio* level, are also well reproduced; Cl_2 dissociates in bulk graphite, whereas it is formed from atomic Cl on the (001) surface. Overall, these results show that the potential can be used with confidence and be applied to more complex systems to study insertion and diffusion processes on a larger scale.

The existing AIREBO/M potential is not able to fully describe the interactions of hydrogen and graphite. Adsorption on surfaces with dangling bonds is well-reproduced. However, the covalent on the (001) surface and in bulk graphite are not well-described due to a barrier with overestimated repulsive forces. Thus, it should correctly describe diffusion on surfaces (100) and (110) for a low gas density of hydrogen. At this stage, diffusion on the (001) surface as well as in bulk can not be described correctly.

Chapter 6

Modeling the Interaction of ^{3}H and ^{36}Cl of Nuclear Graphite - Large-scale Molecular Dynamics Simulations of Complex Models

This chapter is dedicated to the application of the *ab initio* results and the potential development to study the properties of radionuclides in nuclear graphite on a large scale. This constitutes the final part of this multi-scale approach. First, the methodology is presented. In the following, the insertion and diffusion of ^{3}H and ^{36}Cl in nuclear graphite are reported. The effects of irradiation and temperature on the microstructure of bulk graphite, several surfaces of graphite and a grain boundary are discussed. By treating the radionuclide as primary knock-on atom (PKA), several aspects can be studied. Classically the PKA describes the atom which is hit by a neutron (or other particles such as electrons) and then starts a cascade by colliding with other atoms of the matrix. Experimentally, atoms are often implanted into graphite to study the microstructural damage of the matrix as well as their diffusion properties in the irradiated material. Both these cases can be investigated with the performed simulations and will be collectively called irradiation simulations. The investigated PKA energy for irradiation ranges from 0.5-10 keV and the temperature from 200-500°C. The temperature range was chosen since the graphite temperature in the reactor was close to this range (the maximum temperature was 450°C in BUA1). In addition to irradiation simulations, the diffusion properties along crystallite edges as well as in the nanopores of nuclear graphite are presented and its temperature dependence is explored. Finally, the results are summarized and conclusions are drawn.

6.1 Methodology

The developed potentials presented in the previous chapter were applied for all simulations. To this end, the software LAMMPS [Pli95] was used. A cutoff for non-covalent interactions of 10.5 Å was applied for the simulations with C and Cl atoms. For the interaction between C and H atoms the Morse cutoff was 10.2 Å. In the following, the different structures used in this study are presented. After that, the different simulation protocols are explained.

6.1.1 Structure Generation

In Table 6.1, the sizes of the different simulation boxes for bulk graphite and the different surfaces are given. Figure 6.1 shows top and side views of the different studied surfaces. All simulations were performed with periodic boundary conditions in all three dimensions. A vacuum slab is needed to allow for swelling in the **c**-direction for irradiation of the (001) surface and removal of carbon atoms that detached sufficiently far from the surface (see section 6.1.2 for details). The thickness is about 75 Å and also given in Table 6.1. For the sake of consistency, a vacuum slab with the same thickness was added to the other surfaces.

For the model of bulk graphite, the **c**-direction of the lattice is parallel to the z-axis of the simulation box. Surfaces were always oriented such that the plane defined by the surface atoms was perpendicular to the z-axis of the box (see Figure 6.1 for the relative orientation with respect to Cartesian axes).

Table 6.1: Dimensions of the small (s) and large (l) simulation boxes in Å, thickness of the vacuum slab (Vac) in Å, and number of C atoms N_C for each model system.

System	Size	x	y	z	Vac	N_C
Bulk	s	100	100	100	-	118080
	l	300	300	300	-	2848320
(001)	s	120	120	185	75	190400
	l	330	330	400	75	4073472
(100)	s	120	120	205	75	219600
	l	310	310	380	75	3315312
(110)	s	120	120	200	75	207648
	l	310	310	375	75	3149280
$(100)_{rec}$	s	120	120	190	75	203904
	l	310	310	380	75	3387384
$(110)_{arch}$	s	120	120	200	75	207638
	l	310	310	375	75	3149228
Grain boundary	-	145	125	215	75	279680

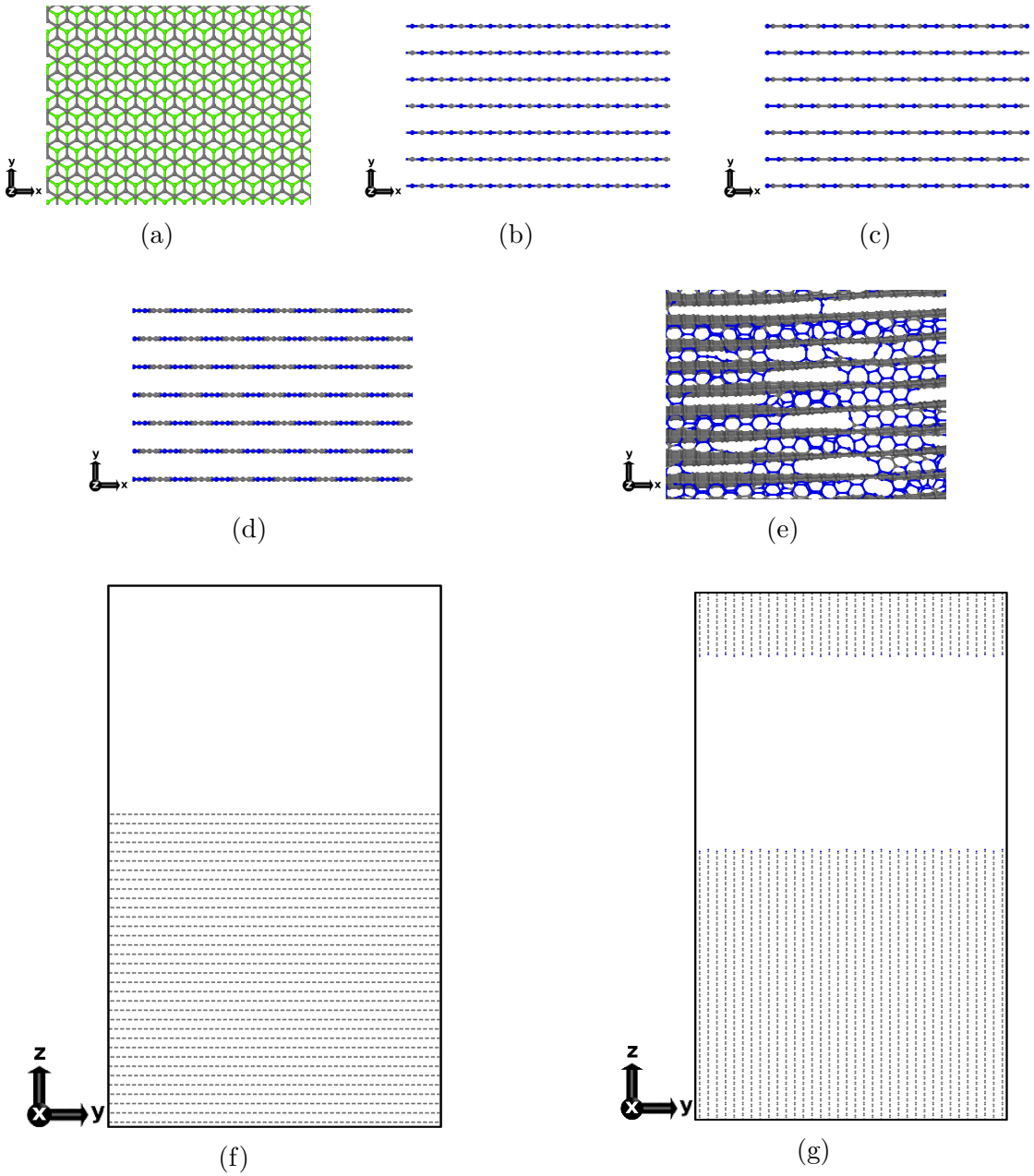

Figure 6.1: Top view of a) the (001) surface (the second layer is green for better visibility), b) the (100) surface, c) the (110) surface, d) the $(100)_{rec}$ surface, and e) the $(110)_{arch}$ surface. Side view of the small systems of f) the (001) surface and g) the (100) surface. Blue atoms are defects as defined in section 6.1.4.

Surfaces (100) and (110) terminated with the same pattern as shown in Figure 4.7 in section 4.2.1. In addition, two reconstructed surfaces were studied: the in-plane reconstruction of the (100) surface called $(100)_{rec}$ (see Figure 4.9a) and an arch-type reconstruction called $(110)_{arch}$.

The arch-type reconstruction was created by simulated annealing of the systems describing the (110) surface. Annealing temperatures ranging from 2500 to 3500 K and annealing times ranging from 0.5 to 3 ns were tested for the small system of the (110) surface. With the simulation protocol presented in the following an arch-type reconstruction was created where the majority of surface carbon atoms formed bonds across the planes, but which also is computationally efficient enough to create the large system of the $(110)_{arch}$ surface (which has over 3 million atoms). A temperature profile of the optimized simulation protocol is shown in Figure 6.2.

After an initial optimization, the system was equilibrated for 2.5 ps (timestep = 0.5 fs) in the NPT ensemble at 300 K and pressure of 1.013 bar. The barostat was only applied in the x- and y-directions to keep the vacuum thickness constant. The lowest layer of carbon atoms in the z-direction was fixed to keep the planes from moving toward the vacuum. Then the system was heated to 3000 K at a rate of $1.08\times10^{13}\,\mathrm{K\,s^{-1}}$. The timestep was reduced to 0.2 fs. The system was annealed for 1.5 ns at 3000 K. Then it was cooled to 300 K at a rate of $1.0\times10^{12}\,\mathrm{K\,s^{-1}}$; after reaching this temperature the run was continued for 2.5 ps and finally optimized. Before further use, all carbon atoms in the vacuum were removed.

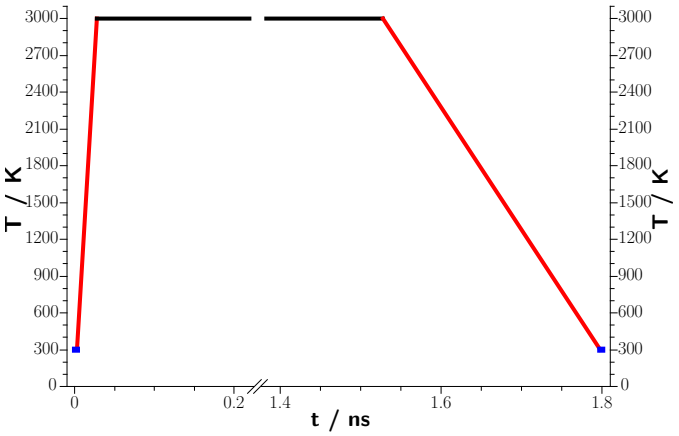

Figure 6.2: Temperature profile for the creation of the $(110)_{arch}$ surface. Equilibration steps are blue, heating/cooling steps are red, and annealing is black. Note the x-axis break in the annealing step.

The grain boundary was created using a modified version of a script for optimization of Mg grain boundaries [mgs] and is shown in Figure 6.3. This script varies the distance between grains and the cutoff for removal of overlapping atoms in an iterative fashion to obtain the grain boundary. Small manual adjustments were applied to the lowest energy structure to obtain the grain boundary.

The nanoporous polycrystalline system was obtained from Alain Chartier and Laurent Van Brutzel [CB] and is shown in Figure 6.4. It consists of 20 graphite

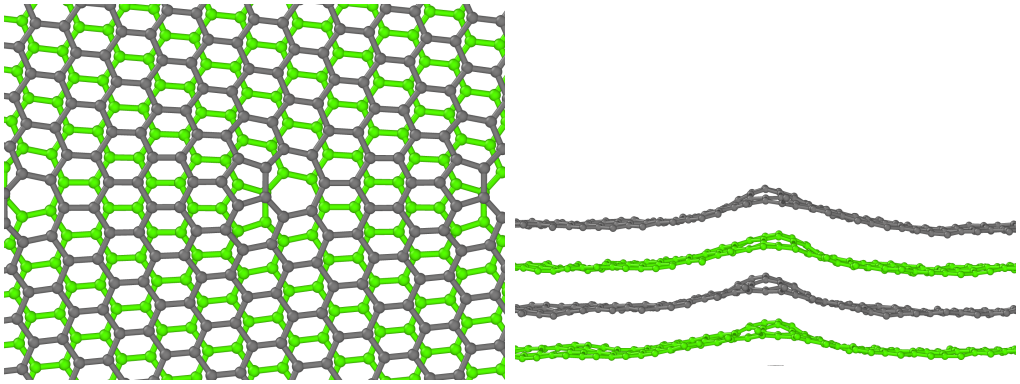

(a) (b)

Figure 6.3: a) Top view of the grain boundary and b) side view perpendicular to the grain boundary.

crystallites measuring 350×350×150 Å (in x-, y-, and z-directions) each. The crystallites have a random relative orientation which varies in the range of 0-20°.

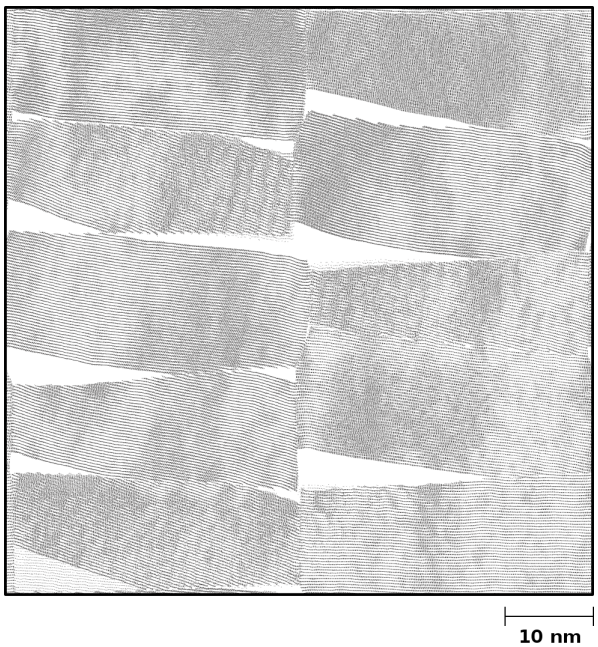

Figure 6.4: Side view of the nanoporous polycrystalline graphite model.

OVITO was used for the visualization of structures and trajectories [Stu10].

6.1.2 Irradiation Simulations

In general, all irradiation simulations were performed by using the same simulation protocol. It will be explained for bulk cascades; differences for surface irradiations will be explained further down. A simplified flowchart is shown in Figure 6.5. The bulk cascades were simulated at 200, 300, 400, and 500°C and PKA energies of 0.5, 1.0, 2.5, and 10 keV. The small systems of Table 6.1 were used for PKA energies of 0.5 and 1.0 keV, the large ones for the higher two energies. After an initial optimization, the system was equilibrated for 2.5 ps with a timestep of 0.5 fs in the NPT ensemble and 1.013 bar and the appropriate temperature. A Nosé-Hoover thermostat and barostat were applied. The initial position of the PKA (Cl atom) was chosen in a way that it would move toward the center of the box during the cascade without exiting the simulation box. Its x- and y-force components were set to zero in the equilibration phase to avoid diffusion.

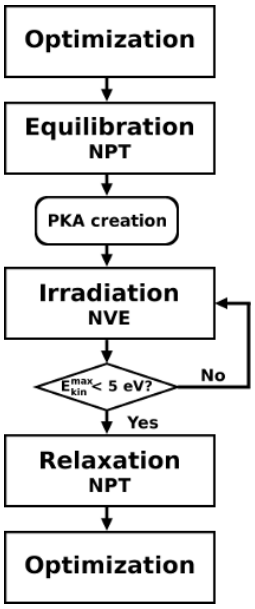

Figure 6.5: Flowchart of a singular bulk displacement cascade and surface irradiation, respectively. Note that in the case of a bulk cascade the PKA is created at the beginning of the simulation.

After equilibration, a velocity equivalent to the kinetic energy was assigned to the PKA. In Table 6.2, the x-, y-, and z-components of the 10 sampled directions are given for bulk cascades. Different directions need to be sampled since the neutron irradiation in the reactor is omnidirectional. The directions were chosen following the approach of Ref. [CRR+15]. Here, the directions are deduced from the solution of the Thomson problem which describes the configuration of N electrons constrained to the surface of a unit sphere with the lowest Coulomb repulsion. For 10 electrons, it takes the form of a gyroelongated square bipyramid. The cascade is performed by using a standard approach for displacement cascades [BC07, BN07, CRR+15]. The NVE ensemble is applied so that the PKA is strictly

Table 6.2: x-, y-, and z-components of the PKA directions.

Direction	x	y	z
1	0.6078	0.6078	0.5111
2	0.6078	-0.6078	0.5111
3	-0.6078	0.6078	0.5111
4	-0.6078	-0.6078	0.5111
5	0.0	0.8595	-0.5111
6	0.0	-0.85953	-0.5111
7	0.85953	0.0	-0.5111
8	-0.85953	0.0	-0.5111
9	0.0	0.0	1.0
10	0.0	0.0	-1.0

slowed down by collisions with the matrix. Velocity rescaling was applied to a 3 Å thick layer at the edges of the box to remove excessive heat. A flexible timestep was used in this stage as implemented in LAMMPS. Within this method, the timestep was adjusted so that no atom would move more than 0.01 Å between two timesteps. The advantage of this approach is a very accurate time integration in the initial stage where the PKA has a much higher velocity than other atoms but a significant speedup for the later stage where it has already slowed down. When the maximum kinetic energy per atom has dropped below 5 eV, additional 2000 timesteps were performed to ensure that the equilibrium was reached within the NVE ensemble. Finally, the system was equilibrated for 1 ps in the NPT ensemble with a timestep of 0.5 fs to remove excessive heat and stress. In the flowchart this is called relaxation to distinguish this step from the initial equilibration. For post treatment, a final optimization was performed.

For surface irradiations, the PKA was placed in the vacuum 3-4 Å above the surface. The x- and y-coordinates were assigned randomly in a way that it would move toward the center of the surface (see Figure 6.6 for a description) and it would be separated at least 30 Å from the boundaries of the box. For the equilibration phase in the NPT ensemble, the barostat was only applied in the x- and y-directions to keep the vacuum layer constant. In contrast to bulk graphite, the surfaces tend to drift in the z-direction after irradiation. This was avoided by fixing a layer of carbon atoms the furthest away from the surface by setting their velocities to zero and excluding them from time integration. Irradiation simulations were performed 10 times in each of the directions 5, 6, 7, 8, and 10 of Table 6.2. Direction 10 only has a z-component, thus it corresponds to an incident angle of 90° with respect to the surface. Directions 5 and 6 have a y- and z-component, whereas directions 7 and 8 have a x- and z-component. Except for the (001) surface, the graphene

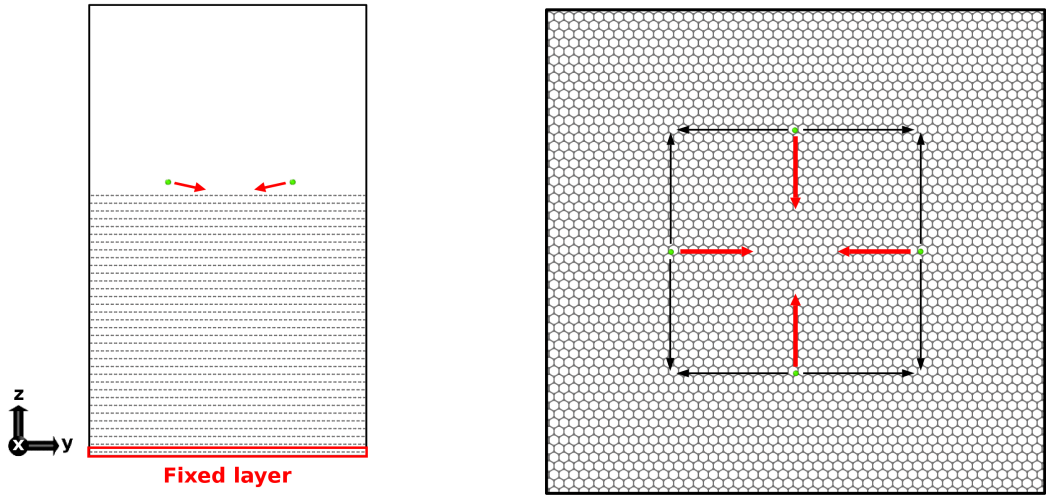

(a) (b)

Figure 6.6: a) Side view of the (001) surface. The fixed layer lies within the red box. The red arrows describe the PKA directions with respect to the relative positioning of the PKA. b) Relative positioning of PKAs in the xy-plane for the different PKA directions. The black arrows indicate the maximum allowed variation for the randomly created PKAs. The red arrows indicate the PKA direction. Note that for both pictures, direction number 10 is omitted for the sake of visibility. For this PKA direction, the position in the xy-plane is randomly chosen in the area bounded by the eight shown black arrows.

planes lie in the xz-plane (see Figure 6.1). Thus, these directions cover two extreme cases: a PKA hitting the surface in the graphene plane direction or perpendicular to it. In both cases the incident angle is <90°, for a perfectly flat surface it corresponds to an incident angle of ≈ 60° (measured between the normal vector of the surface and the velocity vector of the PKA). Since the surfaces are not frozen during the simulations, the incident angle can vary due to thermal vibrations of surface atoms. Thus, in the following these directions will be collectively called irradiation with an incident angle <90°. Atoms that detached from the surface more than 15 Å were continuously removed from the simulation and counted as defect atoms (see section 6.1.4). The surface irradiations were simulated at 200°C and 500°C.

For repeated surface irradiation of the (001) surface and grain boundary, the same protocol was used in an iterative fashion. A simplified flowchart is shown in Figure 6.7. Each of the different simulations explained in the following was performed 5 times. After equilibration in the NPT ensemble, the irradiation was performed in the NVE ensemble (velocity rescaling was again applied to a 3 Å thick layer at the periodic boundaries). At the end of the cascade a NPT run was

again performed, followed by another irradiation in the NVE ensemble. A total of 200 consecutive irradiations were performed. For irradiation of the (001) surface, the small system of Table 6.1 was used.

PKAs were randomly created in a center region at the beginning of each iteration. Their initial positions were at least 30 Å from all edges of the periodic box and 3-4 Å above the surface. The PKA's kinetic energy was randomly assigned in the range of 0.5 to 2.5 keV. Two different cases were explored. For the first simulation type, the PKA's initial velocity was always exactly perpendicular to the surface (direction 10). For the second, the incident angle was varied randomly by assigning an initial velocity in a way that the vector would point to a random position in a core region. This position could vary at most ± 15 Å from the center of the surface. Atoms that detached from the surface more than 15 Å were continuously removed from the simulation and counted as defect atoms (see section 6.1.4). The full simulation is roughly equivalent to a fluence of 4×10^{14} at. cm^{-2}. Experimental implantation of Cl was performed at a comparable fluence ranging from 5×10^{13} to 2×10^{16} at. cm^{-2} [VTM+09, BMT+14].

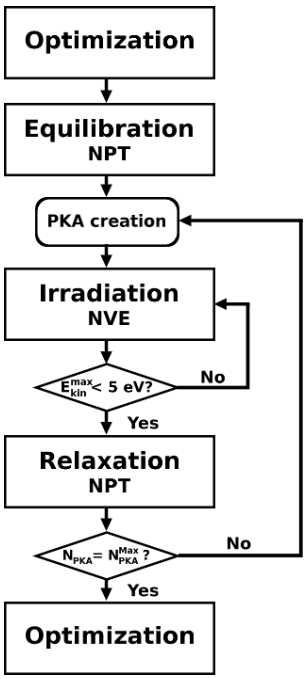

Figure 6.7: Flowchart of a repeated (001) surface and grain boundary irradiation, respectively.

6.1.3 Diffusion Simulations

Diffusion simulations along the crystallite edges were performed at temperatures of 200°C and 500°C. The graphite model was in all cases identical to the models used for irradiations at 0.5 and 1 keV. Cl or H atoms were created randomly in the vacuum space. The system was optimized and then equilibrated for 12.5 ps with a timestep of 0.5 fs in the NPT ensemble at 1.013 bar at the appropriate temperature. The barostat was only applied in the x- and y-directions to keep the vacuum layer constant. After this phase, a production phase of 0.5-1.0 ns was performed in the NVT ensemble. In this phase the mean square displacement (MSD) of the radionuclide (RN) was calculated. Each simulation explained in the following was performed five times.

The concentrations of the RN were 1 at.%, 0.1 at.%, and 0.01 at.% for Cl and 0.1 at.%, and 0.01 at.% for H (thus about 20, 200, and 2000 atoms). For simulations with Cl, an occupation number is defined. Only surface carbon atoms with dangling bonds can become occupied. For "occupied" carbon atoms only the repulsive part of the C-Cl potential is accounted for, thus covalent bonding between an occupied C and a Cl is prohibited. The occupation number is then the ratio between the number of occupied carbon atoms and the total number of surface carbon atoms with dangling bonds. The number of surface carbon atoms with dangling bonds are 3600, 4032, and 3456 for the (100), (110), and $(100)_{rec}$ surfaces, respectively. Simulations were performed with occupation numbers of 0.0, 0.9, 0.99, and 0.999.

The diffusion constant was obtained from the slope of the MSD of Cl atoms.

For diffusion in nanoporous graphite, the same protocol was used. The simulated temperatures were 200°C, 300°C, 400°C, and 500°C, the RN concentration was 10 ppm, and the occupation number was set to 0.999. The Cl atoms were randomly created in the porous zones with a distance of at least 10.0 Å with respect to any other atom. Due to the large number of atoms (over 3.6×10^7 atoms) and the high computational demands, only one simulation per temperature was performed.

6.1.4 Post Treatment

Defect Count

For all cascade simulations, the number of created defects was determined following the approach proposed by Chartier *et al.* [CBPB15]. The coordination number of each carbon atom was determined using a cutoff of 1.85 Å. Carbon atoms with a coordination number $\neq 3$ were counted as defects. In addition, carbon atoms with a coordination number of 3 which are not part of a graphene plane need to be taken into account. A curvature parameter is defined to differentiate between

sp^2-hybridized carbon atoms of a graphene plane and defective carbon atoms with three bonds. For each carbon i with three neighbors (1,2, and 3), the plane which is spanned by the three neighbors is determined. Then, the normal vector $\mathbf{a_i}$ of this plane is assigned to atom i. The curvature of each atom is determined by comparing its vector $\mathbf{a_i}$ to its neighbor vectors $\mathbf{a_1}, \mathbf{a_2}$, and $\mathbf{a_2}$. This is conducted by calculating the average of the scalar product between the vectors as follows:

$$\cos\theta_i = \frac{1}{3}\sum_{j=1,3}\frac{|\mathbf{a_i}\cdot\mathbf{a_j}|}{\|\mathbf{a_i}\|\|\mathbf{a_j}\|}. \tag{6.1}$$

The threshold is set to 32°, carbon atoms with a higher curvature are counted as defects. Chartier *et al.* derived this threshold from considering the curvature of different carbon species. By using this value, fullerene-like carbon atoms with a curvature of 29° would still be counted as regular sp^2-hybridized carbon atoms. The non-defective carbon atoms are in the following referred to as graphitic carbons atoms.

Defect Range

The defect range is an estimate of the extension of a cascade. It is defined as the maximum distance between two defects created in a cascade.

Histograms

Histograms of the number of defects were created with respect to the direction perpendicular to the surface. Bins with a width of 5 Å were used. The surface zero point was defined as the largest z-component of a graphitic surface carbon (which is defined by the previously mentioned curvature parameter $\cos\theta_i$, see section 6.1.4).

Heat Maps

The heat maps were created by dividing the surface into squares of the size 5 Å×5 Å in the xy-plane. Defects within the boundaries were assigned to the respective square regardless of their z-component. Thus, in the heat maps the number of defects is accumulated with respect to bulk depth. The presented heat maps are averages over the heat maps obtained from the five performed simulations.

6.2 Properties of ^{3}H in Nuclear Graphite

In this section, the focus is laid on the diffusion of H along surfaces with dangling bonds. These surfaces are models of crystallite edges. By using these models, the properties of the second trap of Kanashenko's hypothesis can be investigated.

6.2.1 Diffusion Simulations on the (100), (110), and Reconstructed Surfaces

In chapter 4.2, it was concluded that the model surfaces (100), (110), and $(100)_{rec}$ can all act as traps for hydrogen in nuclear graphite.

The diffusion of H along these surfaces was studied. In Figure 6.8, representative snapshots of diffusion simulations are shown. All three surfaces show the same behavior. At a concentration of 0.01 at.%, complete trapping of H is observed. This is possible since the number of available trapping sites is much larger than the number of H atoms and the gas density is sufficiently diluted. This is consistent with the *ab initio* results.

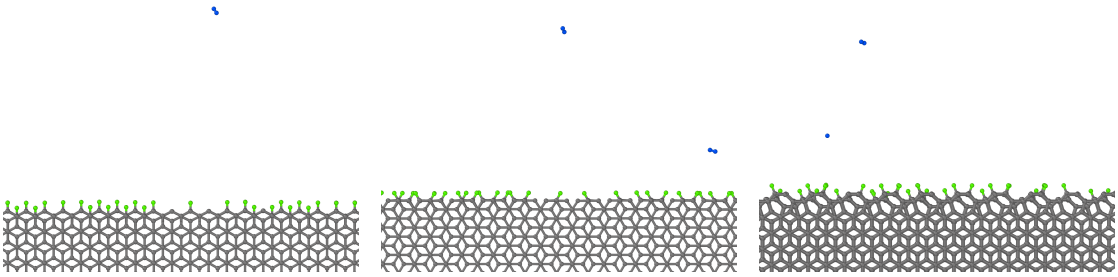

(a) (b) (c)

Figure 6.8: Snapshots of the diffusion simulations at 200°C and a H concentration of 0.1 at.% along the a) (100) surface, b) (110) surface, and c) $(100)_{rec}$ surface. Trapped H is shown in green, whereas gaseous H (in the form of H_2) is shown in blue.

Trapping of hydrogen is also observed at a concentration of 0.1 at.%. However, for all surfaces 2-3 % of the H atoms formed H_2 in the gas phase. For the length of these simulations (1 ns), these molecules were not trapped even though enough surface traps were available.

6.2.2 Discussion

The diffusion along the (100), (110), and $(100)_{rec}$ surfaces confirmed the *ab initio* findings. All three serve as strong traps for hydrogen. This is true for both studied temperatures (200°C and 500°C). For a H concentration of 0.1 at.%, small amounts of H_2 are formed. This indicates that breaking of the H_2 bond in order to trap on the surface involves a significant barrier.

Since the MD simulations also find trapping on the $(100)_{rec}$ surface, this further solidifies Kanashenko's hypothesis with respect to the second hydrogen trap of nuclear graphite.

These simulations could only be performed for low hydrogen concentrations to avoid bulk penetration (which is not correctly described). By using larger H concentrations, the ratio between H_2 and surface-trapped H could be studied as well as possible barriers involved in trapping reactions.

A correct description of bulk diffusion would be needed to study the interaction with dislocation loops which are found inside of graphite crystallites. Thus, as of now the location of Kanashenko's first trap remains inconclusive with respect to the performed simulations. An approach as described in section 5.2.2 would be needed in order to describe all possible interactions of H in nuclear graphite.

6.3 Properties of ^{36}Cl in Nuclear Graphite

This section explores the insertion and diffusion of ^{36}Cl in complex large-scale models of nuclear graphite. The effects of irradiation and temperature on the microstructure of bulk graphite, several surfaces of graphite and a grain boundary are discussed. In addition to irradiation simulations, the diffusion properties along crystallite edges as well as in the nanopores of nuclear graphite are presented and its temperature dependence is reported.

6.3.1 Displacement Cascades in Bulk Graphite

Displacement cascades in bulk graphite with Cl as a PKA were performed with initial PKA energies of 0.5, 1, 2.5, and 10 keV. This energy is transferred to the graphite matrix by collisions with carbon atoms. These collisions decrease the PKA energy and create lattice defects. This can be seen in Figure 6.9. Each large drop of the maximum kinetic energy constitutes a collision where a large amount of energy is transferred. The duration of a displacement cascade in graphite is much shorter compared to other materials, for a PKA energy of 10 keV it is on the order of 0.1-0.2 ps. These results agree with displacement cascades where carbon is the PKA [CBPB15, CRR$^+$15].

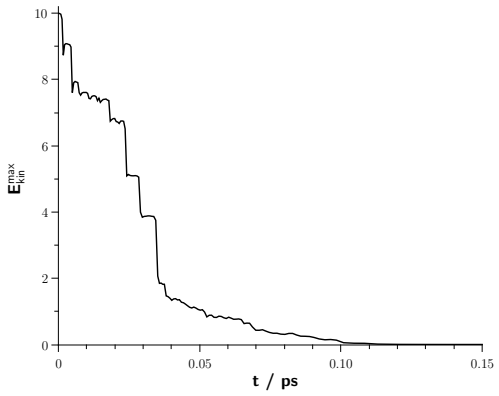

Figure 6.9: Maximum kinetic energy E_{kin}^{max} with respect to time in a displacement cascade.

In Figure 6.10 snapshots of a representative displacement cascade are shown together with the zz-component of the symmetric per-atom stress tensor and the per-atom kinetic energy. As the Cl atom passes through the graphene planes, kinetic energy is transferred to surrounding carbon atoms. Comparison of the per-atom stress tensor components and kinetic energies until 0.05 ps in Figure 6.10 shows a very similar picture. Atoms that experience significant forces also

have significant kinetic energies. Several carbon atoms become secondary knock-on atoms (SKA) and also initiate cascades. When the PKA's energy is no longer high enough to pass through a graphene plane (0.06 ps snapshot of Figure 6.10), a shock wave is created which propagates spherically through the layers (see stress tensor snapshots 0.05-0.45 ps of Figure 6.10). These forces are not strong enough to permanently displace carbon atoms. In the 4.0 ps snapshot of Figure 6.10 the system is in its equilibrium. The energy is almost exclusively stored in the defects which were created by the cascade since only these defects experience significant forces.

In Figure 6.11 the number of created defects and the defect range are shown with respect to the PKA energy for different simulation temperatures. They lie in the range of the graphite temperatures in the reactor. The total number of created defects is almost directly proportional to the PKA energy for the investigated energy range. The defect range saturates at 10 keV. At lower PKA energies almost no SKAs are created, thus the defect range is rather similar to the traveled distance of the PKA (since the largest defect distance is in most cases between the first and last defects created). For higher PKA energies, SKAs are created which significantly reduce the traveling distance of the PKA. However, they do mostly not contribute to the defect range as their cascades are shorter due to their lower energy.

In Figure 6.12 the defect count and the defect range are shown with respect to the simulation temperatures. No clear trend is found for increasing temperatures. For PKA energies up to 2.5 keV the number of created defects is almost constant, which is also the case for 10 keV when the error bars are considered.

The same is true for the defect range which is also rather constant with respect to temperature for all PKA energies when the error bars are taken into account.

Thus, no influence of the temperature is found for the number of created defects as well as the defect range for the considered temperature range of 200-500°C.

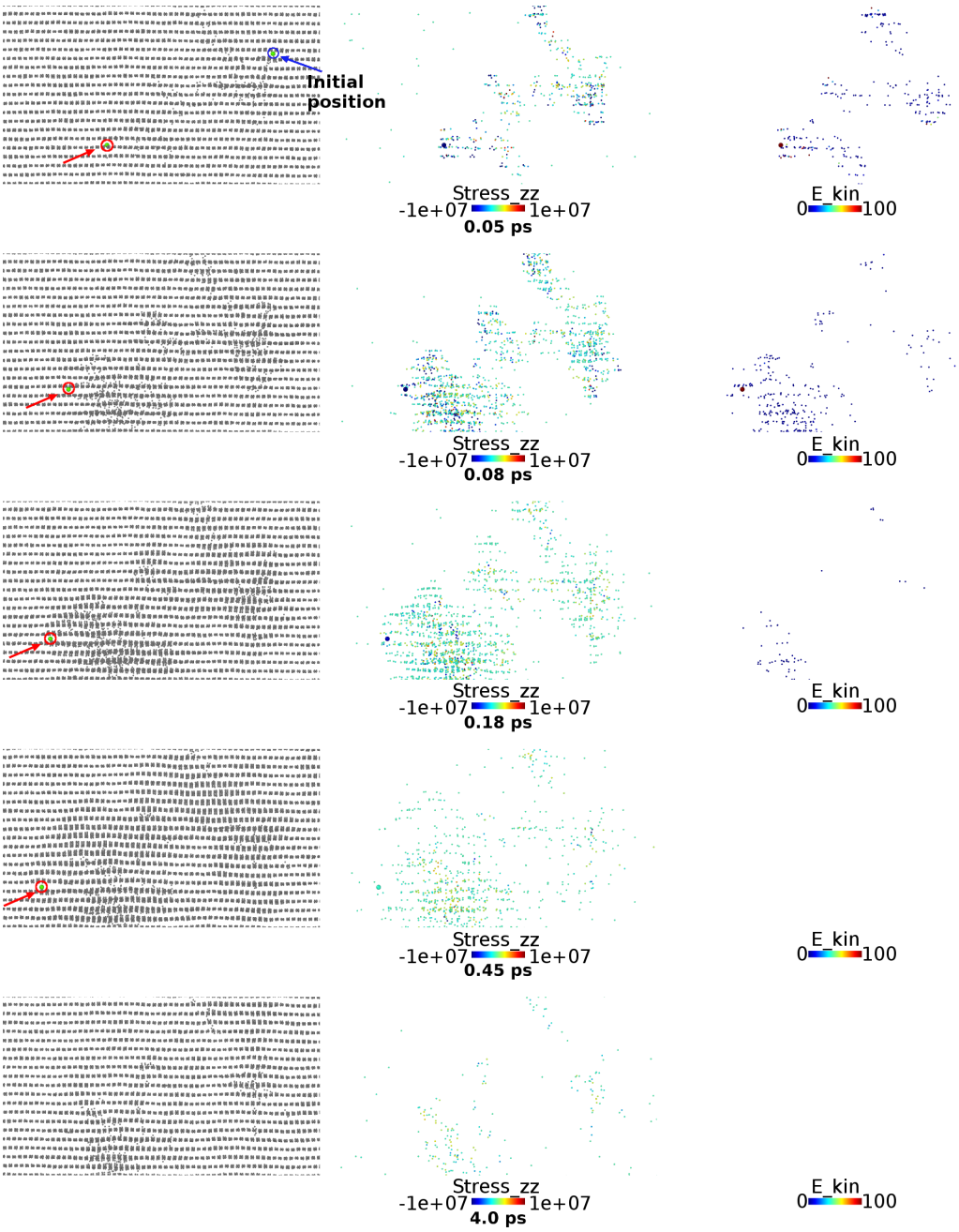

Figure 6.10: Snapshots of a representative displacement cascade with a PKA energy of 10 keV. For each timestep the left image shows the atom's positions, the center image shows the zz-component of the symmetric per-atom stress tensor in eV, and the right image shows the per-atom kinetic energy in eV. The PKA's position in each snapshot is marked by a red circle and arrow. In the first snapshot the initial position of the PKA is also shown (marked by the blue circle and arrow). Only particles with an absolute stress tensor $> 10^6$ eV and a kinetic energy > 2 eV, respectively are shown for better visibility.

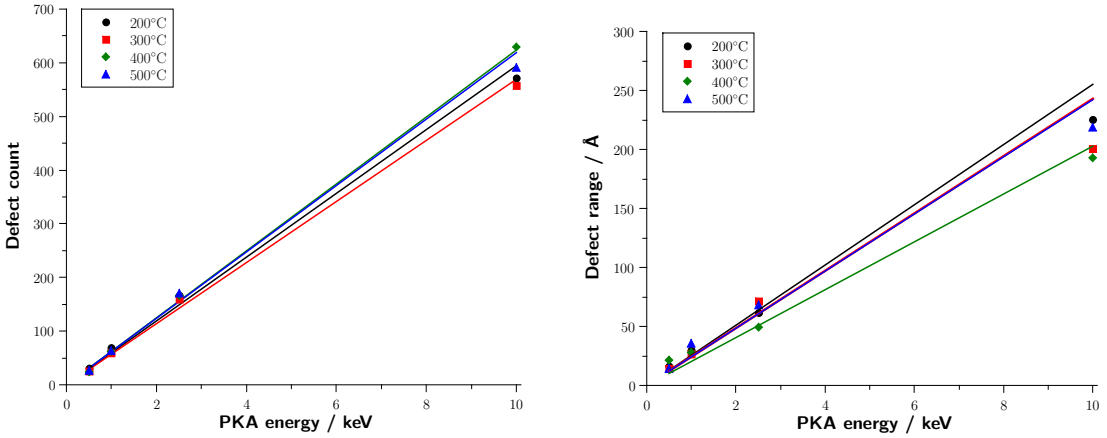

(a) (b)

Figure 6.11: a) Defect count and b) defect range of displacement cascades in bulk graphite with respect to the PKA energy. Solid lines are slope fits ($f(x) = ax$). Error bars were omitted for better visibility (see Figure 6.12).

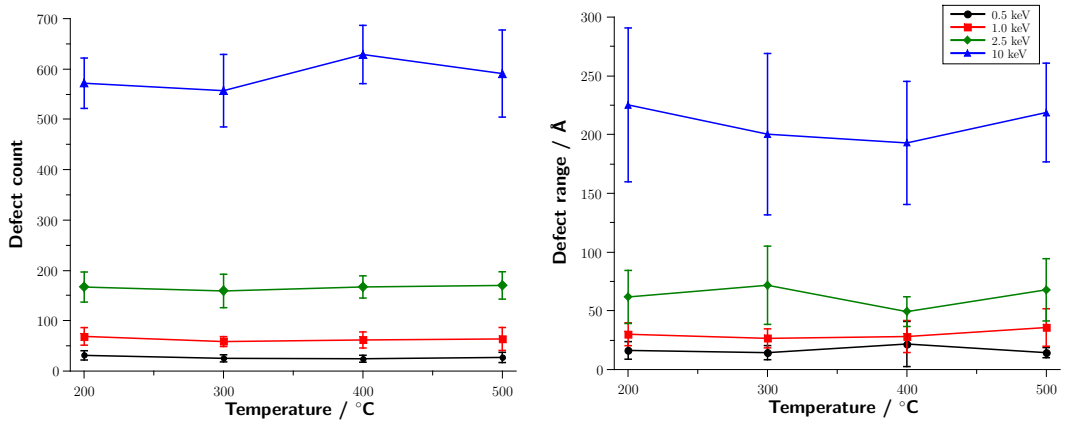

(a) (b)

Figure 6.12: a) Defect count and b) defect range of displacement cascades in bulk graphite with error bars with respect to the simulation temperature.

6.3.2 Irradiation Simulations of Surfaces

The irradiation of surfaces is quite different to the displacement cascades in bulk graphite presented in the previous section. In bulk graphite forces act on the PKA from all sides. On a surface this is no longer the case. Thus, several new factors have to be considered such as the type of surface as well as the PKA's incident angle. This will be presented in the following for the studied surfaces.

(001) Surface

In Figure 6.13, the defect count for irradiation of the (001) surface is shown for the sampled PKA directions. As seen in the previous section, the defect count increases almost proportionally to the PKA energy for the investigated energy range. Table 6.3 gives the slopes of the fits obtained for the different incident angles as well as a global average. The fit functions for all irradiation directions are very similar. At 2.5 keV and 200°C, irradiation along directions 7 and 8 seems to produce a higher amount of defects. However, this is not seen for any other energy or temperature, thus it might simply be an outlier.

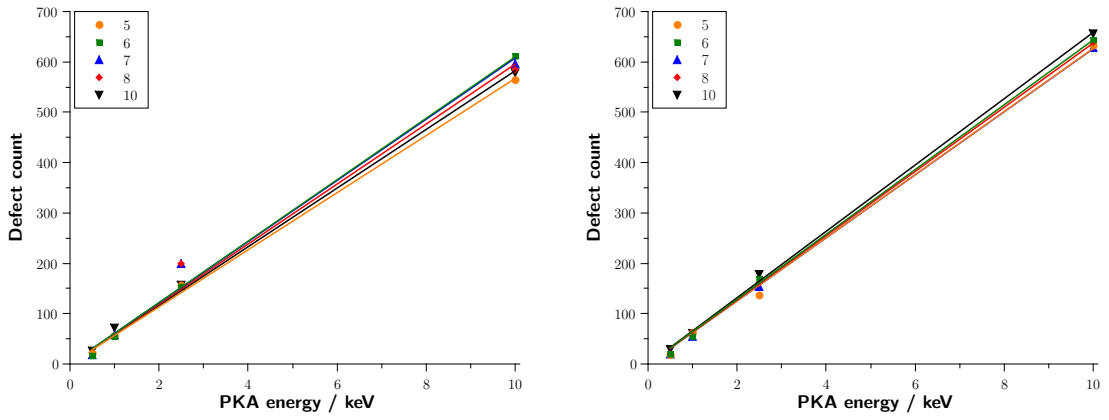

(a) (b)

Figure 6.13: Defect count with respect to the irradiation direction for a sample temperature of a) 200°C and b) 500°C.

Figure 6.14 shows the averaged results over all incident angles compared to the bulk results. As can be seen, the slope of the fit function for (001) surface irradiation is higher than for bulk defects. Compared to bulk cascades, less damage is created for PKA energies of 0.5 keV and 1 keV and more damage is created for 2.5 and 10 keV. This is true for all of the sampled directions.

Contrary to bulk graphite, a higher sample temperature seems to yield a larger amount of damage.

Table 6.3: Slopes of fit curves for the defect count vs. PKA energy obtained for irradiation of the different surfaces. The fits for incident angles of 90°, <90°, and a global average are given.

	90°		<90°		Average	
System	200°	500°	200°	500°	200°	500°
(001)	58.24	65.88	59.52	63.36	59.27	63.87
(100)	63.00	76.39	63.85	72.52	63.68	73.29
(110)	67.00	70.81	63.40	68.36	64.12	68.85
$(100)_{rec}$	61.47	70.63	64.64	66.70	65.43	65.72
$(110)_{arch}$	76.63	76.00	72.55	75.19	73.37	75.35

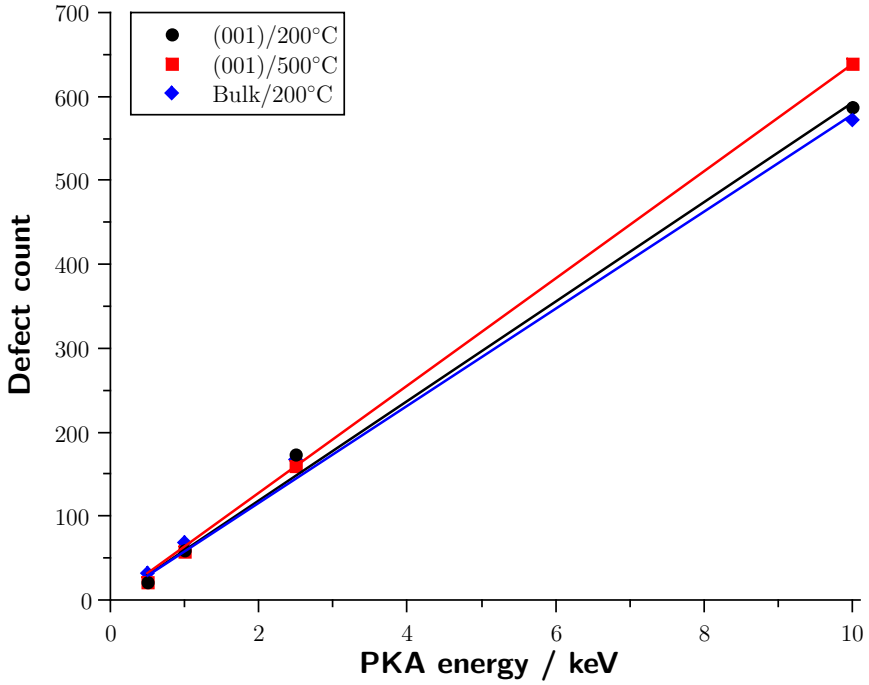

Figure 6.14: Comparison of the averaged defect count for irradiation of the (001) surface at 200°C and 500°C with the results for bulk graphite at 200°C.

Figure 6.15 shows representative examples of the microstructural damage created by (001) surface irradiation at 10 keV for the two different studied incident angles. For both, the damage consists of point defects created by collisions either with the PKA or SKAs. For irradiation with an incident angle <90° the point defects are more compactly distributed compared to an incident angle of 90°.

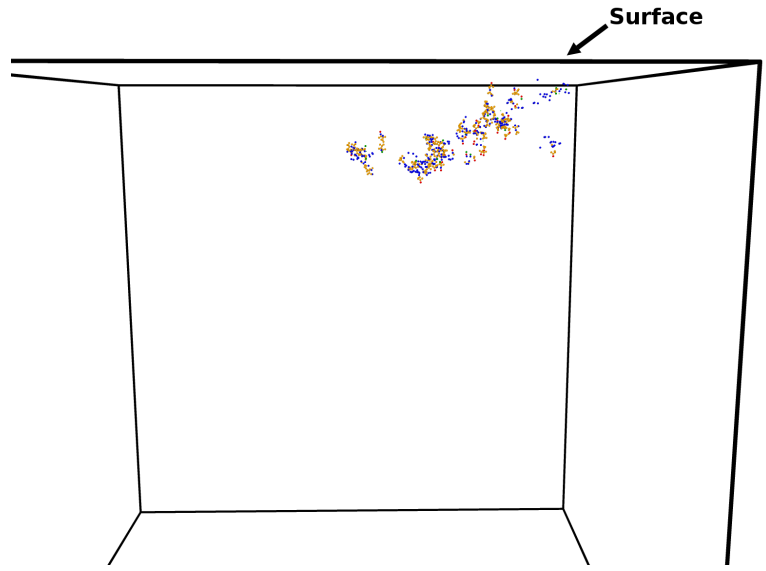

(a)

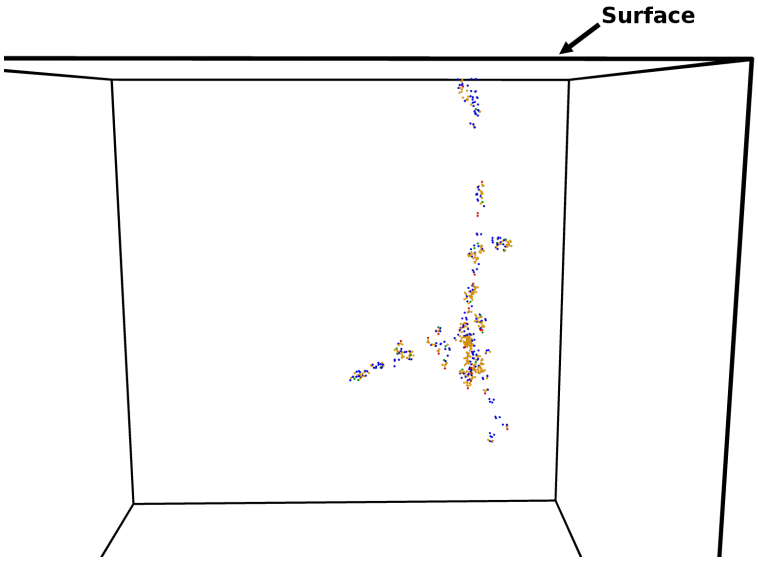

(b)

Figure 6.15: Microstructural damage for a 10 keV irradiation of the (001) surface in a) direction 5 (incident angle <90°) and b) direction 10 (incident angle 90°). Only defects as defined in section 6.1.4 are shown, graphitic carbon atoms are omitted for the sake of better visibility. The box shows the boundaries of graphite, thus the upper plane is equivalent to the surface. Carbon atoms are colored according to their coordination number: 0 neighbors (black), 1 neighbor (green), 2 neighbors (blue), 3 neighbors and defective (orange), 4 neighbors (red).

This observed trend can be treated statistically by analyzing the defect count distribution with respect to the bulk depth. The comparison for irradiation with different incident angles is shown in Figure 6.16. These histograms reveal an important difference. For the studied incident angles <90°, the majority of damage is created very close to the surface (for 10 keV in the range of 0-100 Å). However, for a 90° incident angle the damage is far more spread out. Significant amounts of damage are observed up to 150-200 Å deep in the bulk. The PKA directions 5, 6, 7, and 8 (<90°) produce similar defect distributions with respect to bulk depth. However, the height and width of the peaks show no conclusive trend. Thus, in the following these directions will be averaged and only compared to the 90° incident angle.

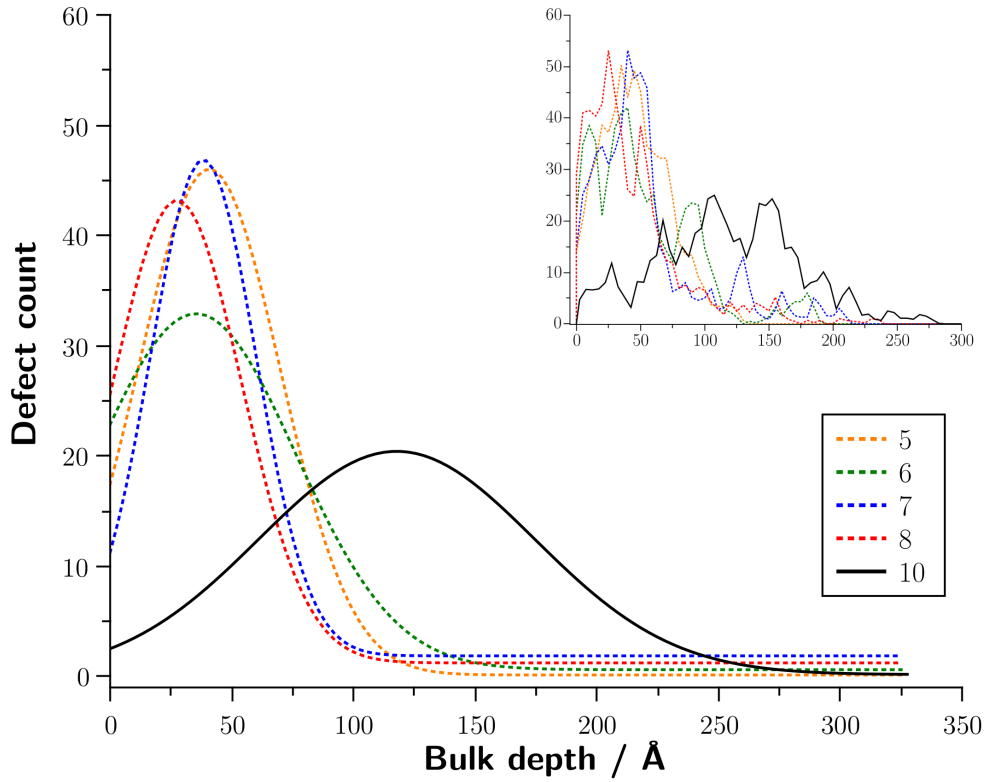

Figure 6.16: Histogram of the defect count with respect to bulk depth for a PKA energy of 10 keV at 200°C. The large image shows a fit to a Gaussian function, the small image in the upper right corner shows the raw data.

In implantation experiments as well as in the reactor, irradiation of the surface is not a singular event. Repeated irradiation of the (001) surface with random PKA energies ranging from 0.5-2.5 keV was simulated, the statistical analysis of the matrix damage is shown in Figure 6.17.

In the case of repeated irradiation at an incident angle of 90°, several trends are observable with respect to the different parameters of the simulations.

For all performed simulations, the defect count consistently increases with an increasing number of irradiations. However, a significant deviation from proportionality is observed for all simulations starting from an accumulated PKA energy of about 50-100 keV. This is directly linked to the graphite matrix damage. The histograms of the defect count distribution with respect to bulk depth are close to a Gaussian distribution. As the number of irradiations increases, they show a shift of the defect maximum deeper into the bulk. However, this shift is rather low (about 5-10 Å) and also broadens significantly. The heat maps show a circular distribution of defects with respect to the center of the simulation box. As the number of irradiations increases, a radial pattern of the defect distribution is observed. These results together show that the energy needed to displace a carbon in a damaged zone is higher which decreases the amount of additional damage created per PKA.

The incident angle of the PKA with respect to the surface affects all studied aspects of the damage evolution of the matrix. For consistent irradiation at an incident angle of 90°, a much larger amount of damage is created, compared to random incident angles. This was not completely clear for a singular irradiation of the (001) surface. However, the repeated irradiation of the surface intensifies the effect that a larger amount of energy is absorbed by the surface when the PKA penetrates it at an incident angle <90°. The damage close to the surface is much higher for random incident angles. 4-5 times more carbon atoms detach from the matrix. This is reflected in a decrease of defects on the surface as shown in the histograms. The heat maps show that the disordered zone is more compact. This is likely a consequence of the simulation protocol (the irradiation zone of the surface is confined to a centered 30 Å×30 Å square).

The sample temperature has little influence on the matrix damage. The overall evolution of the defect count as well as the defect count distribution with respect to bulk depth are rather similar for 200°C and 500°C. However, a higher temperature makes it easier for surface defects to detach. This can be clearly seen from the heat maps for random incident angles. For 200°C, it has a similar distribution as for irradiation at an incident angle of 90° although it is less extended. At 500°C, the heat map has a ring-like maximum with lower damage in the center.

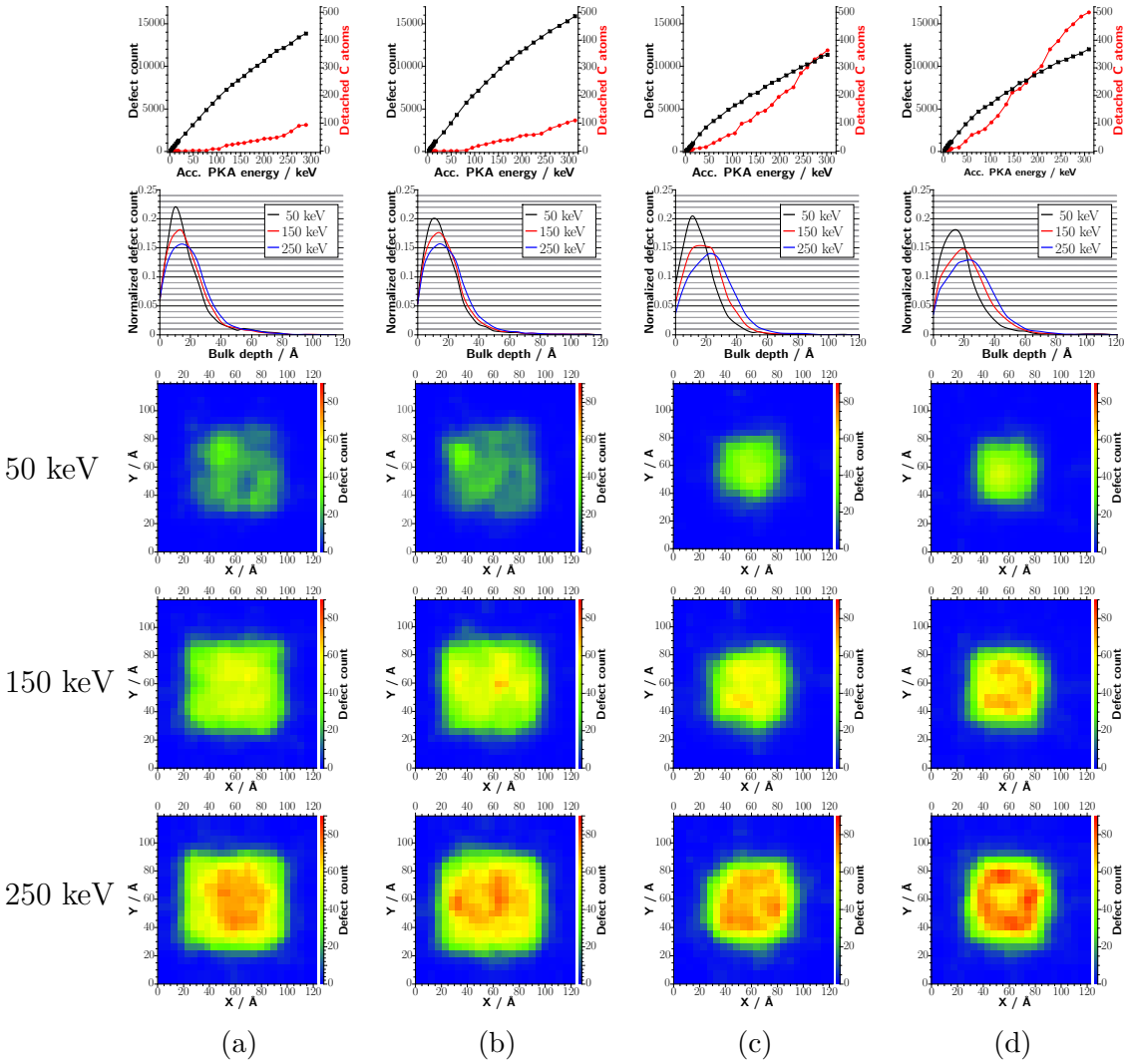

Figure 6.17: Statistical analysis for the irradiation of the (001) surface with an incident angle of 90° at a) 200°C and b) 500°C and a random incident angle at c) 200°C and d) 500°C. The figures from top to bottom are the accumulated defect count and detached surface carbon atoms (note the different scales for the two curves), the normalized defect count distribution with respect to the bulk depth, and heat maps of defect accumulation in the xy-plane at an accumulated PKA energy of 50, 150, and 250 keV.

As already indicated by the heat maps, the microstructure of graphite changes with an increasing number of irradiation simulations. Snapshots of the microstructures are shown in Figure 6.18 for 200°C and an incident angle of 90° and random incident angles, respectively.

For an incident angle of 90°, the damage mostly consists of point defects for an accumulated energy of 50 keV. Except for the center region, graphene planes are mostly intact. The surface shows almost no damage, but is noticeably deformed toward the vacuum in the center region. At 150 keV, the disorder close to the surface increases significantly. The center region is almost completely amorphous. Point defects are mostly found deeper in the bulk. At this point the surface also has deteriorated, the first plane has less graphitic carbon atoms compared to the previous snapshot. Overall, the damaged zone gets more spread out in width and depth which was already indicated by the histograms and heat maps. The graphene planes are intact outside of the heavily damaged center region. Partial graphene planes which link amorphous zones are found deeper in the bulk. At 250 keV, the observed trends intensify. The center region is amorphous up to a depth of about 25 Å. No significant increase of point defects is observed. Thus, the energy seems to be mostly absorbed by the amorphous zone and does not create significant damage deeper in the bulk. In the center region, the surface deterioration has continued and the surface can also be described as largely amorphous. In the center the carbon atoms of the surface are about 5 Å higher than at the boundaries. Graphene planes are almost exclusively found outside of this heavily damaged region.

For random incident angles, the trends of the heat maps are confirmed by the snapshots. The more compact irradiation zone (30 Å×30 Å square in the center of the box) leads to a more compact damage distribution. Already at 50 keV, the center regions seems to be amorphous. Point defects are found deeper in the bulk, but also close to the surface in regions further away from the center. However, compared to an incident angle of 90°, the damage is concentrated much closer to the surface. Apart from this center region, the graphene planes are intact. At 150 keV, this trend is continued. The surface is already missing a significant amount of carbon atoms, a hole in the center region is visible. As for an incident angle of 90°, the surface expands toward the vacuum. The width and depth of the amorphous zone have increased. There are very few point defects deep in the bulk. Closer to the surface, they only are found further away from the damaged zone. Thus, already at this stage a large amount of the PKA energy is lost in the amorphous zone and only a small number of cascades seems to create point defects. At 250 keV, the difference between the two irradiation types is most prevalent. For random incident angles, the size of the hole further increases and a large amount of carbon atoms detach from the surface. The amorphous zone extends in depth, but the width is almost constant. Since the surface is much easier to pass due to the large hole, this could mean that significant amounts of the PKA energy are transferred to carbon atoms which then detach from the surface with the excess kinetic energy.

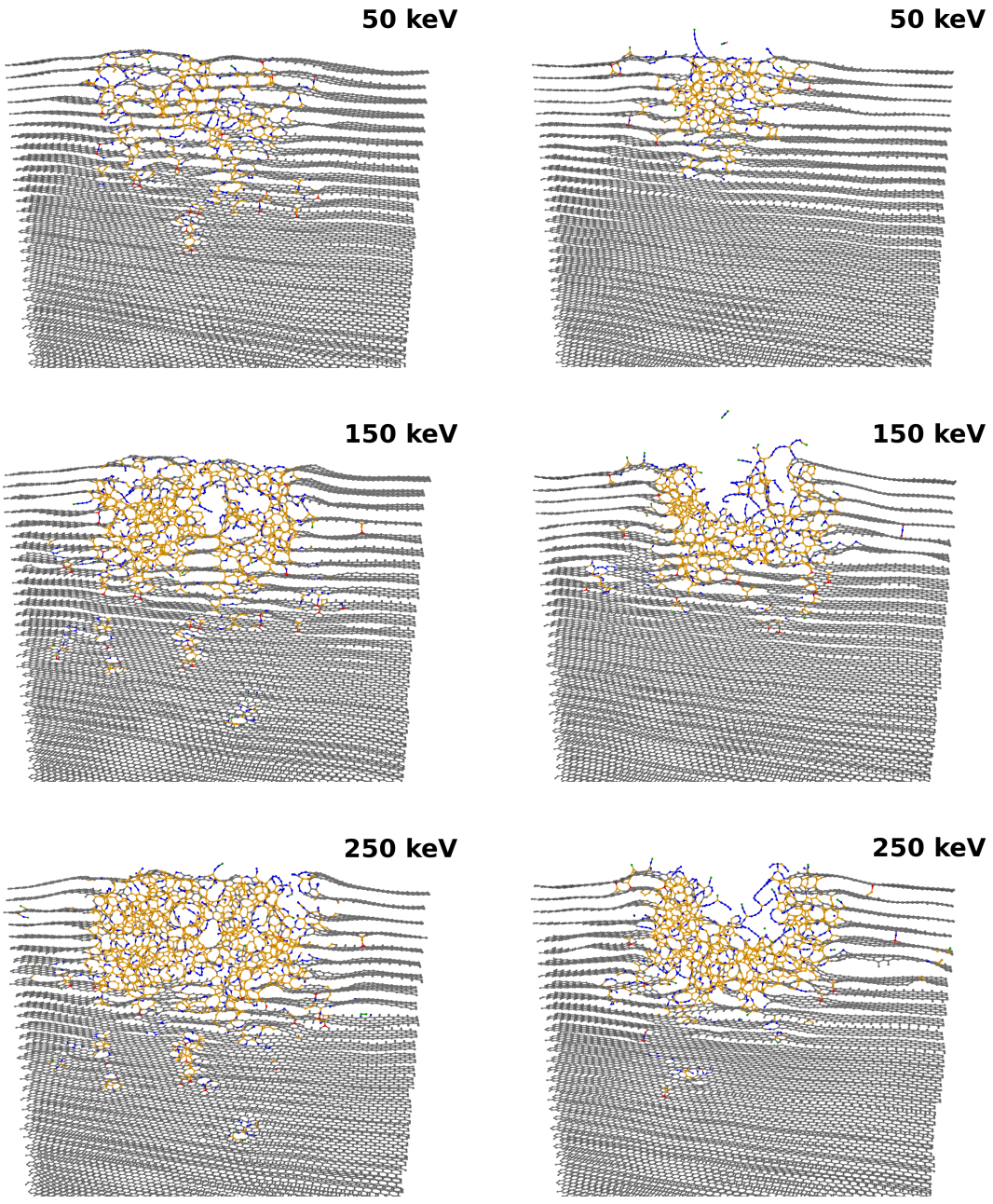

Figure 6.18: Snapshots of irradiation simulations of the (001) surface at 200°C for a) an incident angle of 90° and b) random incident angles. The images are cut along the xz-plane and depict a center region of 10 Å width with the highest damage. The energies 50 keV, 150 keV, and 250 keV refer to the accumulated PKA energies. Carbon atoms are colored according to their coordination number: 0 neighbors (black), 1 neighbor (green), 2 neighbors (blue), graphitic (gray), 3 neighbors and defective (orange), 4 neighbors (red). Chlorine atoms are omitted for the sake of visibility.

These snapshots show a heavily damaged center region. However, since they depict only a centered slab with a width of 10 Å, they contain no information about the damage in zones further away from the center. In Figure 6.19 a side view of the same snapshots is shown. Overall, the trends observed in the previously presented snapshots are confirmed. The damage in the center continuously increases due to the amorphization. Point defects are found deeper in the bulk and outside of the amorphous center region. This is true for both studied incident angles.

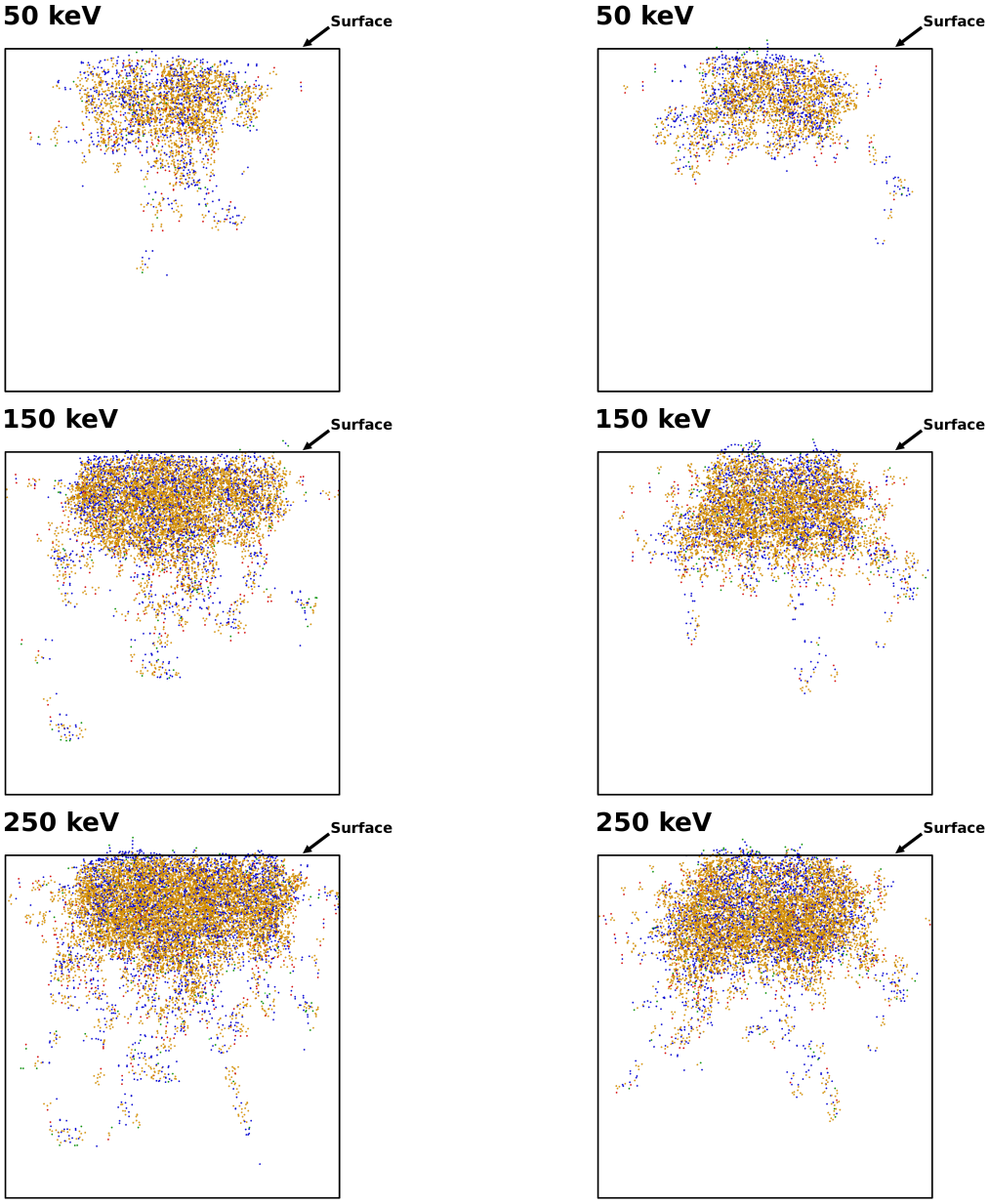

Figure 6.19: Representative microstructural damage of irradiation simulations of the (001) surface at 200°C for a) an incident angle of 90° and b) random incident angles. The upper line of the box refers to the surface in the unirradiated reference state. Carbon atoms are colored according to their coordination number: 0 neighbors (black), 1 neighbor (green), 2 neighbors (blue), 3 neighbors and defective (orange), 4 neighbors (red). Graphitic carbon atoms are omitted for the sake of visibility.

The defect accumulation caused by the repeated irradiation of the (001) surface is high enough to influence macroscopic observables. In Figure 6.20, the relative change of dimensions parallel and perpendicular to the graphene planes is shown. The dimensional change parallel to the graphene planes is given as the change of the product of x- and y-directions which was found to behave more regularly. The change along each of the two directions is more prone to variations since the simulation box is orthorhombic whereas the graphite lattice is hexagonal. The relative change of the dimension perpendicular to the graphene planes was estimated from the average highest and lowest z-component of graphitic carbon atoms belonging to the uppermost graphene plane.

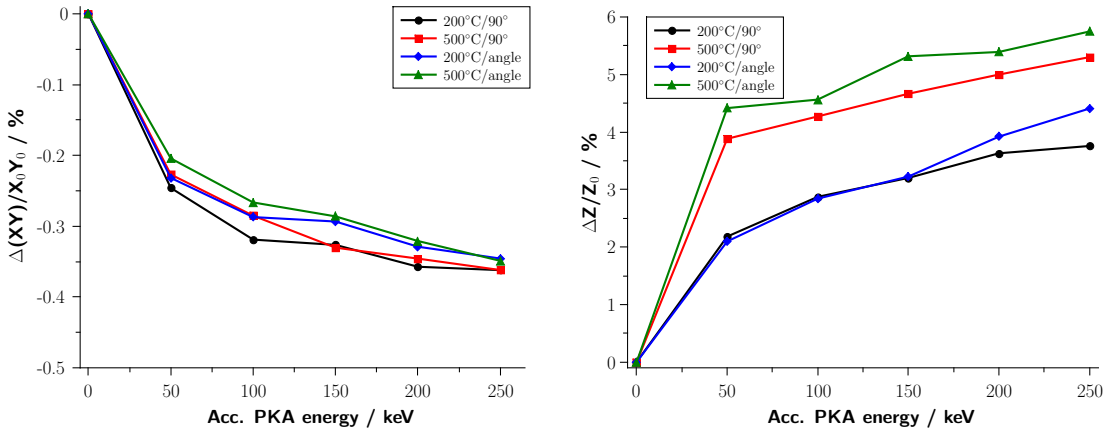

(a) (b)

Figure 6.20: Dimensional change in percent of the a) x- and y-directions (note that the change in x- and y-direction is given as the change of the product of the x- and y-dimensions of the system) parallel to the graphene planes and b) z-direction perpendicular to the graphene planes for repeated irradiation of the (001) surface.

A contraction of the dimension parallel to the graphene planes is observable as the number of irradiations increases. This is consistent with experimentally observed trends [Got97, AMY+05]. The slopes of the curves for different incident angles and temperatures are very similar. The contraction is more pronounced with increasing temperature which is caused by the larger number of created defects. No clear trend is found for different incident angles. The decrease from 0-50 keV differs from the slope for the other data points.

Perpendicular to the graphene planes, the system expands significantly as the the number of irradiations increases. This gives a more reliable estimate since the expansion is more pronounced in the center of the box than at the boundaries. The relative dimensional change in this direction is an order of magnitude higher compared to the dimensional change parallel to the graphene planes. This is also consistent with experimental results [Got97, AMY+05]. Starting from 50 keV, the slopes of the dimensional change for all irradiation types and temperatures are rather similar. An increasing temperature increases the dimensional change due to the accumulation of defects. For random incident angles, the dimensional change is slightly higher.

Both dimensional changes are more pronounced in the initial phase from 0-50 keV. The saturation of these properties starting from about 50 keV is in line with the observed decrease of the additional created damage per PKA.

(100), (110), and Reconstructed Surfaces

When the (100), (110), or the studied reconstructed surfaces are irradiated, the PKA can enter the graphite in the $\langle 0001 \rangle$ direction (parallel to the graphene layers). Along this direction, channeling can occur very easily when the PKA penetrates the surface between the interlayer space of the matrix. In Figure 6.21 a representative snapshot of the microstructural damage caused by channeling is shown. Channeling describes a phenomenon where the PKA propagates through the material along specific channels where high-energy collisions with the matrix are rather rare. Thus, along these channels it can penetrate the bulk much deeper than along other directions. In Figure 6.21 this can clearly be seen. Only a few point defects are created close to the surface, then the PKA enters the channel and propagates 70-80 Å deep into the bulk without defect creation. Once it leaves the channel, the cascade is started and creates the damage over a more compact range.

Next to the $\langle 0001 \rangle$ direction, channels along the $\langle 10\bar{1}2 \rangle$ direction [CRR+15] and the $\langle 11\bar{2}0 \rangle$ direction [Bal62] were reported for carbon atoms as PKA.

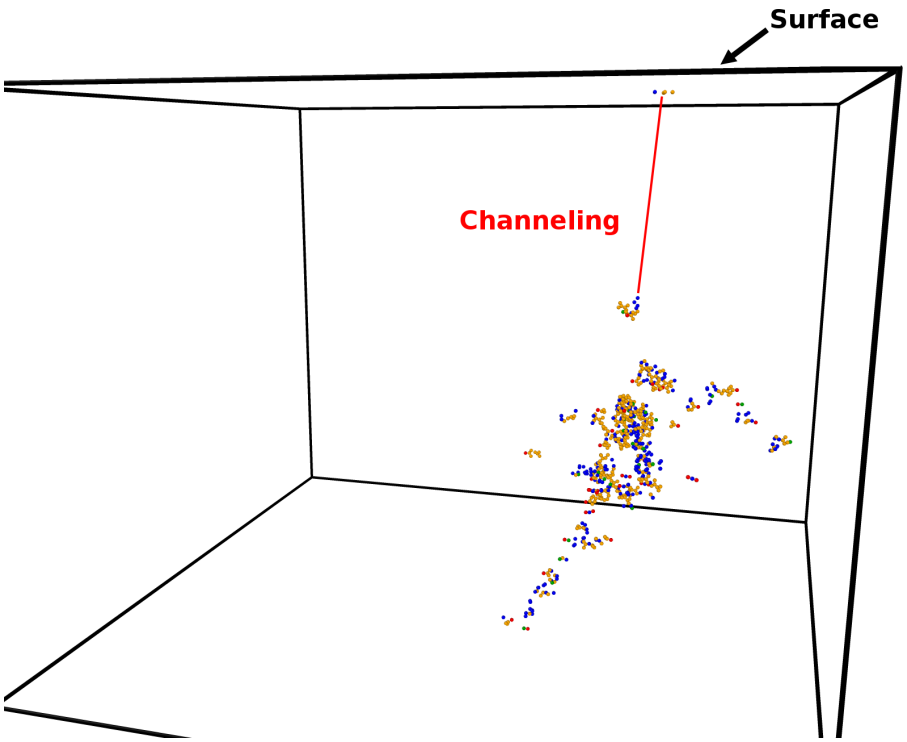

Figure 6.21: Microstructural damage caused by channeling of the PKA. Defects as defined in section 6.1.4 are shown, graphitic carbon atoms are omitted for the sake of better visibility. The box shows the extent of the surface model; the upper plane is equivalent to the surface. Carbon atoms are colored according to their coordination number: 0 neighbors (black), 1 neighbor (green), 2 neighbors (blue), 3 neighbors and defective (orange), 4 neighbors (red).

In Figure 6.22, a comparison of the defect count for different surface types, PKA energies, and sample temperatures is shown. The slopes of the fits are given in Table 6.3. Overall, the amount of damage is rather similar. However, some trends can be noticed. Compared to the (001) surface, all slopes are higher for the other surfaces. This is due to the fact that the irradiation damage at 10 keV is consistently higher for the (100), (110), and the reconstructed surfaces compared to the (001) surface. The $(110)_{arch}$ surface yields the lowest damage for 0.5 keV and 1 keV and the highest for 2.5 and 10 keV. Thus, the restructuring leads to a similar behavior as for the (001) surface for lower energies. However, for higher energies these strained C-C bonds are more easily broken and increase the total damage. Also, a higher sample temperature leads to a higher amount of damage.

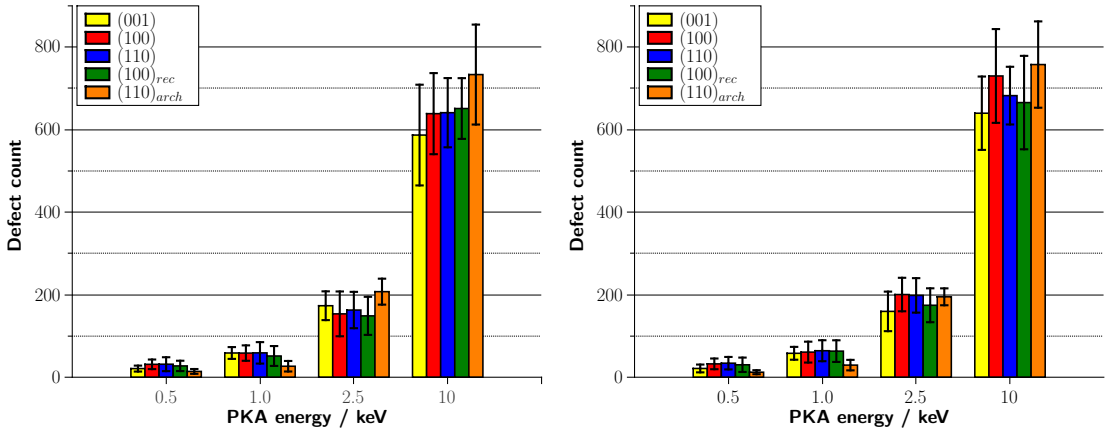

Figure 6.22: Comparison of the defect count for irradiation of the different surfaces with respect to the PKA energy for a) 200°C and b) 500°C.

In Figure 6.23, representative microstructural damage distributions are shown for the two studied incident angles.

For an incident angle of 90°, two extreme cases can be identified. When the PKA penetrates the bulk in the interlayer space, it can channel more easily and create microstructural damage of the type shown in Figure 6.21. The other extreme case is shown in Figure 6.23a. Here, it collides with surface atoms and loses a significant amount of its energy. This shortens the channeling distances and can also deflect the PKA in directions where it penetrates through graphene layers. All these effects combined lead to more compact distributions of defects.

For an incident angle of <90° similar trends are observed. Channeling can also be observed, but depends on the PKA direction. It is more likely to occur when the PKA direction is parallel the graphene planes. However, if the PKA collides with the surface this effect is reduced. Defects are created closer to the surface simply as a consequence of the PKA's direction of propagation compared to the 90° incident angle.

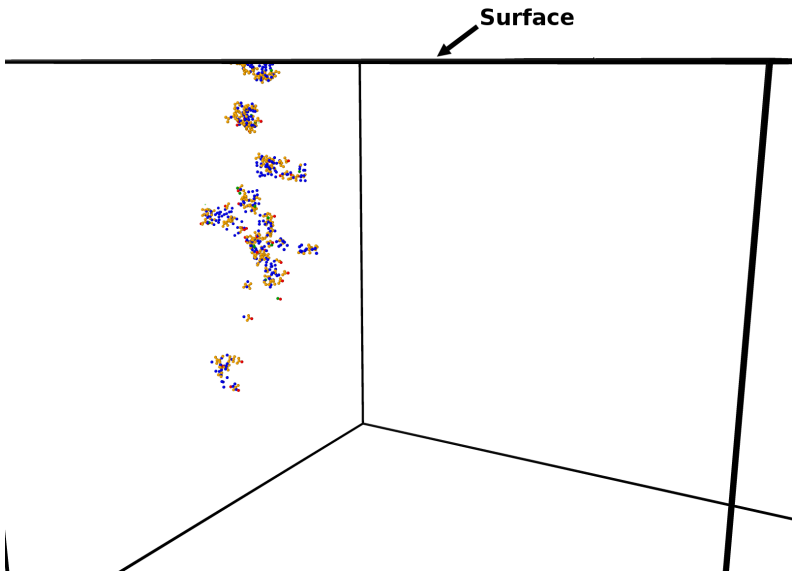

(a)

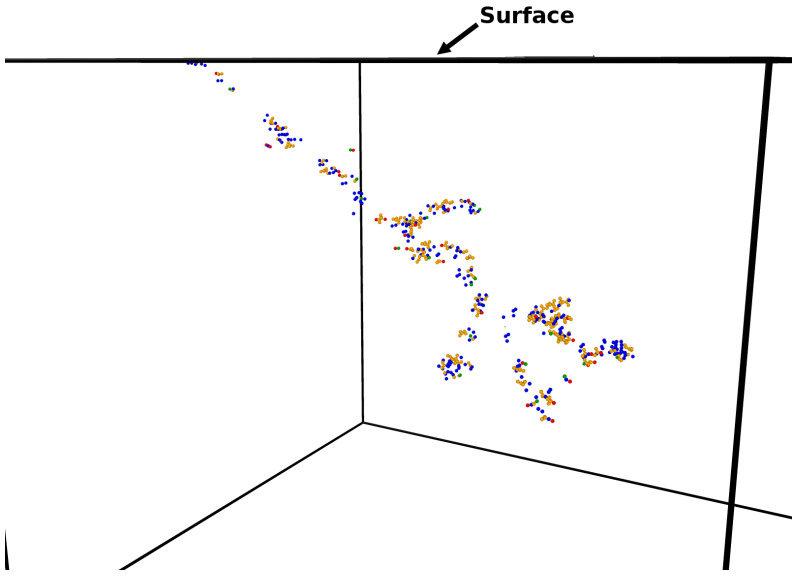

(b)

Figure 6.23: Representative microstructural damage for a) an incident angle of 90° with a surface collision and b) an incident angle of <90°. Defects as defined in section 6.1.4 are shown, graphitic carbon atoms are omitted for the sake of better visibility. The box shows the extent of the surface model, thus the upper plane is equivalent to the surface. Carbon atoms are colored according to their coordination number: 0 neighbors (black), 1 neighbor (green), 2 neighbors (blue), 3 neighbors and defective (orange), 4 neighbors (red).

The qualitative features described before can be treated statistically. In Figure 6.24, the histograms of defect count distribution with respect to bulk depth are shown for the different surfaces for irradiation at 200°C. This is a more convenient measure of the matrix damage, since all of these surfaces intrinsically contain defects. Thus, the defect range is not well-defined. The histograms for an incident angle of <90° are averaged over all four directions since the sample size was too small to extract a directional dependence.

The histograms of the different surfaces for an incident angle of 90° do not show any strong trend. Thus, it is not possible to differentiate between them by analyzing this property. All of them show several peaks with similar intensity which can not be well-represented by a single Gaussian function. This is a direct consequence of channeling. The PKA can propagate over a long range before transferring enough energy to displace lattice atoms. The large peak close to the surface for $(110)_{arch}$ indicates that the high number of created defects might be partially due to an overcounting of pre-existing surface defects which move slightly inward. In fact, the defect count on the surface would be negative due to this difficulty and was set to zero.

The histograms for an incident angle of <90° resemble the ones for irradiation of the (001) surface. Overall, they are rather alike for all studied surfaces. One main peak is found close to the surface. Then the defect count decreases gradually when moving deeper into the bulk. This is similar to the observed trends on the (001) surface. Again, the highest peak is found for the $(110)_{arch}$ and it is also close to the surface. The size of the peak is likely due to the same reason as explained before.

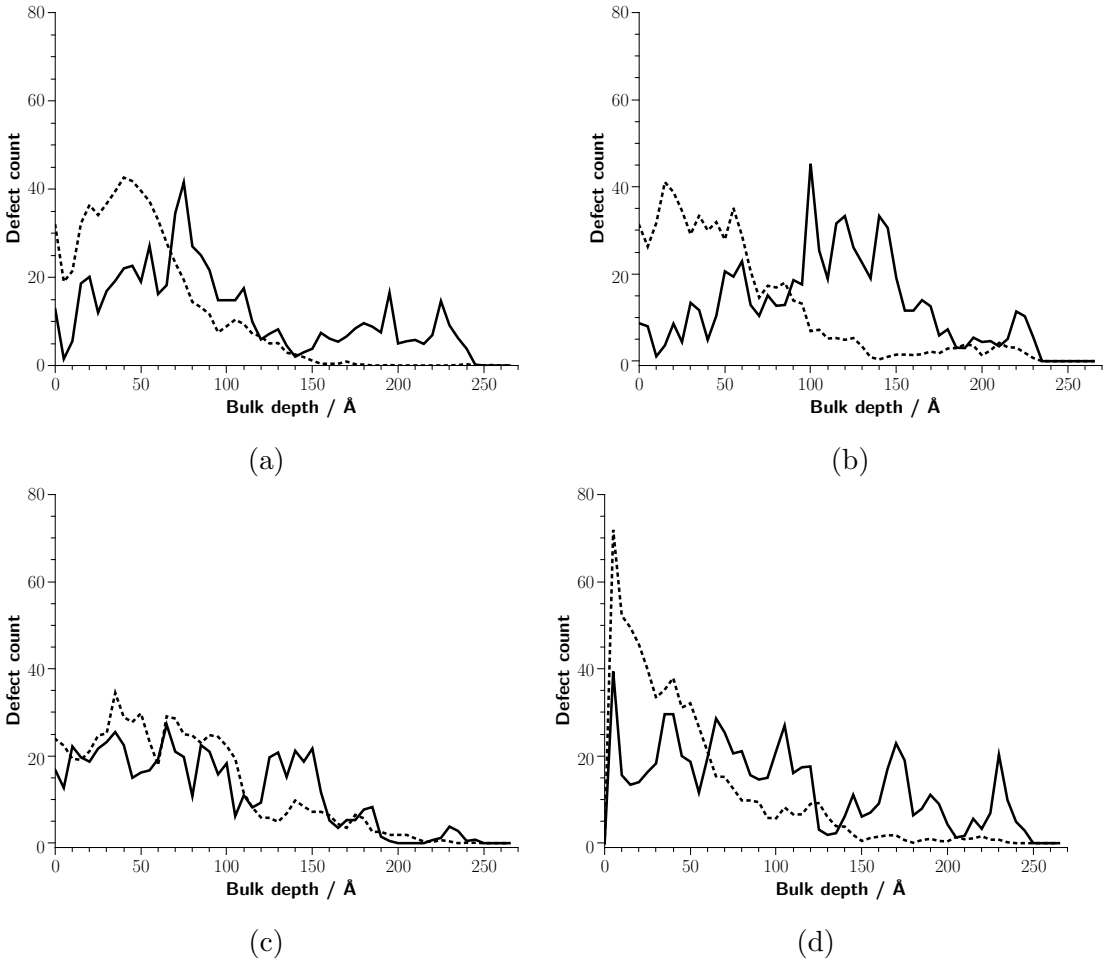

Figure 6.24: Histograms of defect count distributions with respect to bulk depth for irradiation at 200° of a) the (100) surface, b) the (110) surface, c) the $(100)_{reco}$ surface, and d) the $(110)_{arch}$ surfaces for an incident angle of 90° (full lines) and <90° (dashed lines).

Grain Boundary

The studied grain boundary has no dangling bonds. Thus, singular irradiation is not presented since the difference with respect to the (001) surface is not significant. In Figure 6.25, the statistical analysis of the created defects for repeated irradiation of the grain boundary are shown. Overall, similar trends as for irradiation of the (001) surface are obtained.

For an increasing number of irradiations, less defects per PKA are created. The damage is higher for irradiation at an incident angle of 90° and increases with an increasing temperature. More carbon atoms detach for a random incident angle and for a higher temperature. As the number of irradiations increases, the number of carbon atoms detached from the surfaces increases significantly. This is more pronounced for random angles. In the histograms this leads to a broader distribution of damage with respect to the bulk depth for random incident angles since Cl can enter the bulk more easily through the damaged surface. In addition the number of defects decreases close to the surface which indicates that the carbon atoms detach from the surface. The heat maps show an intense ring-like defect maximum around the center.

For irradiation at 90°, one important difference with respect to irradiation of the (001) surface is revealed. The heat maps show that the repeated irradiation of the grain boundary leads to an accumulation of damage along the grain boundary. This effect increases with the temperature. Interestingly, this is not found for random incident angles.

To further investigate these trends, snapshots of the microstructural damage are shown in Figure 6.26 for 200°C and an incident angle of 90° and random incident angles, respectively. Overall, similar trends are observable as for repeated irradiation of the (001) surface.

For an incident angle of 90°, mostly point defects are found for an accumulated energy of 50 keV. The grain boundary and the surface are intact except for local defects. At 150 keV, the disorder close to the surface has significantly increased and amorphous zones are formed. Parts of graphene planes are still intact and connect to disordered zones. The surface starts to deteriorate, but still mainly consists of non-defective carbon atoms. The expansion of the surface toward the vacuum is less noticeable compared to the (001) surface. Point defects are mostly found deeper in the bulk. Below the amorphous zones, damage starts to accumulate exactly at the grain boundary. These effects are intensified at an accumulated energy of 250 keV. The amorphous zone has extended in width and depth (about 25-30 Å deep). The grain boundary is almost completely destroyed in this region. Below the amorphous zone, more defects accumulated at the grain boundary. Point defects are found further away from the heavily damaged center. Large parts of the surface are still intact.

For random incident angles, the similarity of the heat maps for the (001) surface and the grain boundary is confirmed by the snapshots. Due to the more compact irradiation zone, the center region is already heavily disordered at an accumulated energy of 50 keV. In the highly damaged zone the grain boundary is no longer recognizable up to a depth of about 20 Å. Point defects are found deeper in the bulk and further away from the damaged center. The surface is already expanded

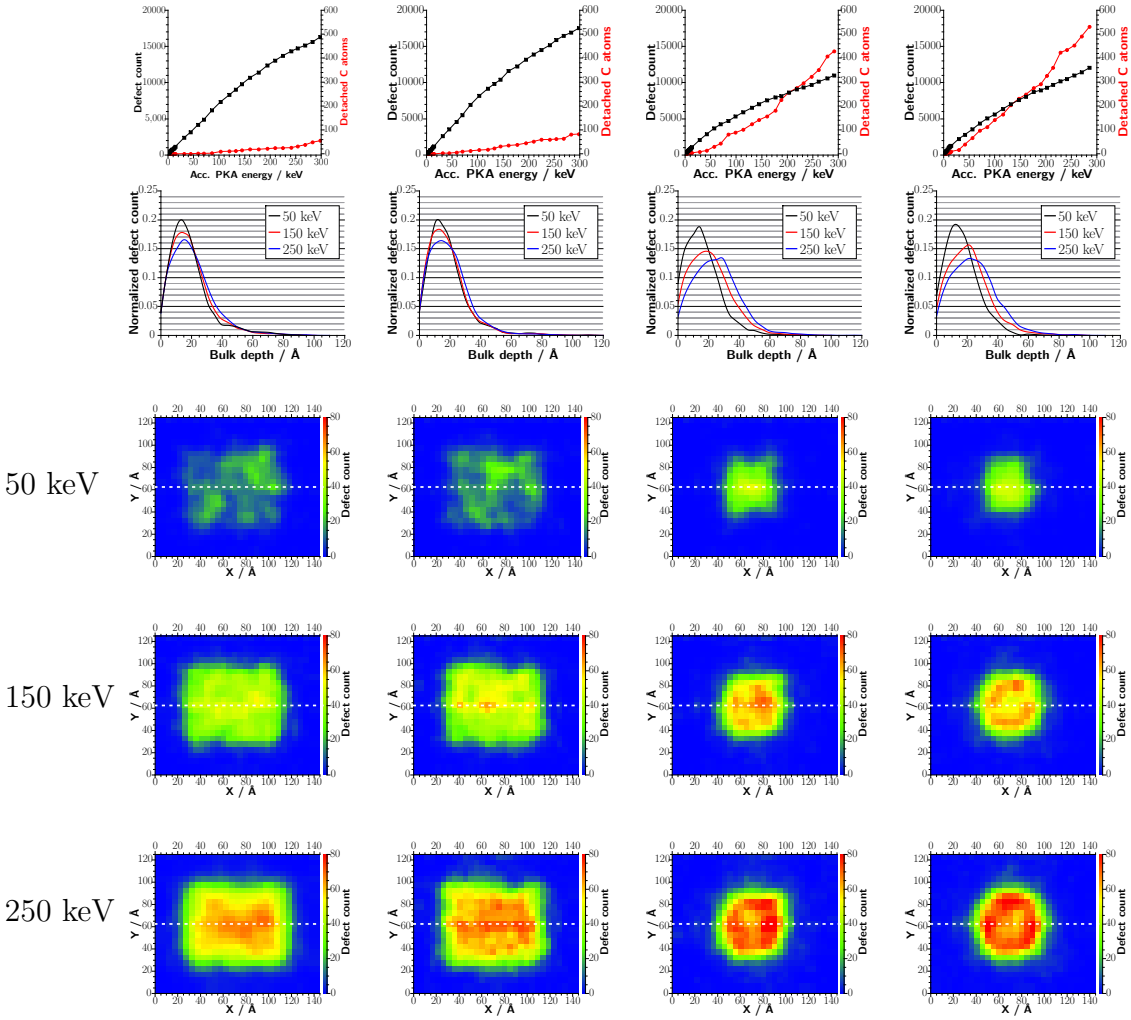

Figure 6.25: Statistical analysis for the irradiation of a grain boundary with an incident angle of 90° at a) 200°C and b) 500°C and a random incident angle at c) 200°C and d) 500°C. The figures from top to bottom are the accumulated defect count and detached surface carbon atoms (note the different scales for the two curves), the defect distribution with respect to the bulk depth, and heat maps of defect accumulation in the xy-plane at an accumulated PKA energy of 50, 150, and 250 keV. The dashed white line in the heat maps shows the grain boundary.

toward the vacuum. At 150 keV, the surface has a hole as indicated by the ring-like defect maximum in the heat maps. The center region is completely amorphous and has extended in width and depth. In addition, significant amounts of carbon atoms have detached. This confirms the results of the statistical defect analysis. Point defects are found deeper in the bulk, but show no clear signs of accumulation at the grain boundary. The surface has further expanded toward the vacuum. At 250 keV, the amorphous zone increases mostly in depth. The size of the hole has increased and much more carbon atoms have detached from the surface. These trends show the same behavior as for the (001) surface.

As for the (001) surface, a side view of the complete simulation box is shown in Figure 6.27 to analyze the point defects in the outer regions. The damage in the center continuously increases due to the amorphization. Point defects are found deeper in the bulk and outside of the amorphous center region for both types of studied incident angles. The amorphous zone is more extended for an incident angle of 90°. The defect accumulation along the grain boundary is not clearly visible due to the large number of defects. However, it can be seen that defects created by displacement cascades are as abundant in the grain boundary region as they are in zones further away from the center.

The relative change of dimensions parallel and perpendicular to the graphene planes is shown in Figure 6.28. Overall, the trends are not as clear due to the intrinsic stress caused by the grain boundary which adds to the stress caused by defect accumulation. The dimensional changes were measured in the same way as described in section 6.3.2.

Parallel to the graphene planes, the system contracts as the number of irradiations increases. These findings agree with those of the (001) surface irradiation. A lower sample temperature leads to a larger contraction for both incident angles. Since more defects are created at a higher sample temperature, this must be due to the interplay of thermal expansion with increasing temperature and the contraction due to defect accumulation. The contraction is more pronounced for an incident angle of 90° compared to random angles since the damaged zone is more spread out for the former as seen from the heat maps and snapshots.

A more complex behavior is found perpendicular to the graphene planes. In the initial stage, all systems seem to contract in this direction, but as the number of irradiations increases, they expand. This is mostly due to the difficulty in determining the dimension perpendicular to the graphene planes. As was shown in Figure 6.3, the surface is rippled due to the grain boundary. Contraction along the directions parallel to the graphene planes increases the rippling and thus the lowest carbon atom belonging to the uppermost plane is found lower than in the reference. Thus in the initial stages, the system seems to contract. When the damage increases, this trend is reversed and expansion is found as expected from experimental results. No clear trend is found for different temperatures or incident angles.

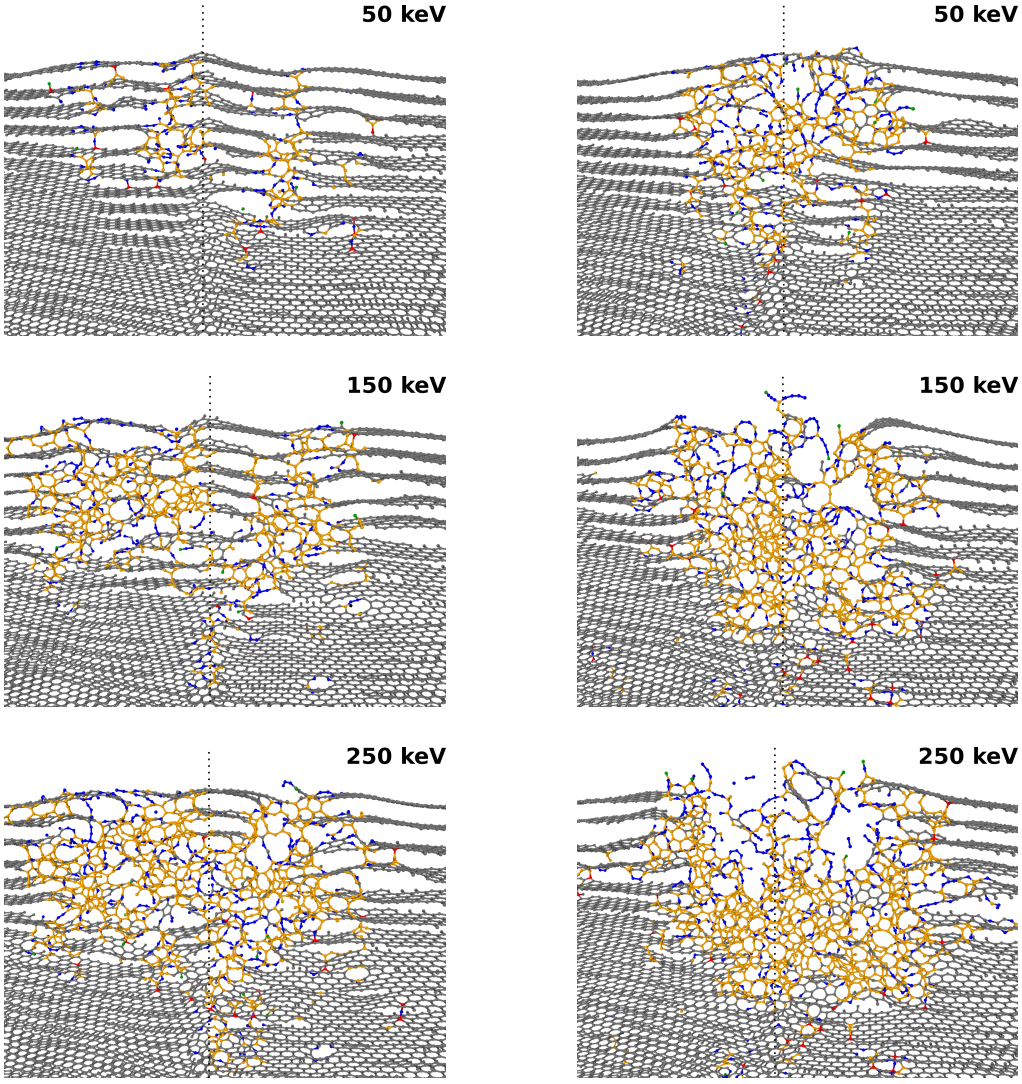

Figure 6.26: Snapshots of irradiation simulations of the grain boundary at 200°C for a) an incident angle of 90° and b) random incident angles. The images are cut along the yz-plane and depict a center region of 10 Å width with the highest damage. The dashed lines indicate the approximate location of the grain boundary. The energies 50 keV, 150 keV, and 250 keV refer to the accumulated PKA energies. Carbon atoms are colored according to their coordination number: 0 neighbors (black), 1 neighbor (green), 2 neighbors (blue), graphitic (gray), 3 neighbors and defective (orange), 4 neighbors (red). Chlorine atoms are omitted for the sake of visibility.

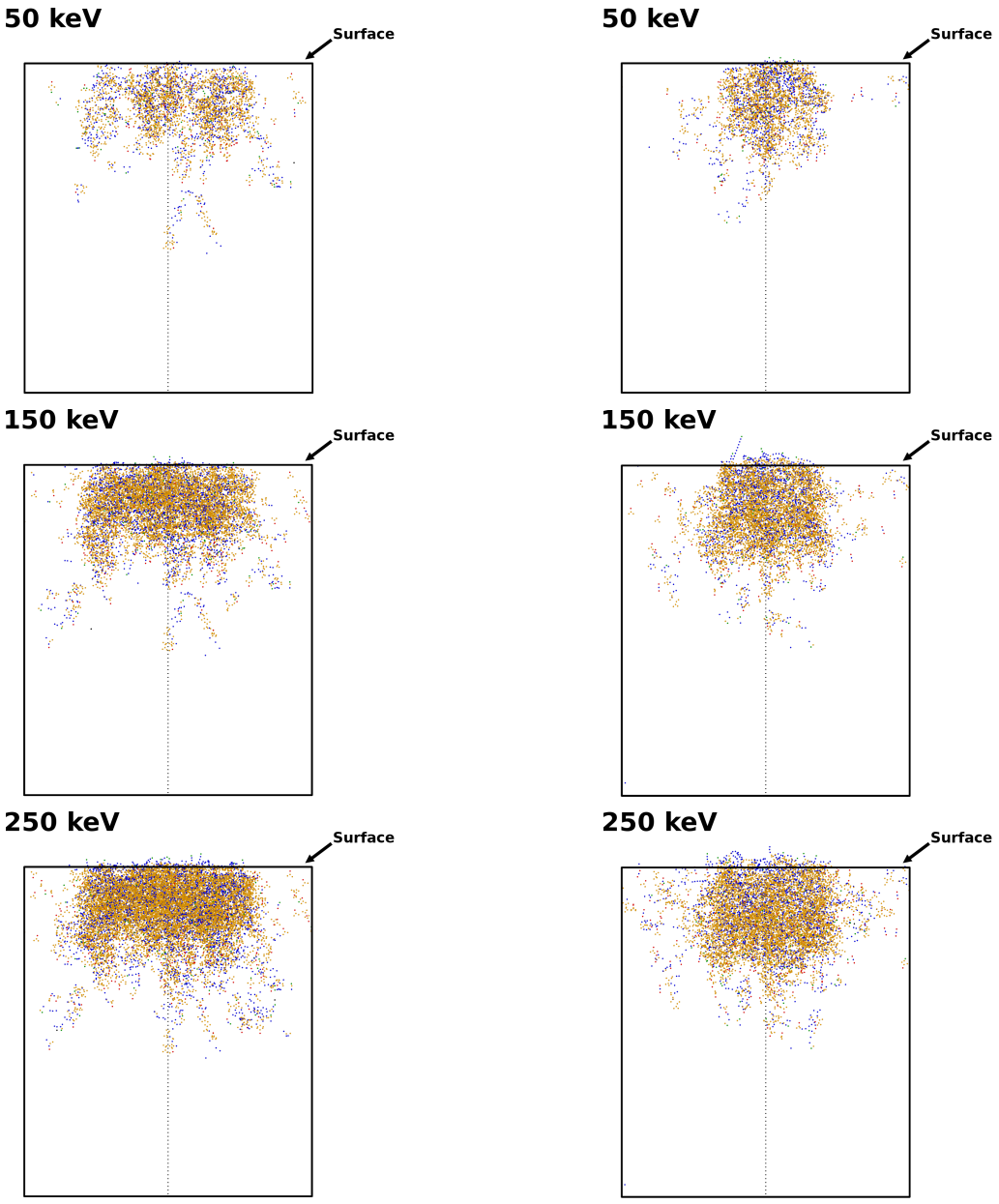

(a) (b)

Figure 6.27: Side view (perpendicular to the grain boundary) of the defect distribution for irradiation simulations of the grain boundary at 200°C for a) an incident angle of 90° and b) random incident angles. The upper line of the box refers to the surface in the unirradiated reference state. The grain boundary is located in the middle, its position is indicated by the dashed line. Carbon atoms are colored according to their coordination number: 0 neighbors (black), 1 neighbor (green), 2 neighbors (blue), 3 neighbors and defective (orange), 4 neighbors (red). Graphitic carbon atoms are omitted for the sake of visibility.

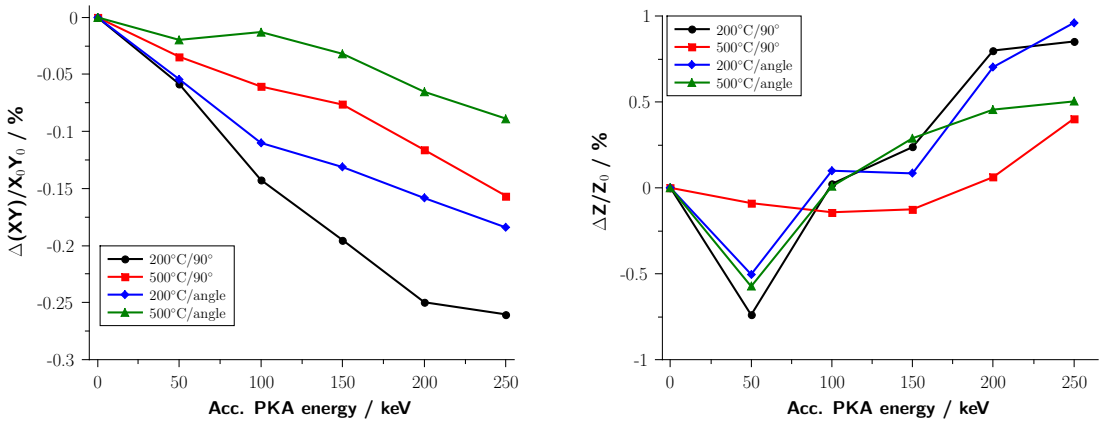

(a) (b)

Figure 6.28: Dimensional change in percent of the a) x- and y-directions (note that the change in x- and y-direction is given as the change of the product of the x- and y-dimensions of the system) parallel to the graphene planes and b) z-direction perpendicular to the graphene planes for repeated irradiation of the grain boundary.

6.3.3 Diffusion Simulations

In chapter 4, it was concluded that surfaces with dangling bonds can serve as strong traps. However, the DFT results only provide static information. To obtain more insight, molecular dynamics simulations are important since they can describe dynamical processes.

Experiments showed that Cl is already present in virgin UNGG graphite and shows a heterogeneous distribution [VGT+11]. It exists mainly in an organic form bound to the graphite matrix [VTMB10, VGT+11]. Thus, by performing diffusion simulations the trapping of Cl at different sites with dangling bonds that reflect the microstructure of virgin UNGG graphite can be investigated.

As shown in the literature review, in the reactor ^{36}Cl is mostly created by neutron capture of ^{35}Cl. Depending on the kinetic energy of the neutron, this collision could lead to the breaking of the C-Cl bond of a chemisorbed Cl. Due to the temperature gradient of graphite in the reactor, the temperature dependence of the diffusion properties of the released Cl is also of interest.

The diffusion of Cl along the (100) and (110) surface and the in-plane reconstruction of the (100) surface was simulated. These surfaces are models of the different crystallite edges which are most likely to occur. This will be presented in the first section.

In order to study the experimentally observed heterogeneous Cl distribution, a model is needed which reflects the microstructure of virgin UNGG graphite on a larger scale. A model of polycrystalline graphite with nanopores offers this level of complexity. This model contains crystallite edges with dangling bonds, (001) surfaces, as well as porosities. It also approximates the polycrystalline filler particles from needle coke used for UNGG graphite.

Diffusion simulations of Cl in this model were performed in order to try to

identify preferential trapping sites. This will be reported in the second section.

Cl was implanted into graphite samples in several experiments. Following the implantation, no diffusion was observed. This can be modeled by using the structures that were created by repeated surface irradiation for Cl diffusion simulations. This will be explained in the third section.

(100), (110), and Reconstructed Surfaces

Two parameters were investigated for the diffusion along these surfaces: the dependence on the Cl concentration and the dependence on the occupation number (see section 6.1.3 for the definition). The aspect of occupation number is important for Cl. In real systems the majority of surface carbon atoms are already saturated by different species (for example H or O). These two can form stronger bonds with carbon (for O this is true for double bonds) which means that an exchange reaction and C-Cl bond formation is not very probable. However, trapped Cl could be replaced by H or O in an exchange reaction and subsequently released. Since the potential can only describe the interaction of C and Cl, a reasonable approximation is to "saturate" surface carbon atoms by explicitly turning off the attractive interaction of C and Cl.

In Tables 6.4-6.6, the diffusion constants obtained from the MSD are given for the studied surfaces. Representative snapshots of selected diffusion simulations are shown in Figure 6.29. All three surfaces show the same trends. For cases where the number of available trapping sites is larger than the number of Cl atoms in the gas phase, all Cl are trapped and the MSD saturates. This is consistent with the *ab initio* results.

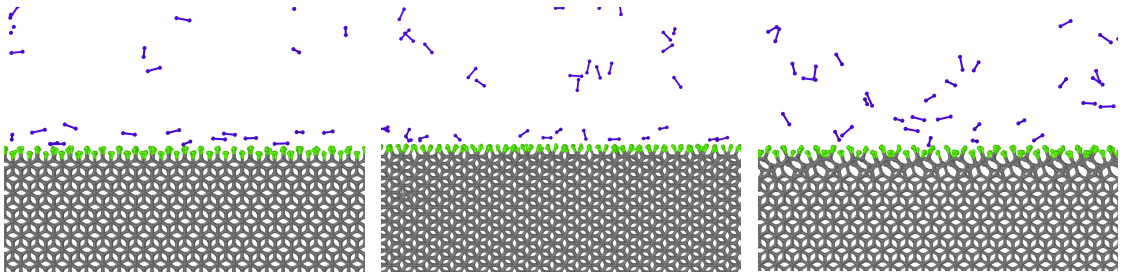

(a) (b) (c)

Figure 6.29: Snapshots of the diffusion simulations at 200° and a Cl concentration of 1.0 at.% along the a) (100) surface, b) (110) surface, and c) $(100)_{rec}$ surface. Trapped Cl is shown in green, whereas gaseous Cl (in the form of Cl_2) is shown in blue. Note that the presented snapshots show structures after an optimization.

For a constant Cl concentration, the diffusion constant increases with an increasing occupation number. In fact, the diffusion constant should not strictly be considered in the sense of a classical diffusion constant, since it is a result of two competing processes: free diffusion which is responsible for the MSD and trapping and fixation on available sites which does not contribute anymore to the MSD after trapping. Thus for an increasing occupation number less trapping sites are available and therefore more Cl is able to freely diffuse in the gas phase. Ultimately, free Cl atoms reacts to give Cl_2.

Table 6.4: Diffusion constants in $10^{10}\,m^2\,s^{-1}$ for diffusion along the (100) surface with respect to the Cl concentration in at.% and the occupation number (Occ. nb.). Saturated MSDs are indicated by "sat."

	200°C			500°C		
Occ. nb.	0.01	0.1	1.0	0.01	0.1	1.0
0.000	sat.	sat.	1.03	sat.	sat.	1.50
0.900	sat.	sat.	9.08	sat.	sat.	9.67
0.990	sat.	38.9	11.9	sat.	44.4	12.3
0.999	6.99	55.5	12.4	11.5	47.9	13.2

Table 6.5: Diffusion constants in $10^{10}\,m^2\,s^{-1}$ for diffusion along the (110) surface with respect to the Cl concentration in at.% and the occupation number (Occ. nb.). Saturated MSDs are indicated by "sat."

	200°C			500°C		
Occ. nb.	0.01	0.1	1.0	0.01	0.1	1.0
0.000	sat.	sat.	1.17	sat.	sat.	1.57
0.900	sat.	sat.	8.57	sat.	sat.	9.05
0.990	sat.	20.7	12.1	sat.	25.4	13.6
0.999	5.48	22.7	12.1	17.2	35.9	13.4

Table 6.6: Diffusion constants in $10^{10}\,m^2\,s^{-1}$ for diffusion along the $(100)_{rec}$ surface with respect to the Cl concentration at.% and the occupation number (Occ. nb.). Saturated MSDs are indicated by "sat."

	200°C			500°C		
Occ. nb.	0.01	0.1	1.0	0.01	0.1	1.0
0.000	sat.	sat.	1.18	sat.	sat.	1.72
0.900	sat.	sat.	8.58	sat.	sat.	9.34
0.990	sat.	21.1	11.0	sat.	27.6	12.1
0.999	9.55	29.8	11.1	10.2	27.4	12.5

With respect to the chlorine concentration, the diffusion constant shows a maximum for 0.1 at.%. A lower concentration results mostly in trapped Cl and almost no diffusion is observed. When the concentration is further increased to 1.0 at.%, the diffusion constant again decreases. This concentration corresponds to a 40 times higher gas density than found under standard conditions (20°C and 1.013 bar). This high density decreases the mean free path and thus the diffusion constant. Non-trapped Cl is found almost exclusively in the form of Cl_2. It should be noted that for this concentration Cl atoms start to enter the bulk. This is not found for the lower concentrations.

Finally, the diffusion constant increases for increasing temperature. This is the standard behavior observed for gases.

Nanoporous Graphite

The diffusion of Cl through the pores of nanoporous graphite was simulated. In this model, the edges of crystallites take the form of the (001), (100), and (110) surfaces. As shown in the previous section, for an occupation number of 0 (all dangling bonds can serve as traps) Cl is immediately trapped when enough traps are available. Since the model consists of 20 crystallites, a large number of trapping sites is available for an occupation number of 0. Due to the large system size (over 3.6×10^7 atoms) a lower Cl concentration of 10 ppm can be simulated which is closer to the experimental conditions. Thus, to respect both, the low concentration and the high number of trapping sites, the occupation number was set to 0.999 to study both trapping and diffusion through pores.

In all diffusion simulations the MSD showed a trend toward saturation. This indicates that a part of Cl gets trapped as seen for the different surfaces of a crystallite. No conclusive trend with respect to temperature was found which allowed to average over the results. The averaged RDF of for C-Cl pairs is shown in Figure 6.30. Three peaks can be identified. The first at about 1.8 Å is the peak for covalent C-Cl bonds. The other two peaks strongly resemble the RDF of diffusion along the (001) surface (see section 5.2.1) and correspond to the average distance of the Cl with respect to the first and second graphene layer of the (001) surface. Figure 6.31 shows a representative image of the final state of a simulation. An analysis of the bonding of Cl atoms shows that about 25% are covalently bound to carbon and about 75% have no neighbors below the cutoff of 1.85 Å. Visual inspection shows that the part of Cl with no neighbors is found on (001) crystallite surfaces. In fact, it seems to migrate toward the corners of nanopores where two different crystallites are only separated by several Å. In such a state the Cl "feels" attractive interactions from two sides, thus its diffusion is at least partially hindered as opposed to diffusion on the (001) surface. A barrier is to be expected when the Cl moves in the direction where the size of the pore increases.

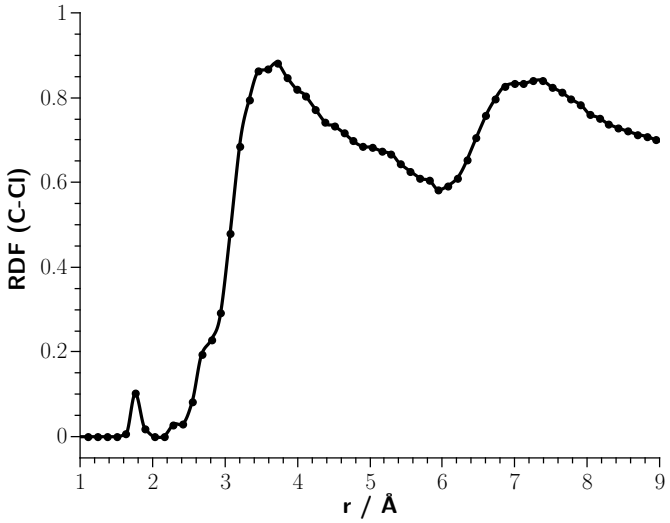

Figure 6.30: RDF of C-Cl pairs for the diffusion of Cl in nanoporous graphite.

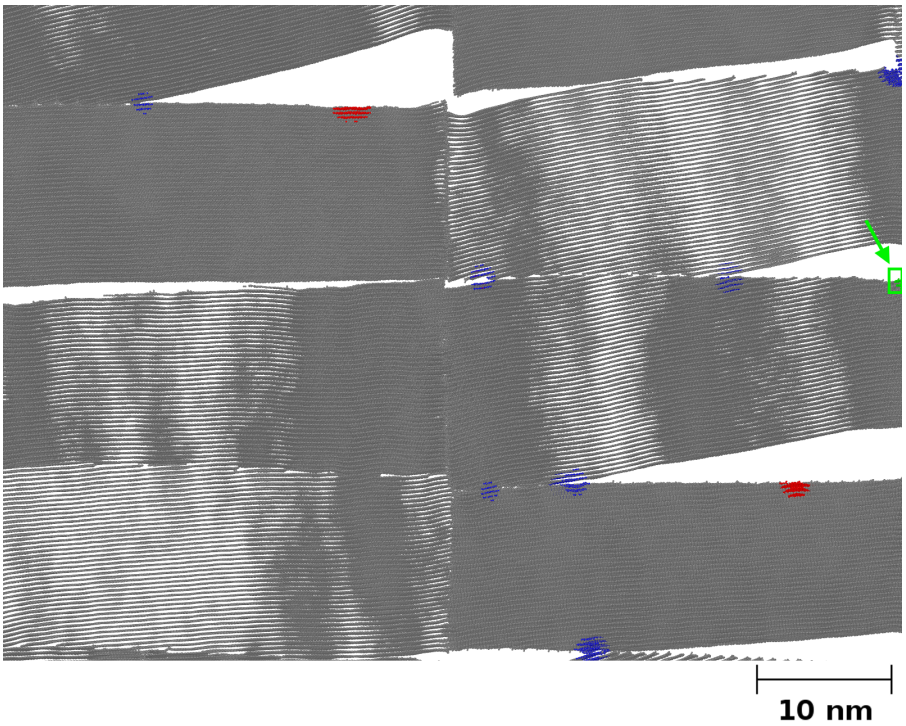

Figure 6.31: Representative snapshot of the distribution of Cl in nanoporous graphite. The color of the Cl atoms depends on their location: red adsorbed on a (001) surface, blue in the corner of a nanopore and green covalently bound at a crystallite edge. Atoms within a radius of 12 Å have the same color for better visibility. The green box and arrow marks the covalently bound Cl and is added for the sake of clarity.

Covalently trapped Cl is more stable than these "semi-trapped" Cl located in the nanopores. However, depending on the saturation of these edges, this trapping mechanism is at least partially blocked.

In all studied cases, the Cl remained in the pores and did not penetrate the crystallites. This is consistent with the observations of the previous section that a very high gas density of Cl is needed for bulk penetration to occur.

Diffusion of Implanted Cl Atoms

In Cl implantation experiments, no significant diffusion of the implanted species was observed [VTM+09]. Thus, diffusion simulations were performed for the final states of the repeated irradiations of the (001) surface and grain boundary. In all studied cases, the MSD did not increase with time, thus no diffusion was found. In Figure 6.32, a representative snapshot of an irradiated graphite matrix and the Cl distribution within is shown. As can be seen, the Cl has formed covalent bonds with the matrix at certain defect sites and thus can not diffuse in graphite. It is localized in the highly disordered zone.

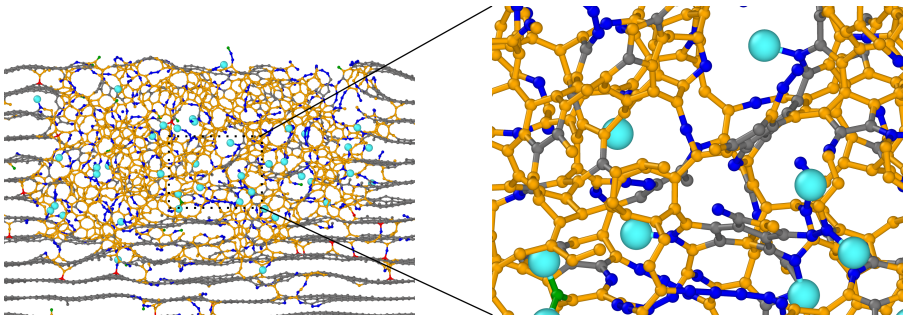

Figure 6.32: Snapshot of the diffusion of implanted Cl obtained from the repeated irradiation simulation of the (001) surface at 200°C and 90° incident angle. Carbon atoms are colored according to their coordination number: 0 neighbors (black), 1 neighbor (green), 2 neighbors (blue), graphitic (gray), 3 neighbors and defective (orange), 4 neighbors (red). Chlorine is shown in ice blue. The right figure shows a zoom into the center region of the snapshot.

In Figure 6.33, the total number of covalent C-Cl bonds formed with the graphite matrix is shown. As can be seen, the large majority of atoms is covalently bound. To break covalent C-Cl bonds at a noticeable rate much higher temperatures are needed than those in the considered range of 200-500°C. This analysis also confirms the findings for irradiation of the surface with a random incident angle. Not all Cl atoms are found in the bulk, some were repelled when colliding with the surface or released due to the large surface damage. This phenomenon is absent for irradiation at a 90° incident angle.

Figure 6.33 also shows the bonding partners of the Cl atoms categorized by the coordination number of the bonding partner. It is clear that aromatic carbon atoms with three neighbors can not be bonding partners as their definition requires 3 carbon neighbors. The large majority of Cl is bound to carbon atoms with a total

coordination number of 3 and 2 carbon neighbors. Thus the main traps are carbon atoms with one dangling bond.

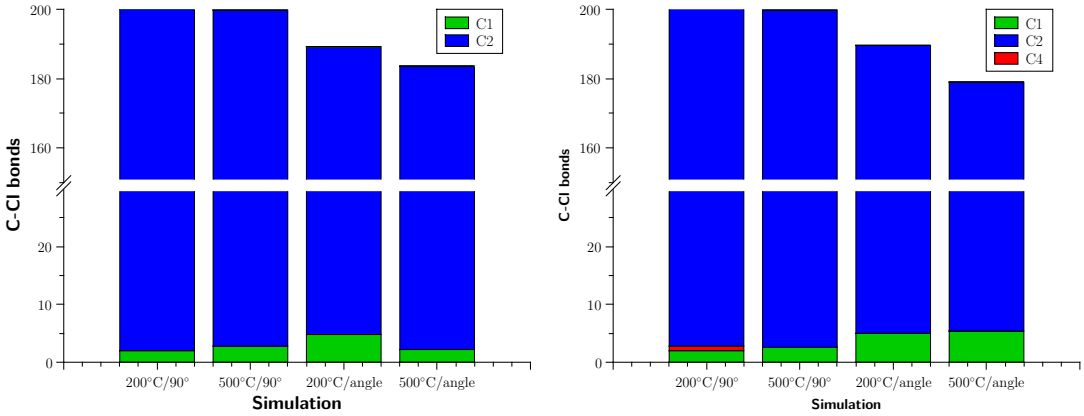

(a) (b)

Figure 6.33: Number and type of bonding partners of implanted Cl for a) the (001) surface and b) the grain boundary. C1 carbon atoms have one, C2 two, and C4 four additional carbon neighbors. In the figure, the two types of studied incident angles are called 90° for an incident angle of 90° and angle for random incident angles, respectively.

6.3.4 Discussion

Several different scenarios were explored regarding the insertion and diffusion of chlorine in models of nuclear graphite. When Cl acts as a PKA in bulk graphite, the obtained cascades are similar to displacement cascades with a C as PKA found in the literature [CBPB15, CRR+15]. However, displacement cascades in bulk neglect the finite size of the real material. There are two cases where surface penetration is relevant. First, when the Cl atom is implanted into graphite. Second, when a PKA propagates through polycrystalline graphite it can leave and reenter graphite crystals. For the (001) surface, this surface effect is the more important the lower the energy of the PKA is. For higher energies, this energy loss is negligible compared to the remaining kinetic energy, in fact even more defects are created. This indicates that the energy needed to displace atoms is lower close to the surface than in the bulk. Bulk cascades can not describe such a situation. However, it is clear that this difference gets smaller for experimental PKA energies of hundreds of keV where the PKA propagates and creates defects hundreds of nm deep in the bulk.

The finite size of crystallites also leads to different locations where the PKA can enter the bulk material. The (100), (110), and studied reconstructed surfaces have large zones of unoccupied interlayer space where the PKA can enter the bulk with almost no loss of energy. The channeling effect is most easily observed for the irradiation of these surfaces with an incident angle of 90°. This leads to more spread out microstructural damage with respect to bulk depth. This is due to the fact that for this incident angle the cascade can be interrupted by channeling in

the ⟨0001⟩ direction and continued deeper in bulk several times. For all studied surfaces, an incident angle of <90° creates damage closer to the surface due to the PKA's propagation direction. Compared to the (001) surface, all other surfaces show higher slopes of the fitted functions. This indicates that an easier surface penetration without significant energy loss is possible at high PKA energies. This effect is intensified with an increasing temperature as can be deduced from the higher slopes of the fit functions. An analysis of different defect distributions showed that channeling can be drastically reduced when the PKA collides with surface atoms. The behavior in real systems where a large number of atoms collides with the surface will lie in between these two extreme cases.

For bulk cascades, there is no observable trend with respect to the sample temperature. This is a stark contrast to the clear increase of damage with increasing temperature for surface irradiation. This could be due to a too low sample size of bulk cascades. However, the same sample size is sufficient to reveal the trends for surface irradiation. Thus, this could also be another aspect that is not covered when replacing surface irradiations by bulk cascades. However, it should be noted that these simulations only account for the primary damage caused by the cascade. The diffusion and subsequent accumulation or the annealing of defects are processes which occur on a longer time scale. In general, they increase with temperature. Thus, the larger primary damage at higher temperature might be somewhat reduced by the increased diffusion and annealing.

Repeated irradiation of the (001) surface reveals several trends. The created disorder seems to increase the energy needed to displace atoms. Thus, less and less defects are created per PKA as the simulation progresses. The defect distribution with respect to bulk depth shows a large maximum at about 15-20 Å which shifts deeper into the bulk with an increasing number of irradiations. Visual inspection of snapshots shows that the maximum is due to the amorphization of the center region as the number of irradiations increases. The heat maps show a spherical maximum of damage in the center. This means that the amorphization is highest in the center and gradually decreases in all directions parallel to the surface. In the amorphous zone, a part of the PKA energy is dissipated without creation of new defects. This decreases the number of created defects per PKA. This is also confirmed by visual inspection of the defect distribution. Even though more point defects are created deeper in the bulk as the irradiation simulation progresses, this increase is much smaller than the growth of the amorphous center. For random incident angles, the surface damage is much more pronounced. In the center a hole is created. This indicates that more energy is transferred to the surface atoms for incident angles <90° which can then detach from the surface. However, it is possible that this effect is overestimated due to the more compact irradiation zone of the surface. For all studied irradiation types and systems, the maximum of the normalized defect distribution with respect to bulk depth shifts deeper into the bulk with an increasing number of irradiations. This is due to the extension in depth of the amorphous zone.

All these effects are increased for a higher sample temperature. As for a single irradiation, more defects are created at a higher temperature. In addition, more carbon atoms detach from the surface due to the higher thermal energy which fa-

cilitates this process. The heat maps show that a higher amount of defects is found in the center region for higher temperatures at all stages of repeated irradiation. This indicates that the amorphization of the matrix is accelerated in hotter zones.

The repeated irradiation of the grain boundary shares many trends with the (001) surface, but also shows some important differences on which this discussion will focus. It can clearly be seen that the grain boundary is the weakest spot of the crystallites. Defects are accumulated in this zone as revealed by the heat maps for an incident angle of 90°. This is not found for the (001) surface where the damage maximum is spherical. Visual inspection of snapshots shows an accumulation of defects at the grain boundary beneath the amorphous zone. An analysis of the point defect distribution created by cascades shows no strong tendency. They were located both in the grain boundary region as well as further away from the center region. These two observations together indicate that the defect accumulation could actually be due to the differences in stress in the highly disordered and the mostly undamaged zones which cause ruptures of the grain boundary. The accumulation at the grain boundary increases with an increasing sample temperature. Thus, the stress differences might be intensified due to the different thermal expansion of amorphous and graphitic zones. Depending on the angle between the grains, grain boundaries usually form in a way which minimizes the number of dangling bonds. Thus, their capability to trap radionuclides should be similar to the (001) surface. However, this is no longer true when irradiation damage causes defects to accumulate at grain boundaries. A preferential trapping at grain boundaries could then be simply a consequence of the higher abundance of trapping sites in this region.

For random angles, surface deterioration is dominant and mostly masks other effects found for an incident angle of 90°. 4-5 more carbon atoms detach from the surface which shows that for random angles more energy is transferred into kinetic energy of carbon atoms which can then detach. Both, the (001) surface and the grain boundary deteriorate in a similar manner.

For both systems, the defect accumulation changes the macroscopic dimensions. Contraction along the directions parallel to the graphene planes is observed. Usually, this is explained by the creation of vacancy lines [TH07, MH12]. However, the studied system is too small to observe this phenomenon. In the present case the contraction is likely due to the highly amorphous zone where bonds have many different orientations instead of the high order of graphene planes. The expansion in the direction perpendicular to the graphene planes is also due to this highly disordered amorphous zone. As the amorphous zone grows it deforms the surface which expands toward the vacuum. This results in an overall expansion along this direction.

At this stage, it should be pointed out that these effects are in general only valid for the studied energy range of 0.5 keV-2.5 keV. The single irradiations at higher energies showed that the microstructural damage is far more spread out in depth. In the reactor, the kinetic energies of neutrons are distributed over a large range with a maximum at about 2 MeV. Thus, the accumulation close to the surface and subsequent amorphization will be less pronounced under reactor conditions. However, the general trends agree with experimental observations. An analysis of

Cl-implanted nuclear graphite by Raman spectroscopy showed an increase of the defect band D3 which is interpreted as an increased amorphization of the sample [ARV+10].

The heterogeneous distribution of Cl in virgin nuclear graphite shows that Cl prefers specific locations even before the material is irradiated. The obtained results for the diffusion of Cl in models of nuclear graphite can be interpreted with respect to this case. However, the diffusion simulations in non-irradiated structures need to be considered. The results for the different crystallite edges confirm the *ab initio* findings. All surfaces with dangling bonds can act as traps. However, the trapping at edges does not only depend on the surface type, but also on the availability of said edges. Other impurities compete with Cl to saturate these edges. Some of these, such as H and O, are present at higher concentrations (both are found in the cooling gas in reactors) and can also form stronger bonds with the surface (for O this is true for a double bond). While this interplay of different species can not be simulated with the used potential, the behavior for a high occupation number (and thus low availability of trapping sites) shows that trapping is hindered for a large part of the Cl atoms.

These free Cl atoms can diffuse toward other zones of the material. This complexity can not be covered by studying the diffusion along one single type of surface. Many different sites are represented in the model of nanoporous graphite. This model describes a filler particle of nuclear graphite which is a polycrystalline material. This means that surfaces with and without dangling bonds are in coexistence and "competition" to interact with the Cl atoms. The use of a complex polycrystalline model system confirmed the *ab initio* results: As soon as a Cl atom passes an edge carbon with a dangling bond, it gets trapped. If it is not yet trapped, it diffuses through the pores along the (001) surface of the crystallites. In addition to these two predicted results, a third unknown process was discovered: The Cl atoms show a tendency to migrate toward the corners of nanopores where two different crystallites are only separated by several Å. The stability of this state as well as the barrier of release should be subject of further studies.

In experiments, Cl was sometimes implanted into graphite (HOPG or samples of UNGG graphite) to investigate the effects of irradiation damage on Cl release. In general these experiments show that the Cl is covalently bound to the graphite matrix and does not migrate after the implantation. This is perfectly confirmed by the performed simulations of repeated irradiation. The Cl damages the matrix which creates dangling bonds. These dangling bonds then act as traps for the Cl. The formed C-Cl bonds are strong enough to keep the Cl in place, thus no diffusion of Cl is observed. The Cl atoms are mostly found in the heavily damaged zone. This is due to two reasons. First, the amount of traps is the highest in this region. Second, the more this zone gets disordered, the more difficult it is for Cl to pass this region without losing its kinetic energy since channels are more and more blocked.

Since the large majority of Cl is bound to under-coordinated carbon atoms, it is clear that heating (and as a consequence annealing of defects) will release the Cl. Once there are no more bonding partners in the bulk, it will diffuse toward the edges and be released since it is not stable between intact sheets of graphite.

6.4 Summary and Conclusion

Large-scale models of nuclear graphite were used to study the insertion and diffusion of ^{3}H and ^{36}Cl in this material.

For H, diffusion along surfaces with dangling bonds for a low H concentration was simulated. For the studied cases, the *ab initio* findings were confirmed. All surfaces with dangling bonds can serve as traps. This further solidifies Kanashenko's hypothesis with respect to the second hydrogen trap of nuclear graphite. However, the existence of H_2 in the gas phase even though there are traps available indicates a barrier for concerted H_2 dissociation and surface trapping.

For Cl, several processes were studied: bulk cascades, surface irradiation, grain boundary irradiation as well as diffusion along the edges of crystallites and in nanoporous polycrystalline graphite.

For the irradiation simulations, a dependence on the incident angle of irradiation, the graphite temperature during irradiation and the PKA energy was investigated. It was shown that bulk cascades can not fully replace explicit irradiation of surfaces. While no dependence on temperature was found for bulk cascades, surface irradiation at higher temperature consistently created more damage. Channeling is more probable to occur for irradiation of the (100), (110) or reconstructed surfaces compared to the (001) surface. This is due to the $\langle 0001 \rangle$ channel which is directly accessible from these surfaces. This leads to a broader distribution of defects with respect to bulk depth. For all surface irradiations, an incident angle $<90°$ created damage closer to the surface. This effect is intensified for repeated irradiation of the (001) surface, the surface damage is much greater for random incident angles. Overall, repeated irradiation of the (001) surface leads to a highly amorphous zone close to the surface and point defects deeper in bulk graphite for the considered PKA energy range. An increased sample temperature increases the amount of defects created as well as the deterioration of the surface.

Similar trends are found for repeated irradiation of a grain boundary. However, an important difference was revealed. The grain boundary is the weakest spot of the crystallites, defects accumulate in this zone. This is likely due to stress differences in the highly damaged and more ordered regions which cause a rupture of the grain boundary beneath the amorphous zone. This effect increases with temperature due to the different thermal expansion behavior of the amorphous and the ordered zone. Radionuclides could then get trapped preferentially in these zones simply due to the larger abundance of defect sites at grain boundaries.

For repeated irradiation of both, the (001) surface and the grain boundary, the defect accumulation changes the macroscopic dimensions. Contraction along the directions parallel to the graphene planes and expansion in the direction perpendicular to the graphene planes is found.

The diffusion simulations confirm the *ab initio* results, but also reveal new trends. All surfaces with dangling bonds can serve as traps for Cl. It was shown that by reducing the number of available trapping sites, Cl is partially trapped and partially diffuses through the pores. These free Cl atoms can move to other sites of the material. Several different environments coexist in the nanoporous graphite model: surfaces with and without dangling bonds as well as porosities.

The diffusion of Cl shows three different processes: The first two are the trapping at available sites on crystallites edges with dangling bonds and free diffusion along the (001) surface of crystallites. The third and previously unknown process is migration toward the corners of nanopores.

Implanted Cl atoms immediately forms bonds with surrounding defect sites and shows no diffusion within the bulk. This is consistent with experimental evidence [VTM$^+$09]. They are concentrated in the regions which are highly damaged by irradiation. The experimentally observed release by heating is due to annealing of defects. When the graphene planes are rebuilt, Cl is no longer stable in bulk graphite and diffuses toward the crystallite edges where it is released into the pores.

General Conclusion and Perspectives

This work contributed to the studies which try to find possible solutions for the waste management of irradiated nuclear graphite. A large amount of this material was used as moderator and reflector in the French first generation UNGG nuclear power plants leading to about 23000 t of graphite waste in France alone. Several options for waste management are evaluated: waste treatment to extract radionuclides and different types of permanent disposal. For all of these options a good knowledge of the behavior of radionuclides in the graphite is needed, *i.e.* the radiological inventory and the physico-chemical properties of the different species within the graphite. For waste treatment, knowing these properties could help finding new approaches to remove radionuclides. For permanent disposal, it could help to show the long-term safety of the sites by understanding the conditions of trapping or release of the radionuclides.

Several preceding experimental theses faced problems due to the low concentrations of the radionuclides. Thus, a modeling approach was used to offer complementary informations which are difficult to obtain experimentally. Within this work the focus was laid on two radionuclides: ^{3}H and ^{36}Cl. ^{3}H has short half-life but high activity, ^{36}Cl has a long half-life but low activity. The complex multiscale structure of nuclear graphite demanded a description of the system which can account for the processes that happen on different length scales. By using a multiscale modeling approach, processes occurring on different length and time scales have been studied.

On the smallest scale, nuclear graphite consists of graphite crystallites. The radionuclides can interact with different parts of these crystallites, *i.e.* the bulk material or surfaces, but also lattice defects which are created in high numbers by irradiation. These local interactions have been studied accurately by applying *ab initio* methods.

H can form covalent bonds with all studied surfaces, (001), (100), and (110), with bulk graphite, and also with point defects such as mono- and divacancies. New insight was gained regarding the deep trap of hydrogen in nuclear graphite. The existing hypothesis needs to be refined: The deep traps in bulk graphite can either be the zigzag or armchair edges of dislocation loops. Different surface reconstructions of graphite have been studied for the first time in order to investigate the weaker H traps located on crystallite edges. It has been shown that the trap is most likely a crystallite edge formed by an in-plane reconstruction of the (100) surface. An arch-shaped surface reconstruction was also investigated. This was a much weaker

trap compared to experiment. This is indirect evidence that the crystallite edges are mostly open in nuclear graphite. From a thermodynamic point of view, the formed bonds are very stable (on the order of several eV); a large amount of energy would be needed to break them.

In experiments both organic and inorganic Cl was found, the inorganic Cl has a lower concentration and is more easily released. This permitted to focus on the interaction of Cl and Cl_2 with bulk graphite, surfaces, and point defects. The behavior of Cl is much more complex compared to H. The interaction with graphite is strongly dependent on the site as well as on the Cl species: Cl forms strong covalent bonds with surfaces which have dangling bonds and surface vacancies (2.5-4.1 eV). Breaking of these C-Cl bonds would also need a large amount of energy.

In contrast to that, Cl interacts non-covalently with the (001) surface via charge transfer. The adsorption is weaker compared to the other surfaces (about 0.9 eV). Thus it can be more easily desorbed from this surface. When Cl_2 adsorbs on this surface, the behavior changes again. Here, only a weak van der Waals interaction is observed between the surface and Cl_2. Since it is more stable than two isolated adsorbed Cl atoms, Cl_2 formation is thermodynamically favorable. Due to the weaker interaction with the surface, desorption is much easier in this state.

In bulk graphite, both species again change their properties. Cl is not stable in bulk graphite. Cl_2 spontaneously dissociates to atomic Cl. Contrary to H, this indicates that any kind of trap is most likely located on sites which are located at the solid/gas interface where dangling bonds are prevalent.

Thus, both H and Cl can be trapped at the same sites on crystallite edges. When graphite samples are heated, Cl is only released in the form of HCl. From the *ab initio* results, three scenarios can be proposed: first, a gas phase reaction of H_2 + $Cl_2 \rightarrow$ 2 HCl. Second, an exchange reaction on crystallite edges of the type ∼C–Cl + $H_2 \rightarrow$ ∼C–H + HCl. These are thermodynamically driven reactions which are confirmed by the presented calculations. A third scenario is kinetically driven. Concerted detrapping of HCl might have a lower barrier compared to detrapping of H_2 or Cl_2. This scenario needs to be investigated further by calculating the barriers of the different detrapping reactions.

To study the insertion and diffusion of the radionuclides in nuclear graphite, an approximate interaction model has been developed which is computationally less demanding. This was an important step since these processes occur on much larger length- and time scales than what is currently achievable by *ab initio* methods. For C-Cl, a bond order potential has been developed from scratch which can correctly describe all different interactions found on the *ab initio* level. For C-H, an existing potential was modified. It can correctly describe interactions on surfaces with dangling bonds.

Diffusion simulations of H along different crystallite edges showed trapping on unsaturated surface carbon atoms. This further confirmed the existing hypothesis regarding the weaker H trap of nuclear graphite. The behavior in bulk graphite and on the (001) surface is not correctly described. Further work is needed to reparametrize the potential in order to investigate the hypothesis of the deep H trap (dislocation loops).

For Cl, several scenarios were explored: First, the insertion into models of perfect and irradiated graphite crystallites with PKA energies ranging from 0.5-10 keV. Second, the diffusion in complex models of virgin nuclear graphite and in graphite crystallites damaged by irradiation.

Displacement cascades in bulk graphite with Cl as PKA overall show the same trends as observed for displacement cascades found in the literature with C as PKA. However, it has been shown in this work that they are not able to fully replace explicit irradiation of graphite surfaces. A clear temperature dependence of the created damage is found for surface irradiation, whereas it is absent in bulk cascades. In addition, a dependence of the damage on the incident angle of the PKA is only possible to study if a solid/gas interface is included in the simulations.

For all surface irradiations, a higher temperature increases direct irradiation damage. Incident angles <90° lead to damage closer to the surface. The higher occurrence of channeling for irradiation of the (100), (110), and considered surface reconstructions with an incident angles of 90° leads to a broader distribution of defects with respect to bulk depth.

Under reactor conditions, irradiation is not a singular event. Thus, the (001) surface as well as a grain boundary have been repeatedly irradiated with PKA energies in the range of 0.5-2.5 keV to study the influence on microscopic and macroscopic properties.

Less defects are created per PKA with increasing damage of the crystallite microstructure. Repeated irradiation leads to large amorphous zones close to the surface and point defects deeper in the bulk. The amorphous zone absorbs the PKA energy partially which decreases the number of defects created per PKA. The surface deteriorates and for incident angles <90° a hole is formed due to detaching surface atoms. All these effects are intensified when the irradiation temperature is increased.

The repeated irradiation of the grain boundary has revealed a new aspect. An accumulation of defects is observed at the grain boundary beneath the amorphous zone for irradiation at an incident angle of 90°. An analysis has shown that this is most likely due to stress differences in the amorphous zone and deeper lying more ordered zones. This trend intensifies with increasing temperature. This indicates that grain boundaries can be preferred trapping sites for radionuclides simply due to the higher abundance of defects in this region. The temperature difference also shows that the trapping at these sites will be more prevalent in hotter zones.

Crystallite edges with dangling bonds act as strong traps for Cl. When the concentration of available trapping sites is lower then the concentration of Cl in the gas phase, Cl freely diffuses in the gas phase in the form of Cl_2. Bulk penetration is only observed for much higher concentrations than those found in nuclear graphite. The Cl can then freely diffuse through the pores.

Diffusion simulations in the complex model of nanoporous graphite have revealed substantial information with respect to the trapping and diffusion of Cl in nuclear graphite. Free diffusion occurs along the (001) surfaces. When Cl passes an available trapping site, it forms a bond and remains fixed. These two observations confirm the *ab initio* results. In addition, a completely unknown process was found: freely diffusing Cl shows a tendency to migrate toward the corners of nanopores

where two crystallites are only separated by several Å. In this zone, it is neither fully trapped by forming covalent bonds nor can it leave in direction of the pores without overcoming a barrier.

In irradiated graphite crystallites, Cl does not diffuse but immediately forms strong covalent bonds with the surrounding defects. It is localized in the highly damaged zone. This explains the experimental findings when Cl is implanted into graphite. When the system is heated, the defects are annealed and Cl diffuses towards the surface due to the instability in bulk graphite.

In summary, this work could confirm and extend several existing hypotheses regarding the trapping of ^{3}H and ^{36}Cl in nuclear graphite. In addition two new trapping sites are proposed: in irradiated graphite, grain boundaries can be preferred trapping sites for all radionuclides due to the higher abundance of traps. Due to the temperature dependence, grain boundaries in hotter zones will be preferred over colder zone. In addition a new metastable trap in the corners of nanopores is proposed for ^{36}Cl.

Thus, a lot of new insight was gained with respect to the trapping of ^{3}H and ^{36}Cl in nuclear graphite. However, some questions remain and also new questions were raised due to new findings.

Several scenarios were proposed which could explain the experimentally observed existence of HCl in the gas phase. The barriers of these reactions should be determined with *ab initio* methods to identify the most probable scenario.

The diffusion properties regarding the trapping of H at dislocation loops could not be studied due to the potential's shortcomings in describing the bulk diffusion. The potential should be adjusted to properly describe the bulk and surface interactions. With such a potential the complete hypothesis regarding trapping and release of H in nuclear graphite could be explored.

The reason for the heterogeneity of Cl in nuclear graphite is still somewhat unclear. Crystallite edges with dangling bonds should be distributed rather homogeneously, thus they can not solely be responsible for this phenomenon. The potential trap in corners of nanopores found in the MD simulations might play a role. Trapping and barriers of release might depend on the angle between two crystallites. If such a dependence wold be found, this could possibly explain the experimental findings of preferred trapping sites. Such a study should be performed with *ab initio* methods.

Defect accumulation at grain boundaries has been shown. This effect should be studied for larger crystallites in order to determine the size dependence of the grain boundary ruptures caused by the stress differences.

Together with the findings of this work, this would allow for a more complete understanding of all mechanisms related to the trapping an release of ^{3}H and ^{36}Cl in UNGG graphite.

List of Figures

List of Tables

Bibliography

[AB99] C. Adamo and V. Barone. Toward Reliable Density Functional Methods Without Adjustable Parameters: The PBE0 Model. *J. Chem. Phys.*, 110:6158–6170, 1999.

[ACP+93] E. Apra, M. Causa, M. Prencipe, R. Dovesi, and V. R. Saunders. On the structural properties of NaCl: an ab initio study of the B1-B2 phase transition. *Journal of Physics: Condensed Matter*, 5(18):2969, 1993.

[AF06] A. Allouche and Y. Ferro. Dissociative adsorption of small molecules at vacancies on the graphite (0001) surface. *Carbon*, 44:3320–3327, 2006.

[AFA+05] A. Allouche, Y. Ferro, T. Angot, C. Thomas, and J.-M. Layet. Hydrogen adsorption on graphite (0001) surface: A combined spectroscopy–density-functional-theory study. *J. Chem. Phys.*, 123:124701, 2005.

[AI00] H. Atsumi and M. Iseki. Hydrogen absorption process into graphite and carbon materials. *J. Nucl. Mater.*, 283-287:1053–1056, 2000.

[AIS92] H. Atsumi, M. Iseki, and T. Shikama. Hydrogen solubility and diffusivity in neutron-irradiated graphite. *J. Nucl. Mater.*, pages 368–372, 1992.

[AIS96] H. Atsumi, M. Iseki, and T. Shikama. Hydrogen behavior in carbon-based materials and its neutron irradiation effect. *J. Nucl. Mater.*, 233-237:1128–1132, 1996.

[AKNK93] E. Asari, M. Kitajima, K. G. Nakamura, and T. Kawabe. Thermal relaxation of ion-irradiation damage in graphite. *Phys. Rev. B*, 47:11143–11148, 1993.

[ALO+13] J.-J. Adjizian, C.D. Latham, S. Oberg, P.R. Briddon, and M.I. Heggie. DFT study of the chemistry of sulfur in graphite, including interactions with defects, edges and folds. *Carbon*, 62:256–262, 2013.

[AMY+05] A. Asthana, Y. Matsui, M. Yasuda, K. Kimoto, T. Iwata, and K.-I. Ohshima. Investigations on the structural disordering of neutron-irradiated highly oriented pyrolytic graphite by X-ray diffraction and electron microscopy. *J. Appl. Crystallogr.*, 38:361–367, 2005.

[And65] D. G. Anderson. Iterative Procedures for Nonlinear Integral Equations. *J. ACM*, 12:547–560, 1965.

[AND12] ANDRA. Etude des scénarios de gestion à long terme des déchets de faible activité massique à vie longue. Technical report, ANDRA, 2012.

[AND15] ANDRA. Projet de stockage de déchets radioactifs de faible activité massique à vie longue (FA-VL). Technical report, ANDRA, 2015.

[AR12] M. R. Ammar and J.-N. Rouzaud. How to obtain a reliable structural characterization of polished graphitized carbons by Raman microspectroscopy. *J. Raman Spectrosc.*, 43:207–211, 2012.

[Arn92] L. Arnold. *Windscale 1957 - Anatomy of a Nuclear Accident.* Macmillan, 1992.

[ARV+10] M.R. Ammar, J.N. Rouzaud, C.E. Vaudey, N. Toulhoat, and N. Moncoffre. Characterization of graphite implanted with chlorine ions using combined Raman microspectrometry and transmission electron microscopy on thin sections prepared by focused ion beam. *Carbon*, 48:1244 – 1251, 2010.

[ASN] ASN. `https://www.asn.fr/Informer/Dossiers-pedagogiques/Le-demantelement-des-installations-nucleaires/Les-strategies-de-demantelement-en-France/EDF-des-retards-sur-le-programme-de-demantelement`. Accessed: 2017-11-12.

[AT03] H. Atsumi and K. Tauchi. Hydrogen absorption and transport in graphite materials. *J. Alloy. Compd.*, 356-357:705–709, 2003.

[ATM88] H. Atsumi, S. Tokura, and M. Miyake. Absorption and desorption of deuterium on graphite at elevated temperatures. *J. Nucl. Mater.*, 155-157:241–245, 1988.

[ATM+13] H. Atsumi, Y. Takemura, T. Miyabe, T. Konishi, T. Tanabe, and T. Shikama. Desorption of hydrogen trapped in carbon and graphite. *Journal of Nuclear Materials*, 442:S746–S750, 2013.

[Ats02] H. Atsumi. Hydrogen bulk retention in graphite and kinetics of diffusion. *J. Nucl. Mater.*, 307-311:1466–1470, 2002.

[Ats03] H. Atsumi. Hydrogen retention in graphite and carbon materials under a fusion reactor environment. *J. Nucl. Mater.*, 313-316:543–547, 2003.

[ATS11] H. Atsumi, T. Tanabe, and T. Shikama. Hydrogen behavior in carbon and graphite before and after neutron irradiation – Trapping, diffusion and the simulation of bulk retention. *Journal of Nuclear Materials*, 417:633–636, 2011.

[Ave05] J. Averous. Le démantèlement des installations nucléaires : le nouveau panorama. DGSNR - Installations de recherche, démantèlement, sites pollués, déchets. Technical report, Cour des Comptes, 75 - Paris (France), 2005.

[Bak70] D. E. Baker. Graphite as a Neutron Moderator and Reflector Material. *Nuclear Engineering and Design*, 14:413–444, 1970.

[Bak80] R.T.K. Baker. *Gas chemistry in nuclear reactors and large industrial plant*, pages 18–25. John Wiley 'I&' Sons Ltd, 1980.

[Bal62] M. Balarin. Fokussierungsbedingung für elastische Atomstöße in Graphit. *Physica status solidi (B)*, 2:60–72, 1962.

[Bas89] D. Bastien. Twenty-nine years of French experience in operating gas-cooled reactors. Technical report, IAEA, 1989.

[Bas93] D. Bastien. Réacteur à uranium naturel-graphite-gaz. *Techniques de l'ingénieur [Archives] Génie nucléaire*, B3180v1:1–7, 1993.

[Bas96] D. Bastien. French activities on gas cooled reactors. Technical report, IAEA, 1996.

[BB70] S.F. Boys and F. Bernardi. The Calculation of Small Molecular Interactions by the Differences of Separate Total Energies. Some Procedures with Reduced Errors. *Mol. Phys.*, 19:553–566, 1970.

[BB00] I. Brésard and J.-P. Bonal. Caractérisation mécanique, chimique et radiologique du graphite des réacteurs de la filière UNGG. Technical report, CEA/DMT/SERMA & CEA/DMT/SEMI, 2000.

[BB06] B. Barré and B. Bonin. Gas-cooled nuclear reactors. Technical report, CEA, 2006.

[BBO+83] B. R. Brooks, R. E. Bruccoleri, B.D. Olafson, D. J. States, S. Swaminathan, and M. Karplus. CHARMM: A program for macromolecular energy, minimization, and dynamics calculations. *Journal of Computational Chemistry*, 4:187–217, 1983.

[BBP02] J.-P. Bonal, I. Brésard, and S. Parraud. Caractérisation du graphite des réacteurs de la filière UNGG. In *Matériaux*, 2002.

[BC80] A. Blanchard and P. Campion. *Gas chemistry in nuclear reactors and large industrial plant*, pages 90–97. John Wiley 'I&' Sons Ltd, 1980.

[BC07] L. Van Brutzel and J.P. Crocombette. Classical molecular dynamics study of primary damage created by collision cascade in a ZrC matrix. *Nuclear Instruments and Methods in Physics Research Section B: Beam Interactions with Materials and Atoms*, 255:141 – 145, 2007.

[BCC+98] L. X. Benedict, N. G. Chopra, M. L. Cohen, A. Zettl, S. G. Louie, and V. H. Crespi. Microscopic Determination of the Interlayer Binding Energy in Graphite. *Chem. Phys. Lett.*, 286:490 – 496, 1998.

[Bec93] A. D. Becke. Density-Functional Thermochemistry. III. The Role of Exact Exchange. *J. Chem. Phys.*, 98:5648–5652, 1993.

[BHLA10] To. Bučko, J. Hafner, S. Lebègue, and J. G. Ángyán. Improved Description of the Structure of Molecular and Layered Crystals: Ab Initio DFT Calculations with van der Waals Corrections. *J. Phys. Chem. A*, 114:11814–11824, 2010.

[BJW+09] R. Balog, B. Jørgensen, J. Wells, E. Lægsgaard, P. Hofmann, F. Besenbacher, and L. Hornekær. Atomic Hydrogen Adsorbate Structures on Graphene. *J. Am. Chem. Soc.*, 131:8744–8745, 2009.

[BKK11a] F. Banhart, J. Kotakoski, and A. V. Krasheninnikov. Structural Defects in Graphene. *ACS Nano*, 5:26–41, 2011.

[BKK11b] F. Banhart, J. Kotakoski, and A. V. Krasheninnikov. Structural Defects in Graphene. *ACS Nano*, 5:26–41, 2011.

[BKL08] D. W. Boukhvalov, M. I. Katsnelson, and A. I. Lichtenstein. Hydrogen on graphene: Electronic structure, total energy, structural distortions and magnetism from first-principles calculations. *Phys. Rev. B*, 77:035427, 2008.

[Bla84] R. Blanchard. Impuretés dans le caloporteur CO_2 des centrales de Saint-Laurent, campagnes de mesures 1972-1973 et 1983-1984. Internal technical document. Technical report, EDF, 1984.

[Blo13] A. Blondel. *Effets de la température et de l'irradiation sur le comportement du chlore 37 dans le graphite nucléaire : Conséquences sur la mobilité du chlore 36 dans les graphites irradiés.* PhD thesis, Université de Lyon, 2013.

[BLOD01] Ph. Baranek, A. Lichanot, R. Orlando, and R. Dovesi. Structural and Vibrational Properties of Solid $Mg(OH)_2$ and $Ca(OH)_2$ – Performances of Various Hamiltonians. *Chem. Phys. Lett.*, 340:362–369, 2001.

[BM55] Y. Baskin and L. Meyer. Lattice Constants of Graphite at Low Temperatures. *Phys. Rev.*, 100:544–544, 1955.

[BMT+14] A. Blondel, N. Moncoffre, N. Toulhoat, N. Bérerd, G. Silbermann, P. Sainsot, J.-N. Rouzaud, and D. Deldicque. New advances on the thermal behaviour of chlorine in nuclear graphite. *Carbon*, 73:413 – 420, 2014.

[BMTP07] M. Bonfanti, R. Martinazzo, G. F. Tantardini, and A. Ponti. Physisorption and Diffusion of Hydrogen Atoms on Graphite from Correlated Calculations on the H-Coronene Model System. *The Journal of Physical Chemistry C*, 111:5825–5829, 2007.

[BN07] C. Björkas and K. Nordlund. Comparative study of cascade damage in Fe simulated with recent potentials. *Nuclear Instruments and Methods in Physics Research Section B: Beam Interactions with Materials and Atoms*, 259:853 – 860, 2007.

[BPW99] F.J. Brown, J.D. Palmer, and P. Wood. Derivation of a radionuclide inventory for irradiated graphite-chlorine-36 inventory determination. pages 1 – 10. 1999.

[BSA+09] D. Bachellerie, M. Sizun, F. Aguillon, D. Teillet-Billy, N. Rougeau, and V. Sidis. Unrestricted study of the Eley-Rideal formation of H_2 on graphene using a new multidimensional graphene-H-H potential: role of the substrate. *Phys. Chem. Chem. Phys.*, 11:2715–2729, 2009.

[BSH+02] D. W. Brenner, O. A. Shenderova, J. A. Harrison, S. J. Stuart, B. Ni, and S. B. Sinnott. A second-generation reactive empirical bond order (REBO) potential energy expression for hydrocarbons. *Journal of Physics: Condensed Matter*, 14(4):783, 2002.

[CB] Alain Chartier and Laurent Van Brutzel. Personal communications.

[CBPB15] A. Chartier, L. Van Brutzel, B. Pannier, and Ph. Baranek. Atomic scale mechanisms for the amorphisation of irradiated graphite. *Carbon*, 91:395 – 407, 2015.

[CCB+95] W. D. Cornell, P. Cieplak, C. I. Bayly, I. R. Gould, K. M. Merz, D. M. Ferguson, D. C. Spellmeyer, T. Fox, J. W. Caldwell, and P. A. Kollman. A Second Generation Force Field for the Simulation of Proteins, Nucleic Acids, and Organic Molecules. *Journal of the American Chemical Society*, 117:5179–5197, 1995.

[CCPC07] L. Chen, A. C. Cooper, G. P. Pez, and H. Cheng. Mechanistic Study on Hydrogen Spillover onto Graphitic Carbon Materials. *J. Phys. Chem. C*, 111:18995–19000, 2007.

[ČF09] J. Červenka and C. F. J. Flipse. Structural and electronic properties of grain boundaries in graphite: Planes of periodically distributed point defects. *Phys. Rev. B*, 79:195429, 2009.

[CLMT09] S. Casolo, O. M. Løvvik, R. Martinazzo, and G. F. Tantardini. Understanding adsorption of hydrogen atoms on graphene. *J. Chem. Phys.*, 130:054704, 2009.

[Cor81] P. Cornuault. Modérateurs, Graphite. *Techniques de l'Ingenieur [Archives] Génie nucléaire*, B3680, 1981.

[CP64] C.A. Coulson and M.D. Poole. Calculations of the formation energy of vacancies in graphite crystals. *Carbon*, 2:275–279, 1964.

[CPDS93] M. Catti, A. Pavese, R. Dovesi, and V. R. Saunders. Static Lattice and Electron Properties of $MgCO_3$ (magnesite) Calculated by *Ab Initio* Periodic Hartree-Fock Methods. *Phys. Rev. B*, 47:9189–9198, 1993.

[CPR+09] G. I. Csonka, J. P. Perdew, A. Ruzsinszky, P. H. T. Philipsen, S. Lebègue, J. Paier, O. A. Vydrov, and J. G. Ángyán. Assessing the Performance of Recent Density Functionals for Bulk Solids. *Phys. Rev. B*, 79:155107, 2009.

[CRR+15] H.J. Christie, M. Robinson, D.L. Roach, D.K. Ross, I. Suarez-Martinez, and N.A. Marks. Simulating radiation damage cascades in graphite. *Carbon*, 81:105 – 114, 2015.

[CSA12] F. Costanzo, P. L. Silvestrelli, and F. Ancilotto. Physisorption, Diffusion, and Chemisorption Pathways of H_2 Molecule on Graphene and on (2,2) Carbon Nanotube by First-Principles Calculations. *J. Chem. Theor. Comp.*, 8:1288–1294, 2012.

[CZWVU08] B. Civalleri, C. M. Zicovich-Wilson, L. Valenzano, and P. Ugliengo. B3LYP Augmented with an Empirical Dispersion Term (B3LYP-D*) as Applied to Molecular Crystals. *CrystEngComm*, 10:405–410, 2008.

[DBD+95] G. E. Davico, V. M. Bierbaum, C. H. DePuy, G. B. Ellison, and R. R. Squires. The C-H Bond Energy of Benzene. *J. Am. Chem. Soc.*, 117:2590–2599, 1995.

[DCO+90] R. Dovesi, M. Causa', R. Orlando, C. Roetti, and V. R. Saunders. Ab initio Approach to Molecular Crystals: A Periodic Hartree-Fock Study of Crystalline Urea. *J. Chem. Phys.*, 92:7402–7411, 1990.

[Del00] P. Delhaes. *Graphite and Precursors*. World of carbon. Taylor & Francis, 2000.

[DGHkAt15] M. Darvish Ganji, S. M. Hosseini-khah, and Z. Amini-tabar. Theoretical insight into hydrogen adsorption onto graphene: A first-principles B3LYP-D3 study. *Phys. Chem. Chem. Phys.*, 17:2504–2511, 2015.

[Dir30] P. A. M. Dirac. Note on Exchange Phenomena in the Thomas Atom. *Math. Proc. Cambridge Philos. Soc.*, 26:376–385, 1930.

[DJ89] T. H. Dunning Jr. Gaussian basis sets for use in correlated molecular calculations. I. The atoms boron through neon and hydrogen. *The Journal of Chemical Physics*, 90:1007–1023, 1989.

[DM82] A. Dyer and G. E. Moorse. The radiolysis of simple gas mixtures–I: Rates of production and destruction of methane in mixtures with carbon dioxide as a major constituent. *Radiation Physics and Chemistry (1977)*, 20:315 – 321, 1982.

[DMN+04] W. A. Diño, Y. Miura, H. Nakanishi, H. Kasai, T. Sugimoto, and T. Kondo. H_2 dissociative adsorption at the armchair edges of graphite. *Solid State Commun.*, 132:713–718, 2004.

[DNK+04] W. A. Diño, H. Nakanishi, H. Kasai, T. Sugimoto, and T. Kondo. H_2 Dissociative Adsorption at the Zigzag Edges of Graphite. *J. Surf. Sci. Nanotechnol.*, 2:77–80, 2004.

[DOC+05] R. Dovesi, R. Orlando, B. Civalleri, C. Roetti, V. R. Saunders, and C. M. Zicovich-Wilson. CRYSTAL: A Computational Tool for *ab initio* Study of the Electronic Properties of Crystals. *Z. Kristallogr.*, 220:571–573, 2005.

[Dol06] K. Doll. Calculation of the work function with a local basis set. *Surface Science*, 600:L321 – L325, 2006.

[Don74] J. Donohue, editor. *The Structures of Elements*. Wiley, New York, 1974.

[DP01] D. A. Dixon and K. A. Peterson. Heats of formation of CCl and CCl_2 from ab initio quantum chemistry. *The Journal of Chemical Physics*, 115:6327–6329, 2001.

[DP10] Sudipta D. and Swapan K. P. Edge reconstructions induce magnetic and metallic behavior in zigzag graphene nanoribbons. *Carbon*, 48:4409–4413, 2010.

[dPRMIM02] I. de P. R. Moreira, F. Illas, and R. L. Martin. Effect of Fock exchange on the Electronic Structure and Magnetic Coupling in NiO. *Phys. Rev. B*, 65:155102, 2002.

[DSL04] E. J. Duplock, M. Scheffler, and P. J. D. Lindan. Hallmark of Perfect Graphene. *Phys. Rev. Lett.*, 92:225502, 2004.

[DSR+09] R. Dovesi, V. R. Saunders, C. Roetti, R. Orlando, C. M. Zicovich-Wilson, F. Pascale, B. Civalleri, K. Doll, N. M. Harrison, I. J. Bush, Ph. D'Arco, and M. Llunell. *CRYSTAL09 User's Manual*. University of Torino, Torino, 2009.

[EDF67] EDF. Corrosion radiolytique du graphite - Interprétation des résultats d'analyses du gaz caloporteur dans les centrales EDF 1 et EDF 2. Technical Report C 34-04, EDF/Service d'Etudes Générales Nucléaires., 1967.

[END] Endf: Evaluated nuclear data file - IAEA nuclear data services. `https://www-nds.iaea.org/exfor/endf.htm`. Accessed: 2017-10-20.

[FDC10] R. M. Ferullo, N. F. Domancich, and N. J. Castellani. On the performance of van der Waals corrected-density functional theory in describing the atomic hydrogen physisorption on graphite. *Chem. Phys. Lett.*, 500:283–286, 2010.

[FMA03] Y. Ferro, F. Marinelli, and A. Allouche. Density functional theory investigation of the diffusion and recombination of H on a graphite surface. *Chem. Phys. Lett.*, 368:609–615, 2003.

[FNP80] R. L. Faircloth, K. S. Norwood, and H. A. Prior. Coolant chemistry of the advanced carbon dioxide cooled reactor. Technical report, IAEA, 1980.

[FPH+82] M. M. Francl, W. J. Pietro, W. J. Hehre, J. S. Binkley, M. S. Gordon, D. J. DeFrees, and J. A. Pople. Self-consistent molecular orbital methods. XXIII. A polarization-type basis set for second-row elements. *The Journal of Chemical Physics*, 77:3654–3665, 1982.

[FS96] D. Frenkel and B. Smit. *Understanding Molecular Simulation: From Algorithms to Applications*. Academic Press, 1996.

[GAEK10] S. Grimme, J. Antony, S. Ehrlich, and H. Krieg. A Consistent and Accurate Ab Initio Parametrization of Density Functional Dispersion Correction (DFT-D) for the 94 elements H-Pu. *J. Chem. Phys.*, 132:154104, 2010.

[Gau86] M. Gauthron. *Introduction au génie nucléaire: Neutronique et matériaux*. Collection Enseignement - INSTN CEA. Institut national des sciences et techniques nucléaires, 1986.

[GBB+09] P. Giannozzi, S. Baroni, N. Bonini, M. Calandra, R. Car, C. Cavazzoni, D. Ceresoli, G. L .Chiarotti, M. Cococcioni, I. Dabo, A. Dal Corso, S. de Gironcoli, S. Fabris, G. Fratesi, R. Gebauer, U. Gerstmann, C. Gougoussis, A. Kokalj, M. Lazzeri, L. Martin-Samos, N. Marzari, F. Mauri, R. Mazzarello, S. Paolini, A. Pasquarello, L. Paulatto, C. Sbraccia, S. Scandolo, G. Sclauzero, A. P. Seitsonen, A. Smogunov, P. Umari, and R M. Wentzcovitch. QUANTUM ESPRESSO: A Modular and Open-Source Software Project for Quantum Simulations of Materials. *J. Phys.: Condens. Matter*, 21:395502, 2009.

[GDLK11] L. Gan, H. Du, B. Li, and F. Kang. Surface-reconstructed graphite nanofibers as a support for cathode catalysts of fuel cells. *Chem. Commun.*, 47:3900–3902, 2011.

[GMT+16] M. Le Guillou, N. Moncoffre, N. Toulhoat, Y. Pipon, M.R. Ammar, J.N. Rouzaud, and D. Deldicque. Thermal migration of deuterium implanted in graphite: Influence of free surface proximity and structure. *Nuclear Instruments and Methods in Physics Research Section B: Beam Interactions with Materials and Atoms*, 371:307 – 311, 2016.

[Got97] Y. Gotoh. Interlayer structure changes of graphite after hydrogen ion irradiation. *J. Nucl. Mater.*, 248:46 – 51, 1997.

[GPS+13] R. Golesorkhtabar, P. Pavone, J. Spitaler, P. Puschnig, and C. Draxl. ElaStic: A tool for Calculating Second-Order Elastic Constants from First Principles. *Comput. Phys. Commun.*, 184:1861 – 1873, 2013.

[Gri04] S. Grimme. Accurate Description of van der Waals Complexes by Density Functional Theory Including Empirical Corrections. *J. Comput. Chem.*, 25:1463–1473, 2004.

[Gri06] S. Grimme. Semiempirical GGA-Type Density Functional Constructed with a Long-Range Dispersion Correction. *J. Comput. Chem.*, 27:1787–1799, 2006.

[Gri15] S. Grimme. DFT-D3 - a Dispersion Correction for Density Functionals, Hartree-Fock and Semi-Empirical Quantum Chemical Methods. `http://www.thch.uni-bonn.de/tc/index.php?section=downloads&subsection=DFT-D3&lang=english`, 2015. [Online; accessed 30-July-2015].

[GTP+14] M. Le Guillou, N. Toulhoat, Y. Pipon, N. Moncoffre, N. Bérerd, A. Perrat-Mabilon, and R. Rapegno. Thermal behavior of deuterium implanted into nuclear graphite studied by NRA. *Nuclear Instruments and Methods in Physics Research Section B: Beam Interactions with Materials and Atoms*, 332:90 – 94, 2014.

[GTP+15] M. Le Guillou, N. Toulhoat, Y. Pipon, N. Moncoffre, and H. Khodja. Deuterium migration in nuclear graphite: Consequences for the behavior of tritium in CO_2-cooled reactors and for the decontamination of irradiated graphite waste. *Journal of Nuclear Materials*, 461:72 – 77, 2015.

[Ham79] D. R. Hamann. Semiconductor Charge Densities with Hard-Core and Soft-Core Pseudopotentials. *Phys. Rev. Lett.*, 42:662–665, 1979.

[HDS96] W. Humphrey, A. Dalke, and K. Schulten. VMD – Visual Molecular Dynamics. *Journal of Molecular Graphics*, 14:33–38, 1996.

[Hen52] G. Hennig. The Properties of the Interstitial Compounds of Graphite. III. The Electrical Properties of the Halogen Compounds of Graphite. *The Journal of Chemical Physics*, 20:1443–1447, 1952.

[HHJ+98] A. Halkier, T. Helgaker, P. Jørgensen, W. Klopper, H. Koch, J. Olsen, and A. K. Wilson. Basis-set convergence in correlated calculations on Ne, N_2, and H_2O. *Chemical Physics Letters*, 286:243 – 252, 1998.

[HK99] J. R. Hahn and H. Kang. Vacancy and interstitial defects at graphite surfaces: Scanning tunneling microscopic study of the structure, electronic property, and yield for ion-induced defect creation. *Phys. Rev. B*, 60:6007–6017, 1999.

[HKSJ96] J. R. Hahn, H. Kang, S. Song, and I. C. Jeon. Observation of charge enhancement induced by graphite atomic vacancy: A comparative STM and AFM study. *Phys. Rev. B*, 53:R1725–R1728, 1996.

[HLR82] N. A. W. Holzwarth, S. G. Louie, and S. Rabii. X-ray Form Factors and the Electronic Structure of Graphite. *Phys. Rev. B*, 26:5382–5390, 1982.

[HP73] P.C. Hariharan and J.A. Pople. *Theoretica chimica acta*, 28:213–222, 1973.

[HR10] C. P. Herrero and R. Ramírez. Diffusion of hydrogen in graphite: a molecular dynamics simulation. *Journal of Physics D: Applied Physics*, 43:255402, 2010.

[HRX+06] L. Hornekær, E. Rauls, W. Xu, Ž. Šljivančanin, R. Otero, I. Stensgaard, E. Lægsgaard, B. Hammer, and F. Besenbacher. Clustering of Chemisorbed H(D) Atoms on the Graphite (0001) Surface due to Preferential Sticking. *Phys. Rev. Lett.*, 97:186102, 2006.

[HS52] M.R. Hestenes and E. Stiefel. Methods of Conjugate Gradients for Solving Linear Systems. *J. Res. Natl. Bur. Stand.*, 49:409–436, 1952.

[HSMDH11] M.I. Heggie, I. Suarez-Martinez, C. Davidson, and G. Haffenden. Buckle, ruck and tuck: A proposed new model for the response of graphite to neutron irradiation. *J. Nucl. Mater.*, 413:150 – 155, 2011.

[HŠX+06] L. Hornekær, Ž. Šljivančanin, W. Xu, R. Otero, E. Rauls, I. Stensgaard, E. Lægsgaard, B. Hammer, and F. Besenbacher. Metastable Structures and Recombination Pathways for Atomic Hydrogen on the Graphite (0001) Surface. *Phys. Rev. Lett.*, 96:156104, 2006.

[HYX+12] Z. He, X. Yang, H. Xia, T. Z. Regier, D. K. Chevrier, X. Zhou, and T. K. Sham. Role of defect electronic states in the ferromagnetism in graphite. *Phys. Rev. B*, 85:144406, 2012.

[IAE98] IAEA. Radiological charaterization of shut down nuclear reactors for decommissioning purposes. Technical report, IAEA, 1998.

[IAE00] IAEA. Irradiation Damage in Graphite Due to Fast Neutrons in Fission and Fusion Systems. Iaea-tecdoc-1154, IAEA, 2000.

[IAE06] IAEA. Characterization, Treatment and Conditioning of Radioactive Graphite from Decommissioning of Nuclear Reactors. Iaea-tecdoc-1521, IAEA, 2006.

[IB82] G. D. Purvis III and R. J. Bartlett. A full coupled-cluster singles and doubles model: The inclusion of disconnected triples. *The Journal of Chemical Physics*, 76:1910–1918, 1982.

[icvF09] J. Červenka and C. F. J. Flipse. Structural and electronic properties of grain boundaries in graphite: Planes of periodically distributed point defects. *Phys. Rev. B*, 79:195429, 2009.

[IF61] K. Izui and F. E. Fujita. Observation of Lattice Defects in Fission Fragment-irradiated Graphite. *J. Phys. Soc. Jpn.*, 16:1032–1033, 1961.

[IZTB+10] V. V. Ivanovskaya, A. Zobelli, D. Teillet-Billy, N. Rougeau, V. Sidis, and P. R. Briddon. Hydrogen adsorption on graphene: A first-principles study. *Eur. Phys. J. B*, 76:481–486, 2010.

[IZW15] Niranjan V. I., J. A. Zimmerman, and B. M. Wong. Breaking Badly: DFT-D2 Gives Sizeable Errors for Tensile Strengths in Palladium-Hydride Solids. *Journal of Chemical Theory and Computation*, 11:5426–5435, 2015.

[Jen06] F. Jensen. *Introduction to Computational Chemistry*. Wiley, 2006.

[JJS57] R. Juza, P. Jönck, and A. Schmeckenbecher. Bildung und Eigenschaften des Chlorgraphits. *Zeitschrift für anorganische und allgemeine Chemie*, 292:34–45, 1957.

[JS99] L. Jeloaica and V. Sidis. DFT investigation of the adsorption of atomic hydrogen on a cluster-model graphite surface. *Chem. Phys. Lett.*, 300:157–162, 1999.

[KDJH92] R. A. Kendall, T. H. Dunning Jr, and R. J. Harrison. Electron affinities of the first-row atoms revisited. Systematic basis sets and wave functions. *The Journal of Chemical Physics*, 96:6796–6806, 1992.

[Kel81] B.T. Kelly. *Physics of Graphite*. Applied Science, 1981.

[KGC+96] S.L. Kanashenko, A.E. Gorodetsky, V.N. Chernikov, A.V. Markin, A.P. Zakharov, B.L. Doyle, and W.R. Wampler. Hydrogen adsorption on and solubility in graphites. *J. Nucl. Mater.*, 233-237:1207–1212, 1996.

[KIYL11] Y. Kim, J. Ihm, E. Yoon, and G.-D. Lee. Dynamics and stability of divacancy defects in graphene. *Phys. Rev. B*, 84:075445, 2011.

[KJ08] J. Kerwin and B. Jackson. The sticking of H and D atoms on a graphite (0001) surface: The effects of coverage and energy dissipation. *J. Chem. Phys.*, 128:084702, 2008.

[KLFN06] A.V. Krasheninnikov, P.O. Lehtinen, A.S. Foster, and R.M. Nieminen. Bending the rules: Contrasting vacancy energetics and migration in graphite and carbon nanotubes. *Chemical Physics Letters*, 418:132–136, 2006.

[KMH08] P. Koskinen, S. Malola, and H. Häkkinen. Self-Passivating Edge Reconstructions of Graphene. *Phys. Rev. Lett.*, 101:115502, 2008.

[KN10] A.V. Krasheninnikov and K. Nordlund. Ion and Electron Irradiation-Induced Effects in Nanostructured Materials. *J. Appl. Phys.*, 107:071301, 2010.

[KObuQF11] J. Kunstmann, C. Özdoğan, A. Quandt, and H. Fehske. Stability of edge states and edge magnetism in graphene nanoribbons. *Phys. Rev. B*, 83:045414, 2011.

[KP88] E. Kaxiras and K. C. Pandey. Energetics of defects and diffusion mechanisms in graphite. *Phys. Rev. Lett.*, 61:2693–2696, 1988.

[KP94] S. Kristyán and P. Pulay. Can (semi)local Density Functional Theory Account for the London Dispersion Forces? *Chem. Phys. Lett.*, 229:175 – 180, 1994.

[LBD+07] F. Labat, Ph. Baranek, C. Domain, C. Minot, and C. Adamo. Density Functional Theory Analysis of the Structural and Electronic Properties of Tio_2 Rutile and Anatase Polytypes: Performances of Different Exchange-Correlation Functionals. *J. Chem. Phys.*, 126:154703, 2007.

[LBV18] C. Lechner, Ph. Baranek, and H. Vach. Adsorption of atomic hydrogen on defect sites of graphite: Influence of surface reconstruction and irradiation damage. *Carbon*, 127:437 – 448, 2018.

[LF03] J. H. Los and A. Fasolino. Intrinsic long-range bond-order potential for carbon: Performance in Monte Carlo simulations of graphitization. *Phys. Rev. B*, 68:024107, 2003.

[LF11] Y. Lu and Y. P. Feng. Adsorptions of hydrogen on graphene and other forms of carbon structures: First-principles calculations. *Nanoscale*, 3:2444–2453, 2011.

[LFM+04] P. O. Lehtinen, A. S. Foster, Yuchen Ma, A. V. Krasheninnikov, and R. M. Nieminen. Irradiation-Induced Magnetism in Graphite: A Density Functional Study. *Phys. Rev. Lett.*, 93:187202, 2004.

[LG14] M. Le Guillou. *Migration du deutérium dans le graphite nucléaire : conséquences sur le comportement du tritium en réacteur UNGG et sur la décontamination des graphites irradiés.* PhD thesis, Université Claude Bernard - Lyon I, 2014.

[Lid91] D.R. Lide. *Handbook of Chemistry and Physics*, volume 71^{th}. CRC Press, Boston, 1990-1991.

[LOM+00] A. Lichanot, R. Orlando, G. Mallia, M. Mérawa, and R. Dovesi. VOH center in magnesium oxide: an ab initio supercell study. *Chem. Phys. Lett.*, 318:240–246, 2000.

[LPB+16] C. Lechner, B. Pannier, P. Baranek, N. C. Forero-Martinez, and H. Vach. First-Principles Study of the Structural, Electronic, Dynamic, and Mechanical Properties of HOPG and Diamond: Influence of Exchange–Correlation Functionals and Dispersion Interactions. *J. Phys. Chem. C*, 120:5083–5100, 2016.

[LRR05] L. Li, S. Reich, and J. Robertson. Defect energies of graphite: Density-functional calculations. *Phys. Rev. B*, 72:184109, 2005.

[Luo02] Y.R. Luo. *Handbook of Bond Dissociation Energies in Organic Compounds.* CRC Press, 2002.

[Luo07] Y. R. Luo. *Comprehensive Handbook of Chemical Bond Energies.* CRC Press, 2007.

[LWY+05] G.-D. Lee, C. Z. Wang, E. Yoon, N.-M. Hwang, D.-Y. Kim, and K. M. Ho. Diffusion, Coalescence, and Reconstruction of Vacancy Defects in Graphene Layers. *Phys. Rev. Lett.*, 95:205501, 2005.

[LX04] Y. Suyuan L. Xiaowei, R. Jean-Charles. The Thermal Conductivity of Fast Neutron Irradiated Graphite. *Nuclear Engineering and Design*, 227:273–280, 2004.

[LYP88] C. Lee, W. Yang, and R. G. Parr. Development of the Colle-Salvetti Correlation-Energy Formula Into a Functional of the Electron Density. *Phys. Rev. B*, 37:785–789, 1988.

[LZX14] X.Y. Liu, J.M. Zhang, and K.W. Xu. Chlorine molecule adsorbed on graphene and doped graphene: A first-principle study. *Physica B: Condensed Matter*, 436:54 – 58, 2014.

[McD11] L. McDermott. *Characterisation and Chemical Treatment of Irradiated UK Graphite Waste.* PhD thesis, The University of Manchester, 2011.

[MCP16] M.-T. Pascal M.-C. Perrin, B. Pnocet. Livre blanc du tritium. Technical report, ASN, 2016.

[MFB+15] B.E. Mironov, H.M. Freeman, A.P. Brown, F.S. Hage, A.J. Scott, A.V.K. Westwood, J.-P. Da Costa, P. Weisbecker, and R.M.D. Brydson. Electron irradiation of nuclear graphite studied by transmission electron microscopy and electron energy loss spectroscopy. *Carbon*, 83:106 – 117, 2015.

[mgs] Grain boundary generation in Mg. `https://icme.hpc.msstate.edu/mediawiki/index.php/Grain_boundary_generation_in_Mg`. Accessed: 2017-11-24.

[MH12] B.J. Marsden and G.N. Hall. 4.11 - Graphite in Gas-Cooled Reactors. In R. J.M. Konings, editor, *Comprehensive Nuclear Materials*, pages 325 – 390. Elsevier, Oxford, 2012.

[MP76] H. J. Monkhorst and J. D. Pack. Special Points for Brillouin-Zone Integrations. *Phys. Rev. B*, 13:5188–5192, 1976.

[MS08] G.T. Miller and S. Spoolman. *Living in the Environment: Principles, Connections, and Solutions*. Cengage Learning, 2008.

[MSW95] P.C. Minshall, I.A. Sadler, and A.J. Wickham. *Graphite Moderator Lifecyle Behaviour*, chapter Radiolytic Graphite Oxidation Revisited. IAEA, 1995. IAEA-TECDOC-901.

[MTS00] A. Montoya, T. N. Truong, and A. F. Sarofim. Spin Contamination in Hartree-Fock and Density Functional Theory Wavefunctions in Modeling of Adsorption on Graphite. *The Journal of Physical Chemistry A*, 104:6108–6110, 2000.

[Nei00] G. B. Neighbour. Modelling of dimensional changes in irradiated nuclear graphites. *J. Phys. D: Appl. Phys.*, 33:2966–2972, 2000.

[Ner79] A.V. Nero. *A Guidebook to Nuclear Reactors*. University of California Press, 1979.

[NLS77] R.J. Nemanich, G. Lucovsky, and S.A. Solin. Infrared active optical vibrations of graphite. *Solid State Commun.*, 23:117 – 120, 1977.

[NNST90] K. Niwase, K. Nakamura, T. Shikama, and T. Tanabe. On the amorphization of neutron-irradiated graphite. *Journal of Nuclear Materials*, 170:106 – 108, 1990.

[NS79] R. J. Nemanich and S. A. Solin. First- and second-order Raman scattering from finite-size crystals of graphite. *Phys. Rev. B*, 20:392–401, 1979.

[NST+12] R.R. Nair, M. Sepioni, I-Ling Tsai, O. Lehtinen, J. Keinonen, A.V. Krasheninnikov, T. Thomson, A.K. Geim, and I.V. Grigoreiva. Spin-Half Paramagnetism in Graphene induced by Point Defects. *Nature Physics*, 8:199–202, 2012.

[NSW83] D.J. Norfolk, R.F. Skinner, and W.J. Williams. Hydrocarbon chemistry in irradiated $CO_2/CO/CH_4/H_2O/H_2$ mixtures—i: A survey of the initial reactions. *Radiation Physics and Chemistry (1977)*, 21:307 – 319, 1983.

[NWS72] R. Nicklow, N. Wakabayashi, and H. G. Smith. Lattice Dynamics of Pyrolytic Graphite. *Phys. Rev. B*, 5:4951–4962, 1972.

[OAR15] T. C. O'Connor, J. Andzelm, and M. O. Robbins. AIREBO-M: A reactive model for hydrocarbons at extreme pressures. *The Journal of Chemical Physics*, 142:024903, 2015.

[OGK11] N. Ota, N. Gorjizadeh, and Y. Kawazoe. Multiple Spin State Analysis in Radical Carbon Edge and Oxygen Edge Graphene-like Molecules. *Trans. Magn. Soc. Jpn.*, 35:414–419, 2011.

[Ous98] P. J. Ouseph. Observation of Prismatic Dislocation Loops in Graphite by Scanning Tunneling Microscope. *Phys. Stat. Solidi A*, 169:25–32, 1998.

[PBE96] J. P. Perdew, K. Burke, and M. Ernzerhof. Generalized Gradient Approximation Made Simple. *Phys. Rev. Lett.*, 77:3865–3868, 1996.

[PCP+15] L. Petit, J. Comte, L. Petit, S. Catherin, J. Pageot, L. Gosmain, and H. Peycelon. Référentiel graphite - Bilan des connaissances. Technical report, ANDRA, 2015.

[Pet09] L. Petit. La filière UNGG (Uranium Naturel Graphite Gaz) & Démantèlement des UNGG et gestion des déchets graphites. Technical report, Présentations EDF/R&D, 2009.

[Pet11] L. Petit. Le chlore 36 dans le graphite des centrales UNGG - état des connaissances - Projet P10W5 lot CLT. Technical report, EDF, 2011.

[PF09] G. M. Psofogiannakis and G. E. Froudakis. DFT Study of the Hydrogen Spillover Mechanism on Pt-Doped Graphite. *The Journal of Physical Chemistry C*, 113:14908–14915, 2009.

[PJB95] J.M. Pérez-Jordá and A.D. Becke. A Density-Functional Study of van der Waals forces: Rare Gas Diatomics. *Chem. Phys. Lett.*, 233:134 – 137, 1995.

[Pli95] S. Plimpton. Fast Parallel Algorithms for Short-Range Molecular Dynamics. *Journal of Computational Physics*, 117:1 – 19, 1995.

[pov15] Persistence of Vision Raytracer. `http://www.povray.org/`, 2015. [Online; accessed 16-August-2015].

[PPB93] A. Petit, C. Phalippo, and M. Brié. *The Status of Graphite Development for Gas-cooled Reactors (Proceedings of a Specialists Meeting, Tokaimura, Japan, 9-12 September 1991)*, chapter Radiolytic Corrosion of Graphite Surveillance and Lessons Drawn From the Operation of the Bugey-1 Reactor. IAEA, Vienna, 1993. IAEA-TECDOC-690.

[PRC+08] J. P. Perdew, A. Ruzsinszky, G. I. Csonka, O. A. Vydrov, G. E. Scuseria, L. A. Constantin, X. Zhou, and K. Burke. Restoring the Density-Gradient Expansion for Exchange in Solids and Surfaces. *Phys. Rev. Lett.*, 100:136406, 2008.

[PTY+05] S. Patchkovskii, J. S. Tse, S. N. Yurchenko, L. Zhechkov, T. Heine, and G. Seifert. Graphene nanostructures as tunable storage media for molecular hydrogen. *Proceedings of the National Academy of Sciences of the United States of America*, 102:10439–10444, 2005.

[PY89] R. G. Parr and W. Yang. *Density-Functional Theory of Atoms and Molecules*. Oxford Science Publications, New York, 1 edition, 1989.

[PZ81] J. P. Perdew and A. Zunger. Self-Interaction Correction to Density-Functional Approximations for Many-Electron Systems. *Phys. Rev. B*, 23:5048–5079, 1981.

[RCC+92] A. K. Rappe, C. J. Casewit, K. S. Colwell, W. A. Goddard, and W. M. Skiff. UFF, a full periodic table force field for molecular mechanics and molecular dynamics simulations. *Journal of the American Chemical Society*, 114:10024–10035, 1992.

[RCG13] A. Ramos, I. Cameán, and A. B. García. Graphitization thermal treatment of carbon nanofibers. *Carbon*, 59:2–32, 2013.

[RDN+07] T. Roman, W. A. Diño, H. Nakanishi, H. Kasai, T. Sugimoto, and K. Tange. Hydrogen pairing on graphene. *Carbon*, 45:218–220, 2007.

[RGB+02] P. Ruffieux, O. Gröning, M. Bielmann, P. Mauron, L. Schlapbach, and P. Gröning. Hydrogen adsorption on sp^2-bonded carbon: Influence of the local curvature. *Phys. Rev. B*, 66:245416, 2002.

[RKNB10] M. Rubes, J. Kysilka, P. Nachtigall, and O. Bludsky. DFT/CC investigation of physical adsorption on a graphite (0001) surface. *Phys. Chem. Chem. Phys.*, 12:6438–6444, 2010.

[RKV08] M. Ropo, K. Kokko, and L. Vitos. Assessing the Perdew-Burke-Ernzerhof Exchange-Correlation Density Functional Revised for Metallic Bulk and Surface Systems. *Phys. Rev. B*, 77:195445, 2008.

[RO89] J. N. Rouzaud and A. Oberlin. Structure, Microtexture, and Optical Properties of Anthracene and Saccharose-based Carbons. *Carbon*, 27:517–529, 1989.

[RRP+01] V. A. Rassolov, M. A. Ratner, J. A. Pople, P. C. Redfern, and L. A. Curtiss. 6-31G* basis set for third-row atoms. *Journal of Computational Chemistry*, 22(9):976–984, 2001.

[RT04] S. Reich and C. Thomsen. Raman spectroscopy of graphite. 362:2271–2288, 2004.

[RTPHG89] K. Raghavachari, G. W. Trucks, J. A. Pople, and M. Head-Gordon. A fifth-order perturbation comparison of electron correlation theories. *Chemical Physics Letters*, 157:479 – 483, 1989.

[RW60] J. P. Redmond and P. L. Walker. Hydrogen sorption on graphite at elevated temperatures. *J. Chem. Phys.*, 64(9):1093–1099, 1960.

[SB94] P. J. Steinbach and B. R. Brooks. New spherical-cutoff methods for long-range forces in macromolecular simulation. *Journal of Computational Chemistry*, 15:667–683, 1994.

[SBS+13] Gu. Sophia, Ph. Baranek, C. Sarrazin, M. Rérat, and R. Dovesi. First-Principles Study of the Mechanisms of the Pressure-Induced Dielectric Anomalies in Ferroelectric Perovskites. *Phase Transitions*, 86:1069–1084, 2013.

[SC12] H. Sahin and S. Ciraci. Chlorine Adsorption on Graphene: Chlorographene. *The Journal of Physical Chemistry C*, 116(45):24075–24083, 2012.

[SGT+02] P. Simonis, C. Goffaux, P. A. Thiry, L. P. Biro, P. Lambin, and V. Meunier. STM study of a grain boundary in graphite. *Surface Sci.*, 511:319 – 322, 2002.

[Sil13] G. Silbermann. *Temperature and irradiation effects on the behaviour of ^{14}C and its precursor ^{14}N in nuclear graphite. Study of a decontamination process using steam reforming.* PhD thesis, Université Claude Bernard - Lyon I, 2013.

[SJ02] X. Sha and B. Jackson. First-principles study of the structural and energetic properties of H atoms on a graphite (0001) surface. *Surface Science*, 496:318–330, 2002.

[SJ04] X. Sha and B. Jackson. The Location of Adsorbed Hydrogen in Graphite Nanostructures. *J. Am. Chem. Soc.*, 126:13095–13099, 2004.

[SMSH+07] I. Suarez-Martinez, G. Savini, G. Haffenden, J.-M. Campanera, and M. I. Heggie. Dislocations of Burgers vector c /2 in graphite. *Phys. Stat. Solidi C*, 4:2958–2962, 2007.

[SR96] A. P. Scott and L. Radom. Harmonic Vibrational Frequencies: An Evaluation of Hartree-Fock, Møller-Plesset, Quadratic Configuration Interaction, Density Functional Theory, and Semiempirical Scale Factors. *J. Phys. Chem.*, 100(41):16502–16513, 1996.

[ŠRH+09] Ž. Šljivančanin, E. Rauls, L. Hornekær, W. Xu, F. Besenbacher, and B. Hammer. Extended atomic hydrogen dimer configurations on the graphite (0001) surface. *J. Chem. Phys.*, 131:084706, 2009.

[SSD+15] X. Song, Y. Sun, M. Dong, C. Li, J. Wang, H. Mimura, and G. Yuan. Effects of Cl adatom on Na-Decorated graphene. *Journal of Physics D: Applied Physics*, 48:225304, 2015.

[STH00] S. J. Stuart, A. B. Tutein, and J. A. Harrison. A reactive potential for hydrocarbons with intermolecular interactions. *The Journal of Chemical Physics*, 112:6472–6486, 2000.

[STP+15] J. M. Skelton, D. Tiana, S. C. Parker, A. Togo, I. Tanaka, and A. Walsh. Influence of the Exchange-Correlation Functional on the Quasi-Harmonic Lattice Dynamics of II-VI Semiconductors. *J. Chem. Phys.*, 143:064710, 2015.

[Stu10] A. Stukowski. Visualization and analysis of atomistic simulation data with OVITO–the open visualization tool. *Modelling and Simulation in Materials Science and Engineering*, 18:015012, 2010.

[TEEBH03] R. H. Telling, C. P. Ewels, A. A. El-Barbary, and M. I. Heggie. Wigner defects bridge the graphite gap. *Nat. Mater.*, 2:333 – 337, 2003.

[Ter88] J. Tersoff. New empirical approach for the structure and energy of covalent systems. *Phys. Rev. B*, 37:6991–7000, 1988.

[TGK69] R. Taylor, K.E. Gilchrist, and B.T. Kelly. The Thermal Conductivity of Fast Neutron Irradiated Graphite. *J. Phys. Chem. Solids*, 30:2251 – 2267, 1969.

[TH07] R. H. Telling and M. I. Heggie. Radiation defects in graphite. *Philosophical Magazine*, 87:4797–4846, 2007.

[THR81] R.C. Tatar, N.A.W. Holzwarth, and S. Rabii. Energy Band Structure of Three Dimensional Graphite. *Synth. Met.*, 3:131 – 138, 1981.

[TK70] F. Tuinstra and J. L. Koenig. Raman Spectrum of Graphite. *J. Chem. Phys.*, 53:1126–1130, 1970.

[TLH+14] T. Trevethan, C. D. Latham, M. I. Heggie, P. R. Briddon, and M. J. Rayson. Vacancy diffusion and coalescence in graphene directed by defect strain fields. *Nanoscale*, 6:2978–2986, 2014.

[TOTS10] G. Teobaldi, H. Ohnishi, K. Tanimura, and A. L. Shluger. The effect of van der Waals interactions on the properties of intrinsic defects in graphite. *Carbon*, 48:4145–4161, 2010.

[TP11] V. Tozzini and V. Pellegrini. Reversible Hydrogen Storage by Controlled Buckling of Graphene Layers. *The Journal of Physical Chemistry C*, 115:25523–25528, 2011.

[UBV88] P. Ugliengo, G. Borzani, and D. Viterbo. *MOLDRAW* - Program for the Graphical Manipulation of Molecules on Personal Computers. *J. Appl. Crystallogr.*, 21:75, 1988.

[UV88] G. Ugliengo, P. Borzani and D. Viterbo. New Developments in the MOLDRAW Graphics Program. *Z. Kristallogr.*, 185:712, 1988.

[UVC93] P. Ugliengo, D. Viterbo, and G. Chiari. MOLDRAW: Molecular Graphics on a Personal Computer. *Z. Kristallogr.*, 207:9 – 24, 1993.

[UZWTC09] P. Ugliengo, C. M. Zicovich-Wilson, S. Tosoni, and B. Civalleri. Role of Dispersive Interactions in Layered Materials: A Periodic B3LYP and B3LYP-D* Study of $Mg(OH)_2$, $Ca(OH)_2$ and Kaolinite. *J. Mater. Chem.*, 19:2564–2572, 2009.

[Val17] E. Valembois. La centrale nucléaire du Bugey. Une production d'électricité au cœur de la région Rhône-Alpes. Technical report, EDF, 2017.

[Vau10] C.E. Vaudey. *Effets de la température et de la corrosion radiolytique sur le comportement du chlore dans le graphite nucléaire : conséquences pour le stockage des graphites irradiés des réacteurs UNGG.* PhD thesis, Université de Lyon, 2010.

[VBG+10] M. Valiev, E.J. Bylaska, N. Govind, K. Kowalski, T.P. Straatsma, H.J.J. Van Dam, D. Wang, J. Nieplocha, E. Apra, T.L. Windus, and W.A. de Jong. NWChem: A comprehensive and scalable open-source solution for large scale molecular simulations. *Computer Physics Communications*, 181:1477 – 1489, 2010.

[Ven12] L. Vende. *Nuclear graphite waste's behaviour under disposal conditions : Study of the release and repartition of organic and inorganic forms of carbon 14 and tritium in alkaline media.* PhD thesis, Ecole des Mines de Nantes, October 2012.

[VGT+11] C.E. Vaudey, C. Gaillard, N. Toulhoat, N. Moncoffre, M.L. Schlegel, and L. Raimbault. Chlorine speciation in nuclear graphite studied by X-ray Absorption Near Edge Structure. *Journal of Nuclear Materials*, 418:16 – 21, 2011.

[VTM+09] C.E. Vaudey, N. Toulhoat, N. Moncoffre, N. Bérerd, L. Raimbault, P. Sainsot, J.N. Rouzaud, and A. Perrat-Mabilon. Thermal behaviour of chlorine in nuclear graphite at a microscopic scale. *Journal of Nuclear Materials*, 395:62 – 68, 2009.

[VTMB10] C.E. Vaudey, N. Toulhoat, N. Moncoffre, and N. Bérerd. Chlorine speciation in nuclear graphite: consequences on temperature release and on leaching. *Radiochimica Acta*, 98:667 – 673, 2010.

[WA05] F. Weigend and R. Ahlrichs. Balanced basis sets of split valence, triple zeta valence and quadruple zeta valence quality for H to Rn: Design and assessment of accuracy. *Phys. Chem. Chem. Phys.*, 7:3297–3305, 2005.

[WBW77] A.J. Wickham, J.V. Best, and C.J. Wood. Recent advances in the theories of carbon dioxide radiolysis and radiolytic graphite corrosion. *Radiation Physics and Chemistry (1977)*, 10:107 – 117, 1977.

[WDJ93] D. E. Woon and T. H. Dunning Jr. Gaussian basis sets for use in correlated molecular calculations. III. the atoms aluminum through argon. *The Journal of Chemical Physics*, 98:1358–1371, 1993.

[WGB93] J. D. Watts, J. Gauss, and R. J. Bartlett. Coupled-cluster methods with noniterative triple excitations for restricted open-shell Hartree-Fock and other general single determinant reference functions. Energies and analytical gradients. *The Journal of Chemical Physics*, 98:8718–8733, 1993.

[WKL09] T. O. Wehling, M. I. Katsnelson, and A. I. Lichtenstein. Impurities on graphene: Midgap states and migration barriers. *Phys. Rev. B*, 80:085428, 2009.

[Woo82] C.J. Wood. Application of radiation chemistry research to the operation of nuclear reactors. *Annals of Nuclear Energy*, 9:195 – 208, 1982.

[WSS+08] T. Wassmann, A. P. Seitsonen, A. M. Saitta, M. Lazzeri, and F. Mauri. Structure, Stability, Edge States, and Aromaticity of Graphene Ribbons. *Phys. Rev. Lett.*, 101:096402, 2008.

[XZL06] Y. J. Xu, Y. F. Zhang, and J. Q. Li. The interaction of X_2 (X = F, Cl, and Br) with active sites of graphite. *Chemical Physics Letters*, 418(4–6):413 – 417, 2006.

[Yva73] M. Yvars. Caractéristiques physico-chimiques des dépôts carbonés obtenus par radiolyse de l'oxyde de carbone - Oxydation des dépôts. Technical Report D.Tech/SPCM/73-225/MY/ES (Note 904), CEA/DMECN, 1973.

[YXQ+09] X. Yang, H. Xia, X. Qin, W. Li, Y. Dai, X. Liu, M. Zhao, Y. Xia, S. Yan, and B. Wang. Correlation between the vacancy defects and ferromagnetism in graphite. *Carbon*, 47:1399–1406, 2009.

[YY02] F. H. Yang and R. T. Yang. *Ab initio* molecular orbital study of adsorption of atomic hydrogen on graphite: Insight into hydrogen storage in carbon nanotubes. *Carbon*, 40:437–444, 2002.

[YZW+12] M. Yang, L. Zhou, J. Wang, Z. Liu, and Z. Liu. Evolutionary Chlorination of Graphene: From Charge-Transfer Complex to Covalent Bonding and Nonbonding. *The Journal of Physical Chemistry C*, 116:844–850, 2012.

[ZBL85] J. F. Ziegler, J. P. Biersack, and U. Littmark. *The Stopping and Range of Ions in Matter*. Pergamon, New York, 1985.

[ZGS+02] T. Zecho, A. Güttler, X. Sha, B. Jackson, and J. Küppers. Adsorption of hydrogen and deuterium atoms on the (0001) graphite surface. *J. Chem. Phys.*, 117:8486–8492, 2002.

[ZT08a] Y. Zhao and D. G. Truhlar. Density Functionals with Broad Applicability in Chemistry. *Accounts of Chemical Research*, 41:157–167, 2008.

[ZT08b] Y. Zhao and D. G. Truhlar. The M06 suite of density functionals for main group thermochemistry, thermochemical kinetics, noncovalent interactions, excited states, and transition elements: two new functionals and systematic testing of four M06-class functionals and 12 other functionals. *Theoretical Chemistry Accounts*, 120:215–241, 2008.

[ZUH04] R. Zacharia, H. Ulbricht, and T. Hertel. Interlayer Cohesive Energy of Graphite from Thermal Desorption of Polyaromatic Hydrocarbons. *Phys. Rev. B*, 69:155406, 2004.

[ZW06] C.M. Zicovich-Wilson. *LoptCG (Shell Procedure for Numerical Gradient Optimization)*. Instituto de Technologia Quimica, Valencia, 2006.

[ZZY+10] H. Zhang, M. Zhao, X. Yang, H. Xia, Xi. Liu, and Y. Xia. Diffusion and coalescence of vacancies and interstitials in graphite: A first-principles study. *Diamond and Related Materials*, 19:1240–1244, 2010.

[ZZY+13] L. Zhou, L. Zhou, M. Yang, D. Wu, L. Liao, K. Yan, Q. Xie, Z. Liu, H. Peng, and Z. Liu. Free Radical Reactions in Two Dimensions: A Case Study on Photochlorination of Graphene. *Small*, 9(8):1388–1396, 2013.

List of Contributions and Awards

Publications

A comment on "The interaction of X_2 (X = F, Cl, and Br) with active sites of graphite" [Xu et al., Chem. Phys. Lett., 418, 413 (2006)
Christoph Lechner, Philippe Baranek, and Holger Vach
accepted in *Chem. Phys. Lett.*

Adsorption of atomic hydrogen on defect sites of graphite : Influence of surface reconstruction and irradiation damage
Christoph Lechner, Philippe Baranek, and Holger Vach
Carbon, 2018, *127*, 437

Towards atomic-level mechanics: Adhesive Forces Between Aromatic Molecules and Carbon Nanotubes
Christoph Lechner and Alexander F. Sax
Applied Surface Science, 2017, *420*, 606

Some aspects of interface stability
Alexander F. Sax and Christoph Lechner
AIP Conference Proceedings, 2016, *1*, 1790

First-Principles Study of the Structural, Electronic, Dynamic, and Mechanical Properties of HOPG and Diamond: Influence of Exchange-Correlation Functionals and Dispersion Interactions
Christoph Lechner, Baptiste Pannier, Philippe Baranek, Nancy C. Forero-Martinez, and Holger Vach
The Journal of Physical Chemistry C, 2016, *120*, 5083

Awards

Best Student Presentation Session E: Basic research on ionic-covalent materials for nuclear applications
Multiscale Modeling of the Insertion and Diffusion of H-3 and Cl-36 in UNGG Graphite
E-MRS 2017 Fall Meeting, Warsaw, Poland

Contributions to Conferences

Talk
Multiscale Modeling of the Insertion and Diffusion of H-3 and Cl-36 in UNGG Graphite
Christoph Lechner, Philippe Baranek, and Holger Vach
E-MRS 2017 Fall Meeting, Warsaw, Poland

Talk
Multiscale Modeling of the Insertion and Diffusion of H-3 and Cl-36 in UNGG Graphite
Christoph Lechner, Philippe Baranek, and Holger Vach
CCP2017, Paris, France

Talk
Insertion and Diffusion of ^{3}H and ^{36}Cl in UNGG Graphite: Insights from a Multiscale Approach
Christoph Lechner, Philippe Baranek, and Holger Vach
INGSM-17, Vienna, Austria

Talk
Interaction of Tritium and Chlorine 36 with Defects in Graphite: Insights from Theory
Christoph Lechner, Philippe Baranek, and Holger Vach
DPG Spring Meeting, Regensburg, Germany

Talk
Interaction of Tritium and Chlorine 36 with Defects in Graphite: Insights from Theory
Christoph Lechner, Philippe Baranek, and Holger Vach
HeteroNanoCarb, Benasque, Spain

Poster
Insertion and Diffusion of ^{3}H and ^{36}Cl in UNGG Graphite: Insights from a Multiscale Approach
Christoph Lechner, Philippe Baranek, and Holger Vach
Bunsen Colloquium on Defects and Diffusion in Solids, Aachen, Germany

Appendix

A Résumé

Au cours des prochaines années, neuf centrales nucléaires de type UNGG (Uranium Naturel Graphite Gaz) devront être démantelées en France. Ces centrales utilisent le graphite comme modérateur et réflecteur de neutrons. Pendant leur exploitation, celui-ci est activé. Leur démantèlement conduira à 23000 tonnes de déchets de graphite irradiés à gérer. Ce travail focalise sur deux radionucléides contenus dans ces déchets : le ^{36}Cl et le ^{3}H. Le ^{36}Cl a l'une des demi-vies les plus longues (301 000 ans). Par contre, le ^{3}H a une demi-vie plus courte (12 ans), mais contribue beaucoup à l'activité initiale des déchets. Différentes données expérimentales suggèrent que le ^{36}Cl et le ^{3}H sont piégés à différents endroits du graphite, comme les boucles de dislocation, les surfaces ou les joints de grains. Le seul mécanisme de migration des radionucléides est le relâchement. Pour cette raison, il est important de comprendre quels sont les pièges et les différentes conditions du relâchement.

Le graphite UNGG a une structure complexe, hétérogène et multi-échelle qui diffère du monocristal idéal du graphite. Cependant, pour comprendre les données macroscopiques, les études théoriques à l'échelle nanoscopique et microscopique sont des outils importants, même si elles reposent sur des modèles plus simples. Dans cette thèse, une approche multi-échelle a été utilisée afin d'étudier les interactions des radionucléides avec le graphite ainsi que les mécanismes de diffusion et de piégeage à l'échelle du nm-μm.

Les interactions du ^{3}H et du ^{36}Cl avec différents défauts du graphite ont été étudiées dans le cadre de la théorie fonctionnelle de la densité (DFT). L'hydrogène peut former des liaisons covalentes aussi bien avec les différentes surfaces (001), (100) et (110) qu' avec le graphite massique et les défauts ponctuels contenus dans celui-ci. Les différentes hypothèses existantes de piègeage de l'hydrogène doivent être affinées: il peut être soit sur les bords zigzag ou armchair des boucles de dislocation. Différentes reconstructions de surface ont été étudiées pour la première fois afin d'étudier les pièges de l'H moins réactifs situés sur les bords des cristallites. Il a été montré que l'un d'eux est très probablement un bord de cristallite formé par une reconstruction dans le plan de la surface (100). Une reconstruction de surface en forme d'arc a également été étudiée. C'était un piège beaucoup moins réactif par rapport à l'expérience. Ceci est une preuve indirecte que les bords de cristallite sont principalement ouverts dans le graphite nucléaire. D'un point de vue thermodynamique, les liaisons formées sont très stables (de l'ordre de plusieurs eV); une grande quantité d'énergie serait ainsi nécessaire pour les briser.

Expérimentalement, le Cl existe sous deux formes dans le graphite : organique et inorganique. Comme le Cl inorganique est plus faible en concentration et donc plus facilement relâché, cela a permis de focaliser l'étude sur l'interaction de Cl et Cl_2 avec le graphite massique, les surfaces et les défauts ponctuels. Le comportement de Cl est beaucoup plus complexe que celui du H. L'interaction avec le graphite dépend fortement du site ainsi que des espèces considérés: le Cl forme de fortes liaisons covalentes avec des surfaces présentant des liaisons pendantes et des lacunes de surface (2,5-4,1 eV). La rupture de ces liens C-Cl nécessiterait également une grande quantité d' énergie. Contrairement à cela, le Cl interagit de manière non covalente avec la surface (001) par transfert de charge.

L'adsorption est plus faible par rapport aux autres surfaces (environ 0,9 eV). Ainsi, il peut être plus facilement désorbé. Lorsque Cl_2 adsorbe sur celle-ci, le comportement change à nouveau. Le Cl_2 n'interagit que par interactions de van der Waals avec celle-ci. Comme il est plus stable que deux atomes de Cl adsorbés isolés, la formation de Cl_2 est thermodynamiquement plus favorable. En raison d'interaction plus faible avec la surface, la désorption est beaucoup plus facile dans cet état.

Dans le graphite massique, les deux espèces changent à nouveau leurs propriétés. Le chlore moléculaire n'est pas stable dans le graphite massique. Cl_2 dissocie pour former du Cl atomique. Contrairement à l'hydrogène, cela indique que les pièges sont probablement localisés sur des sites qui sont situés à l'interface solide/gaz, où les liaisons pendantes sont fréquentes.

Ainsi, H et Cl peuvent être piégés sur les mêmes sites aux bords des cristallites. Lorsque les échantillons de graphite sont chauffés, Cl n'est libéré que sous la forme de HCl. Les résultats ab initio permettent de proposer trois scénarios : d'abord, une réaction en phase gazeuse de $H_2 + Cl_2 \rightarrow 2$ HCl. Deuxièmement, une réaction d'échange sur les bords cristallites du type $\sim$C–Cl + $H_2 \rightarrow \sim$C–H + HCl. Ceux sont des réactions thermodynamiquement favorables qui sont confirmés par les résultats obtenus. Un troisième scénario est cinétique : Le dépiègage concerté de HCl pourrait avoir une barrière plus faible que le dépiègage de H_2 ou Cl_2 . Ce scénario doit être approfondi en calculant les barrières des différentes réactions de dépiègage.

L'étude de l'insertion et la diffusion des radionucléides dans le graphite nucléaire nécessite l'exploration de processus à des échelles de longueur et temps plus longues que ce qui est actuellement réalisable par les méthodes ab initio. Ainsi des modèles de potentiel d'interaction atomique ont été développés pour utiliser des simulations de dynamique moléculaire. Pour C-Cl, un potentiel de type «bond order» a été développé qui peut correctement décrire toutes les différentes interactions trouvées au niveau ab initio. Pour C-H, un le potentiel existant a été modifié. Il peut décrire correctement les interactions sur les surfaces avec des liaisons pendantes.

Des simulations de diffusion de H le long de différents bords de cristallites ont montré un piégeage sur des atomes de carbone insaturés. Cela a confirmé l'hypothèse concernant le piègeage du H plus faible du graphite nucléaire.

Pour Cl, plusieurs scénarios ont été explorés: d'abord, l'insertion dans des modèles de cristallites de graphite parfaits et irradiés avec des énergies de «primary knock-on atom» (PKA) allant de 0,5 à 10 keV. Deuxièmement, la diffusion dans

des modèles complexes de graphite nucléaire vierges et de cristallites de graphite endommagés par irradiation a été étudiée.

Les cascades de déplacement dans le graphite massique avec le Cl comme PKA décrivent globalement les mêmes tendances observées pour les cascades de déplacement trouvés dans la littérature avec le C comme PKA. Cependant, il a été démontré dans ce travail qu'ils ne sont pas en mesure de remplacer l'irradiation explicite des surfaces de graphite. Une dépendance claire de la température de l'endommagement créé est trouvée pour l'irradiation de surface, alors qu'il est absent pour les cascades dans le graphite massique. De plus, une dépendance des dommages en fonction de l'angle d'incidence du PKA a été montrée pour des interfaces solide / gaz.

Pour toutes les irradiations de surfaces, l'accroissement de la température augmente le nombre de dommages directes d"irradiation. Pour les angles d'incidence <90°, des dommages restent localisés proches de la surface. La plus haute occurrence de l'effet «channeling» est trouvée pour l'irradiation des surfaces (100), (110) et des surface reconstruites avec un angle d'incidence de 90°. Cet effet conduit à une distribution de défauts plus large.

Dans les conditions de réacteur, l'irradiation n'est pas un événement singulier. Les surfaces (001) ainsi qu'un joint de grain ont été irradiés d'une façon répéteé avec des énergies PKA comprises entre 0,5 et 2,5 keV pour étudier l'influence sur les propriétés micro- et macroscopiques.

Moins de défauts sont créés par PKA avec des dommages croissants de la microstructure de cristallite. L'irradiation répétée conduit à de grandes zones amorphes proches de la surface et de défauts ponctuel plus en profondeur dans le graphite massique. La zone amorphe absorbe l'énergie de PKA partiellement ce qui diminue le nombre de défauts créés par PKA. La surface se détériore, et, pour les angles d'incidence <90°, un trou est formé en raison de détachement des atomes de surface. Tous ces effets sont intensifiés lorsque la température augmente.

L'irradiation répétée du joint de grains a révélé un nouvel aspect : Une accumulation de défauts est observée au joint de grains sous la zone amorphe à un angle d'incidence <90°. Ceci est probablement en raison des différences de contraintes dans la zone amorphe et les zones ordonnées plus profondes. Cette tendance s'intensifie avec l'augmentation de la température. Cela indique que les joints de grains peuvent être des sites de piègeage préférés pour les radionucléides en raison de l'abondance plus élevée de défauts dans cette région. La différence de température aussi montre que le piégeage sur ces sites sera plus fréquent dans les zones les plus chaudes.

Les bords de cristallites avec des liens pendants sont de forts pièges pour Cl. Quand la concentration des sites de piégeage disponibles est inférieure à la concentration de Cl dans la phase gazeuse, le Cl diffuse librement dans la phase gazeuse sous forme de Cl_2. La pénétration dans le graphite massique est seulement observée pour des concentrations beaucoup plus élevées que celles trouvées dans le graphite nucléaire. Le Cl peut ensuite diffuser librement à travers les pores.

Les simulations de diffusion dans le modèle complexe du graphite nanoporeux donnent des informations substantielles en ce qui concerne le piégeage et la diffusion de Cl dans le graphite nucléaire. La diffusion libre se produit le long des surfaces (001). Quand le Cl passe sur un site de piégeage disponible, il forme une liaison et

reste fixé. Ces deux observations confirment les résultats ab initio. En outre, un processus complètement inconnu a été trouvé: le Cl montre une tendance à migrer vers les coins des nanopores où deux cristallites ne sont séparés que de quelques Å. Dans cette zone, il n'est ni complètement piégé en formant des liaisons covalentes ni ne peut partir en direction de pores sans surmonter une barrière.

Dans les cristallites de graphite irradiés, le Cl ne diffuse pas mais forme immédiatement des fortes liaisons covalentes avec les défauts environnants. Il est localisé dans la zone très endommagée. Ceci explique les résultats expérimentaux lorsque Cl est implanté dans graphite : Lorsque le système est chauffé, les défauts sont recuits et le Cl diffuse vers la surface en raison de l'instabilité du graphite massique.

En résumé, ce travail pourrait confirmer et prolonger plusieurs hypothèses existantes concernant le piégeage du ^{3}H et du ^{36}Cl dans le graphite nucléaire. En outre deux nouveaux sites de piégeage sont proposés: dans le graphite irradié, les joints de grains peuvent être les pièges préférés pour tous les radionucléides en raison de leur abondance plus élevée. L'étude en température montre que les joints de grains dans les zones plus chaudes seront préférés à ceux des zones plus froides. En outre, un nouveau piège métastable dans les coins des nanopores est proposé pour le ^{36}Cl.

B Computational Details of the *Ab Initio* Calculations

B.1 Determination of Cohesive Energies and Interlayer Interaction Energies

In the following, the methodology for the determination of cohesive energies and interlayer interaction energies which are presented in section 4.1.1 is described.

Cohesive energies, E_{coh}, were evaluated with respect to the isolated atoms. For both codes, the equilibrium energies of bulk graphite and diamond were corrected by the zero point energy. The cohesive energy follows this definition:

$$E_{coh} = \frac{N_0 E_C - E_{Bulk}}{N_0} \tag{6.2}$$

where E_C, E_{Bulk} and N_0 represent the energy of an isolated carbon, the energy of the primitive cell of the bulk graphite (or diamond) and the number of carbon atoms per primitive cell, respectively. The E_C calculations have been performed in the spin-polarized framework and carbon in its triplet state.

Contrary to plane wave basis sets, Gaussian-type basis sets are non orthogonal and therefore suffer from the BSSE. Thus, for CRYSTAL, E_{coh} was corrected for the BSSE according to the counterpoise method of Boys and Bernardi[BB70]. To evaluate it, a three layer (001) HOPG surface, periodic along the [100] and [010] directions, was defined; then, the energy of an isolated carbon was determined by placing it at the center of a 4 × 4 supercell of the slab with all of its neighbors treated as ghost atoms. For diamond, the BSSE was evaluated from the energy of an isolated carbon at the center of a cluster of 80 ghost atoms "cut" in the bulk material.

For QUANTUM-ESPRESSO, the energy of the isolated carbon was obtained by using a cubic supercell with a lattice parameter of 15 Å.

The interlayer interaction energy, E_{IL}, follows this definition:

$$E_{IL} = E_I - E_{IL}^{Bulk} \tag{6.3}$$

where E_I and E_{IL}^{Bulk} are the energies of an isolated graphene plane and of a graphene plane in graphite, respectively. E_{IL}^{Bulk} is the energy difference between a seven and a six layer (001) surface.

For CRYSTAL, E_{IL} was also corrected for the BSSE following the scheme of Boys and Bernardi [BB70]. To evaluate it, the energy of an isolated graphene plane with a single layer of ghost atoms above and below was determined.

For QUANTUM-ESPRESSO, which uses a 3D model of the surfaces, the various slabs were separated by a void of 10 Å.

B.2 Surface Energies

The surface energy E_{surf} is as presented in section 4.2.1 is calculated with the following equation:

$$E_{surf} = \frac{E(n) - n \cdot E_{bulk}}{2A} \tag{6.4}$$

Here, $E(n)$ is the energy of a n-layer slab, E_{bulk} the energy of a single layer of bulk material, and A is the area of the created surface. The surface energy tends to converge much slower than other properties, therefore we increased n to 36, 16, and 7, for the surfaces (100), (110), and (001), respectively.

B.3 Formation Energies

The formation energies E_{form} of the reconstructed surfaces as presented in section 4.2.2 was calculated as the energy difference between the energy of the reconstructed surface and the unreconstructed surface.

The determination of E_{form} of the vacancies at the (001) surface is more complex since it involves removal of carbon atoms out of the system. It is defined as follows:

$$E_{form} = E_G^{vac} - E_G + n\mu_C \tag{6.5}$$

Here, E_G^{vac} is the energy of the graphite structure with vacancies, E_G is the energy of the pristine graphite structure, n is the number of removed carbon atoms and μ_C is the chemical potential of carbon. It is approximated as the energy of a carbon in its triplet state. The formation energy is corrected for the basis set superposition error with the same approach as described in the next section.

B.4 BSSE Correction of Adsorption Energies

Gaussian-type basis sets suffer from the basis set superposition error (BSSE). For all *ab initio* calculations which describe adsorption processes (see sections 4.2-4.3, the counterpoise method of Boys and Bernardi [BB70] was modified by using a dressed particle approach to get rid of the BSSE. The adsorption energy E_{ad} is the energy difference between a hydrogen dressed with all the interactions with its surroundings (E_H^{dr}) and an isolated hydrogen in its atomic reference state. E_H^{dr} is defined as follows:

$$E_H^{dr} = \frac{E_0 - E_G^{opt} - E_G^{X\,H} - E_G - \sum_{i=1}^{n} E_{H_i}^{X\,G} + E_H}{n} \tag{6.6}$$

where E_0 is the total energy of the optimized system, E_G^{opt} the energy of the optimized surface without adsorbates, $E_G^{X\,H}$ the energy of the optimized system with all adsorbed atoms treated as ghost atoms, E_G the energy of the surface with the geometry of the optimized system and the adsorbates removed, $E_{H_i}^{X\,G}$ the energy of the system with all adsorbed atoms except the i^{th} atom treated as ghost atom, and E_H the energy of the isolated hydrogen. n is the number of adsorbed atoms.

The BSSE contribution to the graphite matrix is determined in the graphite-adsorbate structure according to the counterpoise method of Boys and Bernardi [BB70].

C Additional Structures for the Adsorption of H on (100) and (110) Surfaces

In this section, additional optimized geometries as described in section 4.2.1 are shown in Figure C.1. They refer to adsorption of two H atoms per edge carbon on the (100) and (110) surface, respectively.

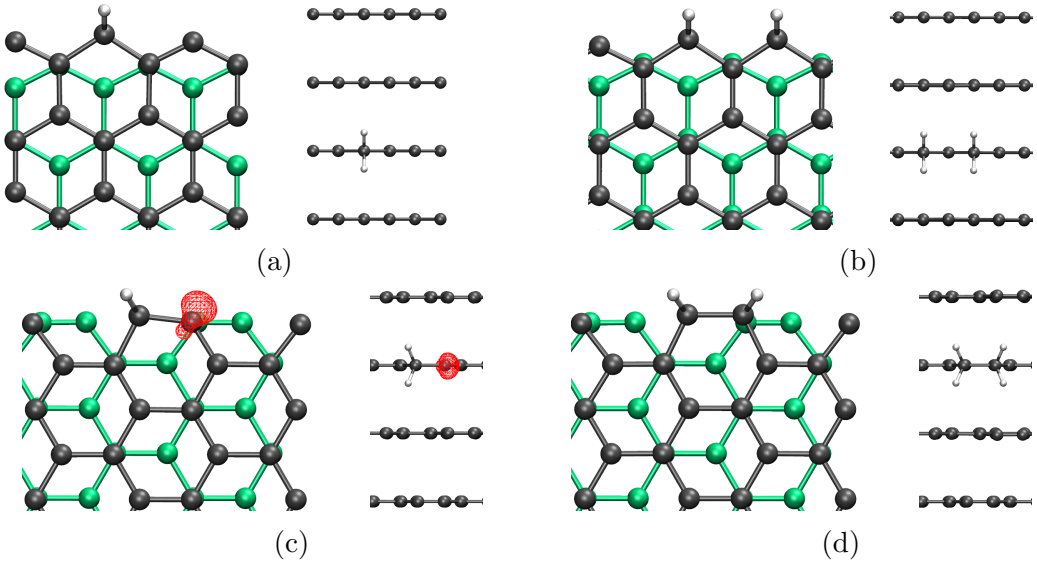

Figure C.1: Side (left) and top view (right) of optimized structures of hydrogen chemisorption on the investigated surfaces. Isovalues for spin density plots are 0.05 e/bohr^3. Two H per edge carbon for the (100) surface for (a) one and (b) two edge carbons and for the (110) surface for (c) one and (d) two edge carbons.

D Additional Structures for the Adsorption of H on Reconstructed Surfaces

In this section, additional optimized geometries as described in section 4.2.2 are shown in Figure D.1. They refer to adsorption of H on the bilayer models of the arch-type surface reconstructions $(100)^{bilayer}_{arch}$ and $(110)^{bilayer}_{arch}$, respectively.

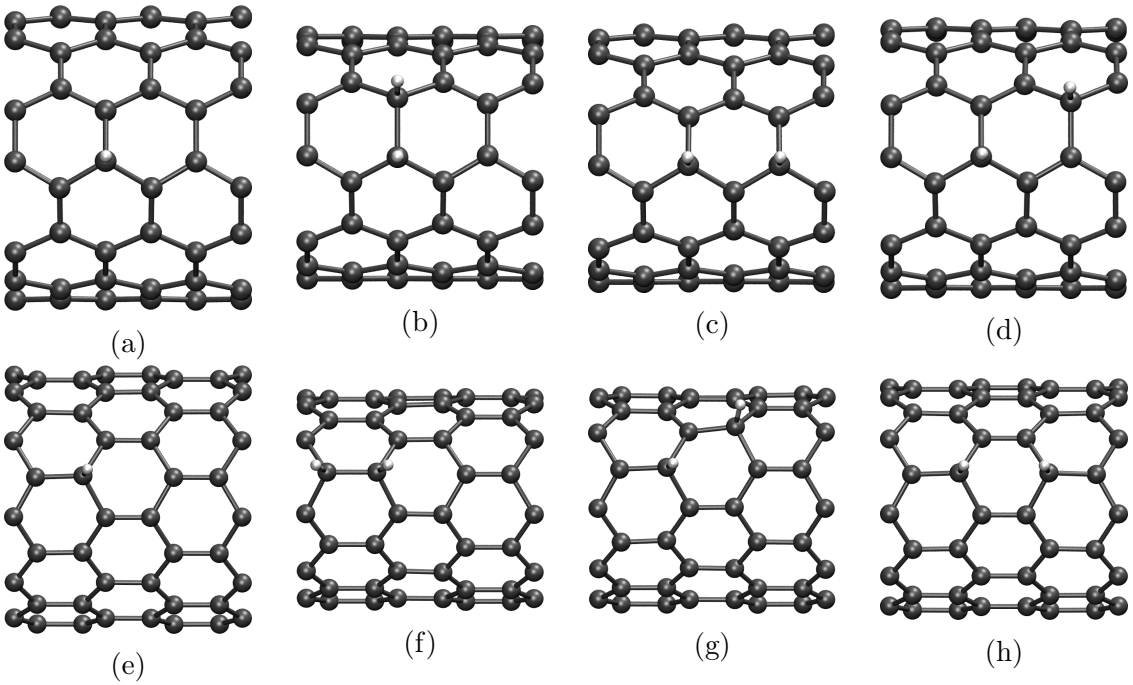

Figure D.1: Top view of optimized structures of hydrogen chemisorption at the graphene bilayer models. (100) surface: (a) 1 H, (b) 2H *ortho*, (c) 2H *meta*, (d) 2H *para*. (110) surface: (e) 1 H, (f) 2H *ortho*, (g) 2H *meta*, (h) 2H *para*.

E The Adsorption of F_2, Cl_2, and Br_2 on Molecular Models of the (100) and (110) Surfaces of Graphite

This section is dedicated to the evaluation of the results published by Xu *et al.* [XZL06] regarding the adsorption of F_2, Cl_2, and Br_2 on active sites of graphite. This was necessary due to the qualitative disagreement between the results of Xu *et al.* and those presented in section 4.3.1.

In their article, Xu *et al.* [XZL06] present the adsorption energies for the chemisorption of the three halogens F_2, Cl_2, and Br_2 on the active sites of graphite. The three investigated systems are finite models of the three most stable surfaces, (001), (100), and (110). The latter two are also called zigzag and armchair surface, respectively. These surfaces were modeled by the molecules in a cluster approach (see Figure **??**), which is an established technique for these systems [MTS00]. While studying similar systems, we compared our results to the published results and found several discrepancies which, we feel, need some clarification. In their paper Xu *et al.* state: *"The correct ground state was determined by means of single point energy calculations for different electronic states and the lowest energy electronic state was determined to be the selected ground state (the ground electronic spin multiplicity is 1, 7 and 3 corresponding to the model A, B and C, respectively).“* It is not completely clear to us if this refrains only to the electronic states of the isolated surface models or as well to the systems containing the adsorbed halogens. We assume that these states were selected for both, the isolated models as well as the models with adsorbed halogens. Performing the calculations in the indicated electronic states for both, the adsorbed surface models as well as the isolated models, did not allow us to reproduce the results of Xu *et al.*; adsorption energies varied up to 20 kcal/mol. Nevertheless, we obtained the same order of the adsorption energies for the different surface models. This leads us to believe that they used this approach.

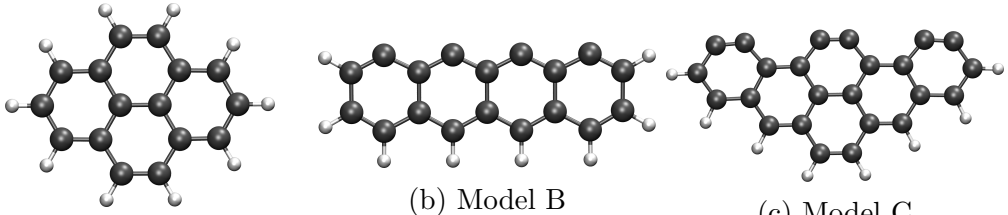

(a) Model A (b) Model B (c) Model C

Figure E.1: Models for the (001) surface (a), the (100) surface (b), and the (110) surface (c).

The ground state of model A has a spin multiplicity of 1 due to the even number of electrons in the system and the two-fold symmetry axis. However, for model B, Montoya *et al.* showed that the ground state has a spin multiplicity of 5 [MTS00], in contrast to the results of Xu *et al.* who found a ground state with a spin multiplicity of 7.

Due to this discrepancy, we decided to re-evaluate the results of Xu *et al.* in order to investigate the impact on the adsorption energies. All calculations were performed with NWChem [VBG+10]. To be able to compare our results to those of Xu *et al.*, we also used the B3LYP functional [Bec93, LYP88] in the spin-unrestricted formulation. Xu *et al.* optimized the systems with the 3-21G(d) basis [HP73, FPH+82, RRP+01] and recalculated the energies of the resulting optimized structures with the bigger 6-31G(d) basis [HP73, FPH+82, RRP+01]. We decided to optimize the systems with the 6-31G(d) basis to avoid possible errors due to this approach. Additionally, all systems were optimized with the larger Def2-TZVP basis set [WA05] for better accuracy. All optimizations were performed in C1 symmetry to let the systems relax out of the plane if needed. For model B, all calculations were performed with spin multiplicities 3, 5, and 7; for model C, the spin multiplicities were 1, 3, and 5. VMD was used for visualization and image creation [HDS96].

For model A, our results agree with Xu *et al.* Only the optimized distances between adsorbent and adsorbate are mostly longer. For the series F_2, Cl_2, and Br_2 the adsorption energies are 0.62 (-0.01), -0.01 (-0.01), and -0.01 (-0.01) kcal/mol for the basis 6-31G(d) (Def2-TZVP). The distances are 3.23 (4.15), 9.55 (9.58), and 10.91 (11.14) Å. However, since there is next to no interaction due to the missing dispersion interaction in the functional, this is likely caused by different convergence criteria. Since we found agreement for this model, we will no longer discuss these properties and refer to the original paper.

For the zigzag and armchair surface (models B and C), the relative energies of the different electronic states with respect to the ground state are given in Table E.1. They were obtained with the 6-31G(d) basis to compare our results to Xu *et al.*

For model B, our results agree with Montoya *et al.*; the ground state has a spin multiplicity of 5. However, this state shows a significant amount of spin contamination. The expectation value of S^2 is 6.22 compared to the theoretical value of 6. To validate that the order of the electronic states is not wrong due to spin contamination, separate ROHF calculations were performed. In agreement with Montoya *et al.*, the same order as presented in Table E.1 was recovered. This gives us confidence that the unrestricted formulation of the used density functional yields reliable results.

For model C, the ground state has a spin multiplicity of 1. This state is 1.44 eV lower than the triplet state.

At this point, we want to reiterate that Xu *et al.* report ground state spin multiplicities of 7 and 3 for models B and C, respectively. This indicates some systematic error in their results due to the choice of excited states as references.

The optimized ground state structures for adsorption of F_2, Cl_2, and Br_2 on models B and C obtained with the basis Def2-TZVP are shown in Figures E.2 and E.3. In Table E.2, the adsorption energies obtained with the two different basis sets are given. The reference values of Xu *et al.* are also given for comparison.

The optimized ground state structures for adsorption of F_2, Cl_2, and Br_2 on models B and C obtained with the basis Def2-TZVP are shown in Figures E.2 and E.3. In Table E.2, the adsorption energies obtained with the two different basis

Table E.1: Relative energies in eV of the different electronic states of the model systems obtained with B3LYP/6-31G(d).

	Multiplicity		
System	3	5	7
zigzag surface	1.07	0.00	1.04
F_2/zigzag surface	0.00	1.13	5.27
Cl_2/zigzag surface	0.00	1.05	4.36
Br_2/zigzag surface	0.00	1.05	6.37
	Multiplicity		
	1	3	5
armchair surface	0.00	1.44	2.72
F_2/armchair surface-M1	0.00	0.00(4)	1.39
F_2/armchair surface-M2	0.00	1.40	2.79
Cl_2/armchair surface-M3	1.78	0.00	1.60
Cl_2/armchair surface-M4	0.00	1.43	2.87
Br_2/armchair surface-M5	1.44	0.00	1.39
Br_2/armchair surface-M6	0.00	1.41	2.83

sets are given. The reference values of Xu *et al.* are also given for comparison.

For model B, the ground state has a spin multiplicity of 3 after halogen adsorption due to the formation of two covalent bonds. Since Xu *et al.* chose an excited state as ground state for the adsorbed and the isolated surface models, this has a large impact on the adsorption energies. Our results are consistently higher by about 80 kcal/mol. This gives an error of 50-600% for the results of Xu *et al.*!

For model C, the ground state spin multiplicity of the adsorbed species depends on the adsorption site. For structures M3 and M5 the ground state has a spin multiplicity of 3. For M1, the energies of the singlet and the triplet state differ only by 0.004 eV. The singlet state is the ground state. This difference with respect to M3 and M5 is probably due to substantial spin contamination. The expectation value of S^2 is 1.03 compared to the theoretical value of 0. For the larger basis Def2-TZVP, the triplet state is the ground state. In addition, no spin contamination is observed for the singlet state. For M2, M4, and M6, the ground state has a spin multiplicity of 1. Our results for this surface show the same trend as Xu's. However, all our adsorption energies are lower. Depending on the system, the discrepancy is about 10-30 kcal/mol. This gives errors up to 42% for this surface.

Thus, Xu *et al.* chose the right ground state for the (001) surface, whereas they chose excited states for the other two investigated surfaces. This leads to adsorption energies of poor quality. We agree with Xu in the findings, that the order for the adsorption energies with respect to the halogens is $F_2 > Cl_2 > Br_2$. However, as can be seen in Table E.2, the relative stabilities for adsorption on the zigzag and armchair surfaces show some important differences between our results and those of Xu *et al.* We find, that the halogens adsorb the strongest on the zigzag surface. For hydrogen, the same trend was shown by several authors [YY02, LBV18]. The second strongest adsorption is found on the armchair surface for the symmetric configurations (M2, M4, and M6), the third strongest for the

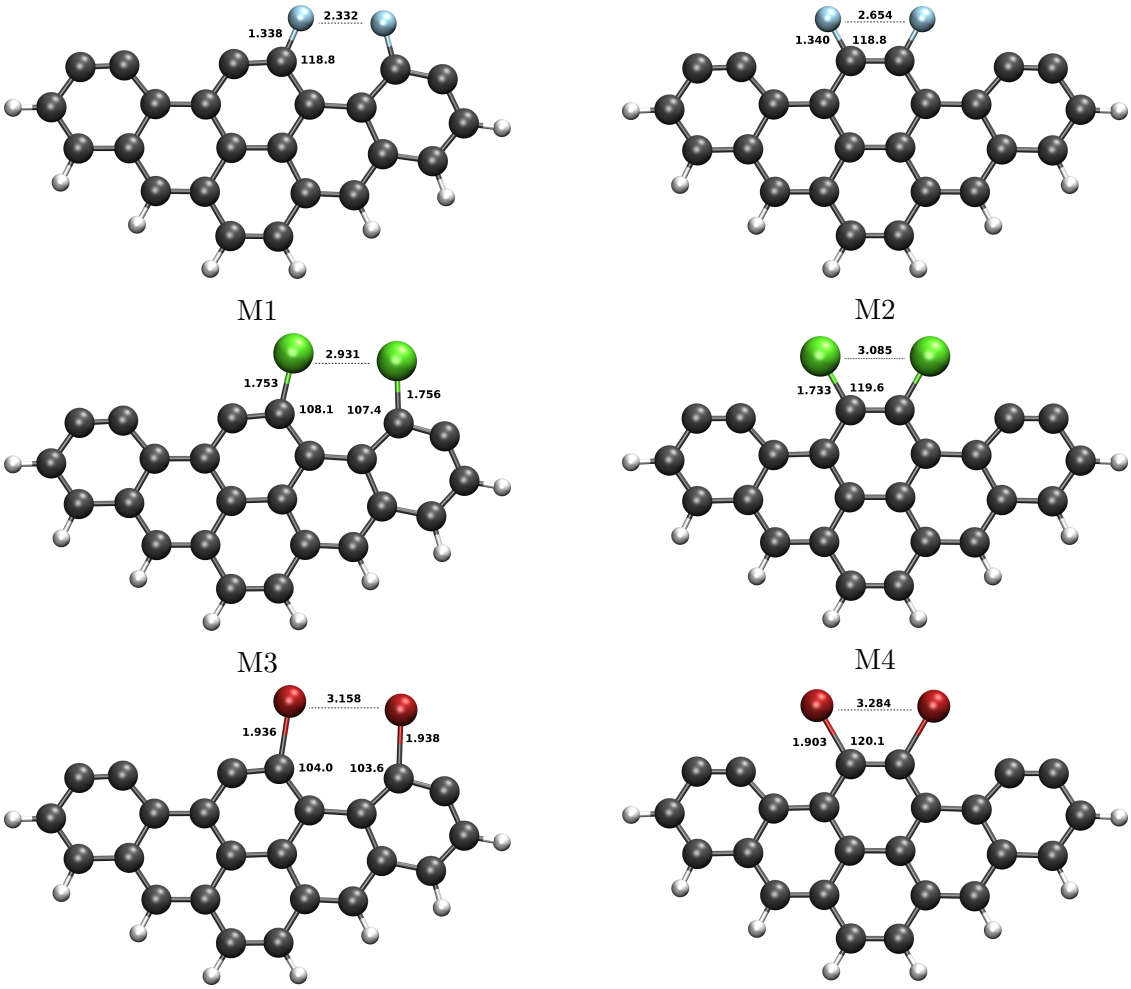

Figure E.2: Optimized geometries of adsorbed F_2 (M1 and M2), Cl_2 (M3 and M4), and Br_2 (M5 and M6) on the armchair surface of graphite.

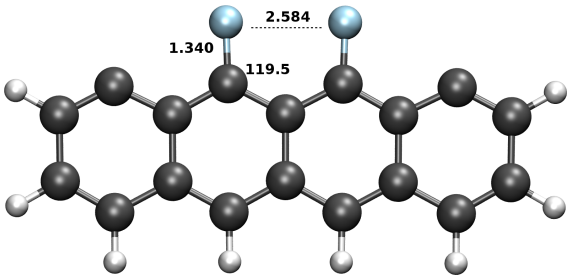

(a)

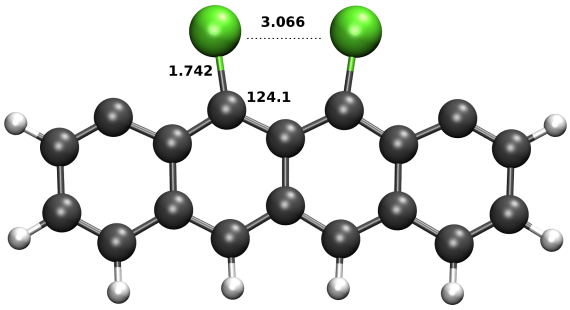

(b)

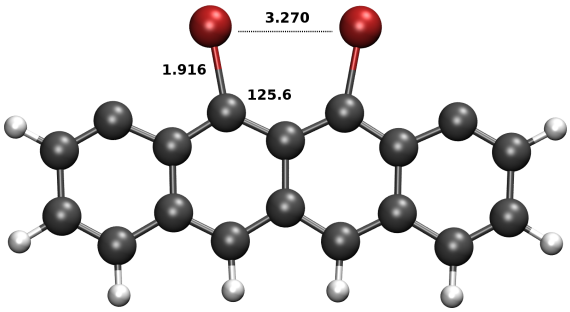

(c)

Figure E.3: Optimized geometries of adsorbed F_2 (a), Cl_2 (b), and Br_2 (c) on the zigzag surface of graphite.

Table E.2: Adsorption energies in kcal/mol for the different systems obtained with B3LYP/6-31G(d) and B3LYP/def2-TZVP, respectively. The results of Xu *et al.* are given for comparison.

System	6-31G(d)	Def2-TZVP	Ref.[XZL06]
F_2/zigzag surface	212.6	209.3	138.7
Cl_2/zigzag surface	124.4	118.1	48.2
Br_2/zigzag surface	100.2	97.1	17.3
F_2/armchair surface-M1	149.9	142.5	177.7
F_2/armchair surface-M2	185.0	179.6	201.4
Cl_2/armchair surface-M3	51.1	40.5	61.9
Cl_2/armchair surface-M4	103.1	94.1	116.1
Br_2/armchair surface-M5	26.0	18.9	37.4
Br_2/armchair surface-M6	80.0	74.3	82.0

asymmetric configurations (M1, M3, and M5).

Lifting symmetry restrictions for optimization of these structures is also important. This is especially true for the adsorption of Cl_2 and Br_2 on the zigzag surface. In C_S symmetry, the ground state has a spin multiplicity of 5. By performing the optimization in C_1 symmetry, the triplet becomes the ground state. We also want to point out that the reported adsorption energies with and without basis set superposition error (BSSE) in Table 1 of Xu *et al.* seem to be interchanged since correcting for the BSSE should result in lower adsorption energies.

To summarize, the determination of adsorption energies by Xu *et al.* seems to be flawed by several errors. By calculating the adsorption of halogens on graphite surface models in excited states, their adsorption energies differ up to 80 kcal/mol from our results. Even more so, their results are also qualitatively wrong. They predict stronger adsorption of the halogens on the armchair surface than on the zigzag surface. However, in fact the opposite behavior is observed as shown by our results. Our results show that in fact, the halogen systems show the same trend of stability as hydrogen. The zigzag surface binds the halogens the strongest. The adsorption energies for the armchair surface are significantly lower. Here, adsorption in the symmetric configuration is more stable than in the asymmetric one.

université PARIS-SACLAY
ÉCOLE DOCTORALE
INTERFACES
Approches Interdisciplinaires : Fondements, Applications et Innovation

Titre : Modélisation multi-échelle de l'insertion du ^{3}H et du ^{36}Cl dans les graphites UNGG

Mots clés : graphite irradié, modélisation multi-échelle , théorie de la fonctionnelle de la densité (DFT), dynamique moléculaire, tritium, chlore-36

Résumé :
Pour optimiser la gestion des déchets de graphite nucléaire qui était utilisé dans les centrales nucléaires de type UNGG (Uranium Naturel Graphite Gaz), il est important de comprendre les propriétés des impuretés activés, comme le ^{3}H et le ^{36}Cl. Le graphite UNGG a une structure complexe, hétérogène et multi-échelle. Dans cette thèse, une approche multi-échelle a été utilisée afin d'étudier les interactions des radionucléides avec le graphite ainsi que les mécanismes de diffusion et de piégeage à l'échelle du nm-µm.

Les interactions du ^{3}H et du ^{36}Cl avec différents défauts du graphite ont été étudiées dans le cadre de la théorie fonctionnelle de la densité (DFT). L'hydrogène forme une liaison covalente avec le graphite massique ainsi qu'avec ses surfaces (001), (100) et (110) et plusieurs reconstructions de surface.
Le comportement du Cl est plus complexe. Sa chimisorption est observée sur les surfaces (100) et (110). Cependant, sur la surface (001), le Cl interagit par transfert de charge. Le Cl_2 n'interagit que par interactions de van der Waals avec celle-ci. Le Cl_2 se dissocie dans le graphite massique.

Les diffusions du H et du Cl dans le graphite irradié ont été étudiées en effectuant des simulations de dynamique moléculaire. Les résultats ab initio ont été utilisés pour développer des potentiels de type « bond order ». Pour le Cl, un nouveau potentiel a été paramétré qui reproduit toutes les données obtenues au niveau DFT.

Plusieurs modèles atomiques ont été utilisés: les surfaces, les joints de grains et les nanopores. Pour le Cl, des simulations d'irradiation ont été réalisées pour une gamme d'énergie allant de 0.5 à 10 keV et une gamme de température de 200 à 500ºC. D'une façon générale, les dommages causés par l'irradiation perpendiculaire aux surfaces augmentent avec la température. Les diffusions du H et du Cl montrent que tous les bords de cristallites avec des liaisons pendantes sont des pièges. Pour le Cl, la diffusion dans le graphite nanoporeux a révélé deux emplacements préférés: les bords des cristallites où le Cl forme une liaison covalente et les coins des microfissures où le Cl interagit par transfert de charge.

Title : Multi-scale Modeling of the Insertion and Diffusion of ^{3}H and ^{36}Cl in UNGG graphite

Keywords : irradiated graphite, multi-scale modeling, density functional theory, molecular dynamics, tritium, chlorine-36

In order to optimize the waste management of nuclear graphite used in UNGG (natural uranium graphite gas) power plants, it is important to understand the properties of the activated impurities it contains, such as ^{3}H and ^{36}Cl. UNGG graphite has a complex heterogeneous multi-scale structure. A multi-scale approach was therefore applied to study the local interactions of the radionuclides with graphite as well as diffusion and trapping mechanisms on the nm-µm length scale.

First, the interaction of ^{3}H and ^{36}Cl with defects in graphite was studied with density functional theory (DFT). Hydrogen interacts covalently with bulk graphite as well as with the studied surfaces (001), (100), and (110) as well as arch-type and in-plane reconstructions. The behavior of Cl is more complex. On the (100) and (110) surface chemisorption is observed. However, on the (001) surface a strong charge transfer interaction is observed for Cl. In contrast to that, Cl_2 only interacts via weak van-der-Waals interactions with this surface. In bulk graphite Cl_2 dissociates.

The diffusion of H and Cl in irradiated graphite has been investigated by performing molecuar dynamics simulations. The ab initio results were used to develop bond order potentials. For Cl, a new potential has been parameterized which is able to describe all aspects obtained with DFT.

Different models were studied : surfaces, grain boundaries and nanopores. For Cl, irradiation simulations of different systems were performed up to an energy of 10 keV for the primary knock-on atom (PKA), and in a temperature range of 200 to 500ºC. Overall, direct irradiation damage increases with temperature. Diffusion of H and Cl along surfaces shows that all crystallite edges with dangling bonds can serve as traps. For Cl, diffusion in nanoporous graphite revealed two preferred locations: Crystallite edges where Cl forms strong covalent bonds and corners of microcracks where Cl interacts via charge transfer.

Université Paris-Saclay
Espace Technologique / Immeuble Discovery
Route de l'Orme aux Merisiers RD 128 / 91190 Saint-Aubin, France